CONSTITUTIVE BEHAVIOR OF ALUMINUM ALLOY SHEET AT HIGH STRAIN RATES

by

Rafal Olaf Smerd

A thesis
presented to the University of Waterloo
in fulfillment of the
thesis requirement of the degree of
Master of Applied Science
in
Mechanical Engineering

Waterloo, Ontario, Canada, 2005

I hereby declare that I am the sole author of this thesis. This is a true copy of the thesis, including any required final revisions, as accepted by my examiners.

I understand that my thesis may be electronically available to the public.

ABSTRACT

The drive to produce lightweight vehicles with improved fuel economy has resulted in an increased interest in utilization of aluminum alloys for automotive body structures due to their higher strength-to-weight ratio. To support the utilization of aluminum alloys in automobile structures, their dynamic behavior must be considered under crash conditions, although traditionally, the strain rate sensitivity of aluminum alloys has been considered to be low. In this work, three aluminum sheet alloys, AA5754, AA5182 and AA6111, which are prime candidates for replacing mild steel in automobile structures, are tested in tension at quasi-static and high strain rates.

In order to characterize the constitutive response of AA5754, AA5182 and AA6111 at high strain rates, tensile experiments were carried out at strain rates between 600 s^{-1} and 1500 s^{-1}, and at temperatures between ambient and 300°C, using a tensile split Hopkinson bar (TSHB) apparatus. As part of this research, the apparatus was modified in order to provide an improved means of gripping the sheet specimens. Quasi-static experiments also were conducted using an Instron machine.

The tensile experiments showed that the rate sensitivity of the flow stress is low for these alloys, with the strain hardening response of AA5754 showing a mild sensitivity to strain rate in the range of strain rates considered. However, increases in strain rate appeared to significantly enhance the ductility of these alloys. Analysis of the stress-strain data demonstrated that the strain at which Considere's criterion is satisfied increased at rates of high strain. This behavior implies that the onset of necking is delayed under high rate conditions, permitting the material to elongate more prior to localization. Levels of damage in AA5754 and AA5182 were also found to increase with strain rate, presumably due to the elevated strains to failure.

The experimental data was fit to the Johnson-Cook and Zerilli-Armstrong constitutive models for all three alloys. The resulting fits were evaluated by numerically simulating the tensile experiments conducted using a finite element approach. Of the two models, the Zerilli-

Armstrong constitutive model was more accurate in predicting the flow stress of these materials at the strain rates and temperatures considered. The finite element simulations using both constitutive models were unable to accurately predict the necking strain of these alloys.

ACKNOWLEDGEMENTS

I would like to thank my supervisor, Professor Michael Worswick for giving me the opportunity to pursue a Master's degree as part of his research group and for his knowledge, guidance and support during my graduate studies. I am grateful to Novelis Global Technology Centre for making this work possible, and would like to acknowledge David Lloyd and Mark Finn for their support.

I would like to thank Chris Salisbury for his guidance and help in understanding various aspects of the split Hopkinson bar and in developing the test method employed in this work. Thanks to Tom Gawel for installing a countless number of strain gauges. Don't worry Tom, I won't be breaking anymore. A special thanks to Dr. Sooky Winkler for her invaluable metallographic work and damage analysis.

There have been many people who have supported me along way. To Dino, thanks for the years of friendship and laughs, and for putting me in contact with Professor Worswick. Thanks to Jose for sharing sources on high rate testing, material properties and FK9. Blake I thank for all his help with LS-DYNA and for his "witty" comments. The office was always a friendly environment with Oleg, Alex B., Rassin, Chris, Sooky, Javad, Zengtao, and Hari around, thanks guys. To all my friends, the soccer boys, and the "Kitchener Crew" (you know who you are), I can't thank you enough for all the years.

And finally, my family. I don't think this would have been possible without your support and understanding. Mom, Dad, my brother Dave, aunt Roma, you have been there for me through thick and thin, and have allowed me to grow into who I am. Words cannot describe my gratitude. Thank you.

TABLE OF CONTENTS

LIST OF TABLES

LIST OF FIGURES

1 INTRODUCTION

The need to produce lightweight vehicles to improve fuel economy has resulted in an increased interest in utilization of aluminum alloys for automotive body structures. Between 1995 and 2000, the use of aluminum has increased by over 80% in automotive applications [1]. Aluminum intensive space frames that reduce vehicle body weight by up to 40% have been successfully employed, the advantage of aluminum lying in its high strength-to-weight ratio [1]. To match the strength-to-weight ratio of an aluminum alloy such as AA5182, the tensile strength of steel would need to be as high as 750 MPa [2]. Although this strength level is quite achievable, the stretch-formability of steels such as high-strength low-alloy steels is generally inferior to that of aluminum alloys at those required strength levels [2]. One issue to be considered prior to the introduction of aluminum alloys in automotive body structures is their performance during crash events. Upon impact, the anticipated local strain rates are high within the folding sections of crush structures, underlying the importance in understanding the material's strain rate sensitivity when simulating these events.

Another application requiring consideration of the high rate constitutive response of aluminum alloys is electromagnetic (EM) forming. Oliveira [3] reported strain rates reaching $3500\ s^{-1}$ during EM forming processes. Imbert *et al*. [4] performed EM forming experiments on AA5754 and AA6111 and their data has shown that strains to failure that are beyond the conventional quasi-static forming limits are achievable for aluminum alloys using EM forming. This increase is attributed to tool/sheet interaction, inertial stabilization of necking, and material rate sensitivity [4].

The purpose of the research presented in this thesis is to determine the high strain rate tensile behavior of aluminum sheet alloys used in the automotive industry. The alloys of interest in this work are AA5754, AA5182, and AA6111. These alloys are alternatives to conventional mild steel in automotive body panels and structures. AA5754 and AA5182 are commonly used for structural members and inner body panels, while AA6111 is utilized for outer body panels. In this work, the three alloys were tested in tension at quasi-static and elevated strain rates.

Dynamic tensile tests were performed between 600 s^{-1} and 1500 s^{-1} at temperatures between room temperature and 300°C using a tensile split Hopkinson bar apparatus. An Instron apparatus was used to conduct quasi-static tests at room temperature. The data from the experiments was fit to existing constitutive models and numerical simulations were performed to validate the constitutive fits. Metallographic analysis was also performed to assess any changes in damage evolution associated with high rate deformation.

The remainder of this chapter presents a review of the literature pertinent to this research. This includes a discussion of the split Hopkinson bar apparatus and its application to test materials at high strain rates. A brief review of material behavior at high strain rates is given, focusing on the high strain rate behavior of aluminum alloys. A review of three constitutive models currently used in modeling the high strain rate behavior of metals is also provided.

1.1 SPLIT HOPKINSON BAR APPARATUS

In 1914, Bertram Hopkinson [5,6,7] used a long elastic bar to study the pressure pulse produced by the impact of a bullet or by the detonation of an explosive. His apparatus consisted of a round steel bar suspended as a ballistic pendulum. The pressure pulse was generated by detonating an explosive at one end of the bar, while a cylindrical pellet was placed at the other end of the bar and held in place using a thin film of grease. During the experiment, a portion of the pressure pulse would enter the pellet and as a result the pellet would fly away from the end of the bar. The momentum trapped in the pellet corresponded to a pulse section equal to twice the length of the pellet. By repeating this procedure using pellets of different length and measuring the momentum in each pellet by capturing it in a ballistic pendulum, the pressure-time relationship of the pulse generated by the explosive could be determined [5,6].

Although Hopkinson [5] used this experiment to determine the pressure-time relationship of pulses generated using explosives, it was Kolsky [6] who introduced the split Hopkinson pressure bar (SHPB) and used it to measure the dynamic response of materials. The configuration consisted of two bars with a specimen placed between them. He used a

detonator to generate a compressive loading pulse and placed hardened steel anvils against the bar in order to protect the bar end from being damaged by the detonation. Using condenser microphones, Kolsky [6] was able to measure the displacement-time relationship of each bar as the stress wave propagated through them. As long as the bars remained elastic, the displacements in the pressure bars were directly related to the stresses, while the length of the pulse in the bar was related to the duration of the impact and the sound velocity through the bar material [7]. Assuming the bars remained elastic, Kolsky [6] was able to determine the stress-strain response of the specimen being tested using this method.

1.1.1 SPLIT HOPKINSON BAR PRINCIPLES

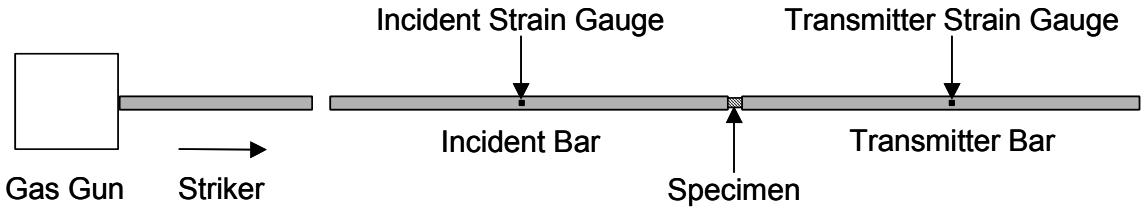

Figure 1.1 – Schematic of a Compressive Split Hopkinson Bar Apparatus

The most commonly used configuration for the split Hopkinson bar apparatus, presented in Figure 1.1, is similar to that used by Kolsky [6] in his experiments. A striker bar is used to impact the end of the bar known as the incident bar. A gas gun is the most common method used to propel the striker. As a result of the impact, an elastic compression wave is generated in the incident bar. The length of the compression wave is proportional to twice the length of the striker used, while the amplitude of the wave is proportional to the striker impact velocity. This compression wave, commonly referred to as the incident wave, travels down the incident bar until it reaches the specimen. At this juncture, part of the wave is transmitted through the specimen to the transmitter bar; this portion is commonly referred to as the transmitted wave. The remainder is reflected back down the incident bar as a tensile wave and is referred to as the reflected wave. Both the incident and transmitter bars remain elastic during the experiment, while the specimen deforms plastically if the amplitude of the loading pulse exceeds the yield strength of the sample. Strain gauges located on both the incident and transmitter bars are used to measure the waves as they travel along the respective bars. From these three waves, the

dynamic stress-strain response of the material being tested can be determined using the equations developed for the split Hopkinson bar apparatus described in Section 1.1.3 [8].

1.1.2 TENSILE SPLIT HOPKINSON BAR

The principles and components of a tensile split Hopkinson bar (TSHB) apparatus are similar to those of a compressive apparatus with the exception of the type of loading experienced by the specimen and the methods to generate a tensile loading, of which there are several. Lindholm *et al*. [8,9,10] used a compressive split Hopkinson bar (CSHB) apparatus, along with a hat-shaped tensile, specimen as shown in Figure 1.2. The apparatus consisted of a solid incident bar that fit inside the hat and a hollow transmitter bar which fit around the hat. In this configuration, when the input bar is loaded with a compressive pulse, the direction in which the incident bar end displaces will load the cylindrical section in tension.

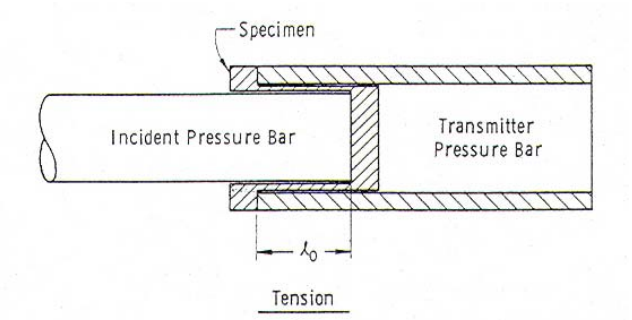

a)

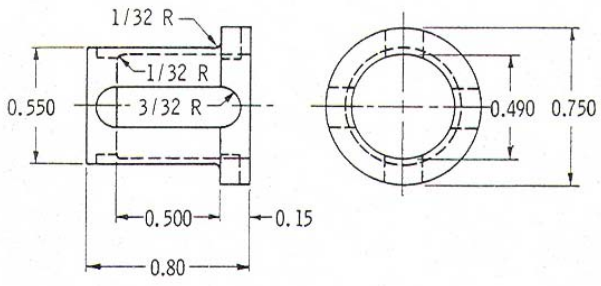

b)

Figure 1.2 – Details of the a) CHSB and b) Tensile Hat-Shaped Specimen used by Lindholm [9]

One advantage of this configuration is that the pressure bars always maintain in contact with the specimen without the use of threads, thus maintaining a planar loading surface and avoiding possible wave dispersion. Secondly, a compressive pulse is easier to generate than a tensile one [8,9]. However, a high degree of accuracy is required in machining the specimen. Furthermore, the hat-shaped specimen geometry is unsuitable for testing sheet material.

A second method using a CSHB was employed by Nicholas [8,11,12]. As shown in Figure 1.3, a cylindrical specimen is threaded onto the ends of the bar. A split shoulder or collar is then placed over the specimen. The collar is made of the same material as the pressure bars in order to avoid any reflections due to a mismatch in material impedance. The assembly is tightened such that the collar fits tightly between both bars and the specimen remains unloaded. A tight-fitting nylon ring is placed over the split collar and the ends of both bars in order to properly align all the components [11]. As the compression wave travels down the incident bar, ideally the entire wave is transmitted through the collar to the transmitter bar. The ratio of the cross-sectional area of the collar to the specimen is designed such that the specimen is loaded elastically when the compression pulse passes. As the compression wave reached the end of the transmitter bar, it reflects off the free surface as a tensile wave. When the tensile wave reaches the specimen, the collar is unable to transmit a tensile wave, since it is not fastened to either pressure bar and as a result only the specimen is loaded in tension. Like the method used by Lindholm [9], this configuration has the advantage in using a compressive loading of the bars, however, it requires fine tolerances in order to be assembled correctly. Failure to remove any play from the threaded joint will result in wave reflections [11]. Furthermore, this configuration has been shown to be prone to wave reflections and interactions that obscure the experimental data as a result of the split shoulder configuration [11,13].

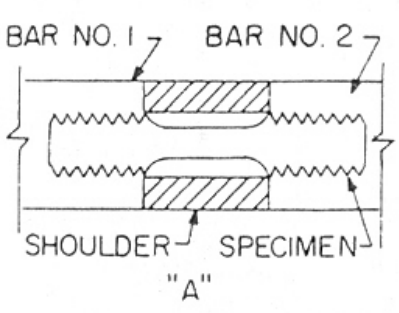

Figure 1.3 – Split Shoulder Tensile Configuration used by Nicholas [11]

The most common method used for high strain rate tensile experiments involves threading the specimen into the bar ends, and generating a direct tensile load in the incident bar [8]. One method of loading, shown in Figure 1.4, involves a hollow striker that travels over the incident bar and is accelerated using a gas gun. The striker impacts an end cap threaded onto the end of the incident bar generating a tensile load in the incident bar. The tensile wave travels down the incident bar and, as it reaches the specimen, part of the tensile wave is transmitted through the specimen, while the remainder is reflected as a compressive wave. The equations used to analyze a TSHB apparatus are the same as those developed for a compressive one, except the sign of the each recorded wave is opposite. The most commonly used specimen geometries consist of: (i) a dumbbell threaded directly into the bar ends; or, (ii) a flat tensile specimen clamped in a grip which is then threaded into the bar ends [8]. The advantage of this system is the simplicity of the specimen geometry and, since the loading is tensile, the elimination of the need for a complex specimen assembly such as the one used by Nicholas [11]. The TSHB apparatus itself does become more complex since a tensile load needs to be generated. Also, like the method used by Nicholas [11], the threads at the ends of the bars are a possible source of wave distortion.

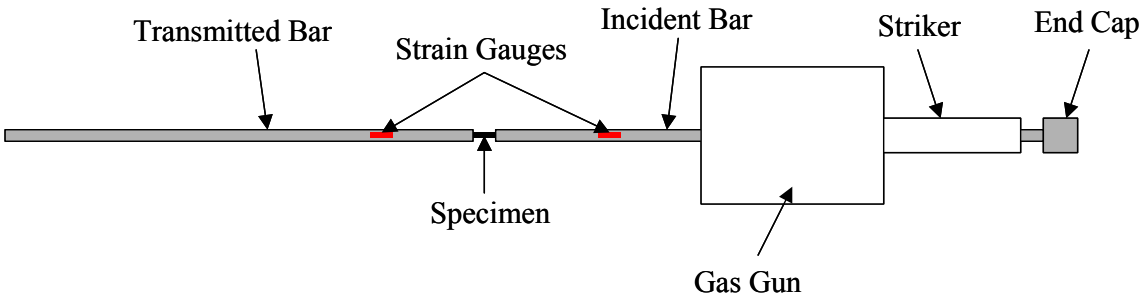

Figure 1.4 – Schematic of a Tensile Split Hopkinson Bar Apparatus

One of the major issues to be overcome in testing sheet materials using a TSHB apparatus, is the method to affix the specimen between the bars and ensure that the clamping force is large enough to prevent the specimen from slipping during the experiment. Since the thickness of the sheet is quite small, it is not possible to machine a top-hat or dumbbell specimen. Mechanical grips are often used to hold sheet specimens. LeBlanc and Lassila [14] devised the clamping system shown in Figure 1.5. As can be seen, all of the components in the clamping system are axi-symmetric; this eliminates major changes in geometry that could distort the propagating waves. As the components are tightened, compression is applied to the ends of the specimen, preventing slip during the test. However, this configuration involves several threaded components, which increases the likelihood of wave distortion.

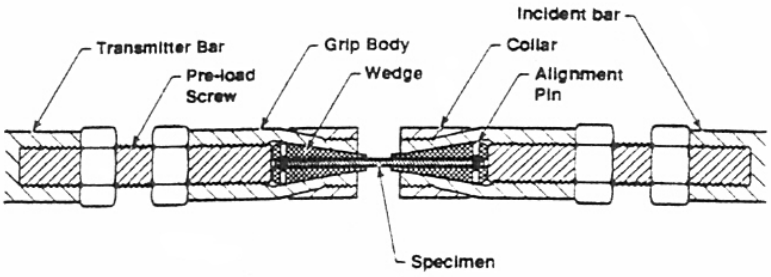

Figure 1.5 – Tensile Specimen Clamping System Used by LeBlanc and Lassila [14]

Similar to LeBlanc and Lassila [14], Quik *et al*. [15] used a threaded grip to affix the specimen between the bars. However, instead of applying a clamping load, glue was used to fasten the specimen to the grips. Although this may provide adequate fastening, the use of glue introduces a material of different impedance than that of the bars and test material, which may introduce spurious wave reflections.

Kang *et al*. [16,17] and Huh *et al*. [18] integrated a slot for the specimen directly into the bar ends as shown in Figure 1.6. Each pressure bar uses two screws to provide clamping pressure. Since the grips are integrated into the bars themselves, the mechanical impedance introduced by each grip is low, thus minimizing wave distortion. However, this does limit the range of sheet thicknesses that can be tested in a particular set of bars, since the specimen should fit precisely in the slot in order to provide an adequate clamping force. Care must be taken in

machining the specimens in order to ensure that no gaps exist between the end of the specimen and the end of the slot.

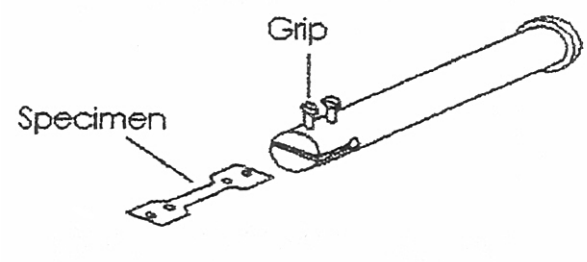

Figure 1.6 – Schematic of Split Hopkinson Pressure Bar With Integrated Grips For Testing of Sheet Alloys in Tension [17]

1.1.3 HOPKINSON BAR EQUATIONS

The use of the split Hopkinson bar technique is feasible in studying the dynamic properties of materials since wave propagation through a cylindrical bar is well understood. The impact of the striker against the incident bar generates a loading pulse that is almost square in shape [19]. If the loading is elastic, the resulting wave propagates through the bar at the elastic sound velocity (c), which is a property of the bar material and is defined as:

$$c = \sqrt{\frac{E}{\rho}} \tag{1.1}$$

where E is Young's modulus and ρ is the density of the material. Next, if the particle velocity at any location is denoted as u, the amplitude of the resulting stress at that location is:

$$\sigma = \rho c u \tag{1.2}$$

Equations (1.1) and (1.2) assume that the pulse propagates without distortion and that the pressure is uniformly distributed over the cross-section of the bar, which is true only if the length of the pulse is long in comparison to the radius of the bar [5]. The direction of the particle velocity in relation to the direction in which the wave propagates depends on the sense of the wave. For a compressive pulse, the particle velocity and propagation direction are the same, while they are in opposite directions for a tensile pulse. When the wave reaches the end of the bar, it reflects off the free surface as a wave in the opposite sense, since the stress at the

free surface must sum to zero. Figure 1.7 shows the relationship between the stress and particle velocity at the free end of a cylindrical bar.

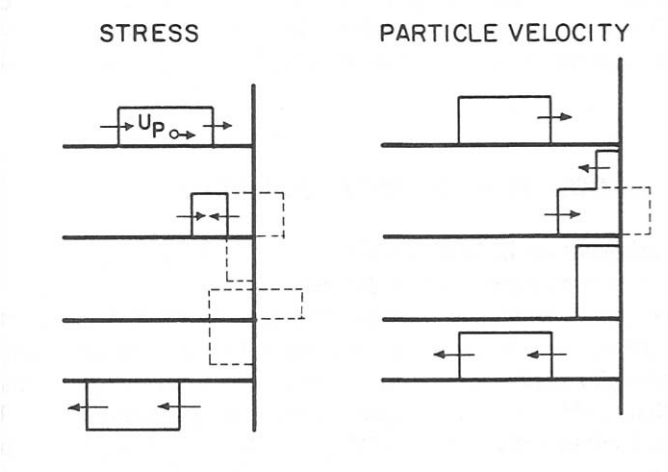

Figure 1.7 – Reflection of a Stress Pulse at a Free Surface [20]

As seen in Figure 1.7, although the stress at a free surface sums to zero during the reflection of the wave, the particle velocity jumps to twice the particle velocity while the wave was traveling down the bar. Thus, knowing the magnitude of the stress pulse, the relationship between the velocity (V) of the bar end and the incident stress (σ) is given by

$$V = \frac{2\sigma}{\rho c}. \tag{1.3}$$

Using the elastic relationship ($\sigma = E\varepsilon$) and the elastic wave velocity, equation (1.3) can be written in terms of strain,

$$V = 2c\varepsilon. \tag{1.4}$$

In the case of the split Hopkinson bar apparatus, the end of the incident bar is not a free surface. The impedance mismatch between the specimen and the incident bar results in part of the incident wave being transmitted through the specimen to the transmitter bar, while the remainder is reflected; hence, there are three waves to consider. The strains associated with each of these waves are designated as the incident strain (ε_i), the reflected strain (ε_r) and the transmitted strain (ε_t). The velocity of the incident bar (V_1) is [9]

$$V_1 = c\left(\varepsilon_i - \varepsilon_r\right), \tag{1.5}$$

while the velocity of the transmitter bar end (V_2) is

$$V_2 = c(\varepsilon_t)\,. \tag{1.6}$$

It is assumed that the specimen is deforming uniformly during the test [8]. Therefore, the instantaneous nominal strain rate can be defined as [8]:

$$\frac{d\varepsilon}{dt} = \frac{V_1 - V_2}{L_0} \tag{1.7}$$

where L_0 is the initial specimen length. Combining equations (1.5), (1.6) and (1.7), the nominal strain rate in terms of strain can be expressed as:

$$\frac{d\varepsilon}{dt} = \frac{c\left(\varepsilon_i - \varepsilon_r - \varepsilon_t\right)}{L_0} \tag{1.8}$$

A second assumption included in the analysis of the spilt Hopkinson bar, is that the specimen is in force equilibrium [8]. If both the incident and transmitter bars are made of the same material and have the same cross-sectional area, the forces at the incident bar end (F_1) and the transmitter bar end (F_2) can be defined as [8]:

$$F_1 = AE\left(\varepsilon_i + \varepsilon_r\right) \tag{1.9}$$

and

$$F_2 = AE\varepsilon_t \tag{1.10}$$

where A is the cross-sectional area of the bar. Equating the two forces yields the following result:

$$\varepsilon_t = \varepsilon_i + \varepsilon_r \tag{1.11}$$

Combining equations (1.8) and (1.11), the nominal strain rate becomes

$$\frac{d\varepsilon}{dt} = -\frac{2c\varepsilon_r}{L_0}\,. \tag{1.12}$$

By integrating equation (1.12), the nominal or engineering strain-time history of the specimen can be determined.

To determine the nominal or engineering stress-time history of the specimen, we consider the average stress in the specimen at any given time to be the average of the forces at each bar end [7]:

$$\sigma = \frac{F_1 + F_2}{2A_0} \tag{1.13}$$

where A_0 is the initial cross-sectional area of the specimen. Expressing F_1 and F_2 in equation (1.13) in terms of strain yields:

$$\sigma = \frac{EA\left(\varepsilon_i + \varepsilon_r + \varepsilon_t\right)}{2A_0} \tag{1.14}$$

This gives the engineering stress in the specimen in terms of all three waves. However, equation (1.11) shows that the transmitted strain is the sum of the incident and reflected strains. Using this relationship in equation (1.14) results in the following:

$$\sigma = \frac{EA\varepsilon_t}{A_0} \tag{1.15}$$

Equation (1.12) and (1.15) are the final forms of the Hopkinson bar equations using a so-called single-wave analysis [8]. These two equations are used to determine the engineering strain-time and stress-time histories. The time histories are then combined to produce a dynamic engineering stress-strain curve for the material tested. This analysis is referred to as a single-wave analysis since it only takes into account the reflected wave when calculating the strain in the specimen, and only the transmitted wave in calculating stress [8]. Although this is the conventional method of analyzing the split Hopkinson bar, other researchers have adopted a three-wave analysis, where all three waves are considered in determining the stress-time history [8]. This approach is used, for example, in cases where the assumption of dynamic equilibrium is not valid or must be confirmed [8,9,21,22].

1.1.4 WAVE PROPAGATION EFFECTS

When the striker impacts the end of the bar, the wave generated is complex due to non-uniformity at the interface and the propagation of other types of waves such as spherical dilation waves [7]. However, these waves dampen after the incident wave has propagated a distance of approximately ten bar diameters [19]. The wave propagation then becomes one-dimensional and can be fully described by the equations of motion for an infinitely long cylinder derived by Pochhammer [23] and Chree [24], which were applied to the Hopkinson bar by Davies [25].

The incident pulse generated by the impact of the striker can be represented using a Fourier series. The propagation velocity of each cosine wave in the Fourier series varies relative to the elastic sound velocity. The investigation conducted by Davies [25] showed that for a given material, the ratio of the propagation velocity (c) to the elastic sound velocity (c_o), is a function of a dimensionless ratio R/λ, where R is the radius of the bar, and λ is the wavelength of the pulse component. For a bar material with a Poisson's ratio of 0.29, the propagation velocity is equal to the sound velocity in the material when $R/\lambda << 1$. However, as R/λ approaches 1, the propagation velocity asymptotically approaches $0.5764c_o$, the velocity of Rayleigh surface waves [25]. Thus higher frequency components lag behind low frequency components, dispersing the incident pulse as the stress wave components propagate down the length of the bar, resulting in oscillations in the recorded data [22]. Clarke [26] investigated dispersion correction and concluded that since the pulse length used in most Hopkinson bar experiments was significantly longer than the bar diameter, correction for dispersion was not required.

Using spectral analysis techniques, Salisbury [27] examined wave propagation through a CSHB apparatus equipped with AA6061-T6 pressure bars. The bars were 25.4 mm in diameter, and the loading pulse was generated using a 605 mm long striker. The recorded signal was converted to the frequency domain using a discrete Fourier transform, and the amplitude and phase velocity of each frequency was calculated. The majority of the energy was contained in frequencies below 10 kHz [27]. Salisbury [27] found the phase velocities in the aluminum bars to remain relatively constant throughout the 30 kHz frequency band considered, and were approximately equal to the sound velocity through the material. No attenuation was observed either. Based on these results, there is no need for dispersion or attenuation correction in the set of experiments presented in this thesis.

The full Pochhammer-Chree solution to elastic wave propagation in an infinitely long cylinder shows that the longitudinal stress will vary across the cross-section of the bar [23,24]. Davies [28] determined that longitudinal displacements at the bar surface differ from the centre by less that 5% for $R/\lambda < 0.10$. Follansbee and Frantz [22] found that at an R/λ ratio below 0.10, the amplitude of the Fourier components of the loading pulse reduce to approximately 2% of the

highest magnitude component in the spectrum. The analysis of Davies [28] and Follansbee and Frantz [22] shows that the majority of the energy is contained in wavelengths exceeding 10R [7]. Hence the longitudinal stress variation can be considered negligible once the wave has propagated a distance greater than 10R.

Wave propagation effects through the specimen must also be considered. Two assumptions associated with the Hopkinson bar equations are that: (i) the specimen is deforming uniformly; and, (ii) a uniform stress state is present. Since the loading is applied to one surface during the experiment, inertia opposes uniform deformation [7]. The specimen requires a so-called "ring-up time" for the stress state to reach equilibrium. Davies and Hunter [29] have estimated that this takes π reverberations of the stress wave. For a plastically deforming solid obeying the Taylor-von Karman theory, this results in a ring-up time (t_e) [8,29]:

$$t_e = \sqrt{\frac{\pi^2 \rho_s L_s^2}{\frac{d\sigma}{d\varepsilon}}} \tag{1.16}$$

where ρ_s is the density of the specimen, L_s is the length of the specimen, and $d\sigma/d\varepsilon$ is the slope of the true stress-strain response of the material being tested. For times less than the ring-up time, the specimen deformation cannot be assumed to be uniform and the stress-strain measurements acquired from the Hopkinson bar experiment cannot be considered valid [7,8]. Thus, it is difficult to determine the yield strength of a material at high strain rates using a split Hopkinson bar apparatus. One method of reducing the ring-up time is to reduce the specimen length. However, this needs to be accompanied by a reduction in cross-sectional area, and in the case of compression testing, a reduction in pressure bar diameter [7]. An alternative method to reducing the ring-up time is to increase the rise time of the incident wave through the use of pulse shaping [7,8]. By placing a soft metal shim between the striker and the incident bar, the rise time of the incident wave can be increased [8]. The thickness of the shim required needs to be determined experimentally.

1.2 HIGH STRAIN RATE MATERIAL BEHAVIOR

Over the years, researchers have investigated the high strain rate behavior of many materials including metals, ceramics and polymers used in a wide spectrum of applications. For most metals, the flow stress has been shown to be dependent on the logarithm of strain rate, as seen in Figure 1.8. Three regimes of strain rate behavior are generally accepted which are defined by three different mechanics governing plastic flow [20]. In region I, thermally activated dislocation motion is the controlling mechanism, while regions II and III are believed to be governed by drag mechanisms and relativistic effects, respectively.

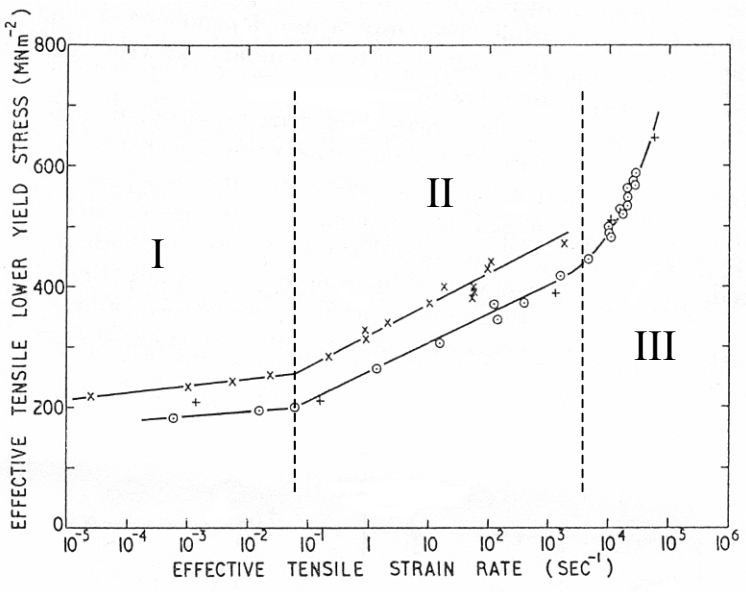

Figure 1.8 – Lower Yield Stress as a Function of Strain Rate for En3B Steel (Shear (O), Tension (X), and Punch (+) Tests) Showing Three Regions of Strain Rate Sensitive Behavior [30]. The present author added the labels and vertical dashed lines.

The increase in strain rate sensitivity exhibited by many metals has often been interpreted as a transition from thermal activation controlled mechanisms to mechanisms governed by dislocation drag at the higher strain rates. However, based on dislocation velocities, Weertman [31] estimates that this transition should occur at strain rates on the order of $1x10^4$ s^{-1}. From experimental results, Follansbee [32] concluded that dislocation drag mechanisms are not rate controlling at strain rates below $1x10^4$ s^{-1} for copper, copper-aluminum and austenitic stainless

steels; hence, thermally activated dislocation motion can still be considered as the governing mechanism at the strain rates considered in the present work.

In the subsequent section, thermally activated dislocation motion is discussed briefly. The reader is referred to other sources for information on the other two mechanisms [20,30, 31,33,34,35].

1.2.1 THERMALLY ACTIVATED DISLOCATION MOTION

As a dislocation moves through the lattice, it continually encounters obstacles such as solute atoms, vacancies and grain boundaries as well as other dislocations. These obstacles can be overcome by either an increase in the applied stress, or random thermal fluctuations at temperatures above absolute zero [21]. The average strain rate ($\dot{\varepsilon}$) can be described by an Arrhenius equation of the form:

$$\dot{\varepsilon} = \dot{\varepsilon}_0 \exp\left(-\frac{H}{kT}\right) \tag{1.17}$$

where $\dot{\varepsilon}_0$ is the limiting strain rate, H is the energy that must be applied thermally to overcome the obstacle, k is the Boltzmann constant and T is the absolute temperature. The thermal energy H is a function of stress, and can be expressed as a linear relationship of the form:

$$H(\sigma) = H_0 - V(\sigma - \sigma^*) \tag{1.18}$$

where H_0 is the total activation energy, V is the activation volume, σ is the applied stress and σ^* is the athermal component of stress. It can be seen from equation (1.18), that as the applied stress is increased, the additional thermal energy required to overcome the obstacle decreases. Substituting equation (1.18) into (1.17), and solving for stress (σ) yields the following result:

$$\sigma = \sigma^* + \frac{H_0}{V} + \frac{kT}{V}\ln\left(\frac{\dot{\varepsilon}}{\dot{\varepsilon}_0}\right) \tag{1.19}$$

In most cases, $\dot{\varepsilon}_0$ and H_0 may be assumed to be constant, while σ^* and V are taken to be functions of strain only [21]. These four internal variables describe the deformed state of the material. The most evident result from this formulation is the logarithmic dependence of the

flow stress on strain rate and its linear dependence on temperature. Most metals have been shown to exhibit this behavior.

1.2.2 INERTIA EFFECTS

At a strain rate of approximately $1x10^3$ s^{-1}, many metals exhibit an increase in strain rate sensitivity. As shown in Figure 1.9, the strain rate sensitivity of oxygen-free-electronic copper increases dramatically at $1x10^3$ s^{-1}. This increase in strain rate sensitivity has often been interpreted as a transition from thermal activation controlled mechanisms to mechanisms governed by dislocation drag at the higher strain rates. As previously mentioned in Section 1.2, Weertman [31] and Follansbee [32] estimate that this transition should occur at strain rates on the order of $1x10^4$ s^{-1}.

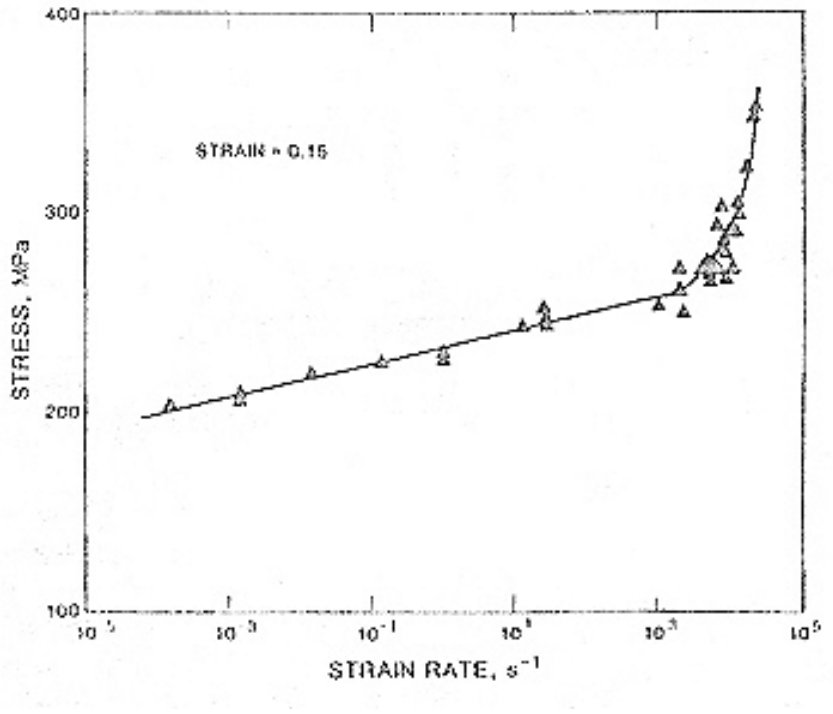

Figure 1.9 – Strain Rate Dependence of Flow of Oxygen-Free-Electronic Copper [33]

In dynamic tests such as split Hopkinson bar experiments, the time to reach a steady-state strain rate is on the order of microseconds. During this transient loading period, the material experiences high accelerations at elevated strain rates. Inertial confinement in the lateral

directions is also present in the material at high deformation velocities. These two factors lead to large inertial forces in both the longitudinal and lateral directions. Figure 1.10 illustrates the range of strain rates that materials are tested at. The range spans 16 orders of magnitude. Although the strain rate at which the transition occurs may not be exact, Figure 1.10 shows that at strain rates above approximately $1x10^{-1}$ s^{-1}, inertial forces become an important consideration when examining the experimental data.

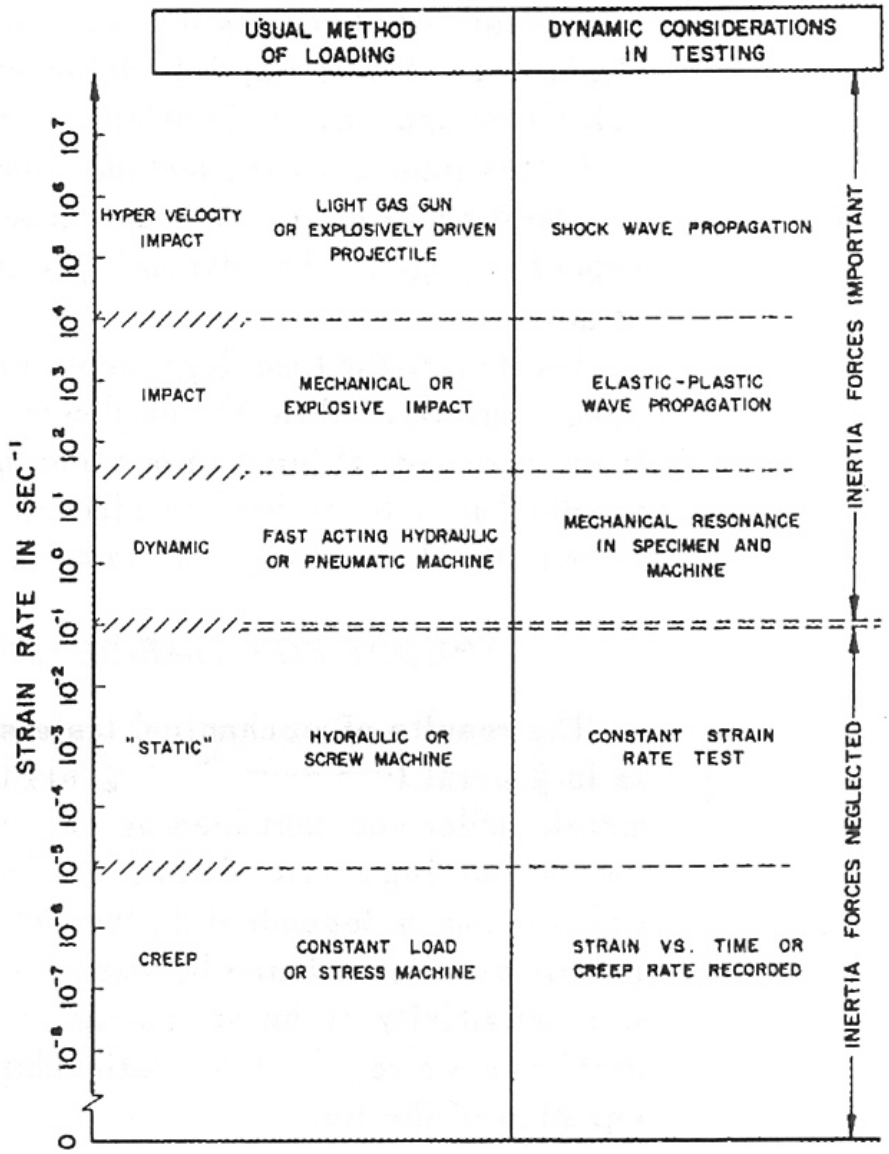

Figure 1.10 – Various Classes of Material Tests and the Strain Rates At Which They Are Performed [21]

Samanta [36] and Gorham *et al*. [37,38,39] analyzed a simplified model of a CSHB experiment shown in Figure 1.11. Using this model, the axial inertial stress measured at the rigid anvil during uniform deformation can be estimated as [38]:

$$\sigma_i \approx \rho\left(\frac{a^2}{16}+\frac{h^2}{6}\right)\dot{\varepsilon}^2 + \rho\left(\frac{h^2}{6}-\frac{a^2}{8}\right)\ddot{\varepsilon} \qquad (1.20)$$

where ρ is the material density and the geometric parameters a and h are as defined in Figure 1.11.

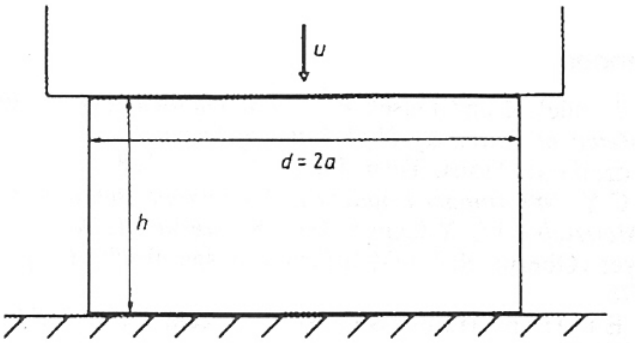

Figure 1.11 – Simplified One-Dimensional Model of a Specimen Compressing During a Split Hopkinson Bar Experiment [38]

From equation (1.20), it can be seen that the magnitude of the inertial stress is proportional to the material density and to the size of the specimen. Field *et al*. [40] performed numerical simulations of a CSHB experiment using a copper specimen 3.8 mm in diameter, and 2.3 mm thick. Values for $\dot{\varepsilon}$ and $\ddot{\varepsilon}$ were extracted from the simulations and used in equation (1.20) to estimate the inertial stress during uniform deformation for a wide range of strain rates. As shown in Figure 1.12, a dramatic increase in the inertial stress occurs at strain rates above $1\text{x}10^4\ \text{s}^{-1}$.

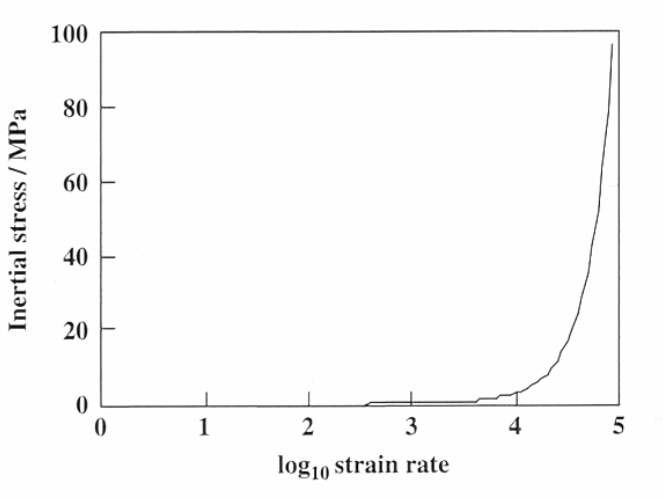

Figure 1.12 – Inertial Stress as a Function of Strain Rate Calculated for a Copper Specimen, 3.8 mm in Diameter and 2.3 mm Thick [40]

The reader should be aware that this analysis of inertial stresses is based on the assumption that the specimen is deforming uniformly [37,38,39]. Aspects of Hopkinson bar experiments such as elastic and plastic wave propagation, as well as non-homogeneous deformation during the initial stages of the experiment are not considered in this analysis. The influence of the inertial stresses during this phase cannot be assessed using the present understanding of the mechanics governing high strain rate material behavior [39].

Inertia has also been shown to increase the ductility of many metals in tensile experiments, and it has been noted that post-uniform deformation is primarily affected by it [41,42,43,44,45]. Although the effects of inertia on ductility are not completely understood at this time, one theory proposes that at the onset of localization, the material velocity profile changes from a linear profile to one that may resemble a step function like the one shown in Figure 1.13 [41,43,46,47]. This change in the velocity profile produces non-uniform material accelerations and inertial forces opposing the applied force. These inertial forces reduce the force acting through the cross section of the material, and unload the region where the deformation is localizing. As a result, neck growth is stabilized by diffusing deformation throughout the specimen [41,43,46,47].

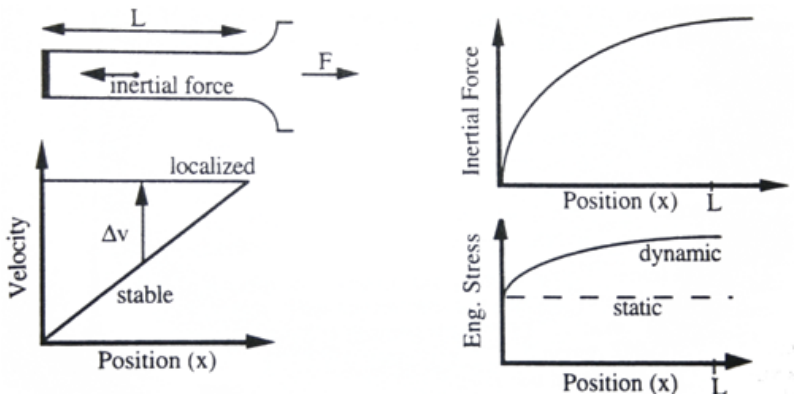

Figure 1.13 – Inertial Forces Produced by a Change in the Material Velocity Profile as Presented by Hu & Daehn [46]

This analysis is only one-dimensional and does not consider the effects of inertia in the lateral directions. Banerjee [48] conducted an analytical analysis on thin-walled cylinders that were radially expanded using electromagnetic forming. He determined that inertial forces in the radial direction had little effect on increasing formability, but rather axial inertia could be reason for increased deformation at high forming rates. From this result, it is reasonable to believe that lateral inertial forces may have an affect on ductility in high strain rate tensile experiments.

1.2.3 HIGH RATE PROPERTIES OF ALUMINUM ALLOYS

Most of the dynamic deformation data found on aluminum and aluminum alloys was gathered from tests conducted on plate material consisting of either cylindrical specimens tested in compression, or dumbbell specimens used in tensile tests. Aluminum and aluminum alloys have been considered to have low strain rate sensitivity; however, experiments conducted by various authors have shown that aluminum and aluminum alloys can exhibit increased strain rate sensitivity at strain rates above $1x10^3$ s^{-1} at room temperature. Work done by Holt *et al*. [49] shows that pure aluminum exhibits moderate strain rate sensitivity. The flow stress of pure aluminum increases linearly with the logarithm of strain rate at room temperature, and the strain rate sensitivity increases at rates above $1x10^3$ s^{-1} [50]. However, with increasing alloy

content or processing, such as heat treating or cold working, the strain rate sensitivity for aluminum alloys tends to decrease [9,49,51].

Tanaka and Nojima [50] performed dynamic compression tests on pure aluminum, aluminum-4.01wt% copper, and commercial 17S Duralumin. From the experimental data, shown in Figure 1.14, pure aluminum exhibited a logarithmic increase in flow stress at strain rates between $1x10^{-4}$ s^{-1} and $1x10^{3}$ s^{-1}, at room temperature. At strain rates above $1x10^{3}$ s^{-1}, the strain rate sensitivity increased. Contrary to this, the two alloys tested showed no strain rate sensitivity at room temperature [50]. Furthermore, these two alloys showed no temperature sensitivity at temperatures between 200 and 400 K, whereas the flow stress decreased monotonically with temperature for pure aluminum [50].

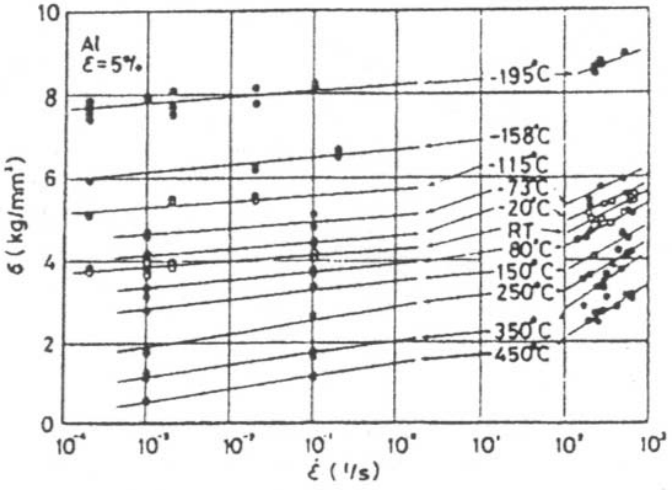

Figure 1.14 – Relationship between Flow Stress and Logarithmic Strain Rate for Pure Aluminum at 5% Strain [50]

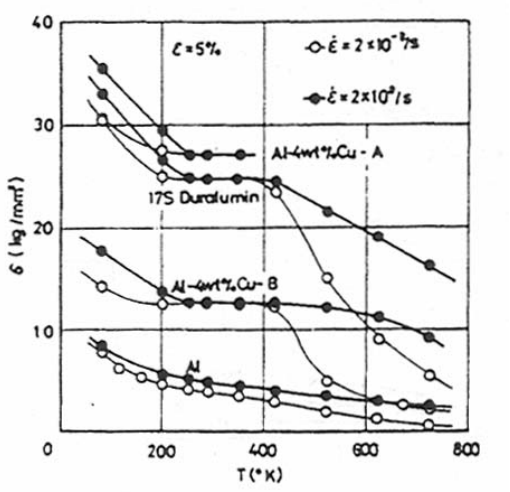

Figure 1.15 – Relationship Between Flow Stress and Temperature for Three Materials at 5% Strain [50]

Tensile experiments performed by Rodriguez *et al*. [52] on 7017-T73 aluminum, showed no distinct changes in flow stress at strain rates between $1x10^{-4}$ s^{-1} and $1x10^{3}$ s^{-1}. Their data, as seen in Figure 1.16, shows oscillations in the stress-strain curve at a strain rate of $1x10^{3}$ s^{-1}. These oscillations are likely a result of wave reflection and distortion occurring in the Hopkinson bar apparatus and cannot be considered a constitutive response.

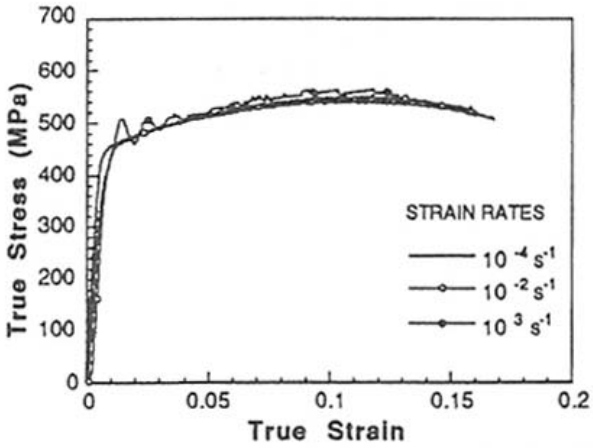

Figure 1.16 – True Stress Versus True Strain for AA7017-T73 [52]

El-Magd *et al*. [53,54] performed high strain rate compression experiments on AA7075 at strain rates between from $1x10^{-3}$ s^{-1} to $5x10^{3}$ s^{-1}, and test temperatures between 20°C and 450°C. At strain rates above $1x10^{3}$ s^{-1}, AA7075 exhibited an increase in flow stress at low

strains. Their data also showed an increase in strain rate sensitivity at elevated temperatures [53]. A sharp increase in the compressive ductility of AA7075 at strain rates over $1x10^3$ s^{-1} was also witnessed [53]. El-Magd *et al*. [55] attribute localized strain rate hardening to this increase in ductility at high strain rates. Once localization occurs, the local strain rates increase dramatically, leading to a higher local flow stress due to strain rate hardening. This stabilizes the deformation process by diffusing deformation to other regions of the specimen [53,54,55].

Masuda *et al*. [56] performed tensile tests on AA6061 in both peak-aged and over-aged conditions using axi-symmetric dumbbell specimens. In the peak-aged condition, the alloy showed no influence of strain rate on the tensile properties at the strain rates considered [56]. In the over-aged condition, AA6061 showed an increase in strain rate sensitivity at strain rates above $1x10^3$ s^{-1} [56].

Lindholm *et al*. [10] define a strain rate sensitivity parameter as the rate of change of the 0.2% offset yield strength with respect to logarithm strain rate, normalized by the yield strength measured at a strain rate of 1 s^{-1}. It can be seen in Figure 1.17 that the strain rate sensitivity parameter decreases with increasing alloy content and heat treating.

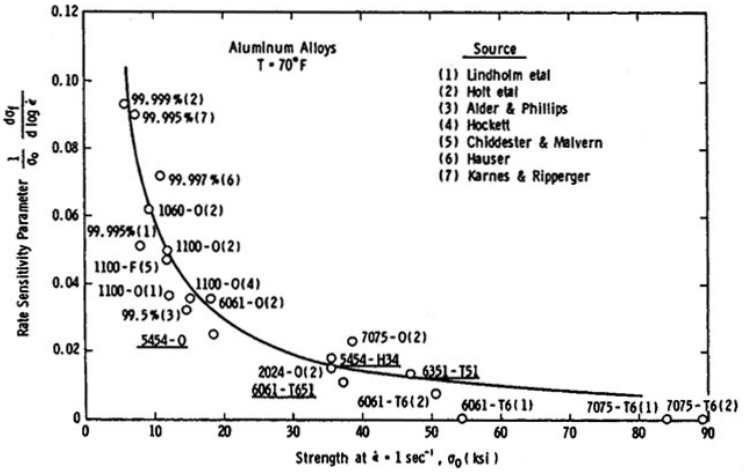

Figure 1.17 – Strain Rate Sensitivity as a Function of Yield Strength at 1 s^{-1} [10]

This body of published work shows that the strain rate sensitivity of aluminum alloys appears to be alloy- and, in some cases, heat treatment-dependent. Mukai *et al*. [57] performed tensile tests on high purity Al-Mg alloys with magnesium concentrations varying from 1.8%wt to

8.4%wt. Dumbbell specimens were machined from extruded material and strain rates from $1x10^{-4}$ s^{-1} to $2x10^{3}$ s^{-1} were considered. At strain rates above $1x10^{3}$ s^{-1}, the 0.2% offset yield strength increased with magnesium concentration [57]. No significant change was observed in the shape of the stress-strain curve at various strain rates [57]. Mukai *et al*. [57] also showed that between strain rates of $1x10^{-3}$ s^{-1} and $1x10^{1}$ s^{-1}, the maximum flow stress increased only for pure aluminum, while the Al-Mg alloys exhibited a decrease in the maximum flow stress in this regime as seen in Figure 1.18 below. The maximum flow stress increased for all the Al-Mg alloys at strain rates above $1x10^{1}$ s^{-1}, with the exception of Al-8%Mg.

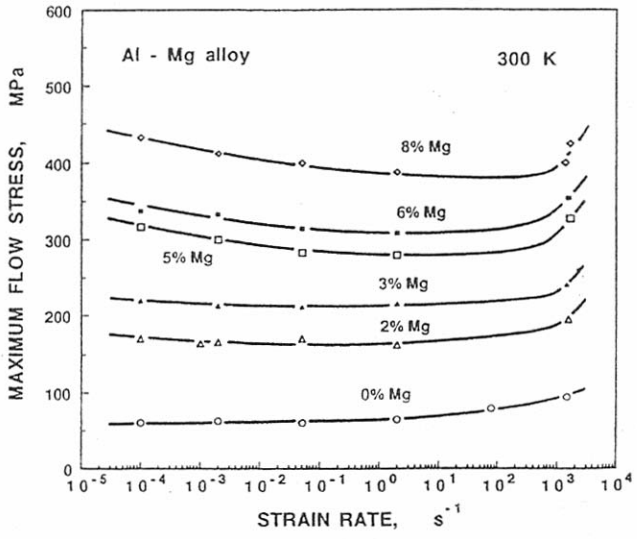

Figure 1.18 – Relationship Between Maximum Flow Stress and Strain Rate for High Purity Al-Mg Alloys [57]

The experiments performed by Mukai *et al*. [57] show that the ductility of Al-Mg alloys at high strain rates is also dependent upon the magnesium concentration. In Figure 1.19, the elongation to failure of pure aluminum increases in a near-logarithmic fashion with strain rate, while the Al-Mg alloys display an initial decrease in elongation to failure with strain rate until a critical strain rate is reached, after which the elongation to failure increases again. Thus, Mukai *et al.* [57] concluded that deformation of high purity Al-Mg alloys appears to be more unstable at strain rates between $1x10^{-3}$ s^{-1} and $1x10^{-1}$ s^{-1}, where strain aging is taking place.

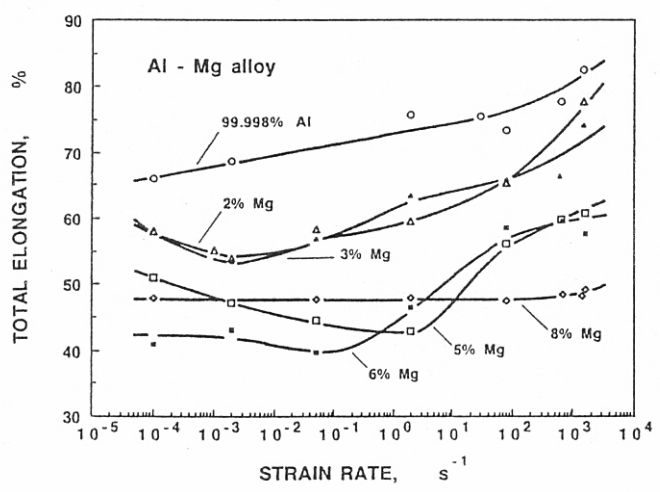

Figure 1.19 – Relationship Between Total Elongation and Strain Rate for High Purity Al-Mg Alloys [57]

Two Al-Mg alloys of interest in the present work are AA5754 and AA5182. These two alloys are currently being used in automotive applications, and have been identified as prime candidates to replace conventional steel in automotive structural and body components.

Higashi *et al*. [58,59] performed tensile tests on AA5182 using dumbbell specimens machined from hot rolled plate. The specimens were oriented in the rolling direction and the strain rates examined were between $1x10^{-3}$ s^{-1} to $4x10^{3}$ s^{-1} at room temperature. At strains of less than 5%, the flow stress increased with strain rate [58,59]. However, as deformation continued a different trend arose. As seen in Figure 1.20, the maximum flow stress decreased with strain rate between $1x10^{-3}$ s^{-1} and $1x10^{3}$ s^{-1}, and began to increase again at strain rates above $1x10^{3}$ s^{-1}.

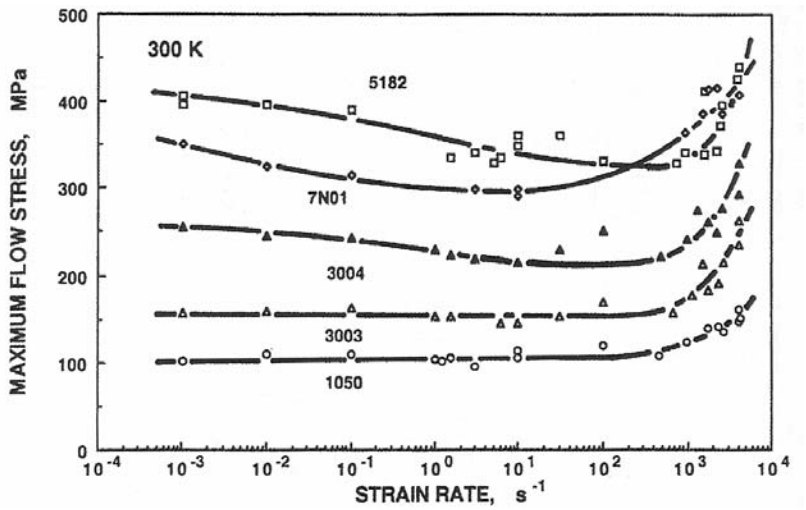

Figure 1.20 – The Relationship Between Maximum Flow Stress and Strain Rate for Various Aluminum Alloys [58]

Elongation data presented by Higashi *et al*. [58,59] on AA5182 shows that the elongation to failure increases with increasing strain rate. Figure 1.21 shows a rapid increase in elongation to failure at strain rates above $1x10^{2}$ s^{-1} for AA5182. Elongations to failure are in excess of 40% at strain rates above $2x10^{3}$ s^{-1} in comparison to approximately 30% at a strain rate of $1x10^{-3}$ s^{-1} [58,59].

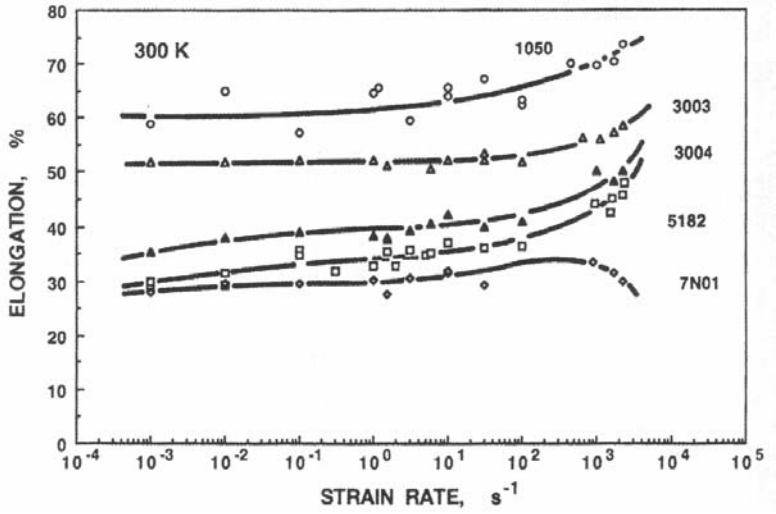

Figure 1.21 – The Relationship Between Elongation to Failure and Strain Rate for Various Aluminum Alloys [58]

Data on high strain rate behavior of AA5754, another alloy commonly used in automotive structural applications, has not been found at this time. However, Lindholm *et al*. [9] conducted tensile tests on AA5454 in an annealed and H34 temper conditions. Top hat specimens were used, allowing testing to be conducted using a CSHB apparatus, with strain rates in the range of $1x10^{-4}$ s^{-1} to $1x10^{3}$ s^{-1}. Figure 1.22 and Figure 1.23 show the results of the experiments performed by Lindholm *et al*. [9] on 5454-O and 5454-H34. The results show that the 0.2% offset yield strength is a weak function of strain rate for AA5454-O and AA5454-H34 [9]. The elongation to failure increased significantly with strain rate for both AA5454-O and AA5454-H34 [9]. Lindholm *et al*. [9] observed that the increase in elongation to failure was a result of deformation that occurred after necking and attributed this to a possible time dependence of the ductile failure mechanism.

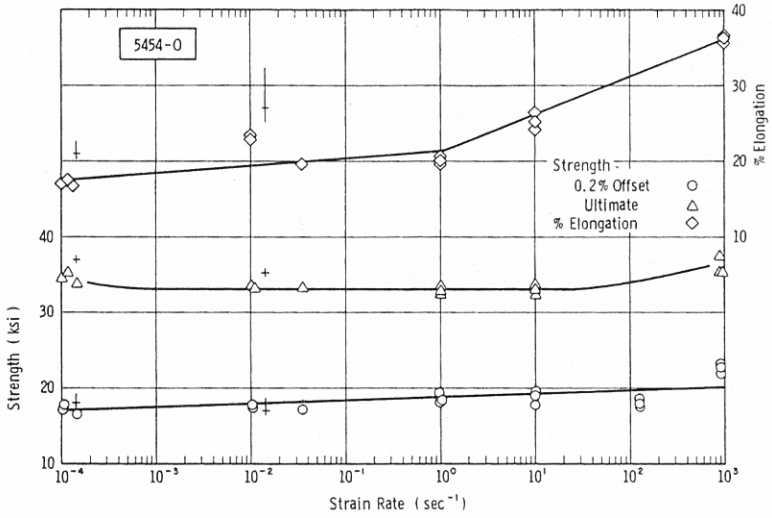

Figure 1.22 – Strength and Elongation Versus Strain Rate for 5454-O Aluminum [9]

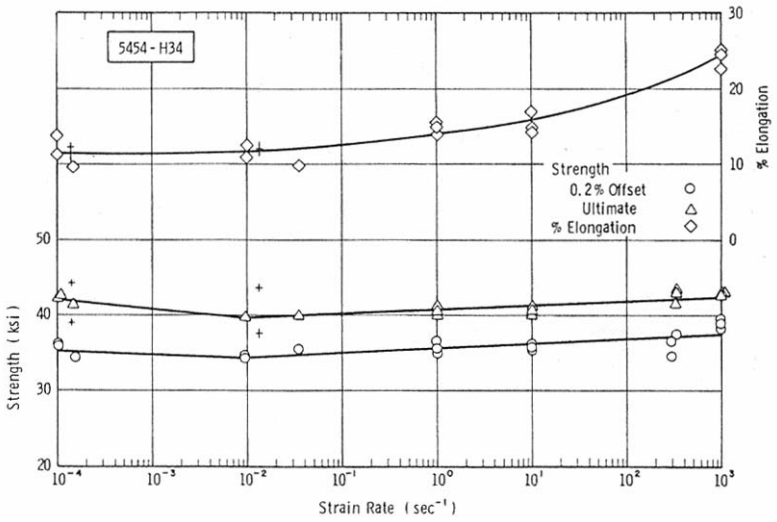

Figure 1.23 – Strength and Elongation Versus Strain Rate for 5454-H34 Aluminum [9]

Shi and Meuleman [60] performed tensile tests on AA6111-T4 at strain rates between $1x10^{-7}$ s^{-1} and $1x10^{2}$ s^{-1}. The material showed no change in yield or tensile strength, and a slight decrease in total elongation in the range of strain rates considered. No published data at higher strain rates has been found at this time for AA6111.

1.3 MATERIAL MODELS

An important component of numerical modeling is the description of the materials being used in the simulation. An accurate representation of the material's constitutive response can increase the accuracy of the numerical predictions. A constitutive model is a mathematical expression that relates flow stress to parameters such as strain, strain rate, temperature and internal state variables. Three material models that are commonly used to describe the constitutive response of metals are presented. All of these models take into account the strain rate and temperature sensitivity of a material and are implemented in many finite element analysis packages.

1.3.1 JOHNSON-COOK MATERIAL MODEL

The Johnson-Cook constitutive model [20,61,62] is an empirical strength model that accounts for the effects of strain, strain rate and temperature on the von Mises flow stress and has the following form:

$$\sigma = \left[A + B\varepsilon_{pl}^{n} \right]\left[1 + C \ln \dot{\varepsilon}^{*} \right]\left[1 - T^{*m} \right] \tag{1.21}$$

where ε_{pl} is the effective plastic strain, $\dot{\varepsilon}^{*} = \dot{\varepsilon} / \dot{\varepsilon}_{0}$ is the dimensionless plastic strain rate for a reference strain rate $\dot{\varepsilon}_{o}$, and T^{*} is a form of homologous temperature given as $T^{*} = \left(T - T_{room} \right) / \left(T_{melt} - T_{room} \right)$. The five material constants *A, B, C, m* and *n* are fit to data collected for a particular material. The first expression in equation (1.21) represents the work hardening response of the material at the reference strain rate, while the second and third expressions account for the strain rate and temperature sensitivity, respectively. This model is easily implemented in computational codes due to its simplicity. All the parameters are coupled due to the multiplicative nature of the model [20]. Furthermore this model assumes that strain rate and temperature sensitivity are independent of each other, while real materials display a strain rate sensitivity which is dependent upon temperature [19].

Johnson and Cook evaluated their model by attempting to predict the deformed shape of Taylor cylinder impact samples fabricated from OFHC copper, Armco iron and 4340 steel [61,62]. The data used for the constitutive fits was collected from torsion tests conducted at strain rates ranging from quasi-static to 400 s^{-1}. The strain rates and strains experienced during the Taylor impact experiments far exceed the range used for the model fit, and can be viewed as an independent test case for comparison purposes [61]. Numerical simulations using the fit model were in very good agreement with experimental data for 4340 and Armco iron. The numerical results for OFHC copper were acceptable, but the correlation was not as close as that witnessed in the other two materials [61].

Examining the Johnson-Cook model presented in equation (1.21), it can be seen that the effect of strain rate on the von Mises flow stress is assumed to be a linear function of the natural logarithm of the effective plastic strain rate. Many ductile materials, such as OFE Copper shown in Figure 1.9, have exhibited a rapid increase in strain rate sensitivity at rates above

$1x10^3$ s^{-1}. To account for this behavior, Rule and Jones [63] proposed a revised Johnson-Cook strength model that enhances the strain rate sensitivity, while at the same time minimizes changes to the model's performance in the loading regimes where it has been effectively employed. Their proposed model is of the form:

$$\sigma = \left(C_1 + C_2\varepsilon^n\right)\left[1 + C_3 \ln \dot{\varepsilon}^* + C_4\left(\frac{1}{C_5 - \ln \dot{\varepsilon}^*} - \frac{1}{C_5}\right)\right]\left(1 - T^{*m}\right) \qquad (1.22)$$

where C_1 through C_5 are material constants. The second term in equation (1.22) is referred to as the strain rate sensitivity factor. The term $1/\left(C_5 - \ln \dot{\varepsilon}^*\right)$ increases the strain rate sensitivity at higher rates, and the parameter C_4 controls the amount this modified Johnson-Cook model deviates from the original formulation [63].

One shortcoming of this model is that the yield stress in unbounded and tends to infinity as $\ln \dot{\varepsilon}^*$ approaches the value of C_5. To prevent this, Rule and Jones [63] have simply imposed an upper limit for the strain rate sensitivity factor in equation (1.22) through a non-dimensional constant C_6 defined as follows:

$$\left[1 + C_3 \ln \dot{\varepsilon}^* + C_4\left(\frac{1}{C_5 - \ln \dot{\varepsilon}^*} - \frac{1}{C_5}\right)\right] \le C_6 \qquad (1.23)$$

This limits the strain rate sensitivity factor to a maximum value.

Rule and Jones [63] evaluated their model by studying its performance in predicting the results of quasi-static tensile tests and Taylor impact tests for four materials: 7075-T6 aluminum, OFHC copper, wrought iron, and Astralloy-V*, a high-strength steel. Data from these tests was fit to the model giving equal weighting to data sets from both types of experiments. Numerical simulations were conducted using EPIC. In general, the model provided a satisfactory correlation between the measured and calculated cylinder shapes with wrought iron exhibiting the largest volume error of 5.3% [63].

Similarly to Rule and Jones [63], Kang *et al*. [16], modified the Johnson-Cook model to include a higher order term in the strain rate sensitivity term after they found that the original

form of the constitutive model was unable to provide an accurately fit for various sheet steels. The form of their modified Johnson-Cook model is as follows:

$$\sigma = \left[A + B\varepsilon^{n} \right]\left[1 + C_1 \ln \dot{\varepsilon}^{*} + C_2 \left(\ln \dot{\varepsilon}^{*} \right)^2 \right]\left[1 - T^{*m} \right] \tag{1.24}$$

As can be seen, the strain rate sensitivity term has been modified to a quadratic form. Kang *et al*. [16] fit their model to tensile tests conducted using SPCEN, SPCC and SPRC sheet steels, which are commonly used in body panels. The strain rates used in their experiments ranged from $1x10^{-3}$ s^{-1} to 5000 s^{-1}. In comparison to the original Johnson-Cook constitutive model, Kang *et al*. [16] found that their modified strength model resulted in a closer correlation between numerical and experimental results for the three sheet steels, in the range of strain rates considered.

1.3.2 ZERILLI-ARMSTRONG MATERIAL MODEL

The Zerilli-Armstrong strength model is a physically-based constitutive model developed based on the consideration of thermally activated dislocation motion [20,35,64,65,66]. Unlike empirical models, physically based models such as this one take into account the evolution of the material's microstructure. Zerilli and Armstrong [35,64,65,66] identified that dislocation interactions in BCC metals are different than those in FCC metals, and have developed relations for each crystallographic structure. Both relations take into account the effects of strain, strain rate, temperature and grain size on the flow stress. In general, the model follows a similar form for both crystallographic structures:

$$\sigma = \Delta\sigma_G' + \sigma_{th} + kl^{-1/2} \tag{1.25}$$

where σ is the von Mises equivalent stress. The first term ($\Delta\sigma_G'$) is an athermal component of stress and considers the contribution of solute and the initial dislocation density on the yield stress. The second term (σ_{th}) is the contribution of strain rate and temperature to the flow stress, while the third term considers the influence of solute and grain size.

Thermal activation in BCC metals is believed to be controlled by the Peierls stress associated with dislocation motion [35,64,65,66,67]. Also, strain rate and temperature have been found to have a stronger effect on the yield stress in BCC compared to FCC metals. For BCC metals,

the contribution of strain, strain rate and temperature on the thermal component of stress σ_{th} is given by:

$$\sigma_{th} = C_1 \exp\left(-C_3 T + C_4 \ln \dot{\varepsilon}\right) \tag{1.26}$$

where $\dot{\varepsilon}$ is the plastic strain rate, T is the absolute temperature and constants C_1, C_3 and C_4 are material parameters. A separate plastic strain hardening contribution is added for BCC metals and assumed to follow a power law dependence on strain as follows:

$$\Delta\sigma_G = C_5 \varepsilon^n \tag{1.27}$$

where the ε is the equivalent plastic strain and parameters C_5 and n are material parameters. The resulting constitutive relationship for BCC metals is:

$$\sigma = \Delta\sigma_G' + C_1 \exp\left(-C_3 T + C_4 T \ln \dot{\varepsilon}\right) + C_5 \varepsilon^n + kl^{-1/2} \tag{1.28}$$

For FCC metals such as aluminum, analysis has shown that thermal activation is primarily controlled by the intersection of dislocations and is strongly dependent on strain [35,64,65,66]. Strain, strain rate and temperature have a coupled effect on the thermal stress component σ_{th} given as:

$$\sigma_{th} = C_2 \varepsilon^{1/2} \exp\left(-C_3 T + C_4 T \ln \dot{\varepsilon}\right) \tag{1.29}$$

where C_2 through C_4 are material constants and the other parameters are as previously defined. Here we can see that the effects of strain rate and temperature on the flow stress are dependent on the strain hardening. Thus, for FCC metals, the Zerilli-Armstrong constitutive model is as follows:

$$\sigma = \Delta\sigma_G' + C_2 \varepsilon^{1/2} \exp\left(-C_3 T + C_4 T \ln \dot{\varepsilon}\right) + kl^{-1/2} \tag{1.30}$$

BCC and FCC constitutive models were evaluated by simulating Taylor impact and tensile tests performed on OFHC copper and Armco iron. It was found that these models resulted in a more accurate prediction of the shape of deformed Taylor impact cylinders than the Johnson-Cook model for both materials [64] and was reasonably good in predicting necking instability in the tensile test [65].

1.3.3 MECHANICAL THRESHOLD STRESS MODEL

Experiments performed by Follansbee [32] on copper and Nitronic 40, an austenitic stainless steel, led to a conclusion that strain alone is not an appropriate variable to incorporate as a path independent state variable in constitutive models, since a constant material microstructure would be implied by a constant strain. The flow stress of a particular crystallographic structure measured at 0 K is known as the mechanical threshold stress and is a measure of the state of the material [20,32]. Follansbee [32] found the mechanical threshold stress to be a function of strain rate at a constant strain of 0.10, thus implying that structural evolution is rate dependent. From this, Follansbee *et al*. [32,68,69] formulated a constitutive model that uses internal state variables to describe the current state of the material. The Mechanical Threshold Stress model uses strain, strain rate and temperature to define the yield stress of a material at a specific internal state. The state variables evolve with strain, strain rate and temperature. The model is of the form:

$$\left(\sigma-\sigma_a\right)^r=\sum\left[s_i\left(\dot{\varepsilon},T\right)\hat{\sigma}_i\right]^r \tag{1.31}$$

where σ is the applied stress, σ_a is the athermal component of stress, $\hat{\sigma}_i$ is the mechanical threshold stress to overcome the i^{th} obstacle, the exponent r accounts for the interaction between different types of obstacles, while s_i specifies the ratio between the applied stress and the mechanical threshold stress, and is defined by glide kinetics [69]. The parameter s_i is expressed as:

$$s_i=\left[1-\left(\frac{kT}{g_{0i}\mu b^3}\ln\frac{\dot{\varepsilon}_0}{\dot{\varepsilon}_i}\right)^{1/q_i}\right]^{1/p_i} \tag{1.32}$$

where k is the Boltzmann constant, μ is the temperature dependent shear modulus, b is the Burger's vector, $\dot{\varepsilon}_o$ is a reference strain rate and considered to be a constant, g_{0i} is the normalized total activation energy, while p_i and q_i are constants that characterize the shape of the obstacle. The evolution of the material state is a result of strain hardening θ and is described by the following differential equation [68]:

$$\frac{d\hat{\sigma}_\varepsilon}{d\varepsilon}=\theta=\theta_0\left(\dot{\varepsilon}\right)\left[1-F\left(\hat{\sigma}_\varepsilon/\hat{\sigma}_{\varepsilon s}\right)\right] \tag{1.33}$$

where θ_0 is the Stage II strain hardening, $\hat{\sigma}_\varepsilon$ is the mechanical threshold stress that characterizes dislocation/dislocation interaction, $\hat{\sigma}_{es}$ is the strain-rate and temperature dependent saturation value, and F is a function that best describes the strain hardening relationship [68].

Although this model has the ability to account for the history dependence of strain, strain rate and temperature on the flow stress, determining the parameters of this model requires a large number of experiments to be conducted. Follansbee and Kocks [69] fit this model to data collected for copper. The model predictions were in good agreement with experimental results within the strain rate regime used for the fit [69]. Model predictions at strain rates beyond the regime which the model was fit to, also correlated well with experimental results [69].

1.4 PRESENT RESEARCH

The goal of the present work is to characterize the high strain rate behavior of three aluminum sheet alloys used in automotive body and structural applications: AA5754, AA5182 and AA6111. This data is needed in order to develop and implement strain rate sensitive constitutive models in numerical simulations used to model vehicle crash events. To provide this information, tensile experiments were conducted along the rolling direction at quasi-static and elevated strain rates. Quasi-static experiments were performed using an Instron servo-electric testing apparatus, while dynamic experiments were conducted using a TSHB apparatus. The experimental results were fit to both the Johnson-Cook and Zerilli-Armstrong constitutive models. Metallographic and scanning electron microscope (SEM) analyses were performed on failed specimens in order to determine if changes in damage evolution occurred at high rates of strain. Numerical simulations were performed using LS-DYNA [70], an explicit dynamic finite element code.

In the following chapters, the mechanical components and instrumentation of the TSHB apparatus used are described, and the design of a specimen geometry suited for high strain rate tensile testing of sheet alloys is presented. Experimental procedures are given and the

numerical modeling conducted is discussed in detail. The results of both are presented for comparison.

2 EXPERIMENTAL METHODS

Quasi-static and high strain rate experiments were conducted to identify the strain rate sensitivity of AA5754, AA5182 and AA6111 aluminum alloy sheet in the range of strain rates corresponding to those witnessed in automotive crash events. Elevated temperature experiments at high strain rates were also performed to capture the thermal softening effect. This data was required in order to determine constitutive model parameters for these alloys.

2.1 MATERIAL

AA5754 and AA5182 are non-heat treatable, work-hardening Al-Mg alloys. These alloys are commonly used for automobile structural or body inner panels. AA6111 is mainly used for exterior body panels since it is heat treatable. During the paint baking process, exterior body panels made from AA6111 precipitation harden, thus improving dent resistance [71]. The nominal compositions of the alloys tested are listed in Table 2.1. The nominal sheet thicknesses available for both AA5754 and AA5182 were 1.6 mm and 1 mm, while AA6111 was only available in 1 mm thick sheet.

Table 2.1 – Composition of Alloys [72,73]

Material	*Nominal Composition wt.%*							
	Mg	*Mn*	*Fe*	*Si*	*Zn*	*Cu*	*Cr*	*Ti*
AA5754	*3.2*	*0.2*	*0.3*	*0.06*	*-*	*-*	*-*	*0.01*
AA5182	*4.5*	*0.35*	*0.27*	*0.08*	*0.05*	*0.05*	*0.03*	*0.1*
AA6111	*0.5-1.0*	*0.1-0.45*	*Max 0.4*	*0.6-1.1*	*Max 0.15*	*0.5-0.9*	*Max 0.1*	*Max 0.1*

Typical microstructures of the undeformed AA5754 and AA5182 sheets are shown in Figure 2.1. EDX analysis found that the second phase particles present in both alloys are rich in Fe and Mn. Compared to AA5754, the undeformed AA5182 microstructure contains higher amounts of second phase particles that are also larger in size. For the 1.6 mm thick sheet in the long-transverse plane, the percent area fraction of second phase particles is 0.60% and 0.98%,

for AA5754 and AA5182, respectively [72]. The respective initial porosities are 0.02% and 0.10% [72].

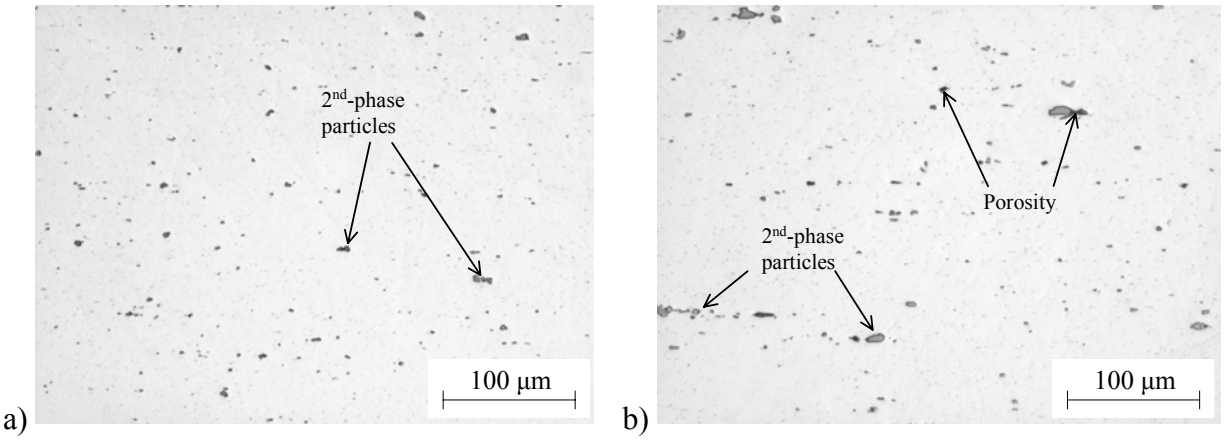

Figure 2.1 – Optical Micrographs of Undeformed, 1.6 mm Thick a) AA5754 and b) AA5182 in the Long-Transverse (Through-Thickness, Along the Rolling Direction) Plane, Polished Only [72]

Unlike AA5754 and AA5182, AA6111 is prone to aging. The material used in this study was approximately four months old when tested. The nominal composition of AA6111 contains less magnesium than AA5754 and AA5182, and contains higher concentrations of silicon and copper. The typical microstructure of undeformed AA6111 is shown in Figure 2.2. For the 1 mm thick sheet used, the percent area fraction of second phase particles and the initial porosity in the long-transverse plane were 0.68% and 0.01%, respectively [4].

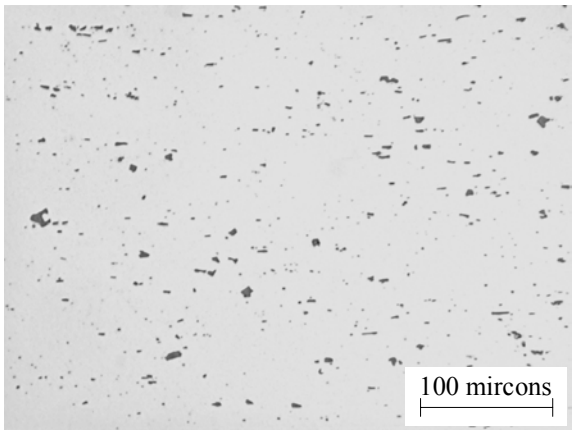

Figure 2.2 – Optical Micrograph of Undeformed, 1 mm Thick AA6111 in the Long-Transverse (Through-Thickness, Along the Rolling Direction) Plane, Polished Only

2.2 EQUIPMENT

2.2.1 TENSILE SPLIT HOPKINSON BAR APPARATUS

The dynamic tensile experiments were conducted using the TSHB apparatus located at the University of Waterloo. The apparatus is equipped with momentum trapping fixtures to facilitate interrupted testing. Clarke [26] and Pelletier [19] provide detailed descriptions of the design of this apparatus. A schematic of the TSHB apparatus is provided in Figure 2.3, while a photograph is shown in Figure 2.4.

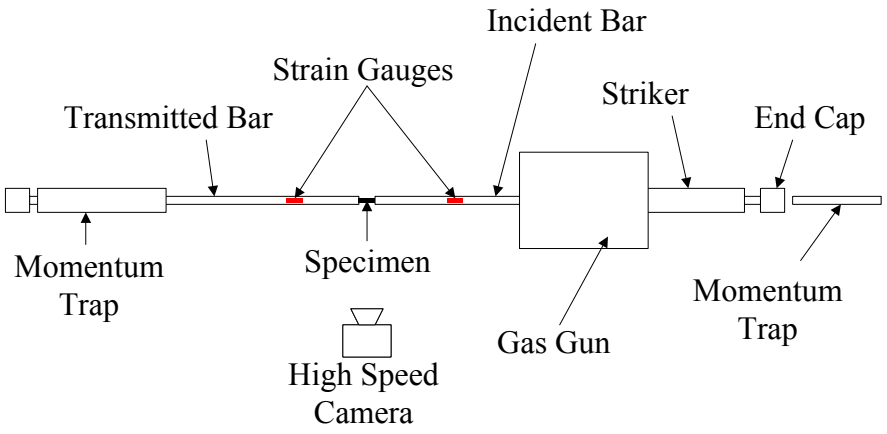

Figure 2.3 – Schematic of Tensile Split Hopkinson Bar Apparatus

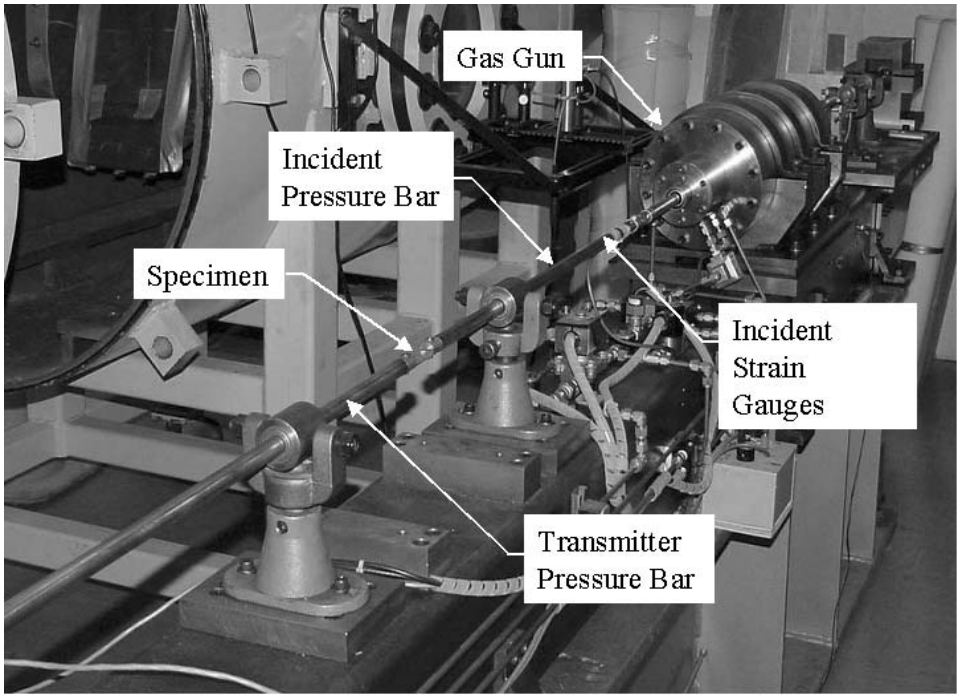

Figure 2.4 – Photograph of TSHB Apparatus at the University of Waterloo

The TSHB apparatus generates a tensile loading pulse acting on the sample. The gas gun uses compressed nitrogen to propel a hollow striker tube, located concentrically on the incident bar, towards the end cap. The maximum striker velocity is approximately 20 m/s [19]. The cross-sectional area of the striker is designed to have the same cross-sectional area as the incident bar in order to avoid an impedance mismatch between them. Upon impacting the end cap, a tensile loading pulse is generated in the incident bar. The length of the pulse is twice that of the striker, and the stress amplitude is proportional to the impact velocity. The pulse travels along the incident bar towards the specimen at the elastic sound velocity of the incident bar material. Strain gauges, placed on the incident bar, record this wave as it passes. When the wave reaches the specimen, the incident wave overwhelms the specimen, which deforms plastically at high rates of strain as a result. The load carried by the sample is transmitted to the transmitter bar. Strain gauges located on the transmitter bar record the transmitted wave. The remainder of the incident pulse is reflected back down the incident bar as a compressive wave. The reflected wave is recorded by the strain gauges on the incident bar as it travels back towards the end cap. A typical set of waves recorded during a tensile Hopkinson bar experiment is given in Figure 2.5.

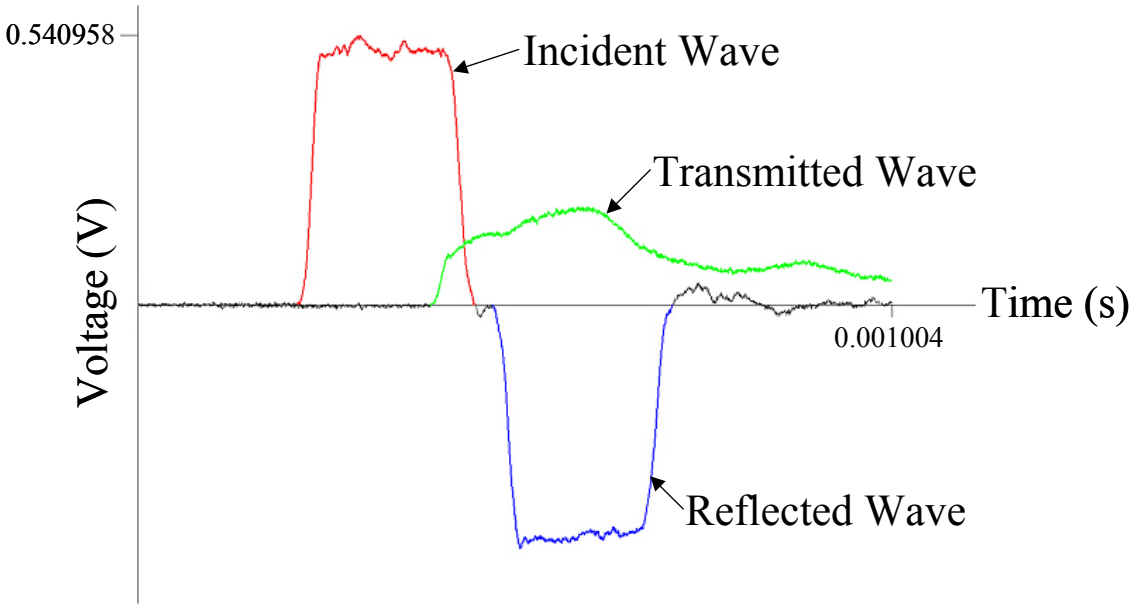

Figure 2.5 – Waves Recorded From a Typical Hopkinson Bar Experiment

Several modifications were made to the Hopkinson bar apparatus in order to permit aluminum alloy sheet to be tested. Initially, the pressure bars were made from 4340 steel. Preliminary tests using these bars found that the strain levels measured in the transmitter bar were low in comparison to the ambient electrical noise. This was due to a combination of the small cross-sectional area of the sheet specimens and the relatively low strength of aluminum compared to materials such as steel or titanium, previously tested using this apparatus. Consequently, the pressure bar material was changed to AA6061-T6 due to the relatively low elastic modulus of aluminum, thus improving the signal-to-noise ratio by a factor of approximately three. The incident and transmitter bars are 15.87 mm in diameter and are 2 m and 1.8 m in length, respectively.

Numerical simulations and experiments using a steel striker and an aluminum incident bar were conducted to determine the effects of the impedance mismatch of the two components. The details of the numerical model are not discussed in this thesis. The axial strain in the incident bar was monitored and is shown as a function of time in Figure 2.6. In both the numerical simulations and the experiments, wave reflections were generated as a result of the

impedance mismatch between the two components, and the incident and reflected waves measured within the incident bar became distorted. When the striker material was changed to aluminum in the numerical simulation, no wave reflections occurred, thus underlining the necessity for matching material impedances.

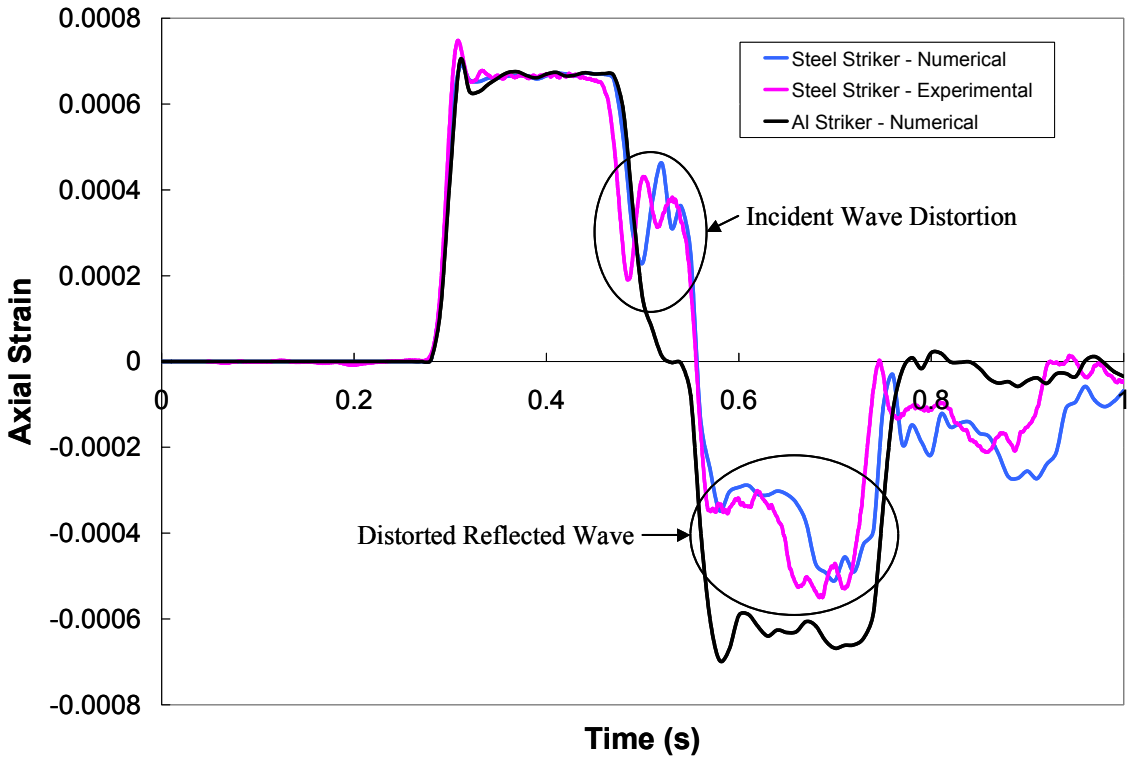

Figure 2.6 – Effect of Striker Material on the Axial Strain vs. Time in an Aluminum Incident Bar

A set of aluminum strikers was manufactured from AA6061-T6, the same material as the pressure bars. Due to the required bore tolerance, gundrilling was necessary. The outside diameter was machined to size after gundrilling in order to maintain concentricity.

Since the material being tested is in sheet form, a novel method of gripping needed to be implemented that provided enough clamping force to prevent the specimen from slipping during the experiment, yet introduced a low mechanical impedance to avoid wave distortion [16,17]. Mechanical grips consisting of a wire-EDM cut slot for a single specimen thickness were manufactured and are shown in Figure 2.8. A steel screw applies clamping pressure to

prevent any sliding between the specimen and the grip, eliminating the need for adhesive bonding. Initially the grips were threaded into the bar, however, it was found that the threads distorted the incident wave when it reached the specimen. As seen in Figure 2.7, as the gas gun pressure is increased, oscillations appear in the reflected wave as a result of the threads. The plateau of the reflected wave also became smaller, reducing the time span at which the nominal strain rate is constant. Integrating the grips directly into the bar ends, as shown in Figure 2.8(b) and Figure 2.9, solved this problem. The result was a grip that minimized wave distortion, as shown in Figure 2.10, and provided enough clamping force to prevent the specimen from slipping during the experiment.

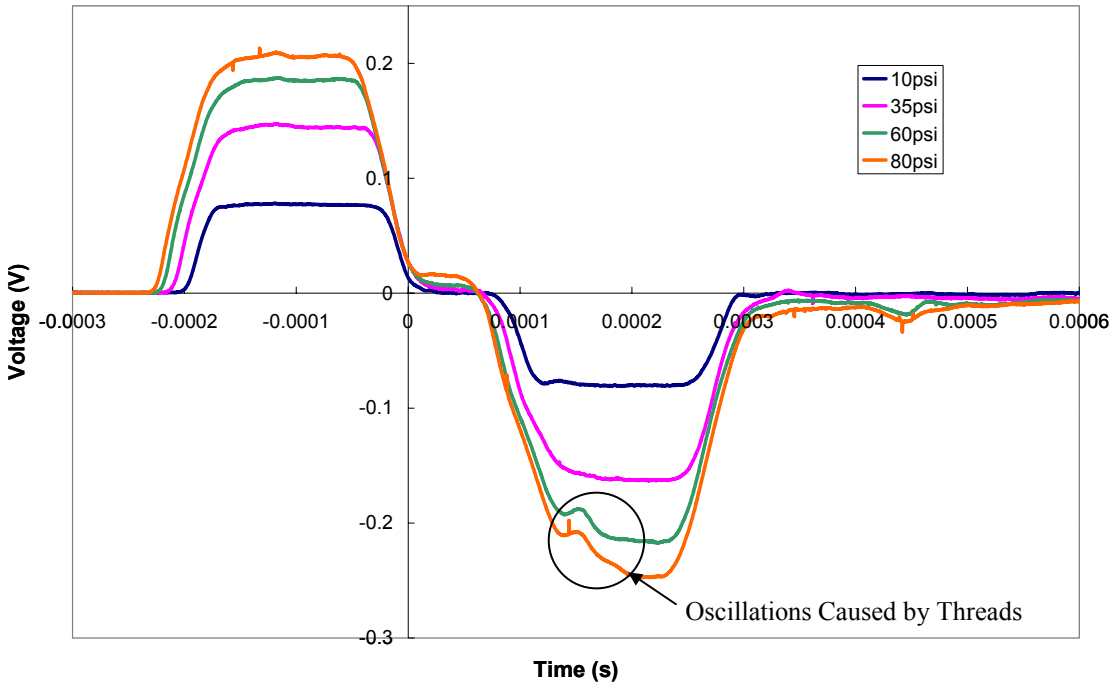

Figure 2.7 – Distortion of the Reflected Strain Waves Caused By Threads in a TSHB Apparatus

a) 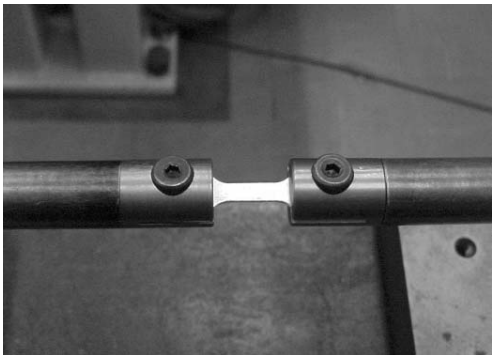 b) 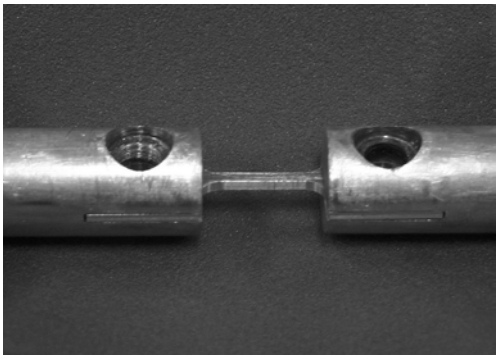

Figure 2.8 – Photos of TSHB Grips For Sheet Material: a) Threaded Grips, b) Integrated Grips

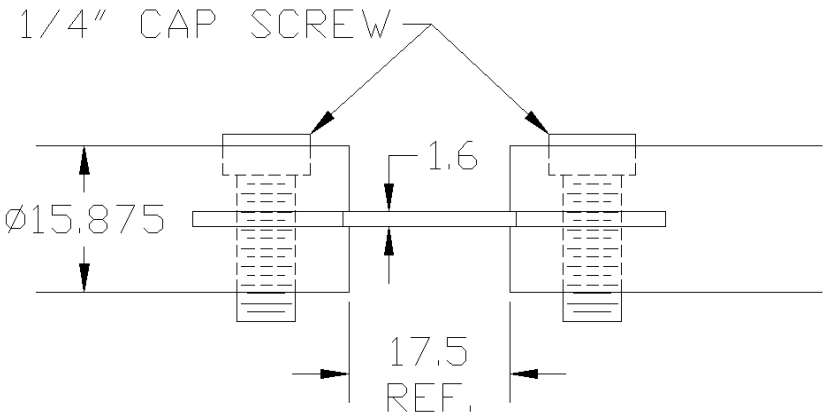

Figure 2.9 – Schematic of Integrated TSHB Grips for Sheet Material (1.6 mm)

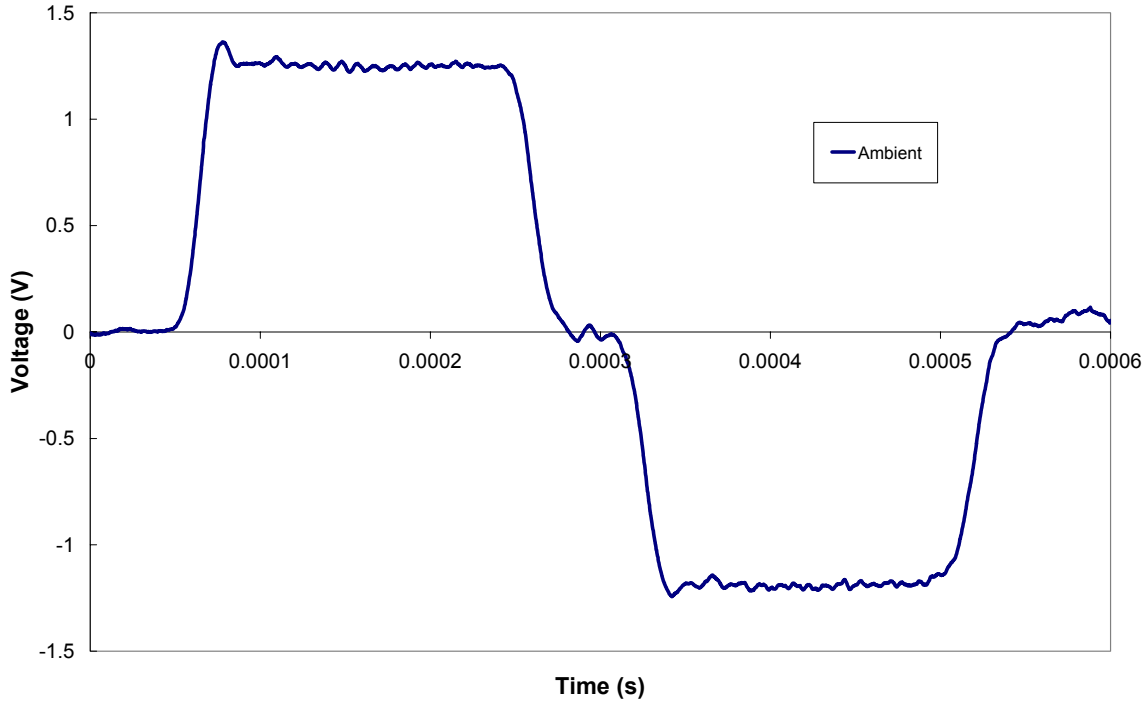

Figure 2.10 – Incident and Reflected Strain Waves Recorded for Incident Bar With Integrated Grips

2.2.2 ELEVATED TEMPERATURE EXPERIMENTS

High strain rate experiments at elevated temperatures were conducted using the radiative furnace shown in Figure 2.11. The external dimensions are 178 mm in diameter by 178 mm long. The heating chamber of the furnace is 50 mm in diameter by 57 mm long and uses four 1000 W quartz heating lamps. A single K-type thermocouple, inserted through the centerline of a shaft, measures the furnace temperature and is used for temperature control. Since this is not a direct measure of the specimen temperature, the system was first calibrated to obtain the correct controller temperature corresponding to the desired specimen temperature.

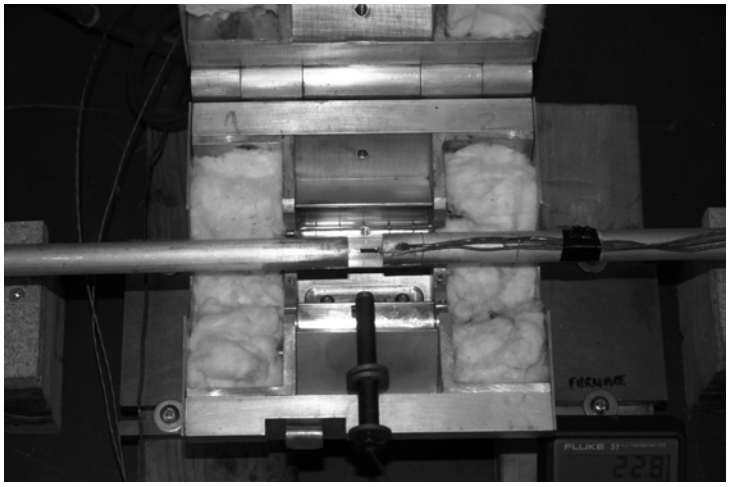

Figure 2.11 – Furnace Used in Elevated Temperature TSHB Experiments

During heating, the specimen remains attached to the incident and transmitter bars as a result of the gripping mechanism. Ceramic insulating tubes were used to shroud the bars to avoid excessive heat input into the bars themselves. To measure the effect this had on maintaining near-isothermal conditions along the length of the bars, the small apparatus shown in Figure 2.12 was constructed, consisting of a specimen and two lengths of AA6061-T6 representing the TSHB pressure bars. The furnace was mounted concentrically over the specimen and bars as it would be in the TSHB apparatus. The specimen and one of the aluminum bars were fitted with a total of 5 K-type thermocouples at various locations as illustrated in Figure 2.13.

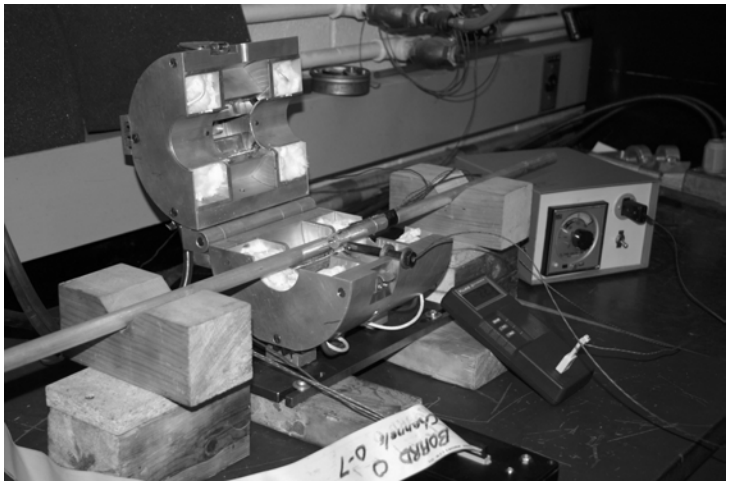

Figure 2.12 – Photograph of Apparatus Used to Determine the Temperature Gradient Along the Pressure Bars

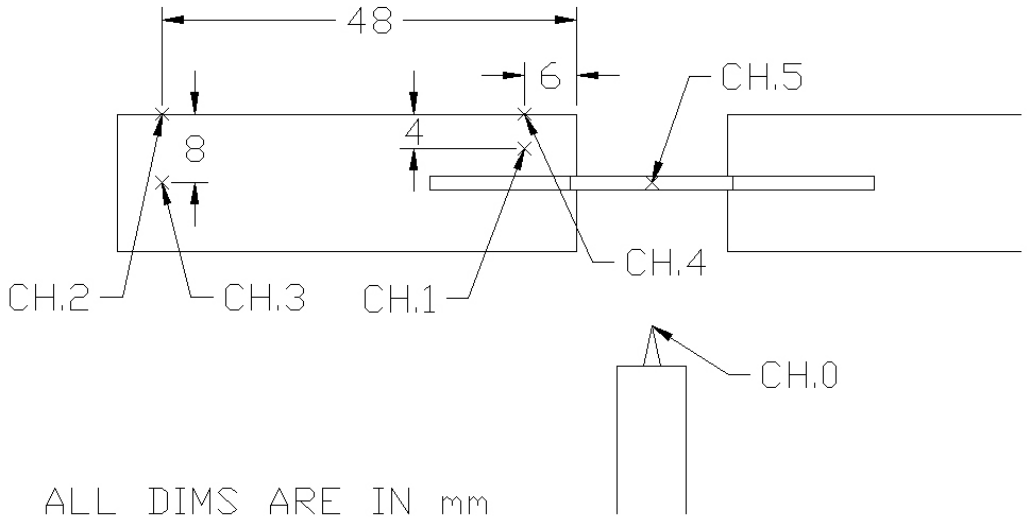

Figure 2.13 – Thermocouple Locations

It was found that the ceramic shrouds helped to maintain much of the bar at near-isothermal conditions. Figure 2.14 shows the temperature distribution along the length of the bar. In both cases, adding the shrouds lowered the bar surface temperature at 6 mm away from the bar end by 73°C. At a specimen temperature of 300°C, the surface temperature of the at 6 mm from the bar end was measured to be approximately 365°C. This is significantly higher than the specimen temperature itself and is possibly due to the proximity of the bar surface to the heating elements in the furnace. Although the bar surface temperature for the 300°C case is high even with the shrouds (292°C and 184°C at 6 mm and 48 mm from the bar end, respectively), Pelletier [19] found that the bar supports in the TSHB acted as heat sinks. Past their positions the bar temperature was within 10°C of room temperature, even when the sample was heated to 750°C [19].

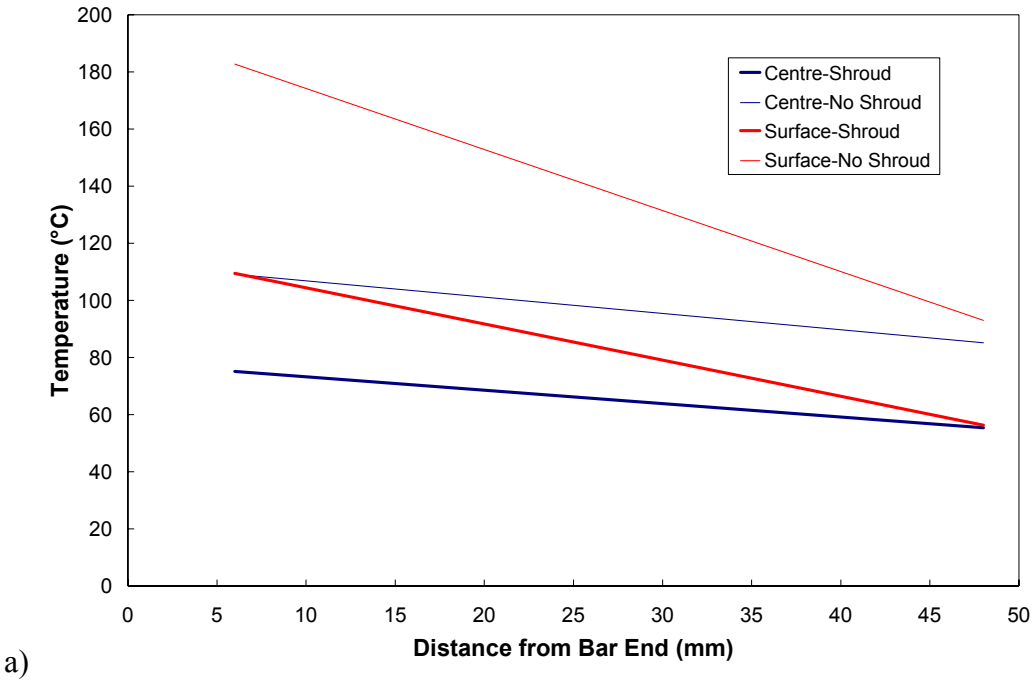

a)

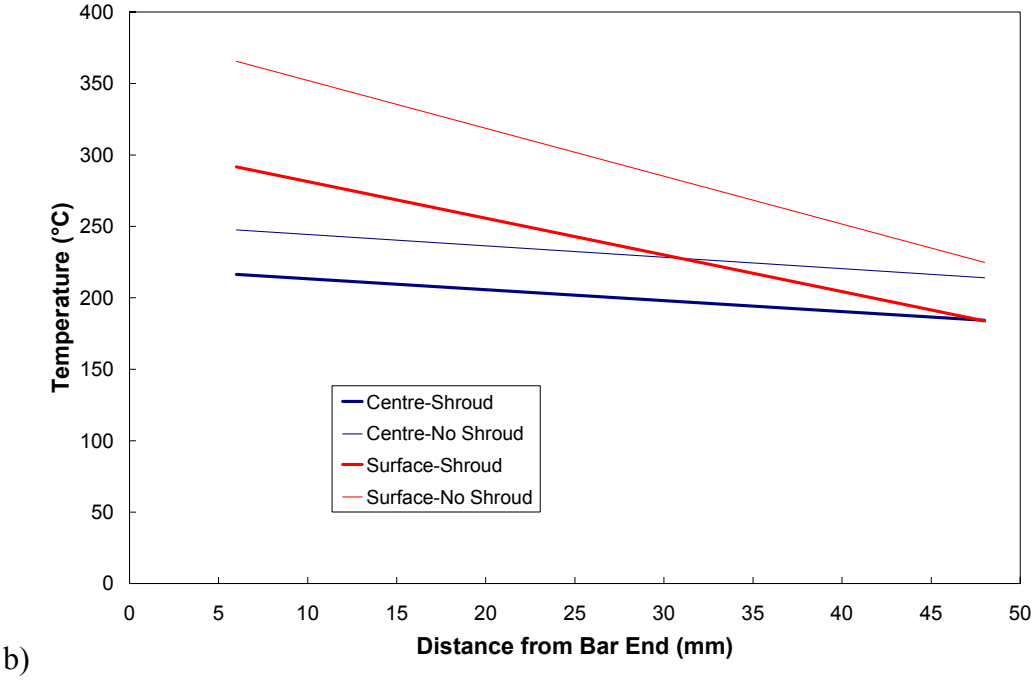

b)

Figure 2.14 – Temperature as a Function of Distance from Bar End for a Specimen Temperature of a) 150°C and b) 300°C

Incident and reflected wave signals recorded for the 300°C case are compared to those recorded at room temperature in Figure 2.15. No apparent distortion in the signals caused by

the increased temperature at the bar ends is seen, and as such no temperature compensation was performed on the experimental data. Differences between the signals in Figure 2.15 fall within the typical variability of the strain waves between experiments.

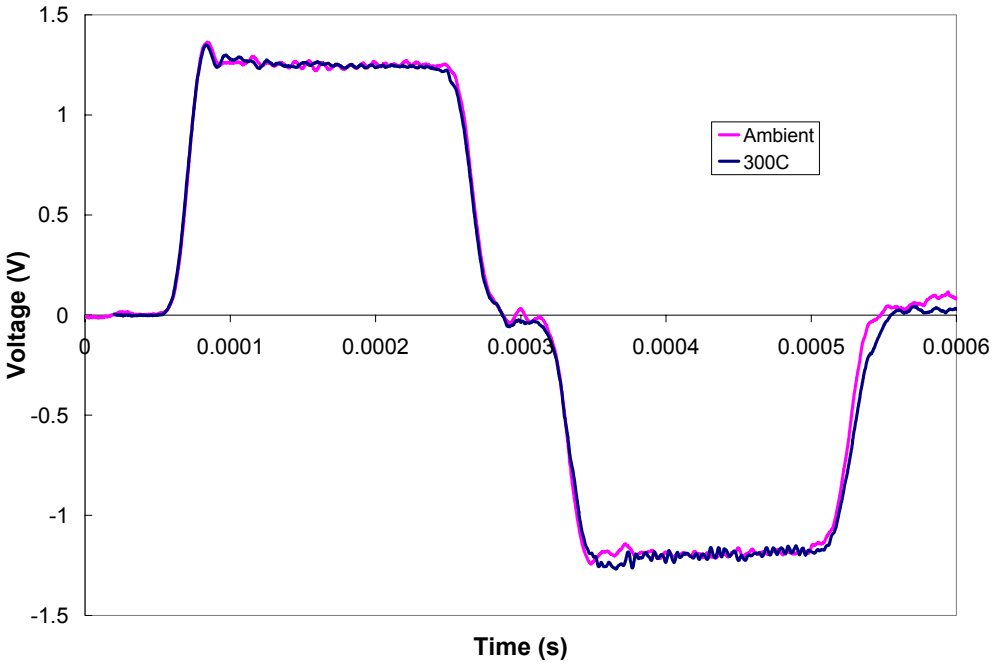

Figure 2.15 – Comparison of Incident and Reflected Wave Signal Recorded at Various Temperatures

2.2.3 INSTRUMENTATION

The strain gauges used on both the incident and transmitter bars are foil-type gauges. Although semiconductors gauges have a much higher gauge factor than foil gauges, the foil gauges adhered better to the aluminum pressure bars. Furthermore, the tolerance of the gauge factor for semiconductor gauges is much wider than that of the foil gauges and requires a calibration to be performed every time a new set of gauges is installed. Two strain gauges were placed on opposite sides of the bar at each location and used in a half-bridge configuration to cancel any possible bending. The gauges used on the incident bar have a nominal resistance of 120 Ω. 1000 Ω strain gauges were used on the transmitter bar allowing a much higher excitation voltage to be used in comparison to the 120 Ω gauges (14 V in

comparison to 2 V), which increases the signal measured. Two resistors of the appropriate resistance were used to complete each Wheatstone bridge, shown in Figure 2.16.

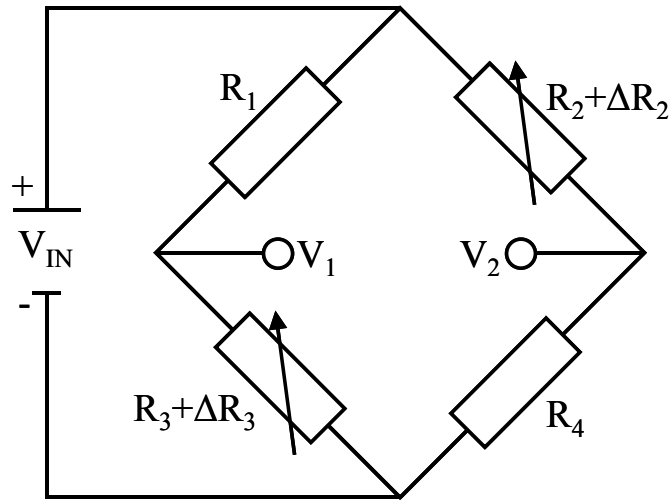

Figure 2.16 – Wheatstone Bridge

The output signal from the Wheatstone bridge shown in Figure 2.16 is measured across V_1 and V_2. If all four nominal resistances in the Wheatstone bridge are equal, and both strain gauges have the same gauge factors, the Wheatstone bridge equation can be reduced to the following:

$$V_1 - V_2 = G\left(\frac{\Delta R}{2R + \Delta R}\right)V_{IN} \tag{2.1}$$

where G is the amplifier gain, R is the nominal resistance of the strain gauges, ΔR is the change in resistance per unit strain of the strain gauges, and V_{IN} is the bridge excitation voltage. ΔR in equation (2.1) is defined as:

$$\Delta R = RG.F.\varepsilon \tag{2.2}$$

where $G.F.$ is the strain gauge factor and ε is the applied strain.

A calibration of the Wheatstone bridges was performed and their output was compared with that calculated using equation (2.1). A photograph of the equipment used to calibrate the strain gauges is shown in Figure 2.17. A hydraulic actuator was used to apply a compressive load to the pressure bars. The load was measured using a model 1210-AF load cell from Interface Advanced Force Measurement, placed between the pressure bars. The strain of the bars was calculated from the applied load, while the output of each Wheatstone bridge was measured

using an oscilloscope. As seen in Figure 2.18, the output measured from the Wheatstone bridge on both incident and transmitter bars follows the response calculated by equation (2.1).

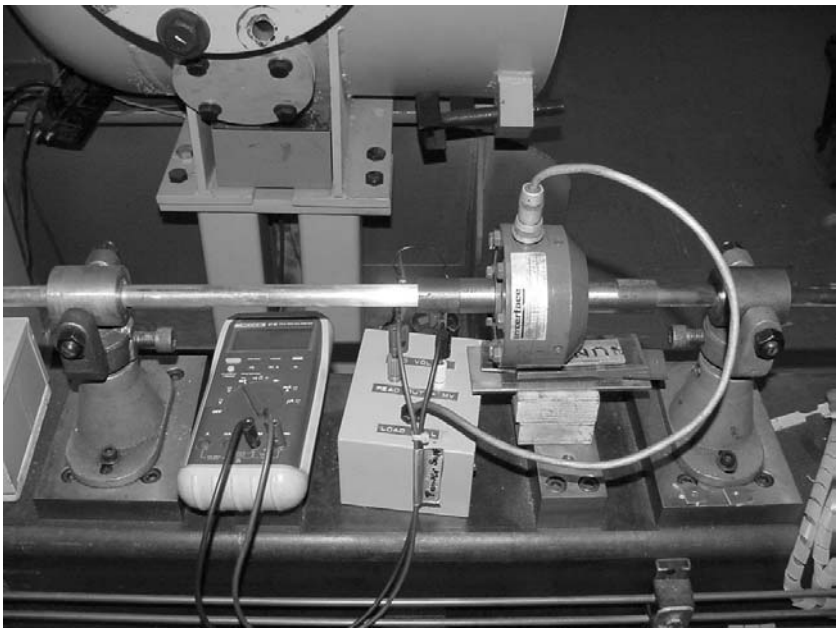

Figure 2.17 – Photograph of Strain Gauge Calibration Setup

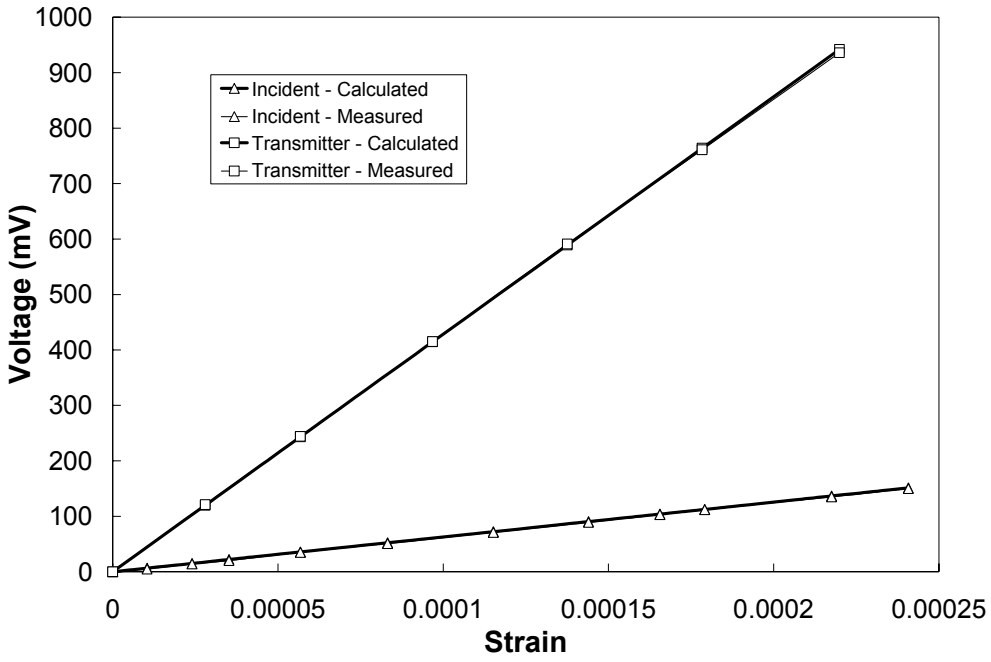

Figure 2.18 – Strain Gauge Calibration

A major drawback of foil strain gauges is that their output signal needs to be amplified due to their relatively low gauge factor. Vishay Micromeasurements model 2210B signal amplifiers were implemented. The gain on the amplifiers was set to 300, resulting in a frequency response of 120 kHz. The output signals from the amplifiers were recorded using a Nicolet Integra Model 40 digital storage oscilloscope. This oscilloscope has a 12-bit resolution and a maximum sampling frequency of 20 million samples per second. A 50 ns sampling rate was selected for the Hopkinson bar experiments, recording 2000 data points per channel during each experiment.

2.3 METALLOGRAPHY

Metallographic investigations were conducted on the AA5754 and AA5182 TSHB specimens to quantify and compare the amount of damage generated when tested under quasi-static (QS) conditions, and at high strain rates. The sample preparation sequence for damage analysis included: cold mounting of sectioned specimens, wet grinding up to 4000 grit SiC paper, 3 μm and 1 μm diamond polishing, and final polishing using a 0.05 μm colloidal silica suspension.

Optical micrographs of the specimens were obtained as digital images with a 1392 x 1040 pixel, 8-bit resolution, using an Olympus BH2-UMA optical microscope equipped with a Photometrics CoolSNAP CCD camera from Roper Scientific Inc. A 20x objective lens was employed, and the resulting resolution was 0.303 μm/pixel. Damage and thickness strain measurements were carried out using the Image-Pro Plus 5.0 software from Media Cybernetics. All measurements were taken along the long-transverse plane of the specimens at regular intervals away from the fracture surface. The long-transverse plane refers to a plane through the thickness of the sheet, along the rolling direction. Intervals of 25 μm were used for the highly necked and strained region adjacent to the fracture surface, followed by larger 50, 100 and 200 μm intervals for measurements conducted further away from the fracture surface. The span of the region examined for each specimen was at least 3,750 μm from the fracture surface.

2.4 EXPERIMENTAL PROCEDURES

The quasi-static experiments were conducted using an Instron model 4465 servo-electric testing machine. The load cell used on this unit has a capacity of only 500 kg, increasing the resolution of the load measurement. Specimen displacement was measured using a model EZ5-50 extensometer manufactured by United Test Systems. The maximum travel of this extensometer is only 5 mm and is well suited for the relatively short gauge section of the TSHB specimens. The specimens were mounted in pair of grips similar to the ones integrated into the TSHB apparatus and the extensometer was fixed to the assembly as shown in Figure 2.19. The advantage of this mounting scheme is that the jaws used for mounting cylindrical specimens in the Instron serve to align the specimen concentrically with respect to the loading axis of the machine. This alignment reduces the likelihood that bending loads will be applied to the specimen, improving the accuracy of the test.

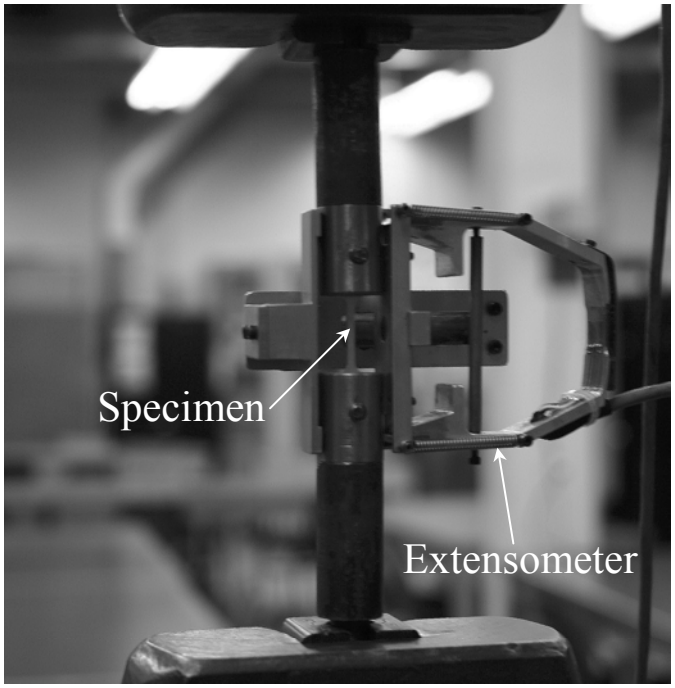

Figure 2.19 – Quasi-Static Experiment Setup Using TSHB Specimen

The high strain rate experiments were performed using the TSHB apparatus at the University of Waterloo. The most critical step involved in the test procedure was inserting the specimens into the grips without twisting them. The specimen was inserted into the grips one end at a

time, and the clamping screws were threaded loosely into each bar. A nylon split collar was inserted over the specimen and the bar ends, and tightened against the bars using a hose clamp. This collar served two purposes: (i) it aligned the specimen and the tensile bar ends; and, (ii) prevented the specimen from being twisted as the clamping screws were tightening. Prior to each experiment, both Wheatstone bridges were balanced using the balancing feature on the amplifier. The split collar was removed, and the gas gun was fired, propelling the striker tube towards the end cap.

With the current apparatus, the maximum striker length is restricted to 508 mm, which results in a maximum loading duration of approximately 200 μs. This limits the strain attainable in a single loading pulse at each strain rate. For example, at a strain rate of 600 s^{-1}, the strain achieved was approximately 12%. Hence, the samples tested in this current work experienced multiple loading-unloading cycles before failure was reached. Consequently, the reader is cautioned that the loading to failure is not monotonic. The elastic unloading of the specimen at the end of the first loading pulse is seen in the sample stress-strain response shown in Figure 2.20. In higher rate experiments, the loading duration remains the same, but the achievable strain increases due to the strain rate. The achievable strain becomes approximately 30% at a strain rate of 1500 s^{-1}.

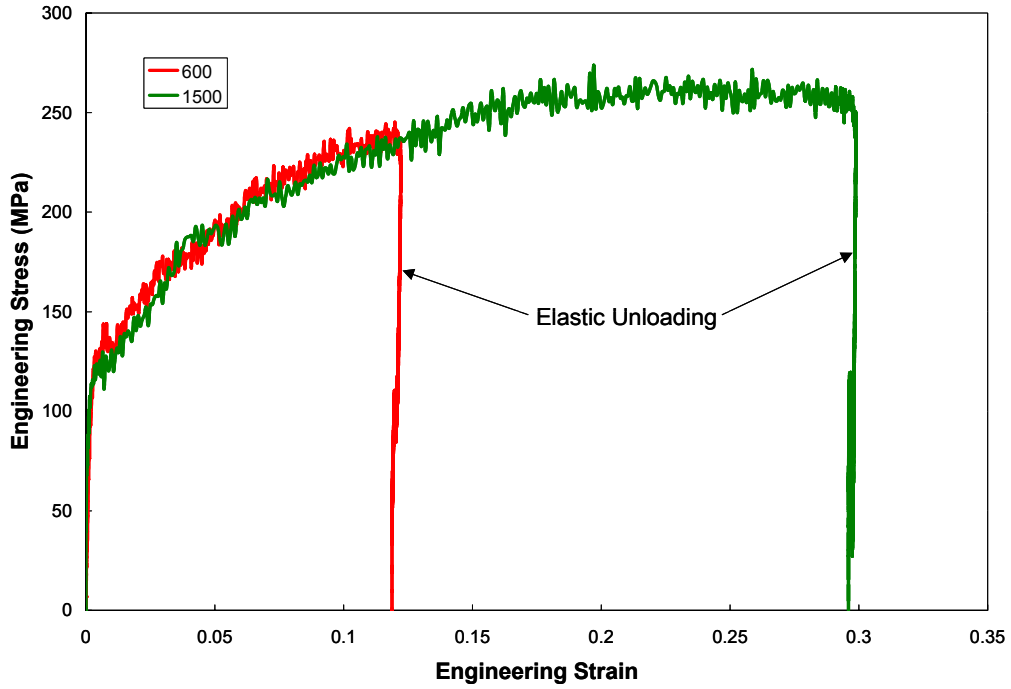

Figure 2.20 – Sample Stress-Strain Response Showing Elastic Unloading of Specimen, Measured at a Strain Rate of 600 and 1500 s^{-1}

Prior to conducting experiments at each elevated temperature, a calibration was performed to determine the proper set point on the furnace temperature controller and the heating time required for the specimen to reach the desired test temperature. A specimen, fitted with a K-type thermocouple through the center of its gauge section, was inserted into the TSHB apparatus and centered in the furnace heating chamber, after which the ceramic shrouds were placed over the bar ends. The furnace was energized, and both the furnace and specimen temperatures were monitored and recorded. This process was repeated until the proper controller set temperature was found. The heating time was taken from the recorded temperature data. Several experiments were done at each temperature to ensure that the controller setting and heating time produced repeatable specimen temperatures.

Once the controller temperature and heating time were found, a specimen was inserted and the experiment was ready to be performed. The furnace was turned on and the specimen was heated. Once the heating time elapsed, the Wheatstone bridges were balanced to remove any offset due to heat input into the strain gauges, and the test was performed. The apparatus and

furnace were cooled between individual tests, using compressed air, to ensure that the heating time resulted in repeatable specimen temperatures.

Once the data was recorded on the Nicolet digital oscilloscope, it was saved to a floppy disk. The raw data was then analyzed using software developed by Salisbury [27]. The software takes the raw data recorded from the TSHB experiment, and analyses it using the Hopkinson bar equations, described in Section 1.1.3, to determine the stress-strain response of the specimen tested. An intercept method is used to split the data recorded on the incident bar into incident and reflected waves. The incident and reflected waves are directly summed to determine the velocity of the incident bar at the specimen interface as per equation (1.5) [27]. For this summation, alignment of the incident and reflected waves is critical. Equally critical is the alignment of the transmitted wave. In order to prevent errors generated by using an *ad hoc* method of arbitrarily choosing the start and end point of each wave, the waves were propagated arithmetically to the bar ends using the speed of sound in the bar material. To more accurately reconstruct the strain waves at each bar end, wave propagation and superposition was performed in the frequency domain using a spectral analysis method, as outlined by Doyle [74] and Salisbury [27]. The software was used to calculate engineering stress, strain and strain rate, as well as the velocity and displacement of the bar ends. For further details on this software, the reader is referred to reference [27].

The engineering stress-strain data was converted to true stress-logarithmic strain in order to be fit to the constitutive models. Logarithmic strain was calculated from the relationship:

$$\varepsilon = \ln\left(\frac{L}{L_0}\right) \tag{2.3}$$

where L_0 is the initial gauge length and L is the instantaneous gauge length which is found by adding the relative displacement of the bar ends to L_0 for each time step. The true strain rate is calculated simply by dividing the relative velocity of the bar ends by L.

In order to calculate the true stress, the instantaneous cross-sectional area of the specimen was determined by applying volume constancy to the gauge section of the specimen. Under this assumption, the true stress becomes:

$$\sigma = \sigma_{eng}\left(1+\varepsilon_{eng}\right) \tag{2.4}$$

where σ is the true stress, σ_{eng} is the nominal or engineering stress, and ε_{eng} is the engineering strain. Only data from the time at which the experiment reached the nominal strain rate to the time when necking occurred in the specimen was used for the constitutive fits since this is the range in which TSHB data can be used directly to measure the stress-strain response of the material.

Since the experiments occur over a short duration, they become adiabatic in nature and the material being tested experiences an increase in temperature due to plastic deformation. Calculation of the temperature rise is based on the portion of plastic work transformed into heat [8],

$$\Delta T = \beta \frac{1}{\rho C_p} \int_0^{\varepsilon_p} \sigma d\varepsilon_p \tag{2.5}$$

where ΔT is the rise in temperature, C_p is the specific heat, ρ is the density, σ is the axial true stress, and ε_p is the axial plastic strain. The integral in equation (2.5) represents the total plastic work and β is the fraction of the total plastic work converted into heat. The actual fraction of work converted to heat has been shown to be a strong function of strain and alloying [75]. Using radiometry to measure temperature, high strain rate compression experiments performed by MacDougall [75] on aluminum alloy BS 2011 demonstrated that β increases from approximately 0.5 at 0% plastic strain, to 1 at approximately 6% plastic strain, and reduces to a steady-state value of 0.9 for plastic strains above 15%. Hayashi *et al*. [76] found a mean value of 0.95 for β in pure aluminum, which was adopted in the current work.

3 NUMERICAL MODELS

Numerical simulations of the split Hopkinson bar and quasi-static tensile experiments were performed to confirm that the constitutive fits would duplicate the specimen response with a finite element model. The models considered the Johnson-Cook and Zerilli-Armstrong fits to the data and were conducted using LS-DYNA [70], an explicit dynamic finite element code. The following section outlines the details of the numerical models. The numerical simulations were of the specimen only. One end of the specimen was fixed, while a velocity profile representative of the velocity-time history measured in the experiments, was applied to the other end of the specimen. The finite element mesh, boundary and loading conditions, material models used, and inertia calculations are discussed in this chapter.

3.1 MESH

The meshes of the specimen geometry required to simulate the tensile experiments were created using Unigraphics. Due to model complexity, it was decided to simulate only the specimen and not include the grips. Originally, a ¼ model was considered, however since this is a high strain rate problem, stress wave propagation and inertia effects must be considered to maintain the integrity of the simulation. The mass of the moving end of specimen may play an important role on the results since its inertia is considered in the explicit dynamic finite element solution. Thus, a ½ model was adopted as shown in Figure 3.1. The full size of the gauge section was 12.5 mm long and 1.75 mm wide. The half model simply splits the specimen lengthwise with a reduced width of 0.875 mm. Two meshes consisting of constant stress solid elements were created; one for each material thickness. Since the area of interest in this problem is the gauge section, the mesh was the finest in that particular region. A near 1-1-1 aspect ratio was used for elements in this region to maintain element integrity. The resulting element sizes within the gauge section were approximately 0.22 x 0.22 x 0.22 mm in size. Elsewhere, the elements were larger in size in order to reduce computation time. The mesh is significantly coarser within the gripped regions. Since no deformation occurs in these regions,

the element size in these regions is not critical, but was still kept reasonable in order to avoid any abrupt geometric changes.

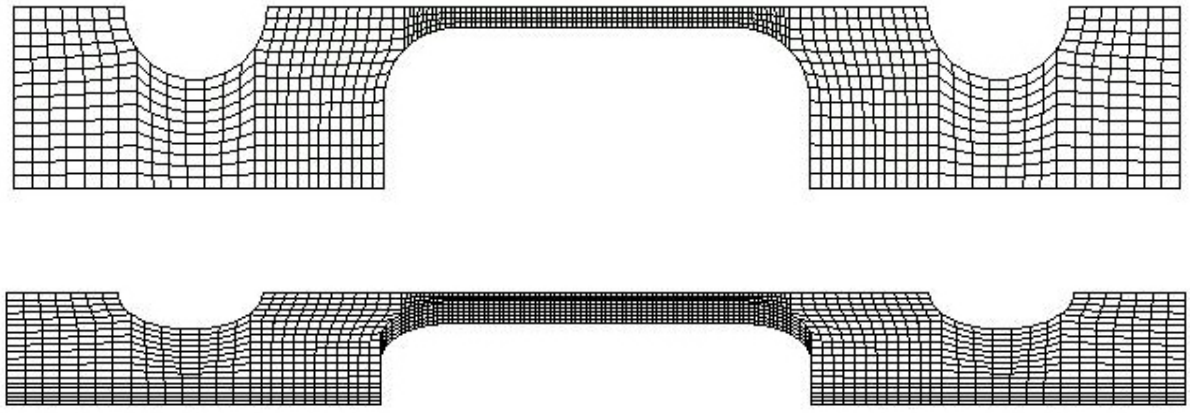

Figure 3.1 – Finite Element Mesh of TSHB Specimen

3.2 BOUNDARY CONDITIONS AND LOADS

Since a ½ model was used for the simulation, boundary conditions needed to enforce symmetry about the Y-axis were applied to the model. A schematic of the boundary conditions is shown in Figure 3.2. Based on the experimental results, an assumption was made that no deformation occurred in the gripped regions. Measurements of the gripped regions were taken before and after a test and no significant changes in dimensions were measured. The measurements taken are summarized in Table 3.1 below. These results show that the friction force resulting from the clamping pressure was sufficient enough to prevent deformation in the clamped regions at this particular strain rate. The variability seen in the before and after measurements can be attributed to measurement error and was within the accuracy of the calipers used.

Table 3.1 – Before and After Measurements of Features in the Gripped Region of the Specimen

Feature	Before	After
Hole Diameter	6.43 mm	6.46 mm
Width	15.91 mm	15.92 mm
Length	16.10 mm	16.10 mm
Thickness	1.0 mm	1.0 mm

Restraints were applied to nodes in both clamped regions preventing translation in the X- and Z-directions. Nodes at the fixed end were also restrained in the Y-direction, while nodes at the moving end were prescribed a velocity profile in the Y-direction. Nodes at the centerline of the specimen were allowed to translate in the Y- and Z-directions.

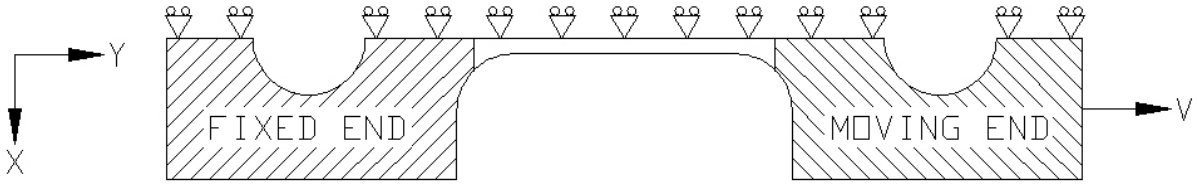

Location	X-Disp.	Y-Disp.	Z-Disp.
Y-Axis Edge	Fixed	Free	Free
Fixed End	Fixed	Fixed	Fixed
Moving End	Fixed	Prescribed	Fixed

Figure 3.2 – Schematic of Restraint Conditions Applied to the Specimen

Loading is achieved by applying a velocity profile to the nodes at the moving end of the specimen representing the clamped region. The required velocity profile was obtained directly from the experimental data by determining the relative velocity between the ends of the incident and transmitted pressure bars. A velocity profile for a strain rate of 600 s^{-1} is given in Figure 3.3. The velocity profile was applied to all the nodes in the clamped region of the moving end of the specimen. In order to save computation time, the quasi-static experiments

were simulated using a strain rate of 10 s^{-1}, which was higher than the QS rate of $3.3x10^{-3}$ s^{-1} but served to reduce computation time while being low enough to avoid artificial inertial effects.

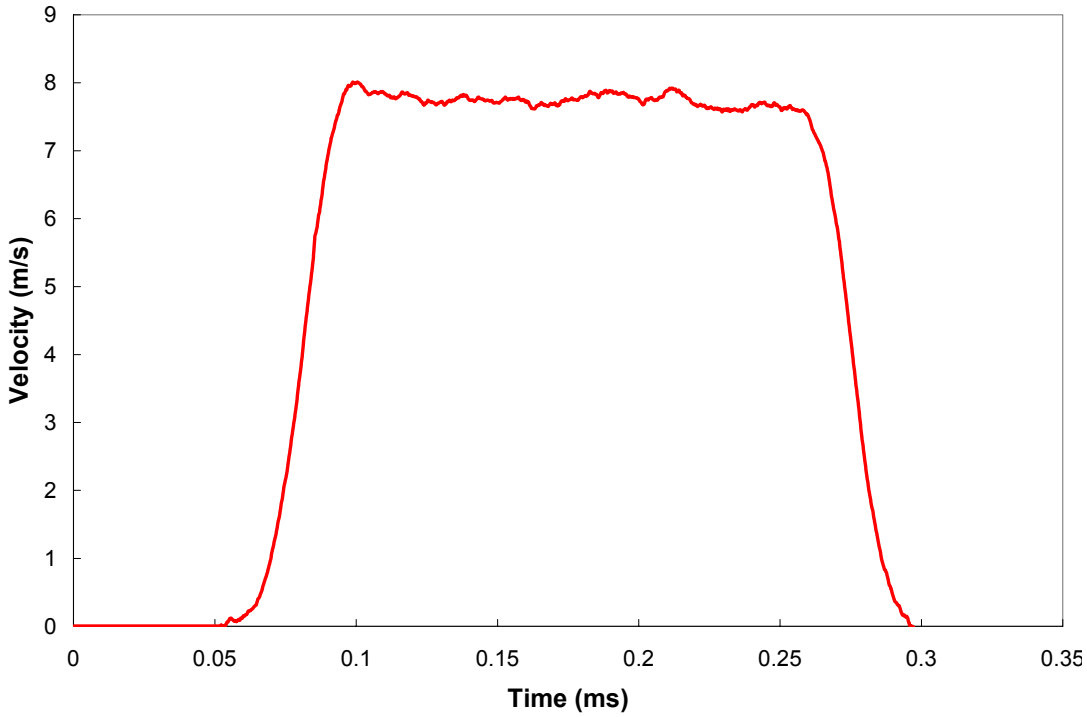

Figure 3.3 – Velocity Profile Applied to Moving End of Specimen For a Strain Rate of 600 s^{-1}

3.3 MATERIAL MODELS

The equations for the Johnson-Cook and Zerilli-Armstrong constitutive models are given in equation (1.21) and (1.30), respectively. The Johnson-Cook model as included in LS-DYNA [70], does not give the user the ability to change the initial temperature of the material. Hence, a user-defined material-model (umat) was used to implement the Johnson-Cook model, while the Zerilli-Armstrong material model included in LS-DYNA [70] was found to be sufficient. The values listed in Table 5.1 and Table 5.2 were used for the parameters in each of the respective models. The material properties used in both constitutive models are listed in Table 3.2. Specific heat values were not found for each alloy examined, hence the value listed in Table 3.2 was used for all of the alloys.

Table 3.2 – Material Properties

Density (ρ)	2630 kg/m^3
Shear Modulus (μ)	25.94 GPa
Elastic Modulus (E)	69 GPa
Specific Heat Capacity (C_p)	900 J/kg·°K

For the simulations of the quasi-static loading conditions that considered an elevated strain rate, the reference strain rate used in the model fits was increased to 3144 s^{-1} in order to scale the $\dot{\varepsilon}/\dot{\varepsilon}_0$ ratio to the value witnessed under quasi-static loading.

3.4 AXIAL INERTIAL STRESS CALCULATIONS

As discussed in Section 1.2.2, several authors have noted that axial inertial stresses are present during dynamic tests due to the high velocities and accelerations experienced by the material. In experiments such as Hopkinson bar tests, these axial inertial stresses are measured by the transmitted bar and can be mistaken as a constitutive response of the material being tested. In order to estimate the magnitude of these inertial stresses, a model similar to one used by Samanta [36] and Gorham *et al*. [37,38,39] has been developed for a rectangular specimen in tension. A schematic of the model is shown in Figure 3.4. The upper surface is moving at a velocity *u*, while the lower surface is fixed.

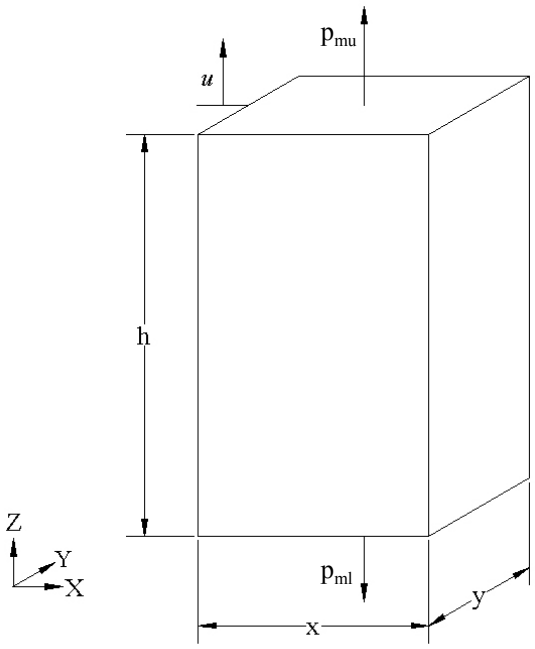

Figure 3.4 – Simplified Model of a Tensile Test

The deformation is assumed to be uniform and incompressible, and the velocity field in a fixed Cartesian coordinate system can be described as [36]:

$$v_z = \frac{u}{H} z \tag{3.1}$$

$$v_x = -\frac{u}{2H} x \tag{3.2}$$

$$v_y = -\frac{u}{2H} y \tag{3.3}$$

Considering the conservation of energy, the following is satisfied [36]:

$$\frac{D}{Dt}(K+W) = \int_s F_j v_j dS \tag{3.4}$$

where K is the kinetic energy, W is energy dissipation, and F_j are surface tractions acting on the surface with a surface area S [36]. The kinetic energy term can be described as:

$$K = \frac{1}{2}\int_V (v_x^2 + v_y^2 + v_z^2)\rho dV \tag{3.5}$$

where ρ is the material density and V is the volume over which the kinetic energy is being considered. Taking the material derivative of equation (3.5) yields:

$$\frac{D}{Dt}K = \int_V \left[\frac{x^2 u}{4H^2}\frac{du}{dt} - \frac{x^2 u^3}{8H^3} + \frac{y^2 u}{4H^2}\frac{du}{dt} - \frac{y^2 u^3}{8H^3} + \frac{z^2 u}{H^2}\frac{du}{dt} + \frac{2z^2 u^3}{H^3} \right] \rho dV \tag{3.6}$$

Integrating equation (3.6) results in:

$$\frac{D}{Dt}K = \rho \left[\frac{x^3 y}{12H}\frac{u}{H}\frac{du}{dt} - \frac{x^3 yz}{24}\frac{u^3}{H^3} + \frac{xy^3}{12}\frac{u}{H}\frac{du}{dt} - \frac{xy^3 z}{24}\frac{u^3}{H^3} + \frac{xyzu}{3}\frac{du}{dt} + \frac{2xyz^3}{3}\frac{u^3}{H^3} \right] \tag{3.7}$$

The energy dissipation can be written as [36]:

$$\frac{D}{Dt}W = \int_V \sigma_{ij} D_{ij} dV \tag{3.8}$$

where σ_{ij} is the Cauchy stress tensor. By introducing a spatial mean value of the flow stress (σ_D), the left-hand side of equation (3.8) becomes:

$$\frac{\sigma_D u V}{H} = \int_V \sigma_{ij} D_{ij} dV \tag{3.9}$$

If no friction is present at the upper boundary surface, the right-hand side of equation (3.4) can be expressed as [36]:

$$\int_S F_j v_j dS = \int_{S_u} p_u u dS \tag{3.10}$$

where p_u is the contact pressure acting on the upper surface area (S_u). Using the mean contact pressure (p_{mu}) at the upper surface, the right-hand side of equation (3.10) can be expressed as [36]:

$$p_{mu} S_u = \int_{S_u} p_u dS \tag{3.11}$$

Inserting equation (3.7), (3.9) and (3.11) into equation (3.4), and solving at the upper surface by setting z and H to the instantaneous height h yields the following result for the mean pressure measured at the moving end of the specimen:

$$p_{mu} = \sigma_D + \rho\left[\left(\frac{x^2+y^2}{12h}+\frac{h}{3}\right)\frac{du}{dt}+\left(-\frac{x^2+y^2}{24}+\frac{h^2}{3}\right)\left(\frac{u}{h}\right)^2\right] \tag{3.12}$$

In the Hopkinson bar experiments, the flow stress versus time of the material is measured at the output bar. Hence, the mean pressure measured at the fixed end of the specimen is desired. This can be found by introducing the axial equation of motion, which under the present assumptions reduces to [36]:

$$\frac{\partial \sigma_z}{\partial z} = \sigma \frac{Dv_z}{Dt} \tag{3.13}$$

For this model, equation (3.13) becomes:

$$\frac{\partial \sigma_z}{\partial z} = \rho \frac{z}{H}\frac{du}{dt} \tag{3.14}$$

Integrating equation (3.14) and solving at the instantaneous height h:

$$p_{mu} - p_{ml} = \rho \frac{h}{2}\frac{du}{dt} \tag{3.15}$$

Substituting equation (3.12) in equation (3.15), and solving for the mean pressure at the lower surface (p_{ml}) yields the following result:

$$p_{ml} = \sigma_D + \rho\left[\left(\frac{x^2+y^2}{12h}-\frac{h}{6}\right)\frac{du}{dt}+\left(-\frac{x^2+y^2}{24}+\frac{h^2}{3}\right)\left(\frac{u}{h}\right)^2\right] \tag{3.16}$$

Finally, introducing the mean axial strain rate $\dot{\varepsilon} = u/H$ [36], equation (3.16) becomes:

$$p_{ml} = \sigma_D + \rho\left[\left(\frac{x^2+y^2}{12}-\frac{h^2}{6}\right)\ddot{\varepsilon}+\left(\frac{x^2+y^2}{24}+\frac{h^2}{6}\right)\dot{\varepsilon}^2\right] \tag{3.17}$$

Hence, the axial inertial stress measured at the output bar can be approximated as:

$$\sigma_i \approx \rho\left[\left(\frac{x^2+y^2}{12}-\frac{h^2}{6}\right)\ddot{\varepsilon}+\left(\frac{x^2+y^2}{24}+\frac{h^2}{6}\right)\dot{\varepsilon}^2\right] \tag{3.18}$$

This shows that the inertial stress increases exponentially with strain rate and specimen size. Using equation (3.18) along with values for $\dot{\varepsilon}$ and $\ddot{\varepsilon}$ extracted from the numerical simulations, the axial inertial stress can be approximated at various strain rates.

4 SPECIMEN DESIGN

Currently there is no standardized specimen geometry for TSHB testing and specimen design became a significant aspect of the current research. The objective was to design a specimen that follows the mechanical response of a standard ASTM specimen, while meeting the requirements for specimens used in dynamic experiments. Two requirements for a TSHB specimen are a small gauge length to reduce ring-up time and inertial effects, as well as a geometry that results in a uni-axial stress state. A preliminary geometry that met these specifications was designed with the aid of numerical simulations conducted using LS-DYNA [70]. A specimen gauge length of 3 mm, shown in Figure 4.1, was selected as an initial geometry based on published literature [77]. Using the numerical simulations, the specimen width was varied to result in a uni-axial stress state.

In meeting the objective of having the mechanical response of the TSHB specimen be comparable to one listed in the ASTM standards, two aspects were considered: (i) uniform elongation, and, (ii) post-uniform elongation. Since only the stress-strain data up to the onset of necking is fit to the constitutive models, it is not only important that the stress-strain response of the TSHB specimen follow the response of an ASTM specimen quite closely during uniform elongation, but also that necking occur at a similar elongation. The post-uniform elongation was also considered since it is used to calculate the final elongation of the material. The gauge length of the specimen is shown to affect the post-uniform elongation, as expressed in terms of engineering strain, as presented in Section 4.2. The uniform and post-uniform elongation responses of several specimen geometries, including the 3 mm gauge length geometry, were compared with that of two ASTM geometries. All of these factors were considered in selecting the final TSHB specimen geometry used in all of the subsequent dynamic and quasi-static experiments.

4.1 NUMERICAL SIMULATIONS OF 3 mm GAUGE LENGTH SAMPLES

The details of the numerical model used to design the preliminary specimen geometry are not covered in this thesis, however, the mesh, boundary conditions and loading are similar to the model discussed in Chapter 3. AA5754 was arbitrarily chosen for this specimen geometry study. A piece-wise plasticity material model was implemented using data collected for a standard ASTM specimen geometry outlined by ASTM Standard E8 [78], tested at a quasi-static strain rate ($3.3x10^{-3}$ s^{-1}). In order to assess whether a uni-axial stress state was achieved, the predicted stresses in the specimen width and thickness directions were examined as a function of axial strain. From the numerical simulations, it was found that a 3 mm long by 2 mm wide gauge section resulted in a uni-axial stress state until localized necking occurred.

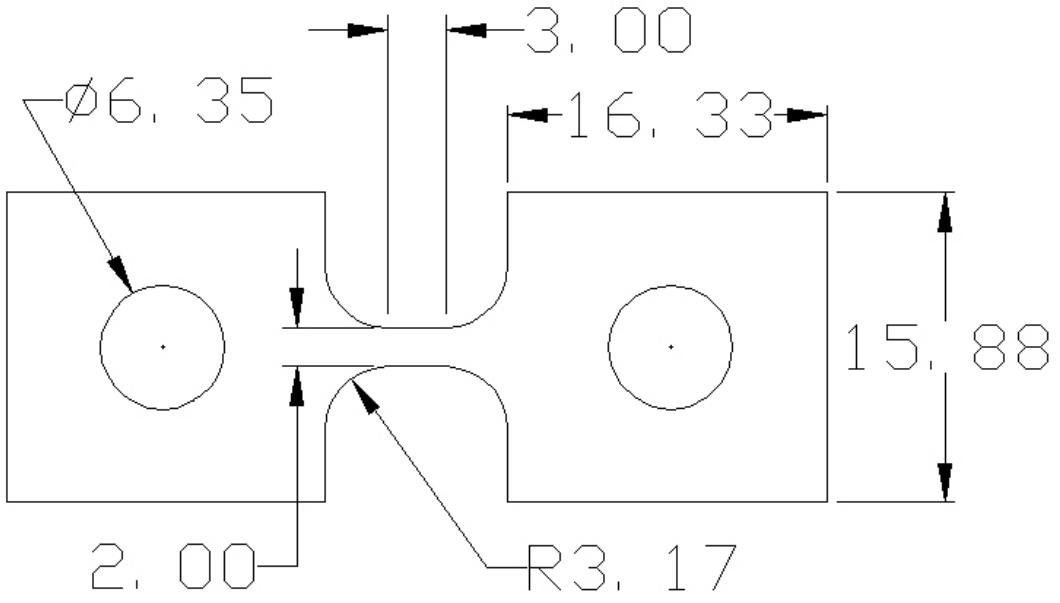

Figure 4.1 – Preliminary TSHB Specimen Geometry

The normal stress in the width direction predicted by the numerical simulation is plotted in Figure 4.2b as a function of axial strain for the elements labeled in Figure 4.2a. The stress in the width direction was predicted to remain near zero until the elongation of the specimen reached approximately 18% at which point necking was initiated in the model (Figure 4.2b). The stresses in the thickness direction showed a similar trend. The model also predicted that

the stresses in both the width and thickness directions increase rapidly after necking, leading to an increase in triaxiality (loss of uni-axial stress). As seen in Figure 4.3, the effective plastic strain begins to localize in the centre of the gauge section at approximately 18% elongation.

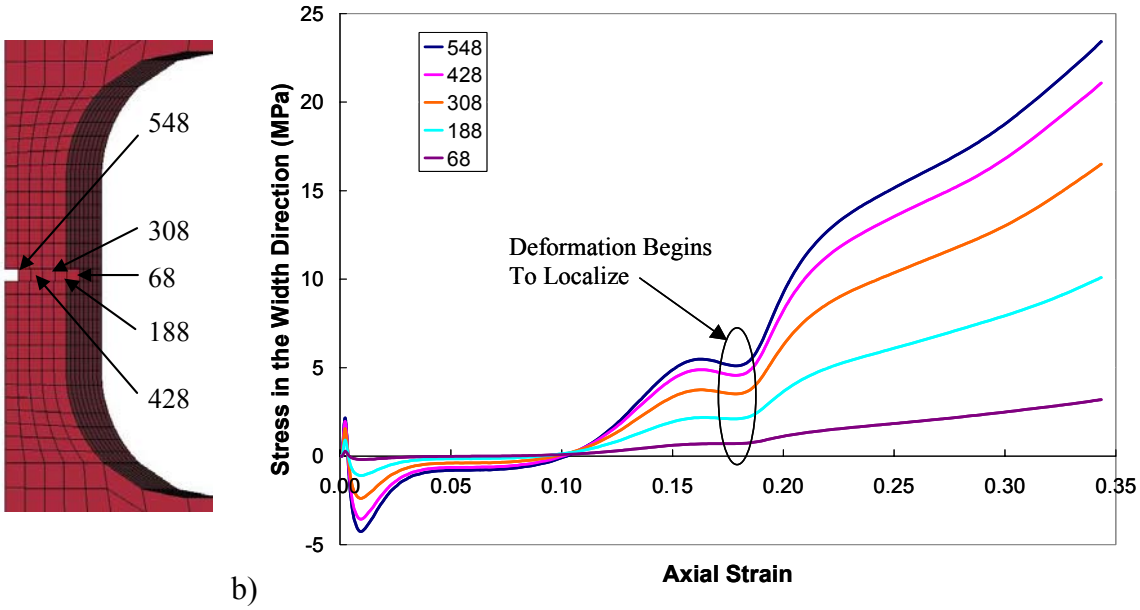

a) b)

Figure 4.2 – Numerical Model Prediction of Lateral Stress Versus Axial Strain For The Preliminary TSHB Specimen Geometry (Note: Elements Were Removed in View to Highlight Elements Located in Neck)

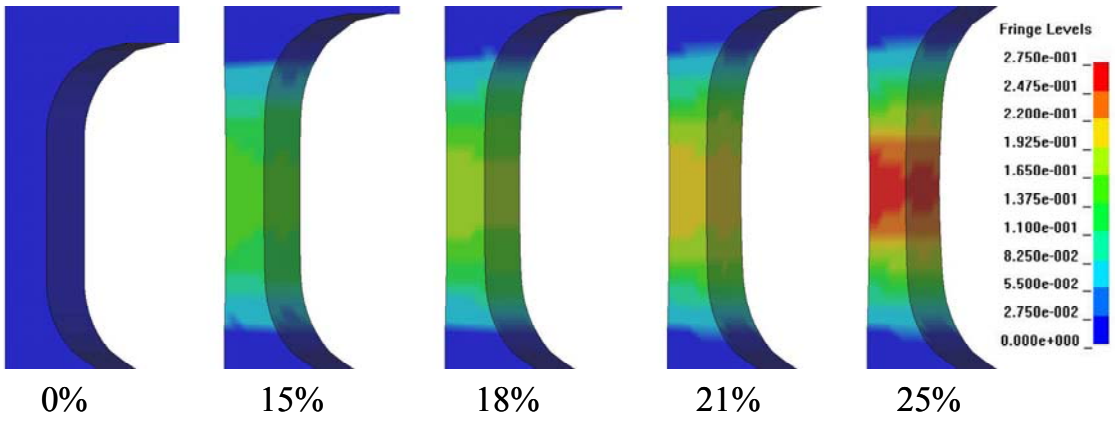

Figure 4.3 – Contour Plots of Effective Plastic Strain at Various Axial Strains for a 3 mm Gauge Length TSHB Specimen

Based upon the data in Figure 4.2, this short gauge length sample satisfies the uni-axial stress condition up until the onset of necking. Using equation (1.16) along with the slope of the true stress-strain curve measured under quasi-static conditions, the ring-up time was found to be approximately 7.69 μs for this geometry. This duration is small compared to the rise time of the incident pulse (approximately 39 μs) and it can be assumed that a uniform stress state will be achieved prior to reaching the nominal strain rate in an experiment. Thus it can be concluded that this specimen does satisfy the stress-state and ring-up time required for uni-axial tensile testing. Unfortunately there is a concern with this geometry associated with the effect of the short gauge length on the post-uniform elongation, as presented in the next section.

4.2 POST-UNIFORM ELONGATION EFFECTS ON GAUGE LENGTH

Quasi-static tensile experiments using the preliminary TSHB specimen were performed employing the procedures outlined in Section 2.4. In Figure 4.4, the resulting stress-strain response is compared with the model prediction and with that of a standard specimen geometry described by ASTM standard E8 [78], which has a gauge length of 50 mm. The strain hardening response of the preliminary TSHB specimen appears to deviate from that of the ASTM specimen and from the numerical model. The nominal stress is under-predicted at strains between 3.5% and 16.7%. Furthermore, the elongation to failure of the 3 mm x 2 mm specimen is more than twice that of the ASTM specimens. The experimental data for the ASTM specimen showed that the additional elongation to failure after the maximum load was reached was approximately 1.6 mm or 3.15% engineering strain, compared to 0.76 mm or 25.3% strain for the 3 mm x 2 mm specimen. As can be seen, the significantly smaller gauge length results in a dramatic increase in the post-uniform deformation when expressed in terms of engineering strain; hence, the much larger apparent elongation to failure.

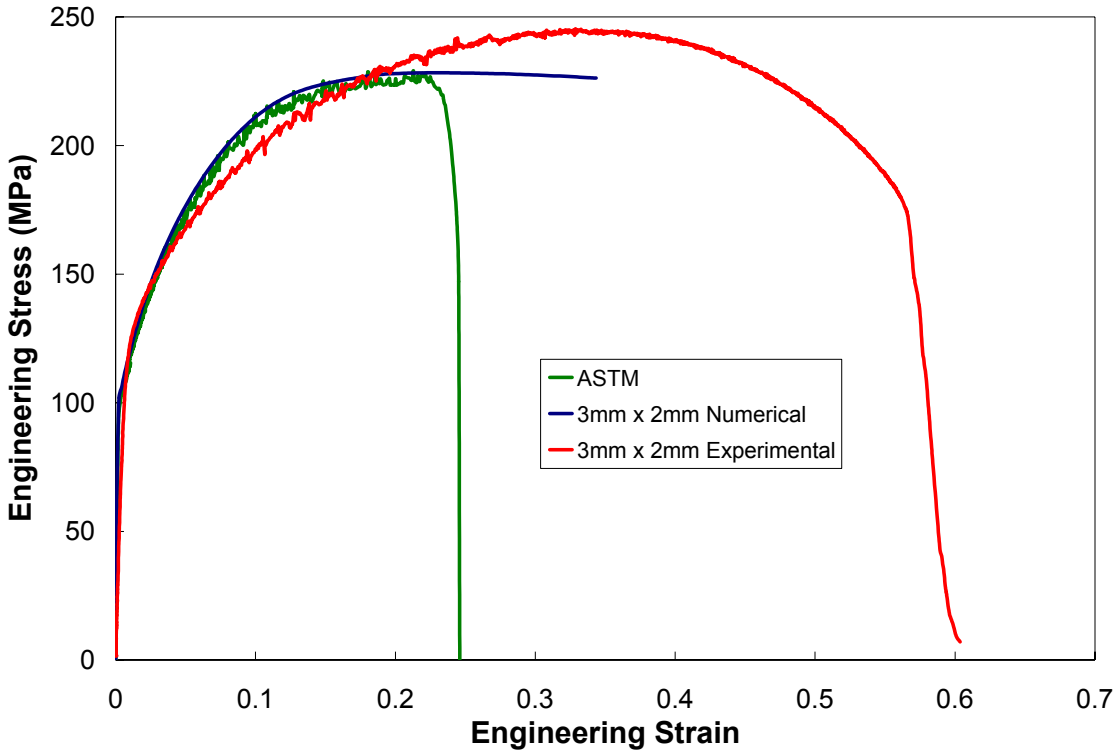

Figure 4.4 – Comparison of Stress Strain Response Between Standard ASTM Specimen and TSHB Preliminary Geometry

Due to this marked specimen size effect, an empirical study was carried out to find a suitable TSHB specimen geometry that would produce a stress-strain response similar to an ASTM specimen. The ASTM Standard E8 [78] contains a specification for a tensile specimen with a reduced gauge size. The gauge size of this reduced ASTM specimen is 25 mm in length and 6 mm wide. Tensile experiments performed using this specimen produced a stress-strain response that followed the standard ASTM specimen quite closely. The reduced ASTM specimen was scaled down by a factor of 2, resulting in a gauge section 12.5 mm long by 3 mm wide. Both specimens are shown in Figure 4.5 alongside the standard 50 mm ASTM geometry and the 3 mm TSHB specimen.

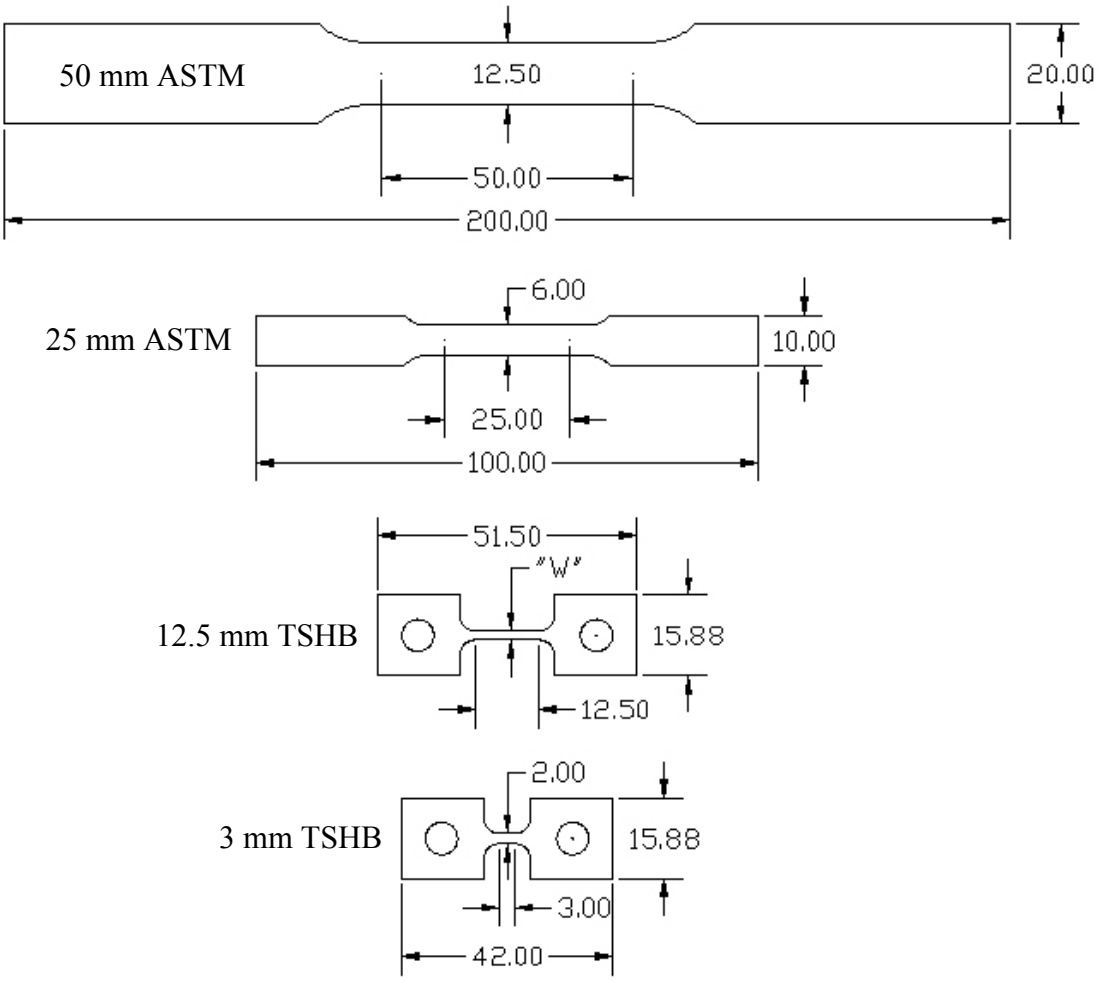

Figure 4.5 – Comparison of Various ASTM and TSHB Specimen Geometries

Quasi-static tensile experiments using the 12.5 mm long TSHB specimen were performed at a strain rate of 3.3×10^{-3} s^{-1}. The width was reduced from 3 mm in subsequent iterations to find a geometry that would produce an acceptable stress-strain response. The focus was to achieve a uniform deformation response similar to that of the ASTM specimens and initiate necking at a comparable strain. Figure 4.6 shows the stress-strain response for several trial specimen geometries in comparison to that from both ASTM specimens. The experiments showed that as the width of the specimen was reduced, the resulting constitutive response began to resemble that of the ASTM specimens. When the specimen width was reduced to 1.5 mm, the response began to diverge from response of the ASTM specimens. Most notably, the

engineering strain at which necking occurred became approximately 18% in comparison to the ASTM 50 mm and 25 mm specimens, which necked at approximately 23% and 22% strain, respectively.

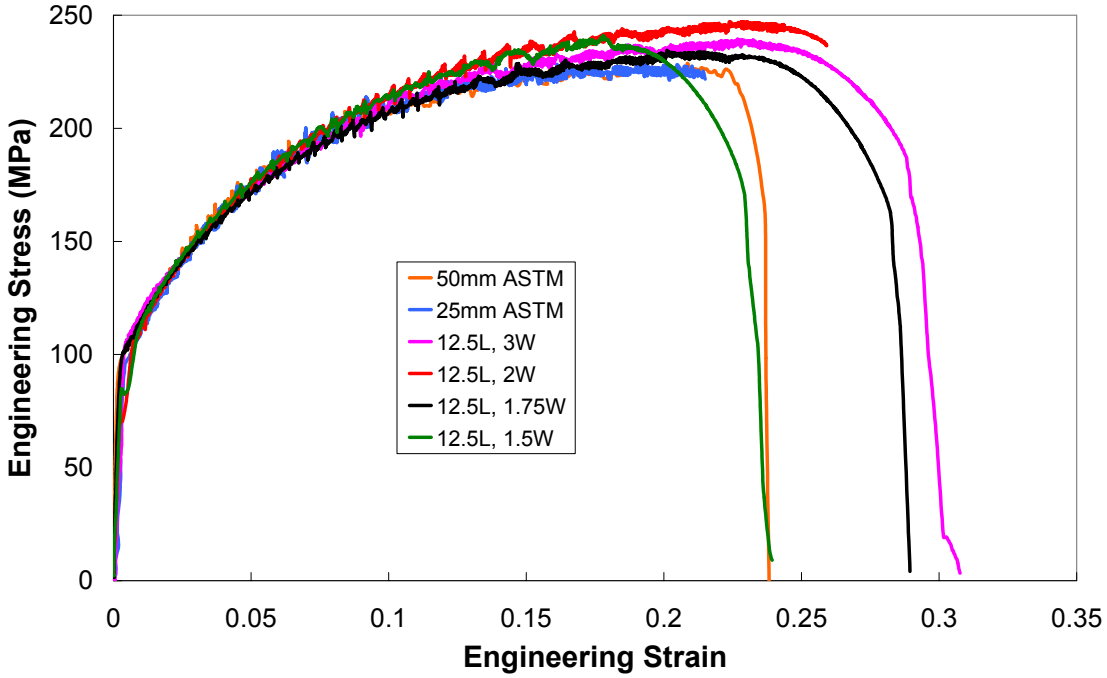

Figure 4.6 – Stress-Strain Response for Various Specimen Geometries

As noted above, the cause for the variation in the post-uniform elongation response is attributed to the fact that the size of the neck remains constant. The wavelength of the necked region was found to similar in both the ASTM and TSHB specimens, as seen in Figure 4.7.

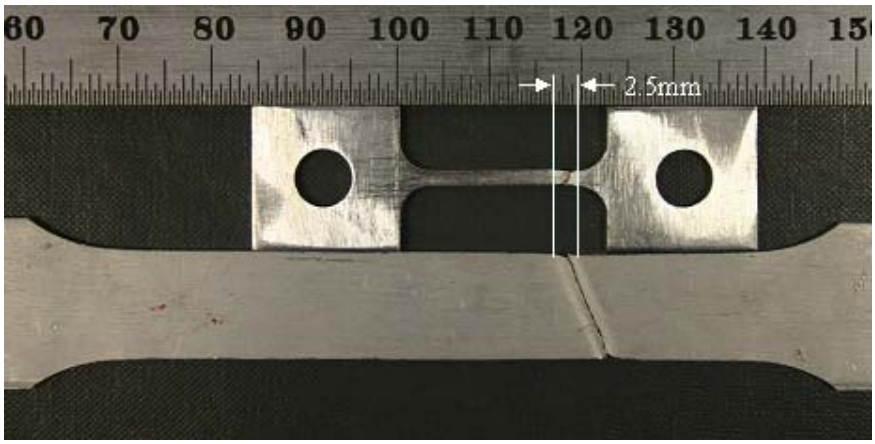

Figure 4.7 – Photograph Comparing the Wavelength of the Necked Region of a 12.5 mm x 1.75 mm TSHB Specimen With That of a 50 mm Long ASTM Specimen.

From this study, 1.75 mm was selected as a gauge width for the TSHB specimen, and the final geometry adopted for all subsequent testing is shown in Figure 4.8. The stress-strain response closely followed that of the ASTM specimens, with necking initiated at a strain of approximately 24%, which is very close to the ASTM specimens. The ring-up time for this geometry was calculated to be approximately 32 μs. This is much longer than the ring-up time calculated for the 3 mm long specimen (7.69 μs), however, it is still less than the rise time of the incident wave (approximately 39 μs). Upon comparing these values we can expect that a steady-state stress state will be achieved in the specimen prior to reaching the nominal strain rate of the experiment.

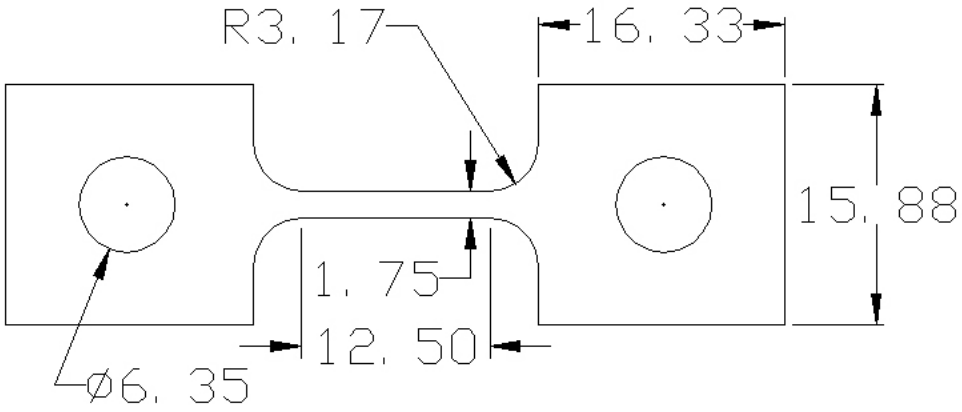

Figure 4.8 – Final TSHB Specimen Geometry

Thus, the TSHB specimen geometry satisfies:

(1) uni-axial stress state up to the onset of necking

(2) post-uniform elongation that is slightly larger than that of an ASTM specimen

(3) ring-up time less than TSHB rise time

5 EXPERIMENTAL RESULTS

Tests were conducted at nominal strain rates of approximately $3.3x10^{-3}$ s^{-1} (quasi-static), 600, 1100 and 1500 s^{-1}. The tests conducted at 23°C considered all four strain rates. The elevated temperature tests were only performed at 600 and 1500 s^{-1}. Three specimens were tested at each set of conditions. The test conditions and results from all tests are summarized in Appendix A through E. The specimen geometry described in Section 4.1 was used in all experiments. Only the median stress-strain responses for each set of test conditions are shown in the following sections, and are shown only for a single loading pulse. The remainder of the data is given in the appendices.

5.1 CONSTITUTIVE BEHAVIOR

5.1.1 EFFECT OF STRAIN RATE

Figure 5.1 through Figure 5.5 show the resulting stress-strain curves at room temperature for all three alloys tested. In Figure 5.1 and Figure 5.2, it is seen that AA5754 exhibits a mild increase in flow stress at higher strain rates. For example, at 5% strain, the flow stress of 1.6 mm thick AA5754 is approximately 203 MPa at a nominal strain rate of 600 s^{-1}, compared to approximately 185 MPa at a strain rate of $3.3x10^{-3}$ s^{-1}. However, while this increase occurred for the change in strain rate from quasi-static to TSHB regimes (6 orders of magnitude), the change in flow stress in the range between 600-1500 s^{-1} was negligible. The thinner 1 mm material shows very similar behavior. The flow stress at 5% strain increases from approximately 195 MPa at $3.3x10^{-3}$ s^{-1} to approximately 206 MPa at 600 s^{-1}. This behavior is expected since it has been shown that the flow stress has a logarithmic dependence on strain rate for aluminum alloys [10,51]. The difference in flow stress between the two thicknesses under quasi-static conditions can be attributed to differences in the raw mechanical processing experienced by the 1 mm thick sheet during cold rolling.

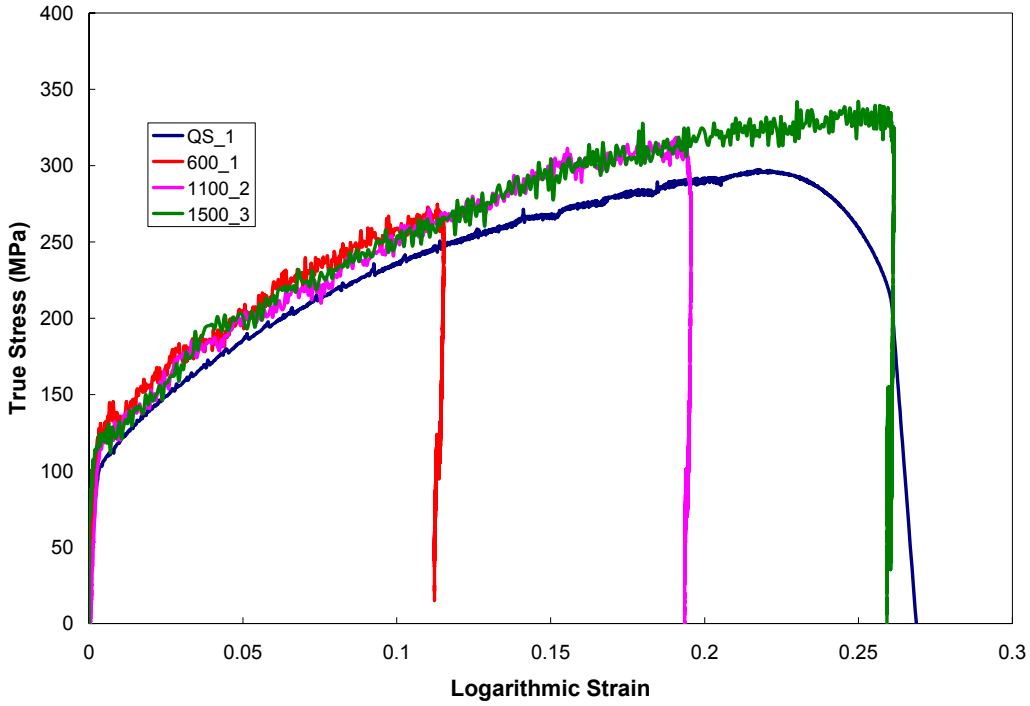

Figure 5.1 – Effects of Strain Rate on Flow Stress for AA5754 – 1.6 mm

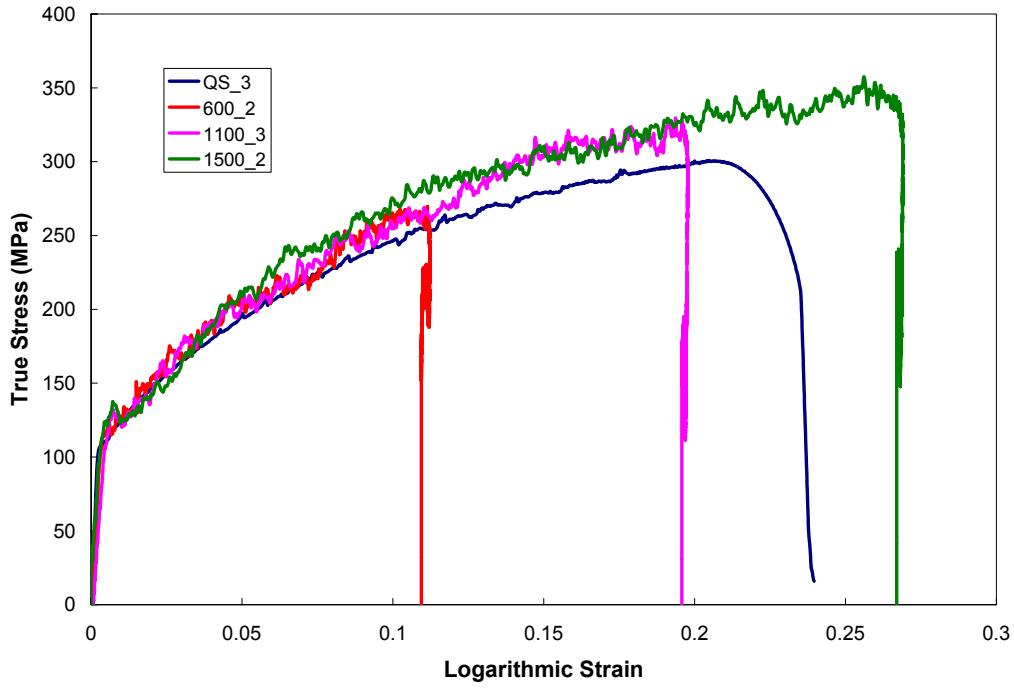

Figure 5.2 – Effects of Strain Rate on Flow Stress for AA5754 – 1mm

AA5182 appears to be strain rate insensitive in the range of strain rates considered. In Figure 5.3 and Figure 5.4, there is no dramatic change in the flow stress, nor any change in the hardening rate as strain rate is increased. Similar to what was witnessed in AA5754, the thinner 1 mm thick sheet exhibits a higher flow stress than the 1.6 mm thick sheet due to additional cold rolling.

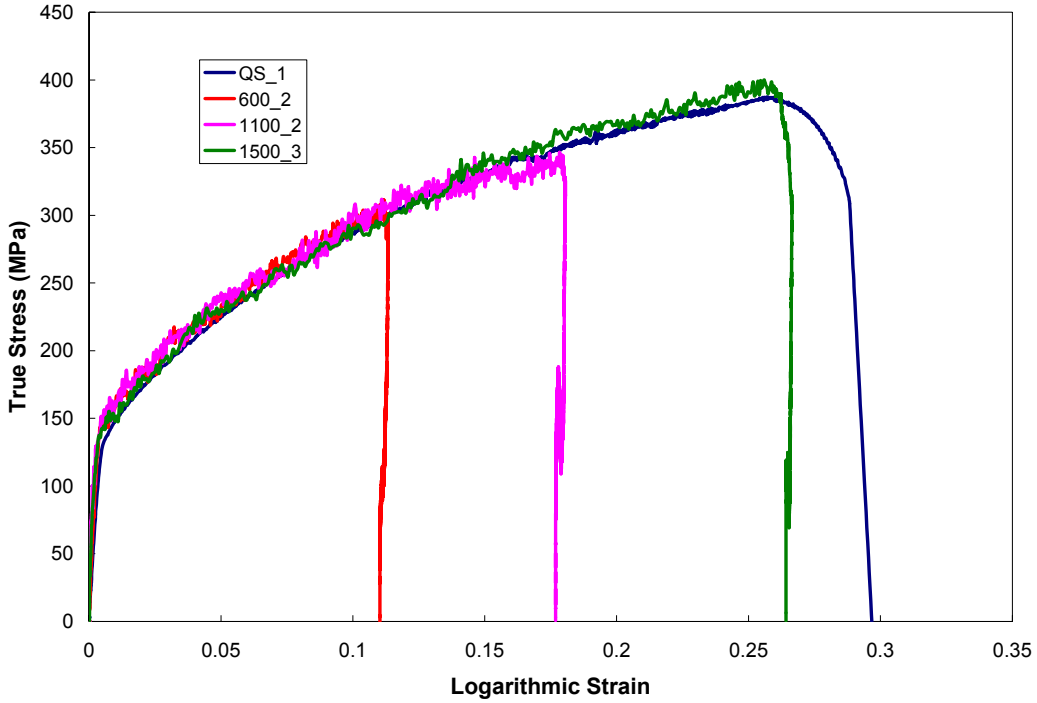

Figure 5.3 – Effects of Strain Rate on Flow Stress for A5182 – 1.6 mm

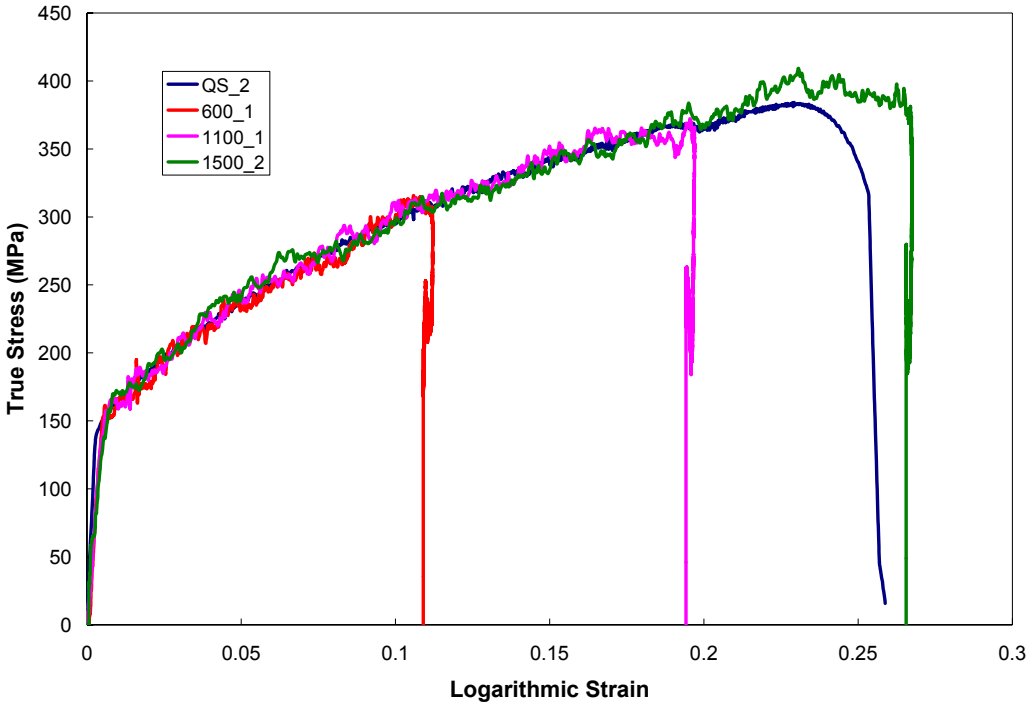

Figure 5.4 – Effects of Strain Rate on Flow Stress of AA5182 – 1mm

Like AA5182, AA6111 shows no significant change in flow stress with increasing strain rate. In Figure 5.5, it is seen that the flow stress at 600, 1100 and 1500 s^{-1} follows the response measured under quasi-static conditions quite closely. The data collected for AA6111 at elevated strain rates shows more oscillations in the stress-strain response than AA5754 and AA5182. The reader should be made aware that this is probably not a material behavior; the cause of these oscillations is unknown at this time. Although these could be artifacts of the dynamic testing procedures, adiabatic shear banding is also a possible source.

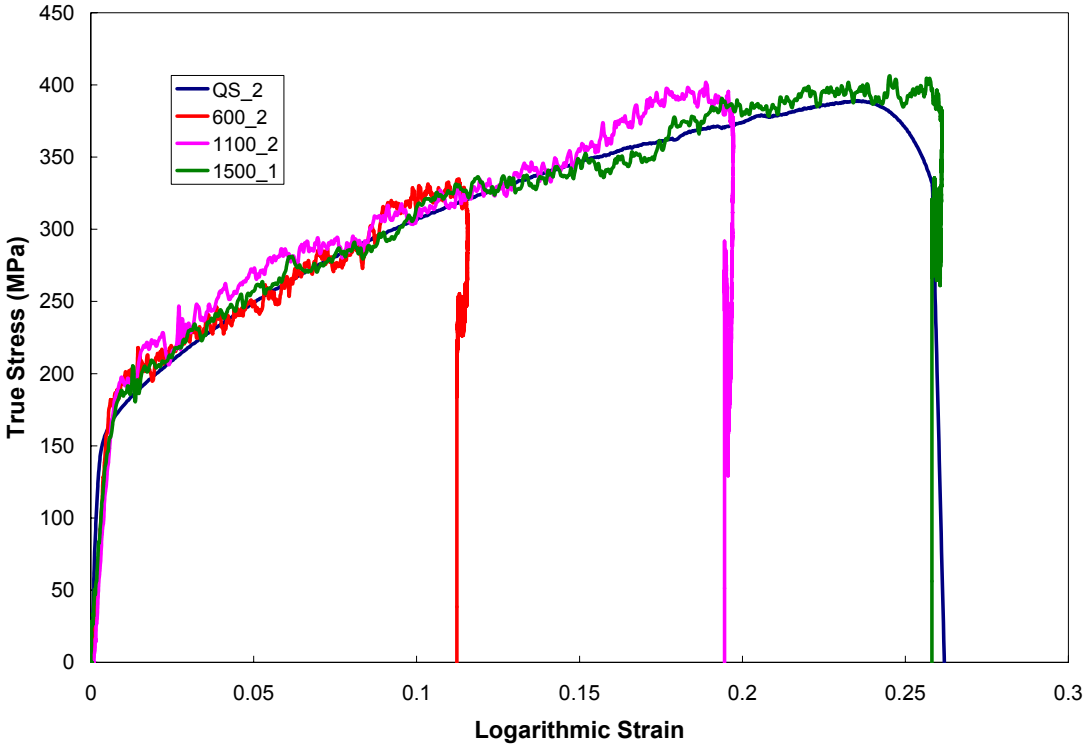

Figure 5.5 – Effects of Strain Rate on Flow Stress – AA6111

In order to compare the strain rate sensitivity of the alloys tested, the flow stress at 7% logarithmic strain has been plotted as a function of $\log_{10}$ strain rate in Figure 5.6. It was found from the experimental data, that at 1500 s^{-1}, a constant strain rate was reached at approximately 3% logarithmic strain. While at 600 s^{-1}, the specimens began to unload elastically at approximately 10% strain. In order to compare flow stress data measured at a constant strain rate, 7% logarithmic strain was chosen since it was midway between the two previously mentioned limits. The curves plotted in Figure 5.6 represent the average flow stress across the three specimens tested. The strain rate sensitivity of these alloys is low in the range of strain rates considered, and the trends appear to be similar to those presented by Mukai *et al.* [57] for high purity Al-Mg alloys.

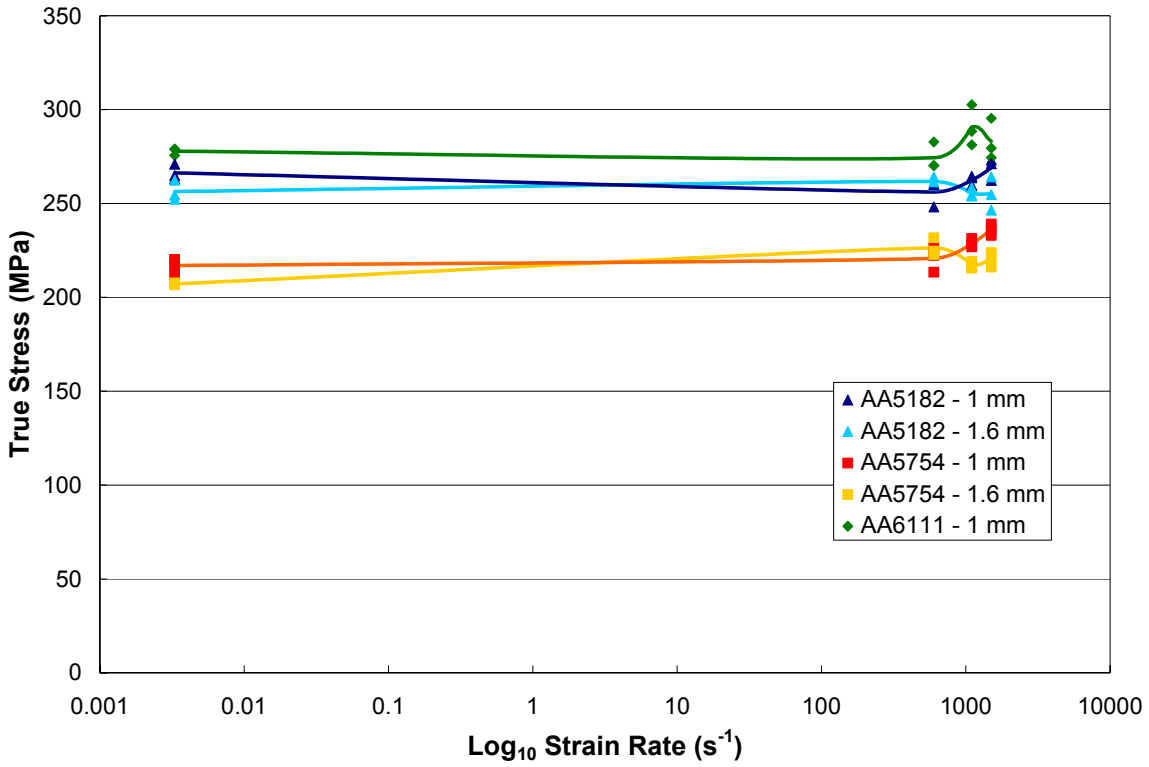

Figure 5.6 – True Stress as a Function of Log_{10} Strain Rate at 7% Logarithmic Strain

5.1.2 Effect of Temperature

The effects of temperature on the stress-strain response of AA5754, AA5182 and AA6111 at nominal strain rates of 600 and 1500 s^{-1} are shown in Figure 5.7 through Figure 5.11. The dynamic experiments were performed at temperatures of 50°C and 150°C for both strain rates, while an additional set of experiments were performed at 300°C at 1500 s^{-1}.

Since TSHB experiments are considered to be adiabatic, plastic work is converted into heat and the temperature of the material rises during the experiment. At room temperature and at a strain rate of 1500 s^{-1}, calculations using equation (2.5) give a temperature rise of approximately 26.5°C for 1.6 mm AA5754, 28°C for 1 mm AA5754, 30°C for both thicknesses of AA5182, and 31°C for AA6111 at 26% logarithmic strain.

The trends shown by all the alloys tested are very similar. At a strain rate of 600 s^{-1}, no visible change in the stress-strain response was witnessed in the experiments with increasing temperature. As seen in the figures below, the stress-strain response at 50°C and 150°C follows the response at ambient temperature very closely. At 1500 s^{-1}, the experiments show only a slight decrease in the flow stress between 23°C and 150°C. However, at 300°C, there is a significant drop in flow stress for AA5754 and AA5182. The data exhibits a decrease in the strain hardening rate as the temperature is increased, which results in a lower maximum flow stress. AA6111 on the other hand does not show as significant a change in the strain hardening rate as seen for AA5754 and AA5182.

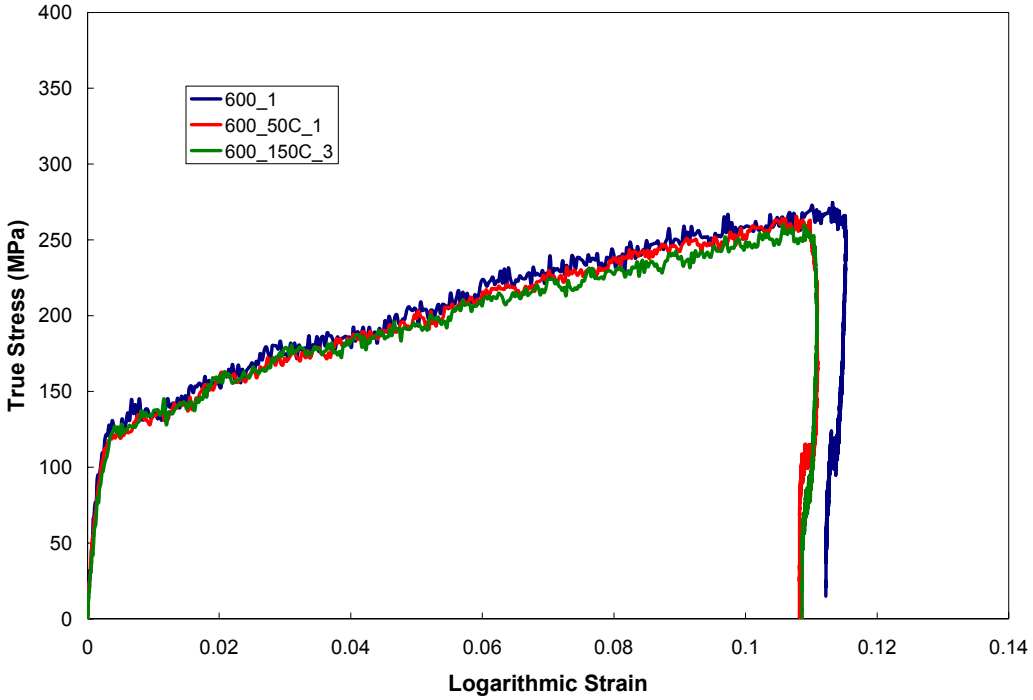

a)

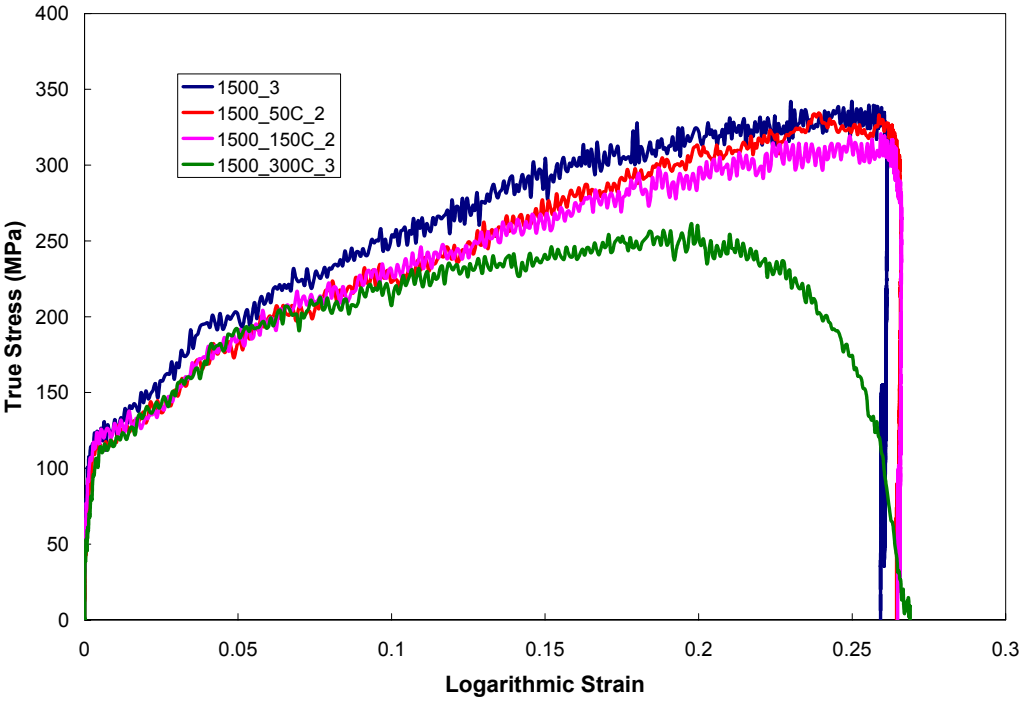

b)

Figure 5.7 – Effects of Initial Temperature on Flow Stress at a) 600 s^{-1} and b) 1500 s^{-1} for AA5754 – 1.6 mm

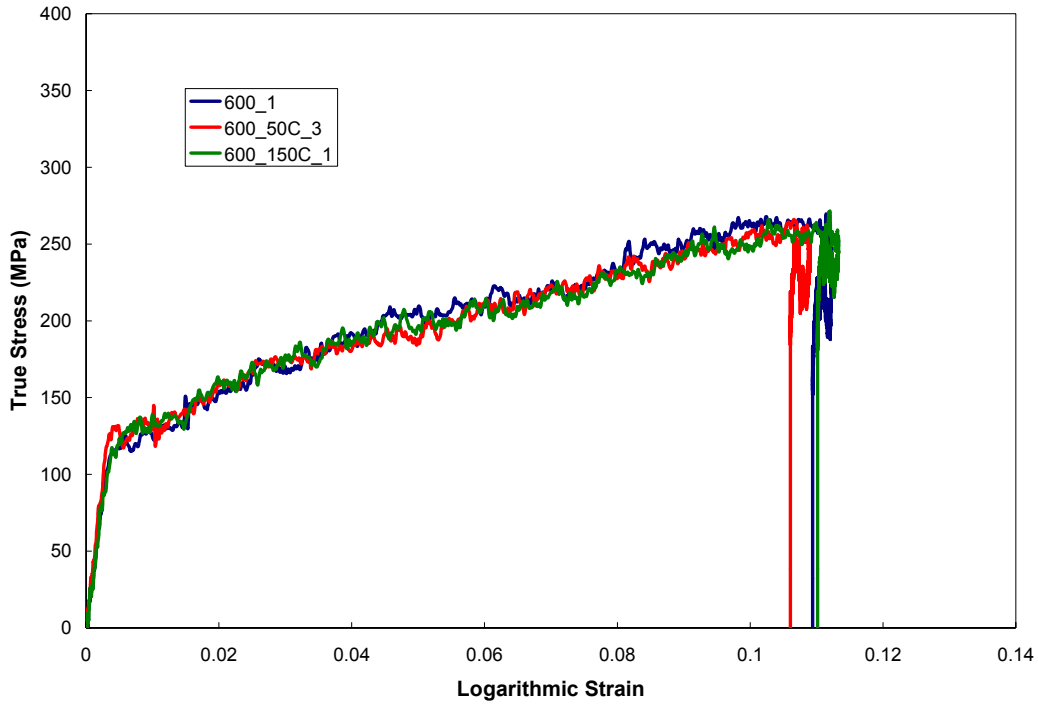

a)

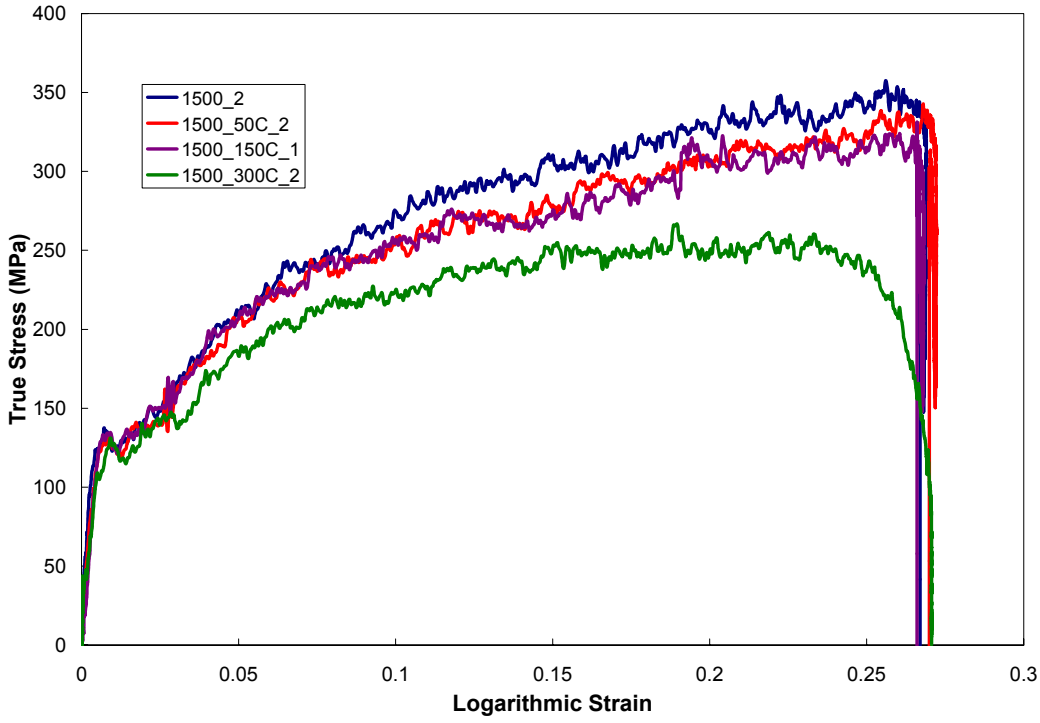

b)

Figure 5.8 – Effects of Initial Temperature on Flow Stress at a) 600 s^{-1} and b) 1500 s^{-1} for AA5754 – 1mm

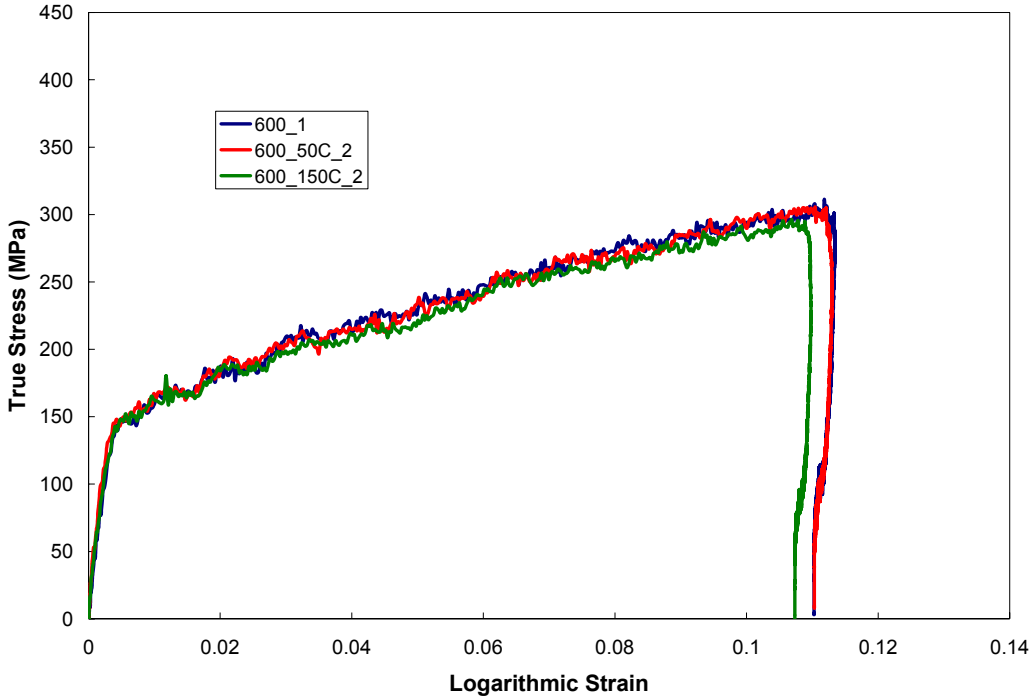

a)

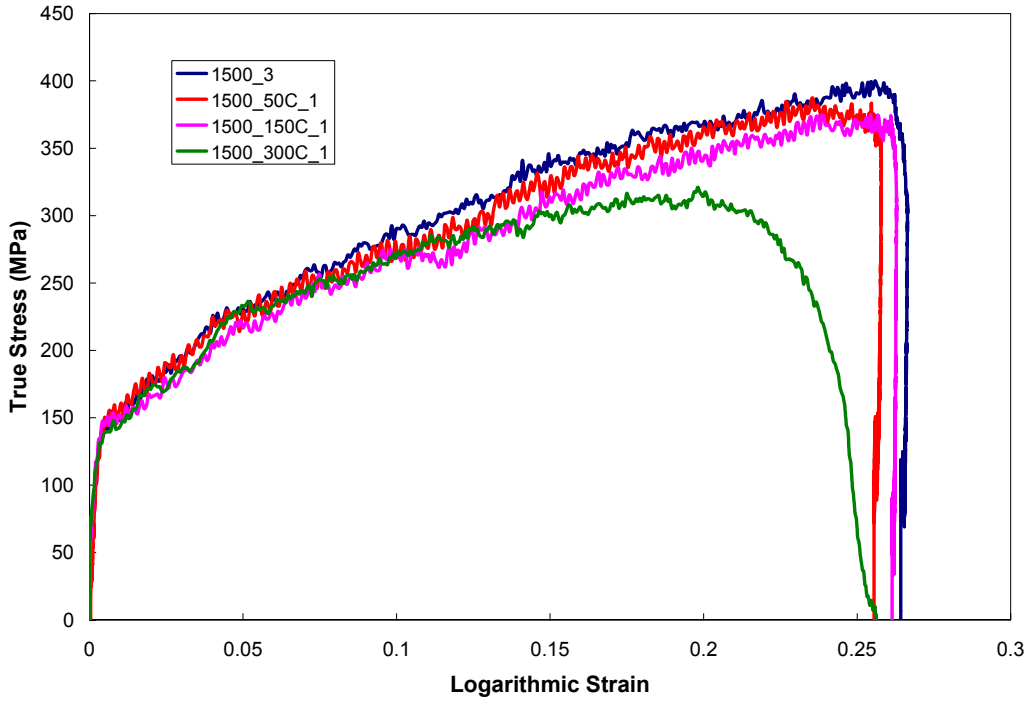

b)

Figure 5.9 – Effects of Initial Temperature on Flow Stress at a) 600 s^{-1} and b) 1500 s^{-1} for AA5182 – 1.6 mm

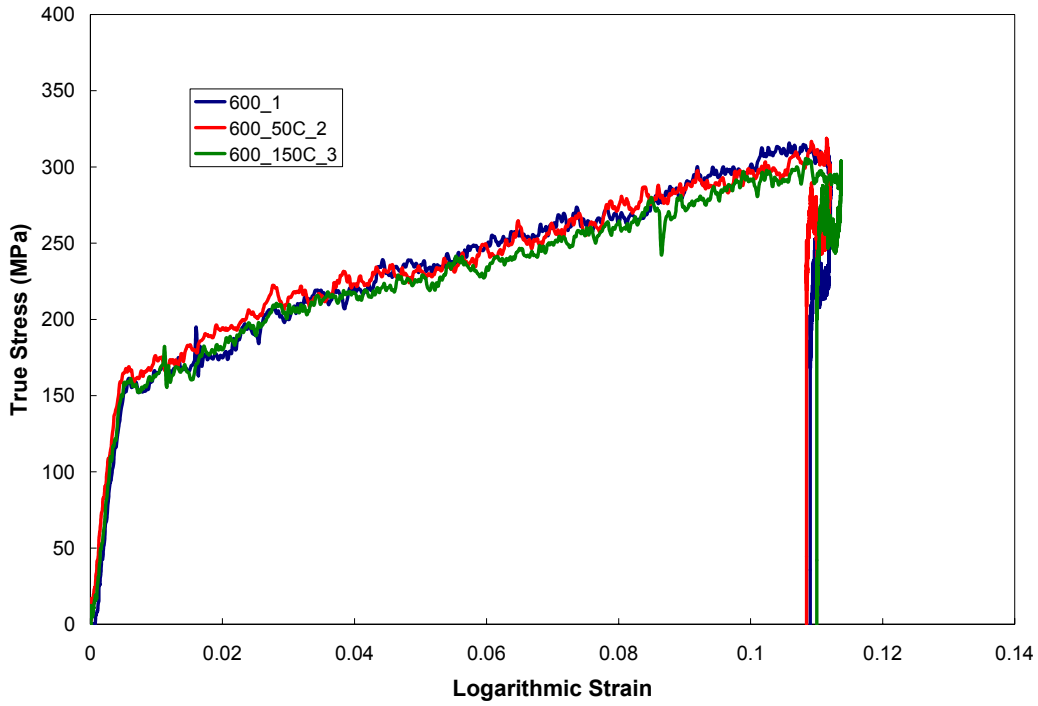

a)

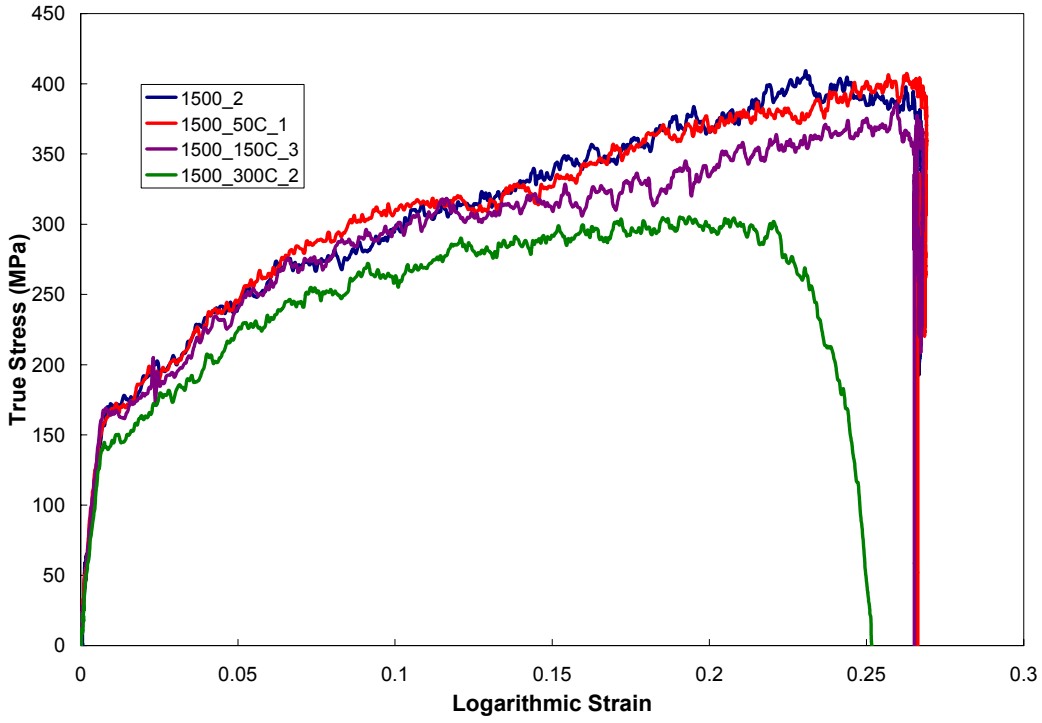

b)

Figure 5.10 – Effects of Initial Temperature on Flow Stress at a) 600 s^{-1} and b) 1500 s^{-1} for AA5182 – 1mm

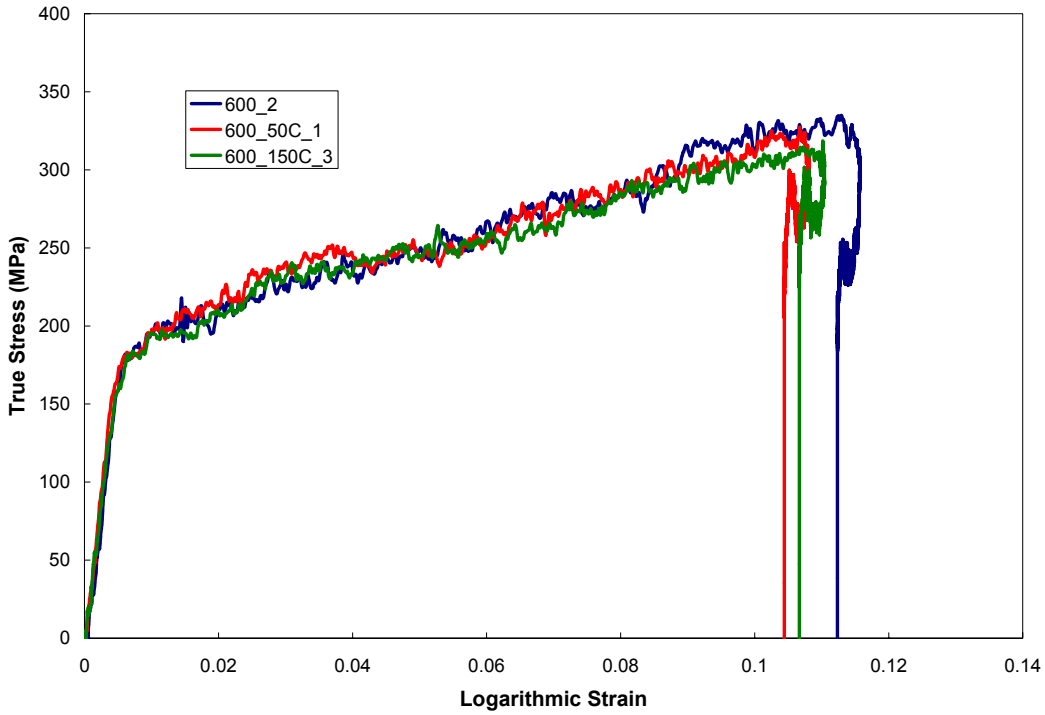

a)

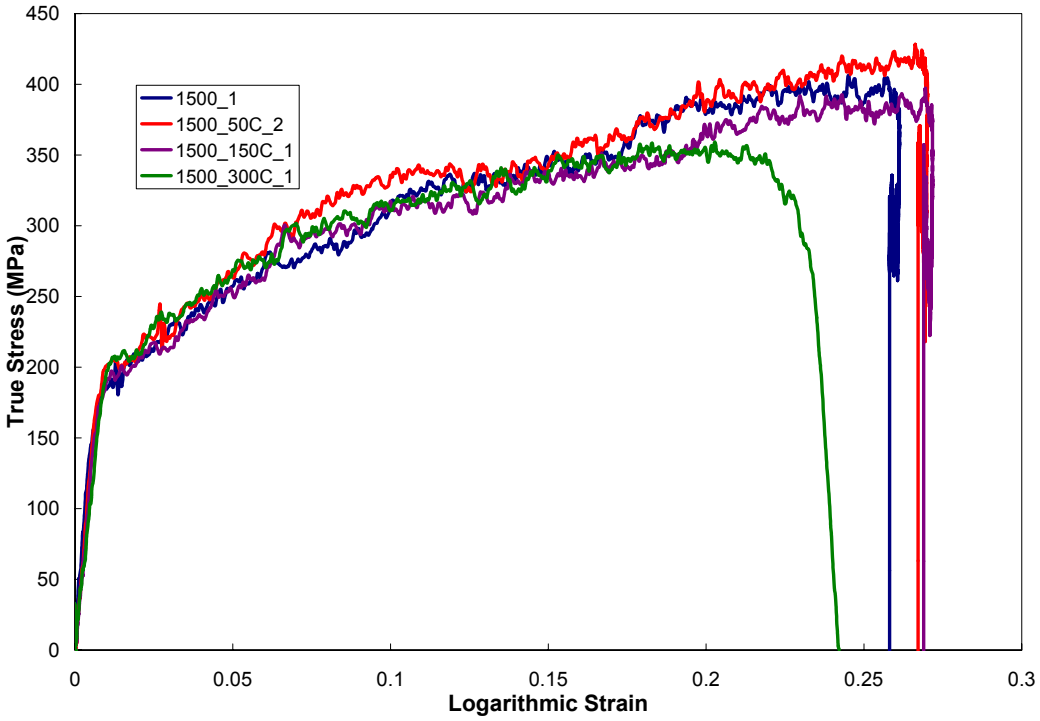

b)

Figure 5.11 – Effects of Initial Temperature on Flow Stress at a) 600 s^{-1} and b) 1500 s^{-1} for AA6111

Comparing the changes in flow stress with temperature at a strain rate of 1500 s^{-1} and 15% strain, it is seen in Figure 5.12, that AA5754 shows the largest decrease in flow stress with temperature. A plateau is observed in the data for AA5754, where no change in flow stress is witnessed between 50°C and 150°C. Outside of this range the flow stress decreases with temperature. AA5182 does not show this plateau in temperature sensitivity between 50°C and 150°C at 1500 s^{-1}, instead the flow stress decreases monotonically in the temperature range considered. In Figure 5.12, AA6111 exhibits the smallest change in flow stress between 23°C and 300°C. The flow stress decreases slightly between 23°C and 150°C, but increases again at 300°C. The reasons for this trend are unknown at this time.

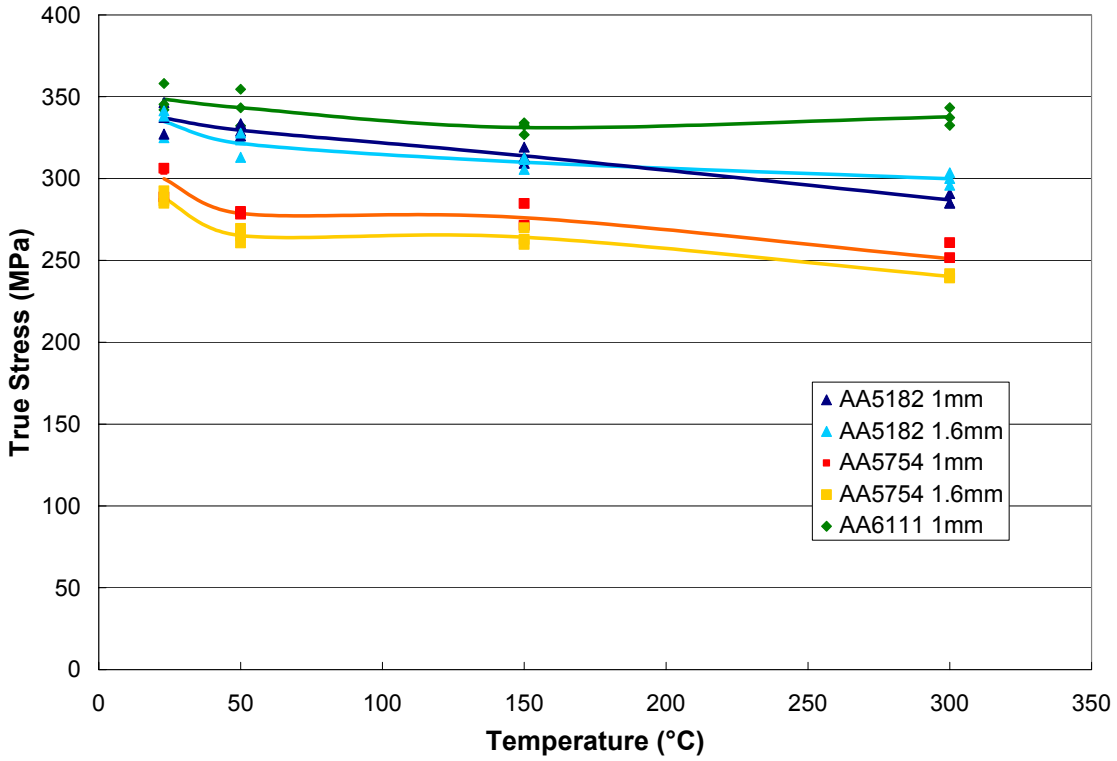

Figure 5.12 – True Stress at 15% Logarithmic Strain as a Function of Initial Temperature at a Strain Rate of 1500 s^{-1}

5.2 Strain Rate and Temperature Effects on Elongation

Final elongation was determined by direct measurement of the failed specimens. Since the specimens were loaded multiple times to failure, the point of failure could not be determined

using the TSHB data. Photographs of failed specimens tested at various strain rates are shown in Figure 5.13 through Figure 5.15 for all the alloys tested.

5.2.1 Effect of Strain Rate on Elongation

All the alloys tested showed similar trends. As the strain rate was increased, the total elongation to failure increased as well. The amount by which elongation increased varied with alloy and also with sheet thickness. In Figure 5.13, the elongation to failure of the two AA5754 sheets tested is compared. From the measurements taken, the thinner 1 mm sheet showed a greater increase in elongation with strain rate. The elongation to failure increased from 30.6% to 43.5% when the strain rate was increased from a quasi-static rate to 1500 s^{-1} for the 1.6 mm thick sheet. While the 1 mm sheet showed an increase from 27.7% to 45.9% for the same respective increase in strain rate. The reader should be cautioned that there is a higher degree of scatter in the elongation measurements taken at elevated strain rates as seen in Figure 5.16.

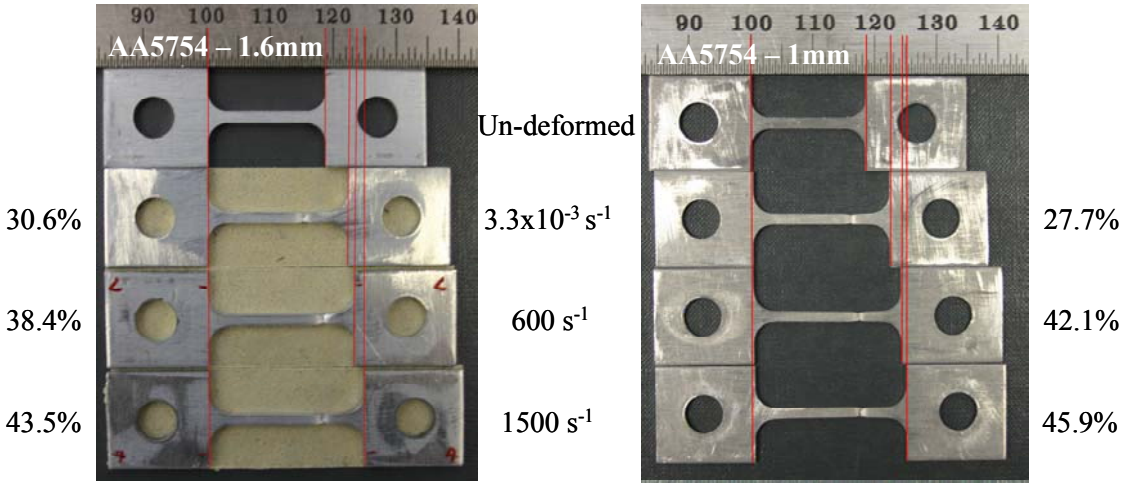

Figure 5.13 – Photographs Showing Increase in Final Elongation With Strain Rate for AA5754 1.6 mm (Left) and 1 mm (Right) TSHB Specimens

Comparing the elongation measurements of 1.6 mm to 1 mm thick AA5182, trends similar to those seen in AA5754 were witnessed. The measurements shown in Figure 5.14 indicate that the 1 mm sheet exhibits a greater increase in elongation to failure with increasing strain rate. The 1.6 mm thick sheet increased in final elongation by 7.9% strain from 29.6% at 3.3x10^{-3} s^{-1}

to 37.5% at 1500 s^{-1}, while the increase for the 1 mm thick sheet was from 30.1% to 42.5% (an increase of 12.4% strain) for the same respective increase in strain rate.

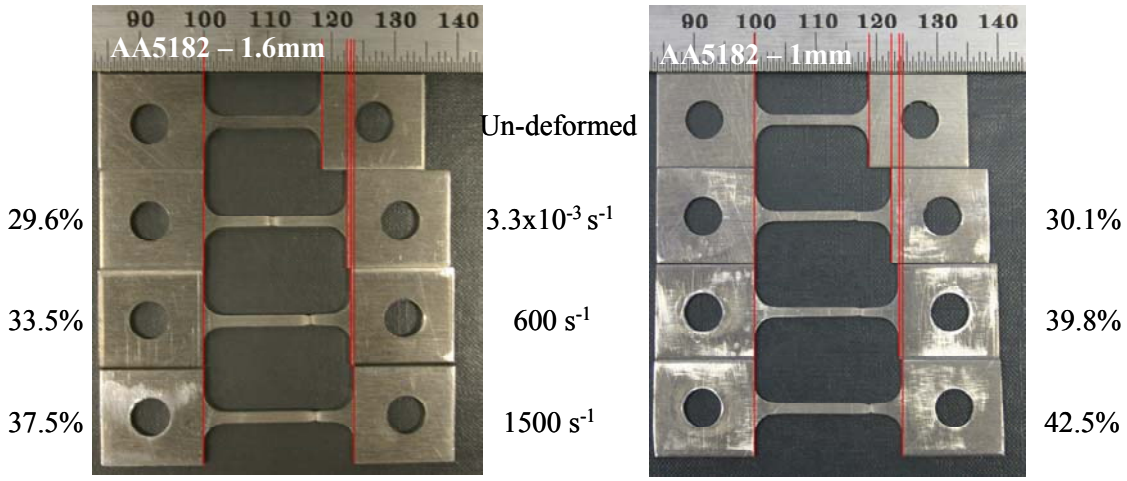

Figure 5.14 – Photographs Showing Increase in Final Elongation With Strain Rate for AA5182 1.6 mm (Left) and 1 mm (Right) TSHB Specimens

Like the other two alloys, AA6111 also exhibited increases in elongation to failure. Figure 5.15 shows that the elongation to failure of the AA6111 specimens increased by approximately 9.9% strain from 28.1% at 3.3x10^{-3} s^{-1}, to 38% at a strain rate of 1500 s^{-1}.

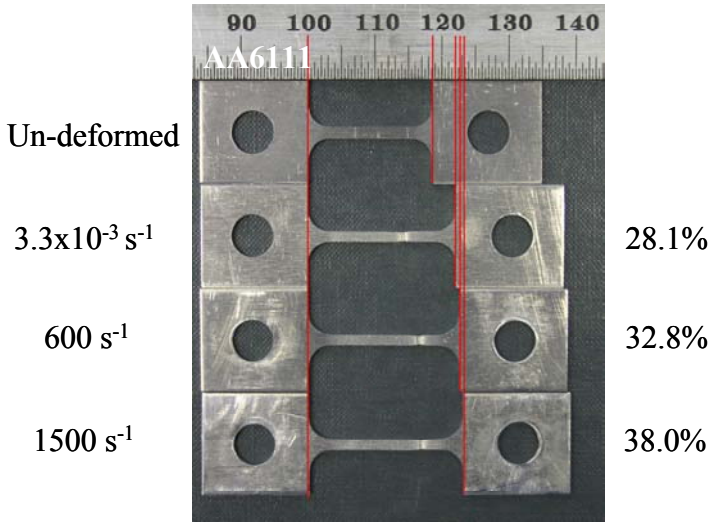

Figure 5.15 – Photograph Showing Increase in Final Elongation With Strain Rate for AA6111

The elongation to failure for all the alloys tested is shown as a function of the logarithm of strain rate in Figure 5.16. Of the three alloys, AA5754 appears to exhibit the largest increase in elongation with strain rate, followed by AA5182 and AA6111. Figure 5.16 also shows that the ranking of the ductility of AA5754 and AA5182 at high rates of strain is the reverse order of the ranking witnessed under quasi-static conditions. Under quasi-static conditions, AA5182 exhibited the more ductility than AA5754, the opposite of that witnessed at 1500 s^{-1}. As previously mentioned, the reader should be aware of the large scatter in the measurements taken from the samples tested at high strain rates in comparison to the specimens loaded at a quasi-static rate. To validate these results, the data presented here should be compared with experiments performed using a long-duration TSHB in future work, where the specimens fail under a single loading pulse.

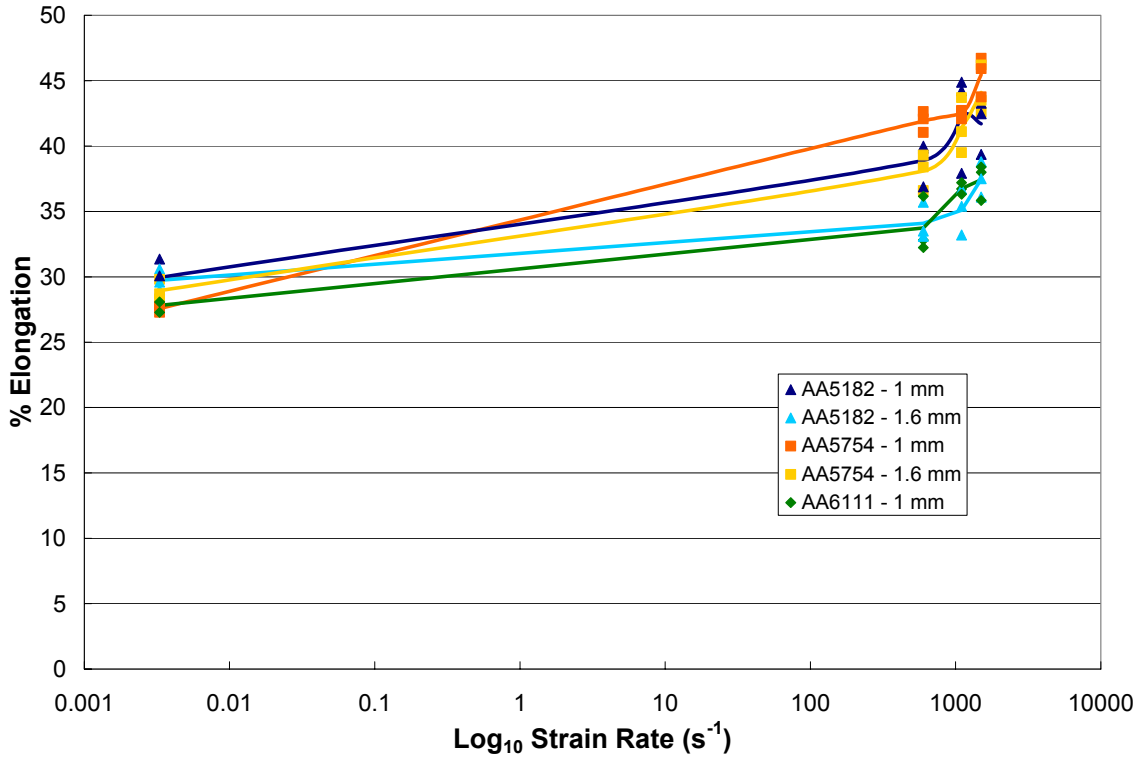

Figure 5.16 – Elongation as a Function of Log_{10} Strain Rate

5.2.2 EFFECT OF TEMPERATURE ON ELONGATION

The elongation of specimens tested at elevated temperatures using a strain rate of 1500 s^{-1} was also measured. Photographs of failed specimens are shown in Figures 5.17 through 5.19 and measured elongation data is plotted in Figure 5.20. The 1.6 mm thick AA5754 and AA5182 alloys showed no significant changes in elongation to failure up to an initial temperature of 150°C. However, at an initial temperature of 300°C, both alloys showed a decrease in elongation to failure. The elongation to failure at a strain rate of 1500 s^{-1} and an initial temperature of 300°C was 29.3% for AA5754, versus 27.9% for AA5182. These values are very close to the elongation to failure under quasi-static conditions (30.6% for AA5754 and 29.6% for AA5182). Like the 1.6 mm thick sheet, the final elongations of the 1 mm sheet measured at 300°C were also very close to those found under quasi-static conditions. However, the 1 mm thick AA5754 and AA5182 sheets already began to exhibit decreases in elongation at 150°C. The elongation of the 1mm thick AA5754 decreased from 45.7% at 50°C to 37.8% at 150°C, compared to a decrease from 43.3% at 50°C to 41% at 150°C for the 1.6 mm sheet. Similar results were found for AA5182, for which the elongation between 50°C and 150°C in the 1 mm sheet decreased from 43.1% to 37.5%, versus a decrease from 37.6% to 37.2% for the thicker 1.6 mm sheet.

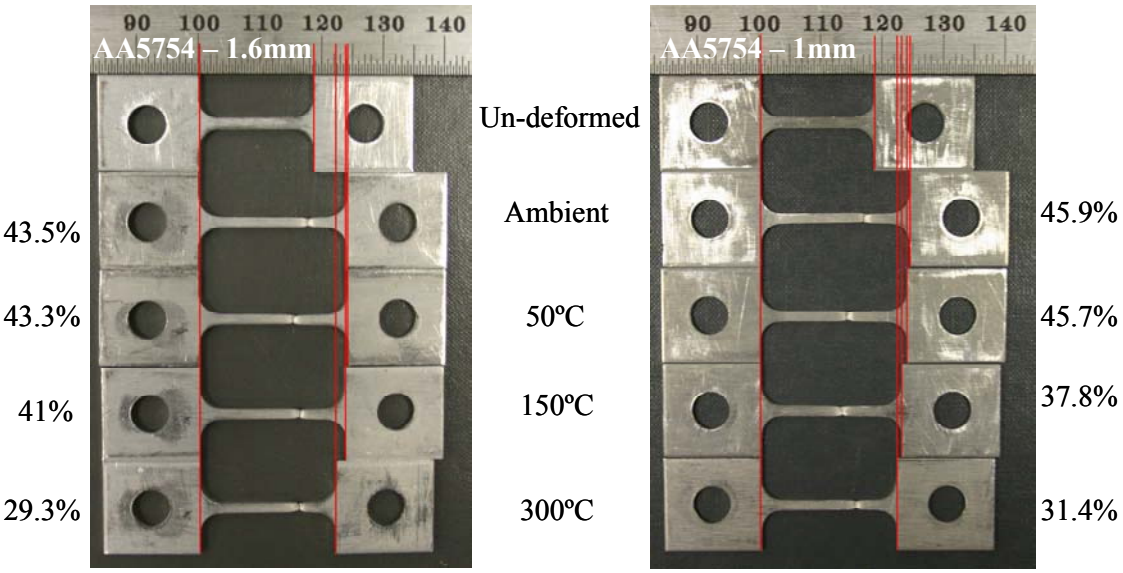

Figure 5.17 – Photographs Showing Changes in Final Elongation With Initial Temperature for AA5754 1.6 mm (left) and 1 mm (right) TSHB Specimens Tested at 1500 s^{-1}

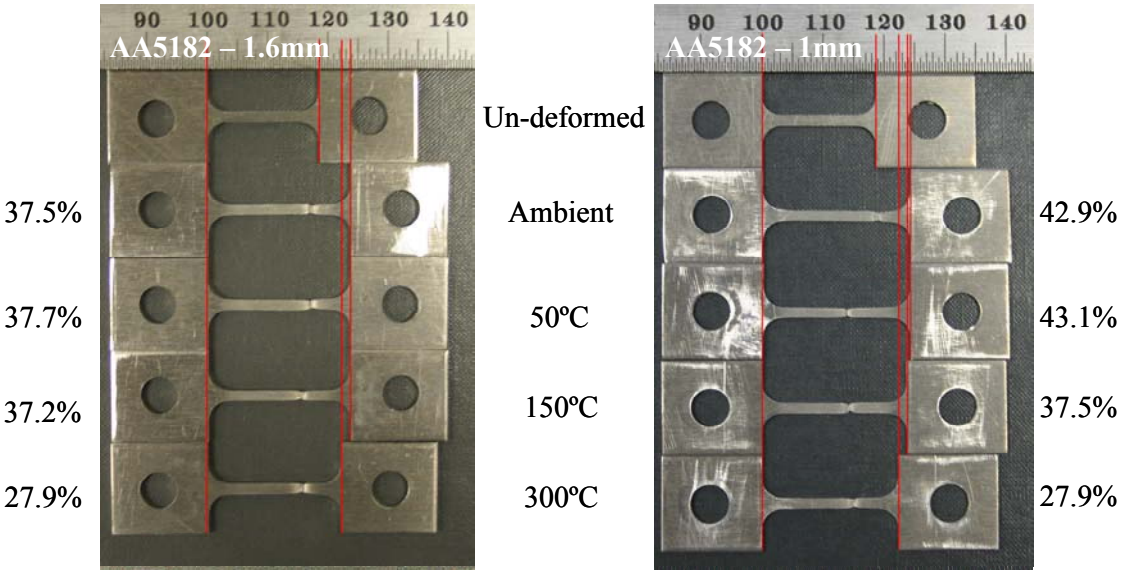

Figure 5.18 – Photographs Showing Changes in Final Elongation With Initial Temperature for AA5182 1.6 mm (left) and 1 mm (right) TSHB Specimens Tested at 1500 s^{-1}

Similarly, the elongation to failure of AA6111 at 1500 s^{-1} and 300°C decreased to values close to those measured under quasi-static conditions (26.9% at 1500 s^{-1} and 300°C, compared to 28.1% at $3.3x10^{-3}$ s^{-1}, RT). Furthermore, a decrease in elongation was witnessed between 23°C and 50°C, where the elongation decreased from 38.8% to 32.1%, respectively.

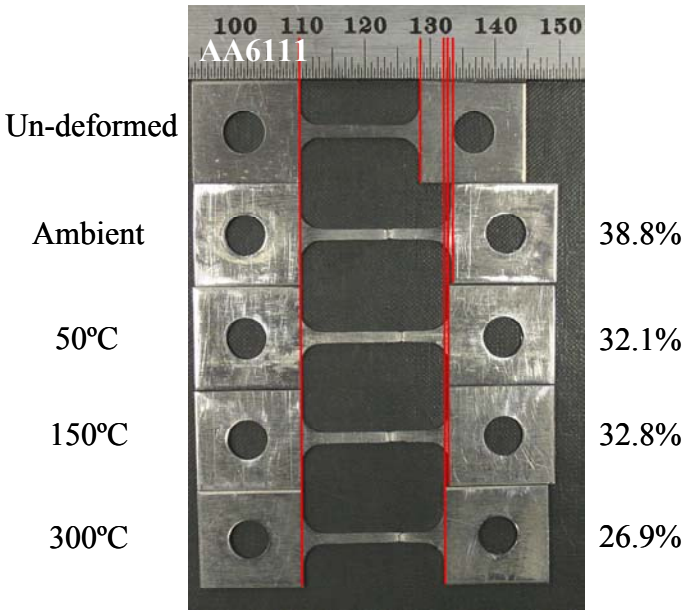

Figure 5.19 – Photograph Showing Changes in Elongation With Initial Temperature for AA6111 TSHB Specimens Tested at 1500 s^{-1}

Of the alloys tested, the final elongation of AA5754 showed the largest degree of temperature sensitivity. Both thicknesses of AA5754 exhibited similar decreases in elongation with temperature, whereas the measurements taken for AA5182 differed greatly between the two sheet thicknesses investigated. This discrepancy is unexpected when comparing it to the data collected for AA5754, and the reasons for it are unknown at this time. Furthermore, the reader should be made aware that the scatter in the elongation measurements at elevated temperatures was greater than in those taken at ambient. Two measurements shown in Figure 5.20 have been considered as outliers; one measurement taken for 1.6 mm AA5182 at 300°C, and one at 50°C for 1 mm AA5754.

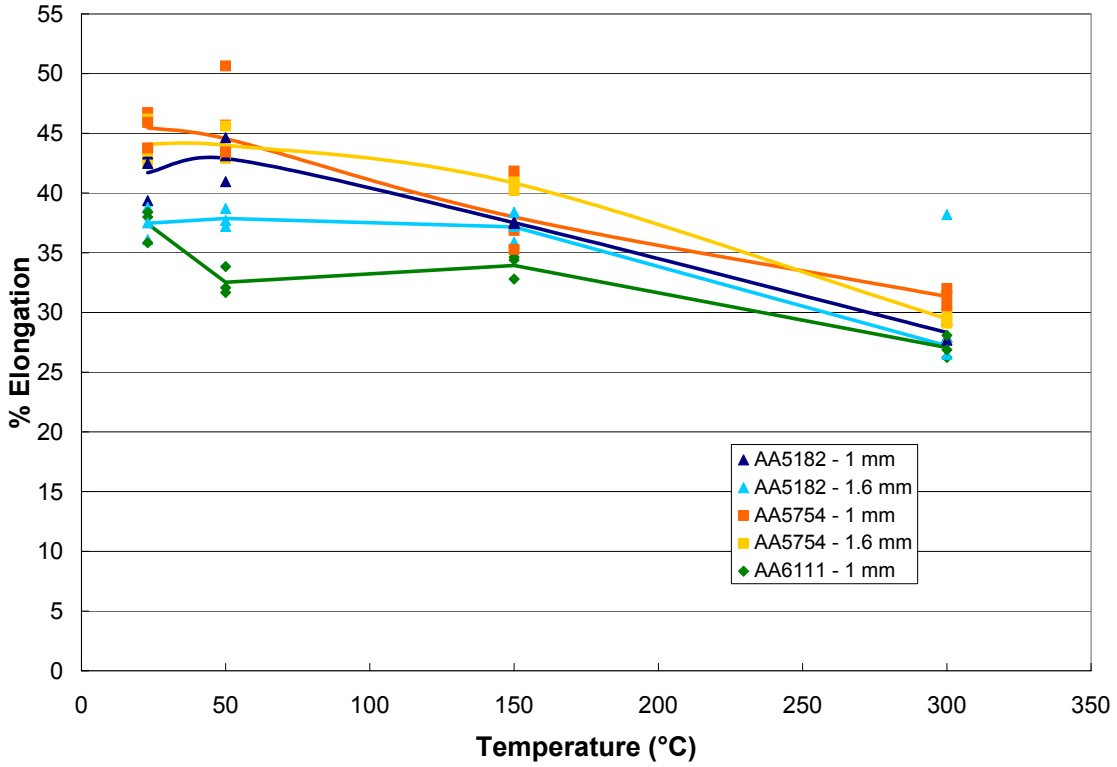

Figure 5.20 – Elongation as a Function of Temperature at a Strain Rate of 1500 s^{-1}

5.3 CONSIDERE TENSILE INSTABILITY PREDICTIONS

Considere's criterion predicts that tensile instability will occur when:

$$\sigma = \frac{d\sigma}{d\varepsilon} \tag{5.1}$$

for a given strain [79]. This condition corresponds to the attainment of the ultimate tensile strength and corresponds to a condition for the onset of diffuse necking. In order to examine the effect of strain rate on the strain to reach the so-called Considere point $\left(\sigma = \frac{d\sigma}{d\varepsilon}\right)$, plots of stress versus $\frac{d\sigma}{d\varepsilon}$ were generated for all of the alloys tested. The experimental data could not be used in its raw form due to the oscillations that were witnessed when the derivative was taken. Instead, 4th and 5th order polynomials were fit to the experimental data and were subsequently differentiated. The polynomial fits, along with their respective derivates, are

plotted in Figure 5.21 through Figure 5.30 for all of the alloys. The data collected at strain rates of 600 and 1100 s^{-1} was not considered since the strain levels reached were limited and would require a large degree of extrapolation.

5.3.1 Strain Rate Effects on Instability Criterion

Figure 5.21 through Figure 5.25 show that as the strain rate is increased from a quasi-static rate to 1500 s^{-1}, the strain at which tensile instability is predicted using Considere's criterion increases for all of the alloys examined. This suggests that the increase in the strain hardening rate with strain rate enhances the ductility by increasing the strain at which localization occurs. This behavior is consistent with the observations presented in Section 5.2.1, where the elongation of AA5754, AA5182, and AA6111 was shown to increase with strain rate. 1 mm AA5754 showed the largest increasing in elongation with strain rate and, also, shows the largest increase in strain at which Considere's criterion is satisfied, as shown in Figure 5.22.

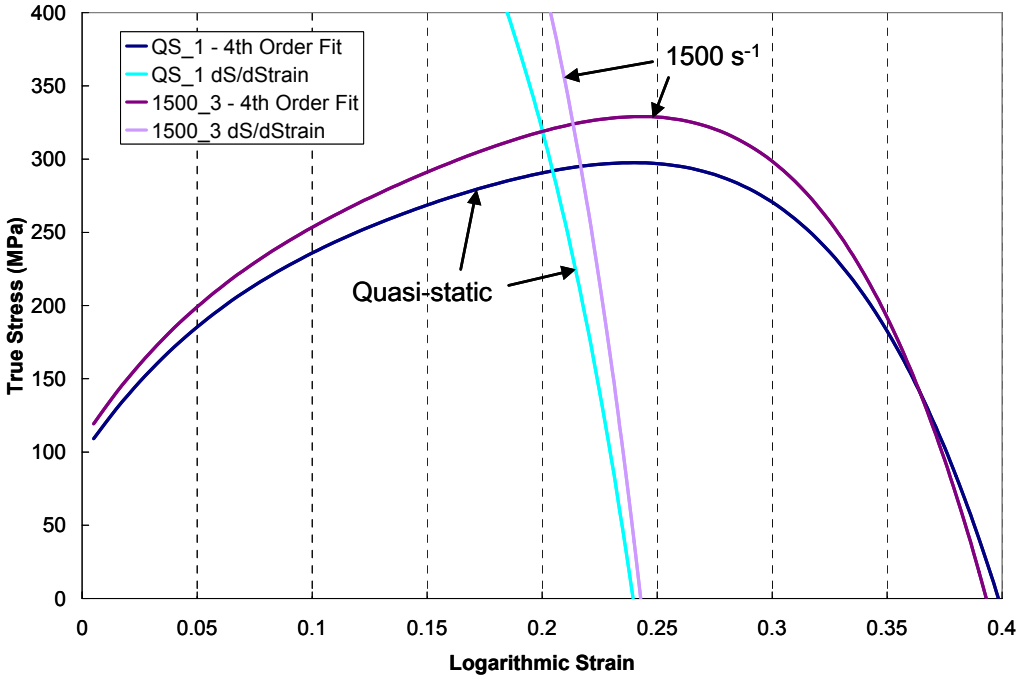

Figure 5.21 – Stress Versus dσ/dε At Various Strain Rates For 1.6 mm AA5754

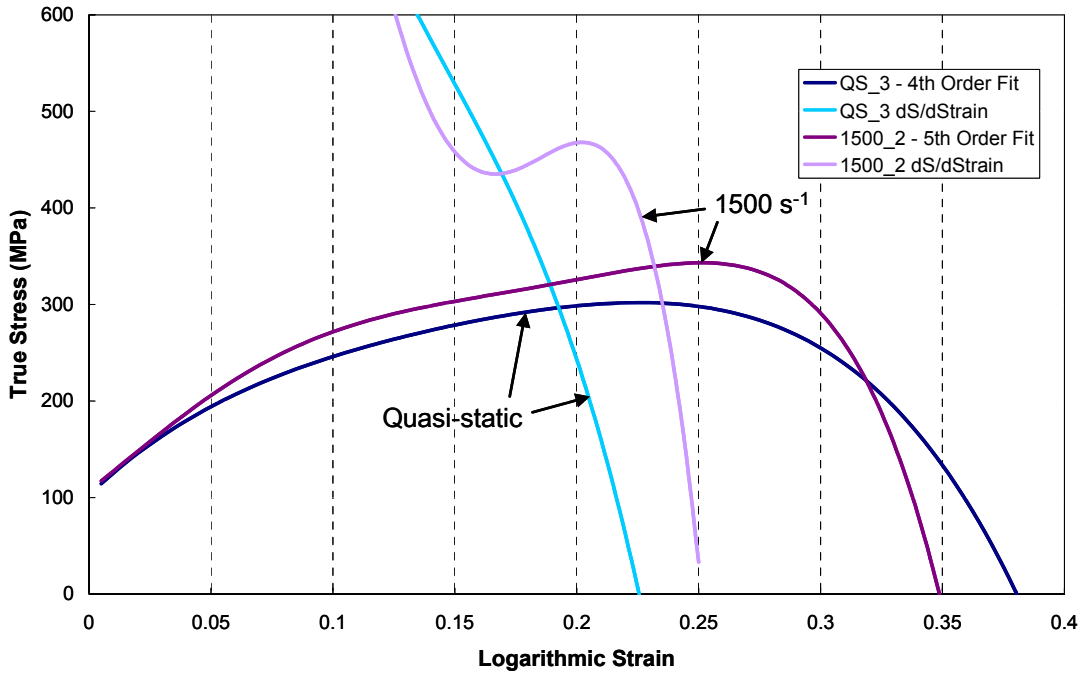

Figure 5.22 – Stress Versus dσ/dε At Various Strain Rates For 1 mm AA5754

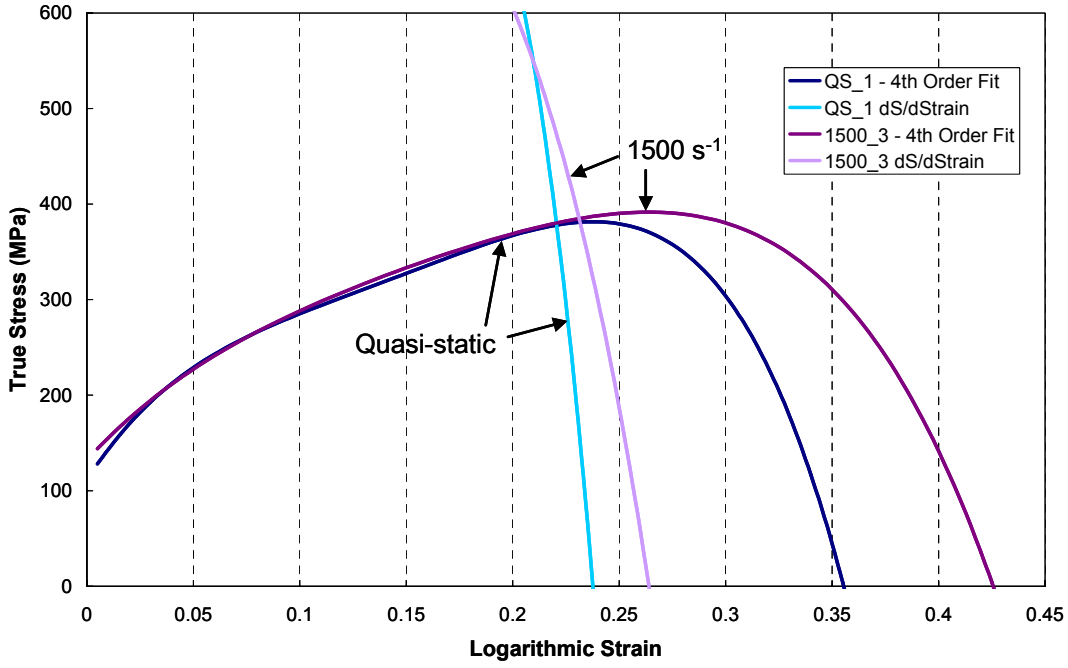

Figure 5.23 – Stress Versus dσ/dε At Various Strain Rates For 1.6 mm AA5182

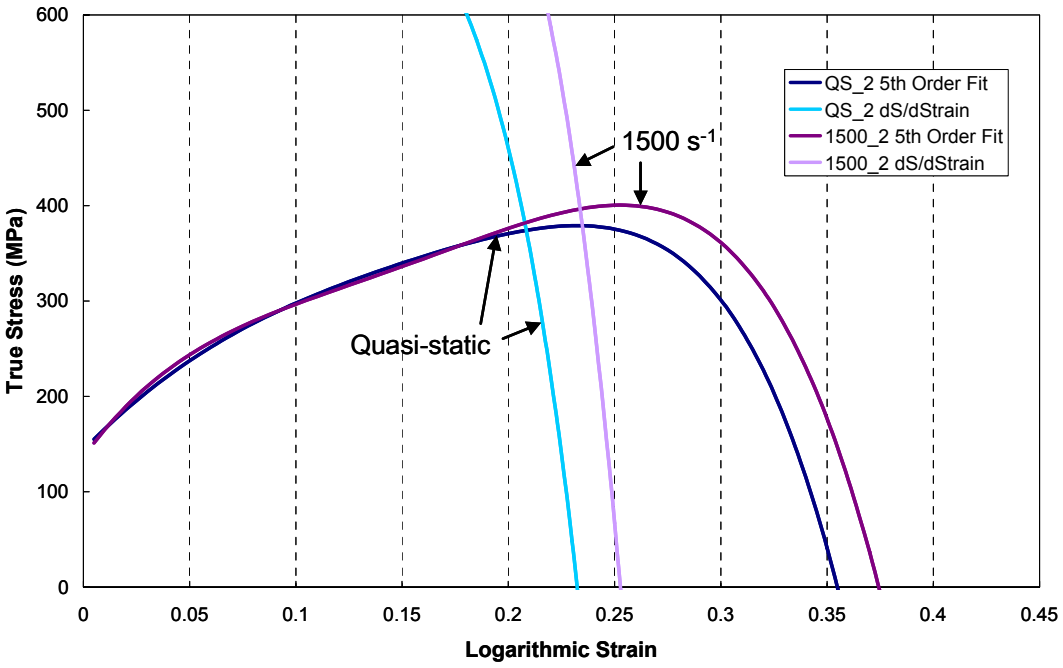

Figure 5.24 – Stress Versus dσ/dε At Various Strain Rates For 1 mm AA5182

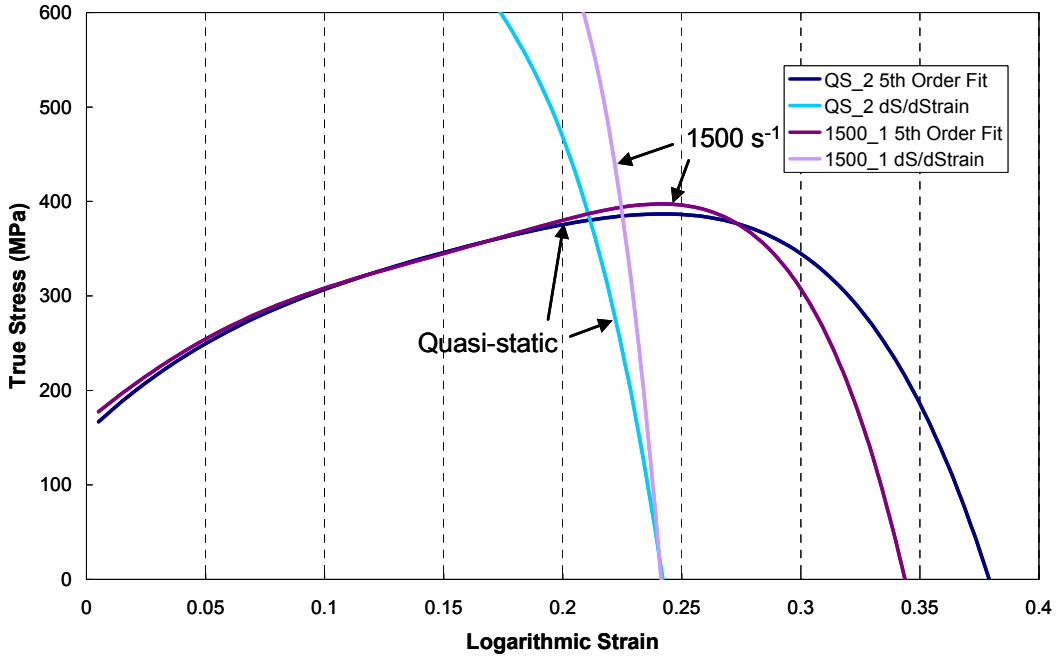

Figure 5.25 – Stress Versus dσ/dε At Various Strain Rates For 1 mm AA6111

5.3.2 TEMPERATURE EFFECT ON INSTABILITY CRITERION

In Figure 5.26 through Figure 5.30, polynomial fits of stress versus strain at various test temperatures are plotted for a rate of 1500 s^{-1} along with their respective derivates for all of the alloys tested. When the temperature increases from 23˚C to 50˚C, the alloys show a slight increase in the strain at which instability is predicted by Considere's criterion, with the exception of 1.6 mm AA5182. However, as the temperature is increased further to 300˚C, the strain at which necking is predicted to occur decreases significantly for all of the alloys according to Considere's criterion. This behavior is consistent with the experimental results presented in Section 5.2.2, where the elongation significantly decreased at a temperature of 300˚C. The higher initial temperature is shown to decrease the strain hardening rate effect, lowering the strain at which a tensile instability is predicted using equation (5.1).

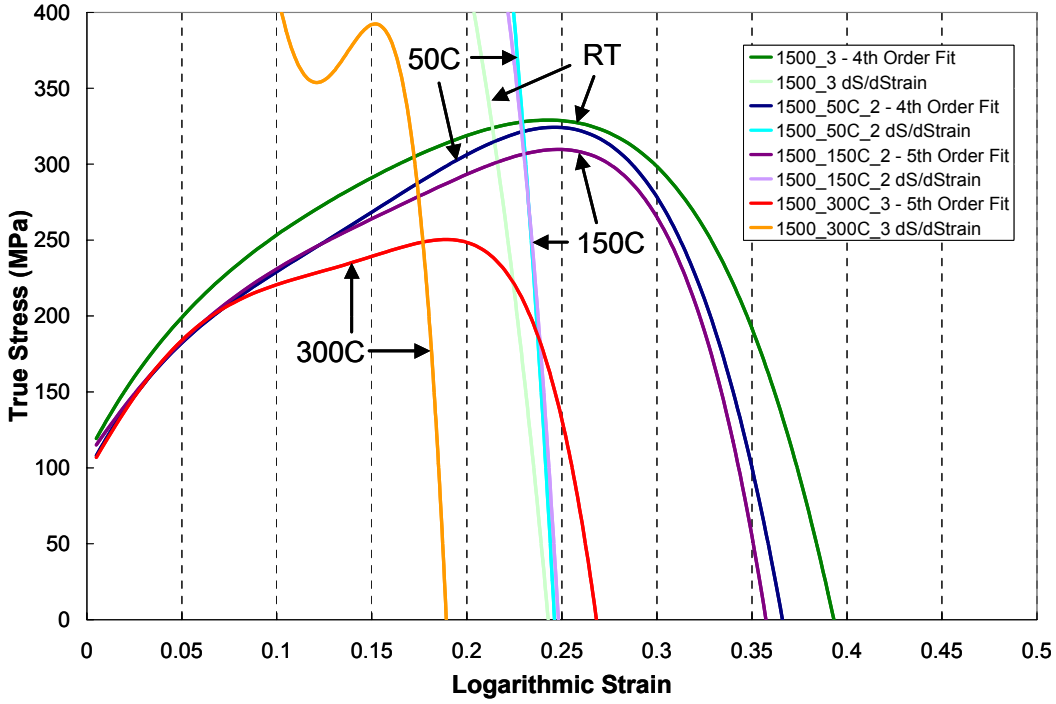

Figure 5.26 – Stress Versus dσ/dε at Various Temperature For 1.6 mm AA5754 For a Strain Rate of 1500 s^{-1}

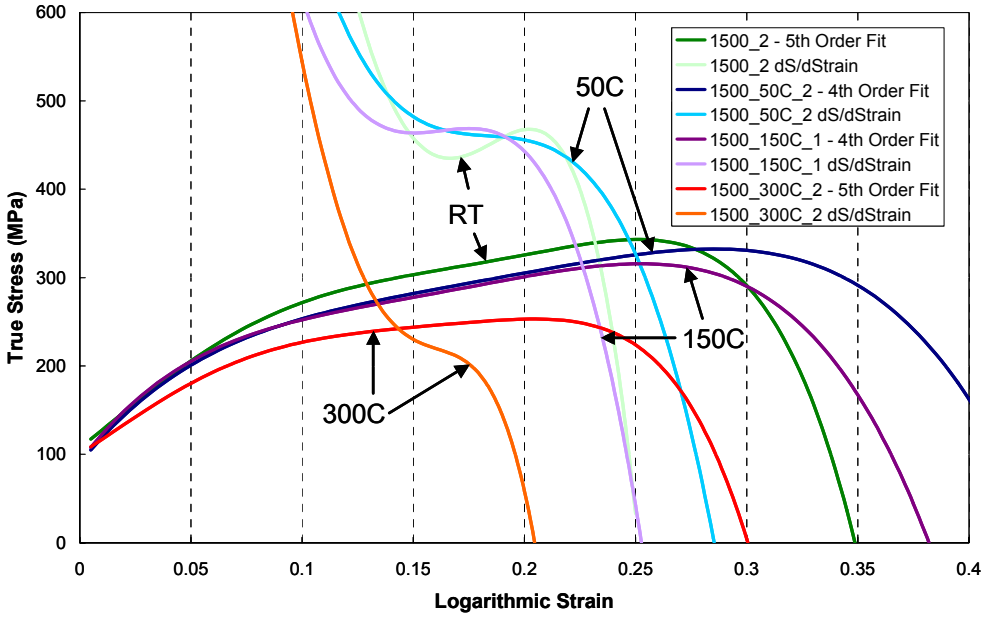

Figure 5.27 – Stress Versus dσ/dε at Various Temperature For 1 mm AA5754 For a Strain Rate of 1500 s^{-1}

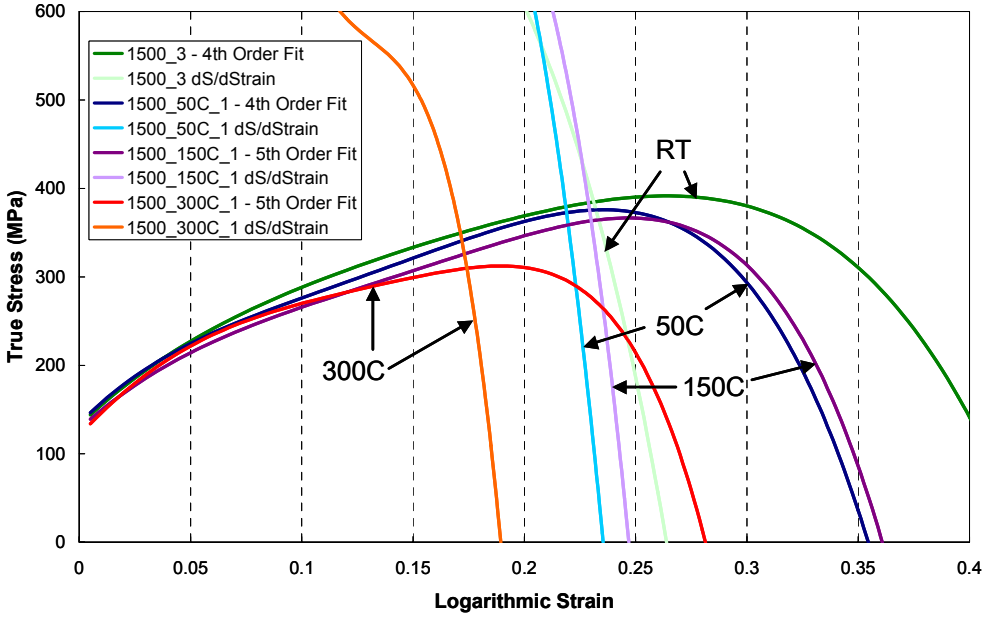

Figure 5.28 – Stress Versus dσ/dε at Various Temperature For 1.6 mm AA5182 For a Strain Rate of 1500 s^{-1}

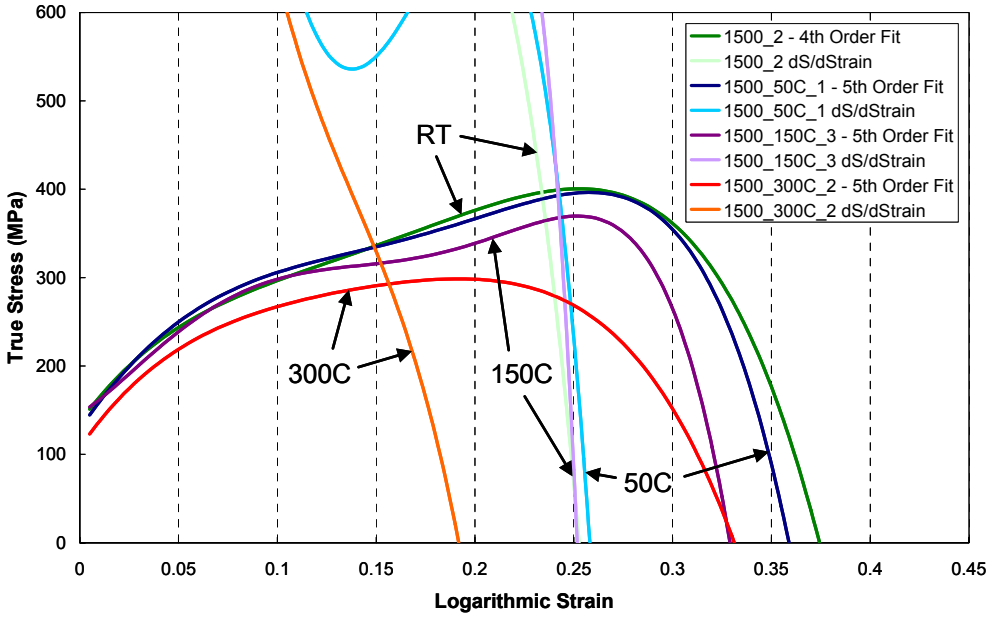

Figure 5.29 – Stress Versus dσ/dε at Various Temperature For 1 mm AA5182 For a Strain Rate of 1500 s^{-1}

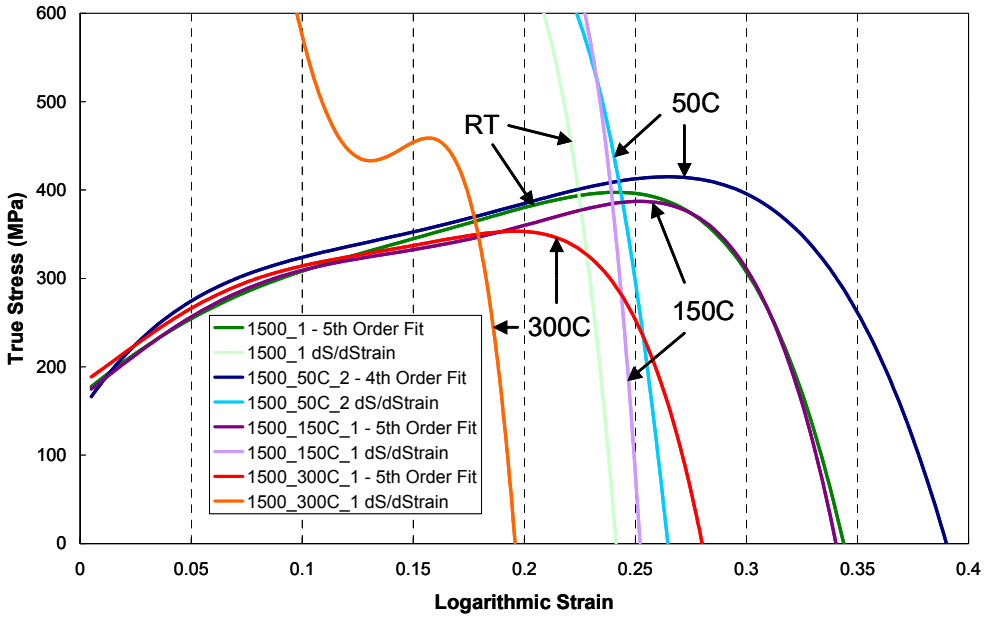

Figure 5.30 – Stress Versus dσ/dε at Various Temperature For 1 mm AA6111 For a Strain Rate of 1500 s^{-1}

5.4 FRACTURE MODES

Optical micrographs were taken of the necked and fractured regions of 1.6 mm thick AA5754 and AA5182, tested under quasi-static and high strain rate conditions, and are shown in Figure 5.31. Failure appears to have occurred by means of a ductile-shear failure mode for all samples and the amount of necking and damage in both alloys is found to increase with strain rate. Damage is observed to occur by void nucleation, growth and coalescence of voids at second phase particles and is concentrated in regions adjacent to the fracture surface where plastic strains and the associated hydrostatic stresses are highest.

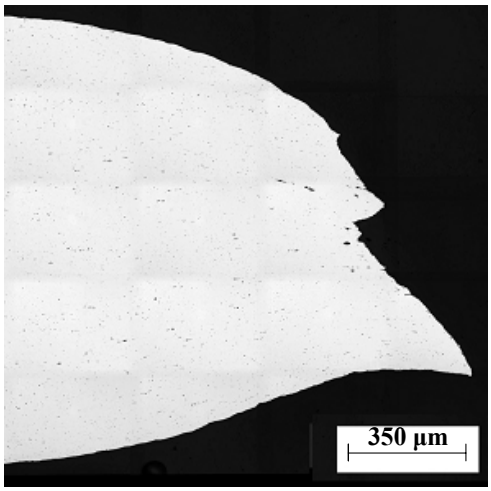

a) AA5754 – Quasi-Static

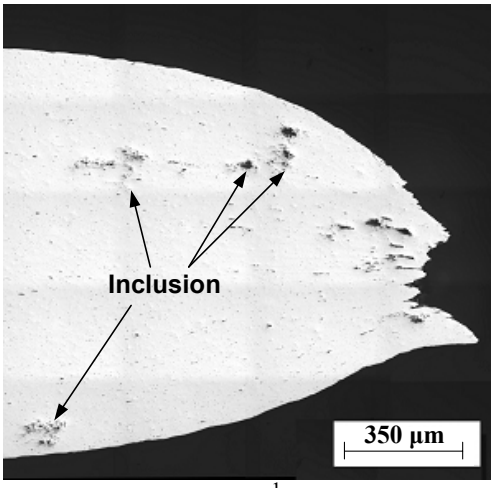

b) AA5754 – 1500 s^{-1}

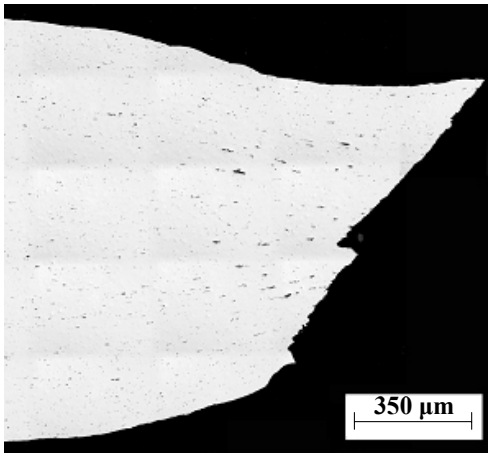

c) AA5182 – Quasi-static

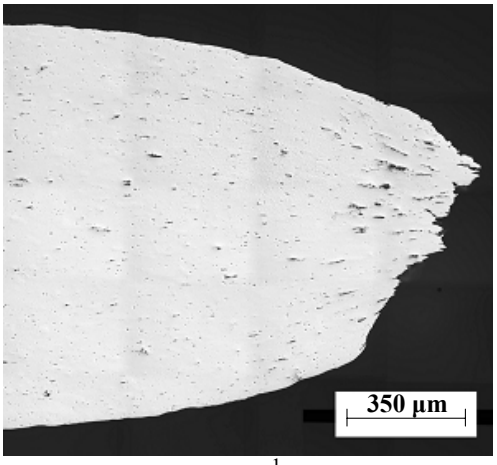

d) AA5182 – 1500 s^{-1}

Figure 5.31 – Optical Images Comparing the Microstructure and Damage Development of 1.6 mm Thick AA5754 and AA5182 TSHB Specimens Tested at Strain Rates of $3.3x10^{-3}$ s^{-1} (QS) and 1500 s^{-1} Viewed in the Long-Transverse Plane

The thickness strains in the region adjacent to the fracture surface increased with strain rate, as shown in Figure 5.32. The samples tested at high strain rate also experience higher strains at locations much further from the fracture surface. This implies that the high rate conditions promote more thinning of the sheet prior to fracture, increasing the formability of these alloys. At 2200 μm away from the fracture surface and beyond, the thickness strains shown in Figure 5.32 remain uniform and are higher at high strain rates. Hence, the additional thinning experienced under high rates is not limited to the neck and fracture regions, but is distributed through the entire gauge section. AA5182 shows higher thickness strains than AA5754 in this region of homogeneous deformation under both quasi-static and high rate conditions, although, AA5754 appears to show the greater increase in thickness strain with strain rate. In regions within approximately 700 μm from the fracture surface, AA5754 shows higher thickness strains than AA5182, implying that more neck growth occurs in AA5754 prior to fracture.

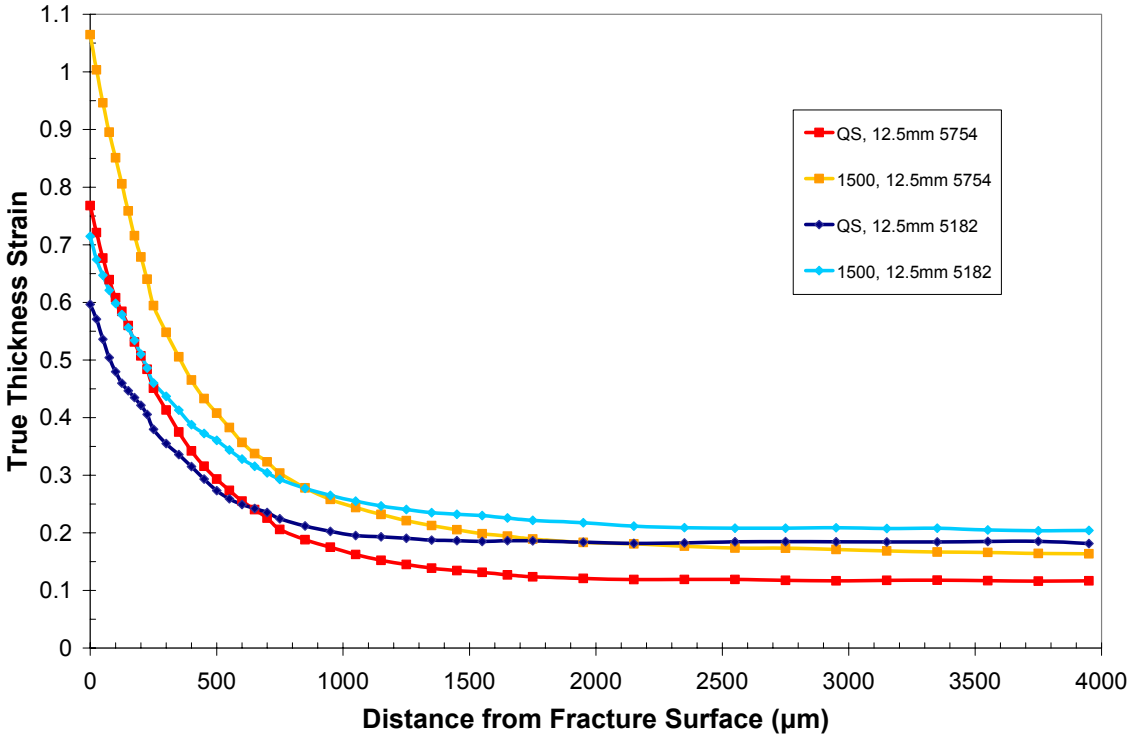

Figure 5.32 - Thickness Strain Variation for AA5754, AA5182 12.5 mm TSHB Specimens Tested Under QS conditions and at 1500 s^{-1}

Porosity measurements were calculated at various intervals along the gauge length. Figure 5.33 shows the percent area porosity as a function of the distance from the fracture surface for

both alloys. The dashed lines in Figures 5.33a and 5.33b represent the initial porosity levels and percent area fraction of second phase particles for each alloy. The reader should be aware that the specimens tested at 600, 1100 and 1500 s^{-1}, for which data is presented in Figure 5.33, were loaded multiple times to failure.

Comparing the porosity values at $3.3x10^{-3}$ s^{-1} to those at 1500 s^{-1}, both alloys show dramatic increases in porosity with strain rate. The maximum porosity in AA5754 increased from approximately 0.37% under quasi-static loading to approximately 3.85% at 1500 s^{-1}. AA5182 exhibited an increase from 0.99% to 3.06% for the same strain rate change. This data suggests that deformation at high strain rates has the effect of delaying the onset of failure and results in higher levels of damage. Regions beyond 1000 μm from the fracture surface for AA5754 and 2000 μm for AA5182 show little change in porosity with strain rate, confirming previous observations that damage is confined to the local region near the fracture surfaces, particularly in AA5754. Note that several large inclusions or oxides are present in the AA5754 specimen tested at 1500 s^{-1}, shown in Figure 5.31, and that the corresponding damage measurements presented in Figure 5.33 exclude data from regions containing these inclusions.

For all strain rates considered, significantly more damage is present in AA5182 compared to AA5754 due to its higher particle fraction and initial porosity. The second phase particles in AA5182 are also larger in size which leads to higher damage nucleation rates. The change of the ranking of alloy ductility with strain rate, shown in Figure 5.16, can possibly be related to this difference in second phase particle population and resulting damage accumulation. The higher damage accumulation rate of AA5182, resulting from a higher initial particle fraction and porosity may, reduce the strain rate effect on ductility in comparison to AA5754, which showed lower damage levels and the greater increase in ductility with strain rate of the two alloys. Mukai *et al.* [57] found similar results in high purity Al-Mg alloys, for which the effect of high strain rate deformation on ductility decreased with increasing magnesium concentration.

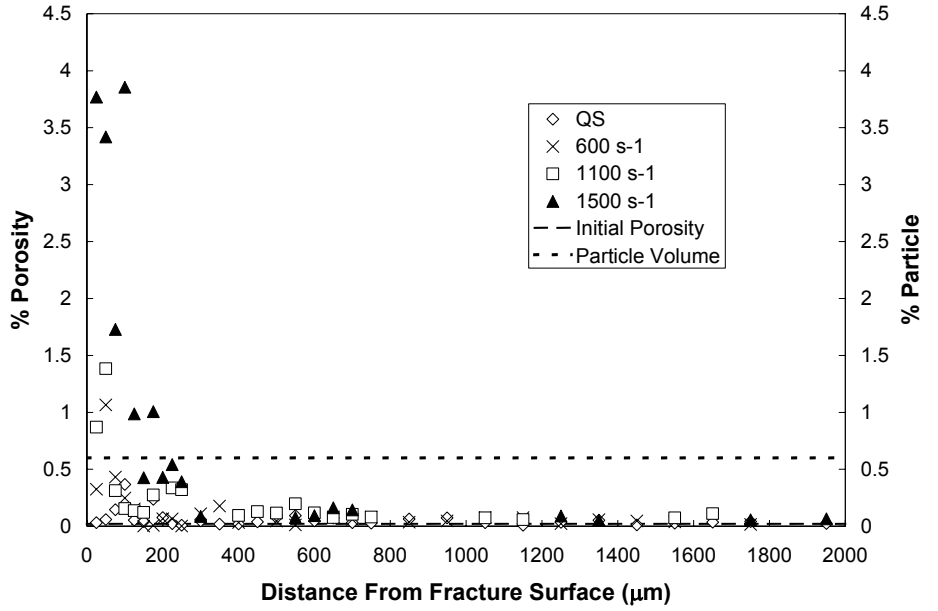

a)

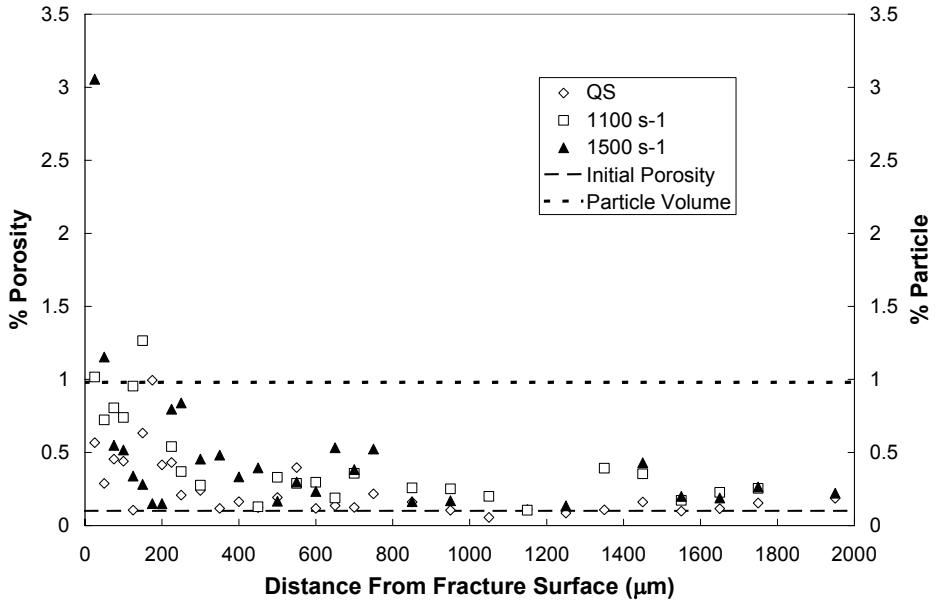

b)

Figure 5.33 – Porosity as a Function of Strain Rate for a) AA5754 and b) AA5182 – 1.6 mm

Figure 5.34 shows some typical fracture surfaces of failed AA5754 and AA5182 TSHB specimens. The dimple-like morphology of the fracture surfaces indicates that a ductile failure

mode is dominant for both alloys at all strain rates used. Other than a change in area reduction with respect to strain rate, the fracture surfaces are similar for the strain rates considered, for both alloys. The fractographs presented in Figure 5.35 are representative of both alloys at all strain rates investigated. The presence of the Fe- and Mn-rich intermetallics at the bottom of the dimples confirms that damage originates from these second phase particles and that the evolution of damage follows a void nucleation, growth and coalescence process. Closer examination of the particles within the dimples shows that the formation of voids in these materials is initiated by fracture of the second phase particles or through cracking along the particle/matrix interface.

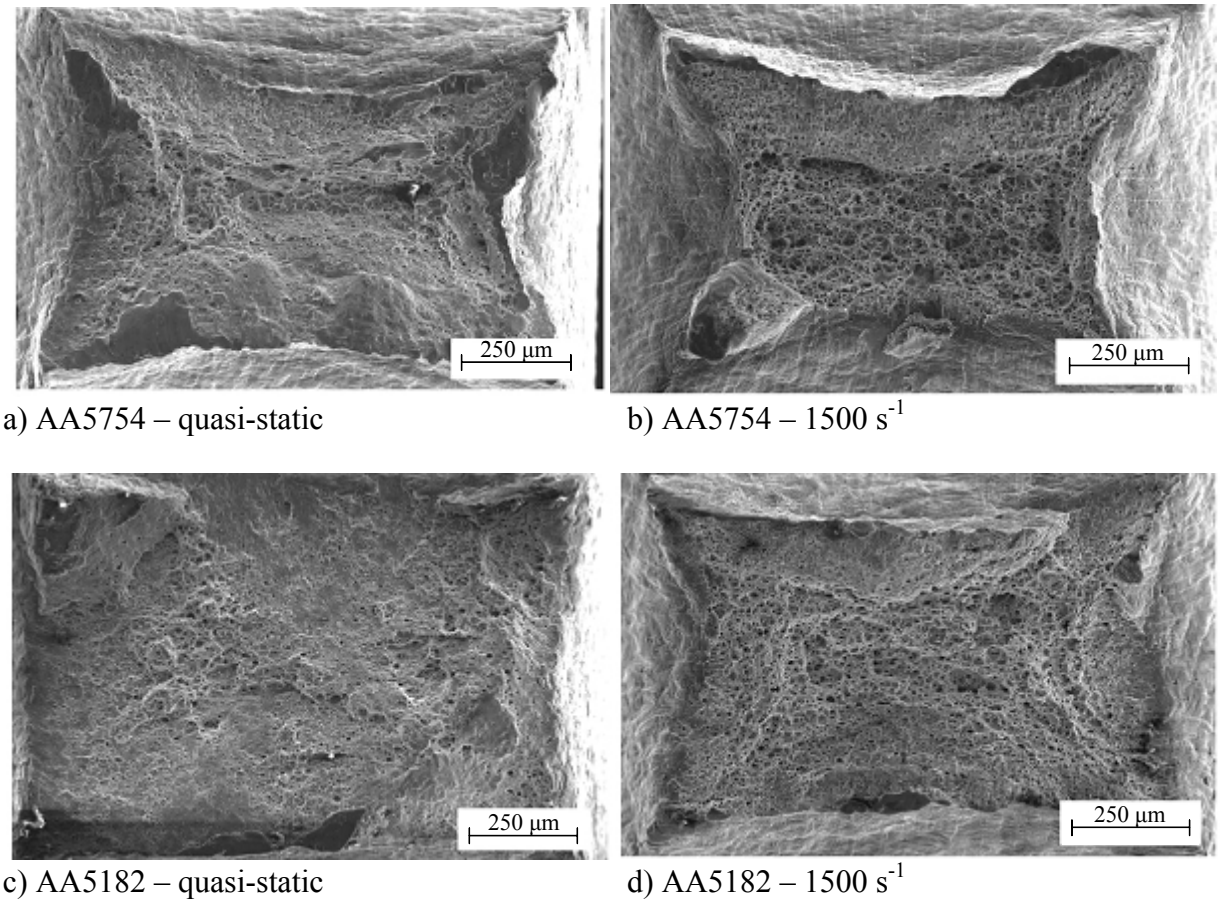

a) AA5754 – quasi-static

b) AA5754 – 1500 s^{-1}

c) AA5182 – quasi-static

d) AA5182 – 1500 s^{-1}

Figure 5.34 – SEM Images Showing Fracture Surfaces of AA5754 and AA5182, 1.6 mm Thick TSHB Specimens Tested at Strain Rates of $3.3x10^{-3}$ s^{-1} (Quasi-Static) and 1500 s^{-1}

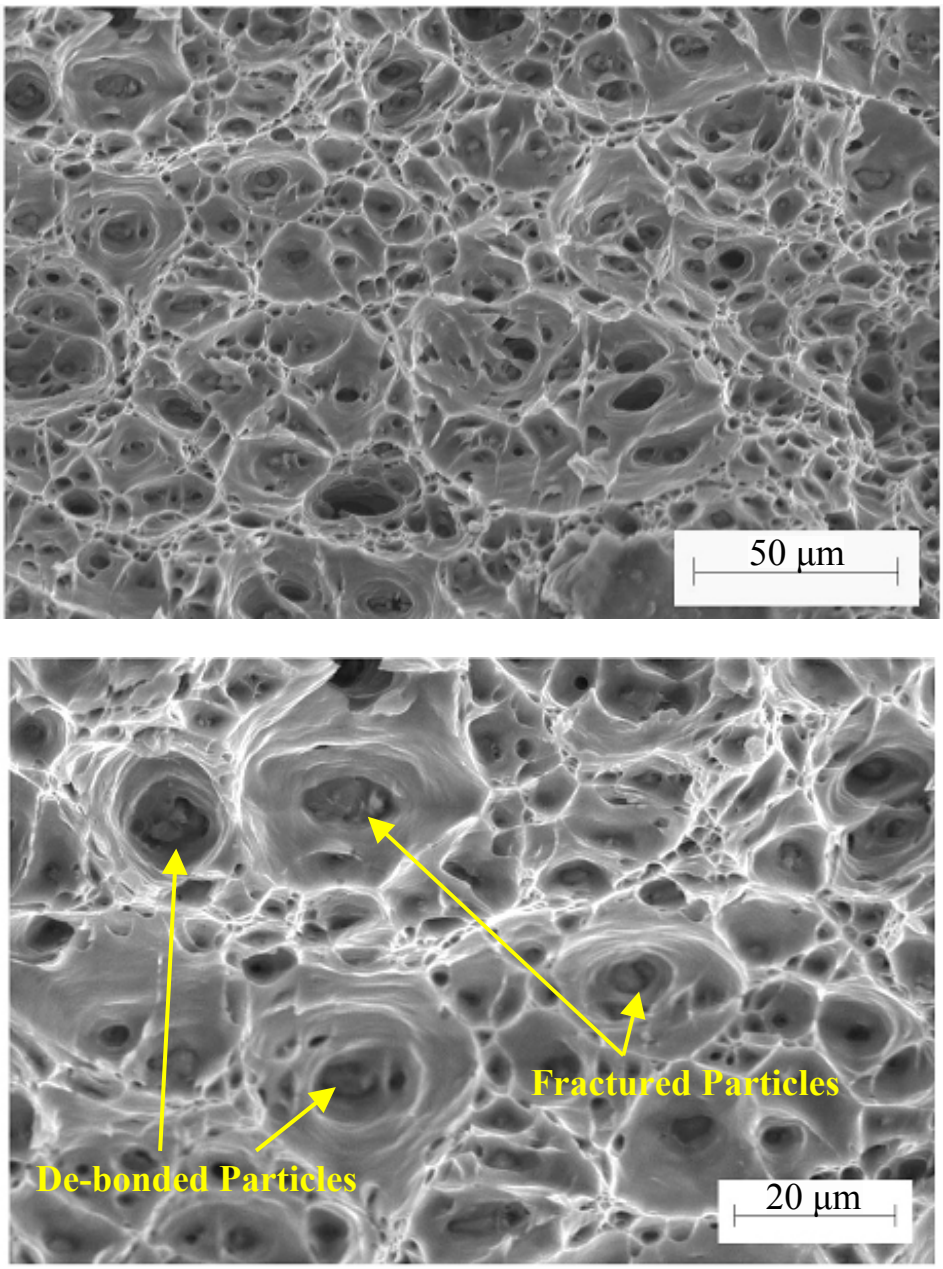

Figure 5.35 – High Magnification SEM Images of the Fracture Surface of a 1.6 mm Thick AA5754 TSHB Specimen Tested at 1500 s^{-1} Showing the Presence of Fe- and Mn-Rich Second Phase Particles at the Bottom of the Dimples

Using the SEM images obtained, the area of the fracture surfaces was measured and the percent area reduction with respect to strain rate was calculated for both alloys. Figure 5.36 shows that the percent area reduction increased from 74.9% to 85.5% for AA5754 and from

63.2% to 75.5% for AA5182 for a change in strain rate from $3.3x10^{-3}$ s^{-1} to 1500 s^{-1}, respectively. This increase is consistent with the optical images shown in Figure 5.31, where higher amounts of damage and greater elongation to failure were measured for specimens tested at high strain rates, indicating that failure is delayed and ductility is enhanced for AA5754 and AA5182 when deformed under high strain rate conditions. These results also correlate well with the data presented in Figure 5.32, where thickness strains adjacent to the fracture surface were higher for AA5754 than for AA5182 under quasi-static and high rate conditions, leading to a higher area reduction. Unlike in the elongation measurements shown in Figure 5.16, the ranking of the alloys shown in Figure 5.36 did not change with strain rate.

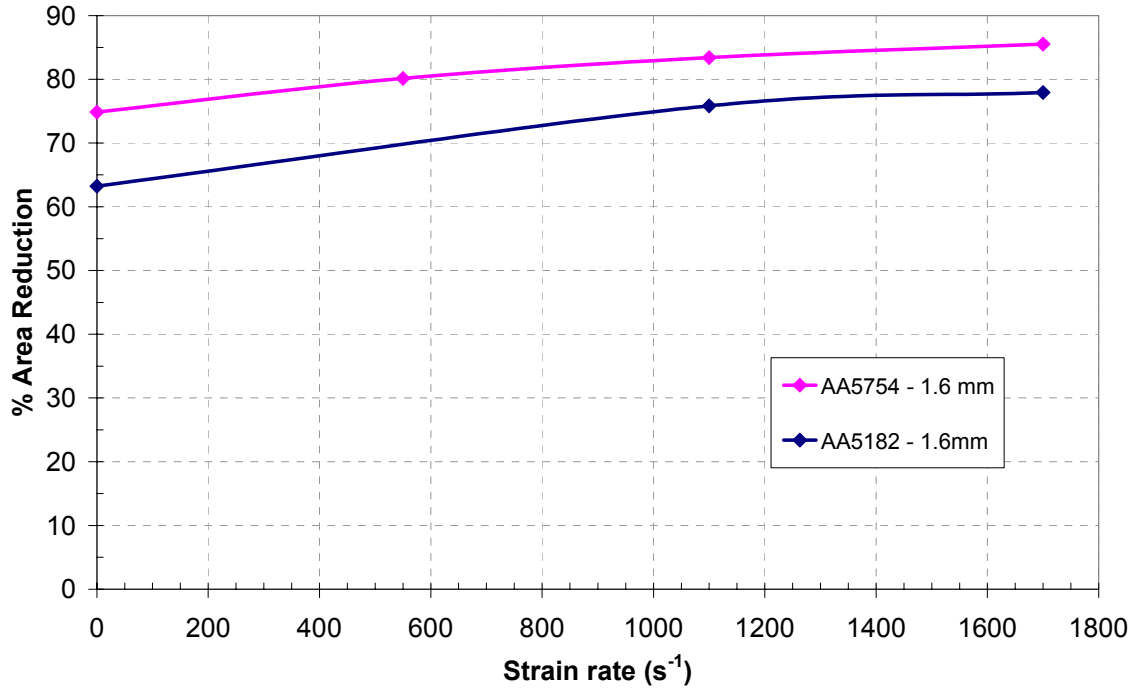

Figure 5.36 – Percent Area Reduction as a Function of Strain Rate

5.5 CONSTITUTIVE FITS

The experimental data was fit to both the Johnson-Cook and Zerilli-Armstrong constitutive models using a non-linear regression procedure in SYSTAT [80], a statistical analysis software. The strain and strain rate values used in the model fitting were taken directly from the experimental data. Only the median stress-strain curves were used for each set of test conditions. Hence, a total of nine experiments were used for each material in determining their respective model parameters. For the dynamic experiments, only data points in the region where the strain rate was approximately constant were used, while the ultimate tensile strength served as an upper bound for the data used from the quasi-static experiments. Approximately 40 data points were extracted from each experiment.

The Johnson-Cook constitutive model is implemented in LS-DYNA [70] in the same form as equation (1.21), and re-stated here:

$$\sigma = \left[A + B\varepsilon_{pl}^{n} \right]\left[1 + C\ln\dot{\varepsilon}^{*}\right]\left[1 - T^{*m}\right]$$

The Zerilli-Armstrong constitutive model, given in equation (1.30), is implemented in LS-DYNA [70] in the form:

$$\sigma = C_1 + \left\{ C_2 \left(\varepsilon_{pl}\right)^{1/2} e^{\left(-C_3 + C_4 \ln\left(\dot{\varepsilon}^{*}\right)\right)T} + C_5 \right\}\left(\frac{\mu(T)}{\mu(293)} \right) \tag{5.2}$$

where the last term is a temperature dependent shear modulus given as:

$$\left(\frac{\mu(T)}{\mu(293)} \right) = B_1 + B_2 T + B_3 T^2 \tag{5.3}$$

If the shear modulus is assumed to be independent of temperature, the constant B_1 is set to one, while B_2 and B_3 are set to zero. Parameter C_5, in equation (5.2), represents the effect of grain size (Hall-Petch effect) on the flow stress of the material. Since this is unknown for these alloys investigated, C_5 was set to zero, reducing the number of required parameter to 4.

The constitutive models implemented in LS-DYNA [70] require the true stress-plastic strain response of the material. Plastic strain (ε_{pl}) was determined using the following relationship:

$$\varepsilon_{pl} = \varepsilon - \sigma / E \tag{5.4}$$

where E is Young's modulus and σ and ε are the true stress and logarithmic strain, respectively. A reference strain rate ($\dot{\varepsilon}_0$) of 1 s^{-1} was chosen for both models. The temperature rise during deformation was calculated using equation (2.5) and used in the fits. A specific heat capacity of 900 J/kg·°K was used in calculating the temperature rise, and is listed in Table 3.2 along with the other material properties. The resulting parameters for the Johnson-Cook and Zerilli-Armstrong constitutive models are tabulated in Table 5.1 and Table 5.2, respectively, along with their upper and lower bounds for a 95% confidence interval.

From the results of non-linear regression fits, AA5182 possesses the lowest strain rate sensitivity parameter of those listed in Table 5.1 and Table 5.2, while AA5754 possesses the highest. This is expected since AA5754 showed the highest strain rate sensitivity in the experiments. It is interesting to note that the Johnson-Cook strain rate parameter, C, was found to be negative for the 1.6 mm thick AA5182, while positive for 1 mm AA5182. For AA6111, the non-linear regression yielded a very high temperature sensitivity parameter m (309.491). Furthermore, SYSTAT [80] did not return upper and lower bounds for m. Although this result reflects the lack of thermal softening exhibited by AA6111, the mean parameter estimate is still nearly 100 times higher than the next highest value of m (3.261 for AA5182 1.6 mm). In comparison, the Zerilli-Armstrong parameters for AA6111 are all in a range similar to the other alloys.

Table 5.1 – Johnson-Cook Constitutive Model Parameters

	A	B	n	C	m
AA5754 – 1.6 mm					
Estimate	67.456	471.242	0.4241	0.002979	2.5186
95% Lower	49.492	456.715	0.3712	0.001811	2.3812
95% Upper	85.420	485.769	0.4771	0.004148	2.6561
AA5754 – 1 mm					
Estimate	40.130	492.642	0.3611	0.004556	2.5272
95% Lower	21.085	483.566	0.3222	0.003626	2.4232
95% Upper	59.174	501.718	0.4000	0.005486	2.6311
AA5182 – 1.6 mm					
Estimate	106.737	569.120	0.4849	-0.001176	3.261
95% Lower	96.077	554.512	0.4504	-0.001912	3.088
95% Upper	117.398	583.728	0.5195	-0.0004405	3.433
AA5182 – 1 mm					
Estimate	107.565	557.266	0.4557	0.0006609	2.688
95% Lower	94.349	541.981	0.4169	-0.0001890	2.565
95% Upper	120.781	572.552	0.4946	0.001511	2.811
AA6111 – 1 mm					
Estimate	152.610	527.347	0.5167	0.002587	309.491
95% Lower	140.633	504.654	0.4672	0.001676	-
95% Upper	164.586	550.040	0.5662	0.003497	-

Table 5.2 – Zerilli-Armstrong Constitutive Model Parameters

	C_1	C_2	C_3	C_4	C_5
AA5754 – 1.6 mm					
Estimate	89.156	669.500	0.001003	0.00002299	0
95% Lower	86.065	645.683	0.0008963	0.00001724	-
95% Upper	92.247	693.318	0.001109	0.00002873	-
AA5754 – 1 mm					
Estimate	89.614	700.933	0.0009909	0.00003104	0
95% Lower	86.831	679.906	0.0009026	0.00002606	-
95% Upper	92.398	721.961	0.001079	0.00003601	-
AA5182 – 1.6 mm					
Estimate	109.123	685.480	0.0005250	0.000000732	0
95% Lower	106.858	669.113	0.0004588	0.000004082	-
95% Upper	111.389	701.846	0.0005911	-0.000002618	-
AA5182 – 1 mm					
Estimate	119.252	754.546	0.0008544	0.00001208	0
95% Lower	116.547	733.257	0.0007711	0.000007941	-
95% Upper	121.956	775.835	0.0009377	0.00001621	-
AA6111 – 1 mm					
Estimate	150.793	552.846	0.0002222	0.00001670	0
95% Lower	147.385	530.730	0.0001118	0.00001102	-
95% Upper	154.200	574.962	0.0003327	0.00002298	-

The values of the Johnson-Cook strain rate parameter for these alloys are also lower than those found by Johnson and Cook [61] for other aluminum alloys. For AA2024-T351 and AA7039, Johnson and Cook [61] found the strain rate parameter C to be 0.015 and 0.010, respectively. In comparison to steel alloys such as 4340 and S-7 tool steel, the strain rate parameters were found to be 0.014 and 0.012, respectively [61]. Kang *et al.* [16] found similar values for the steel sheet materials they tested. The strain rate parameter C_4 in the Zerilli-Armstrong fits for these alloys was also found to be low. In comparison, Zerilli and Armstrong found C_4 to be 0.000115 for copper, approximately an order of magnitude higher than the values listed in Table 5.2.

Using the parameter estimates listed in Tables 5.1 and 5.2, the flow stress was calculated at the strains and strain rates taken from experimental data for all the alloys tested. Model predictions using both constitutive models are compared with the experimental data for 23°C, at strain rates of 3.3×10^{-3} s^{-1} and 1500 s^{-1}, and for 300°C at a strain rate of 1500 s^{-1} in Figure 5.37 through Figure 5.41 for all the alloys investigated. In all cases, it can be seen that the model predictions follow the experimental data quite well, although, in Figure 5.37 and Figure 5.38, the predictions using the Zerilli-Armstrong fit appear to follow the data slightly closer than the Johnson-Cook fit for AA5754. The models follow the general decrease in the flow stress at 300°C, but are unable to capture the change in the strain hardening response precisely. In Figure 5.38, the hardening rate predicted by the models at approximately 15% strain is noticeably higher than that witnessed in the experimental data, and it is expected that the models will over predict the flow stress at strains above 15%. Furthermore, examining AA5754, it is seen in Figure 5.37 that the hardening response predicted for the 1.6 mm sheet at 1500 s^{-1} and 300°C, follows the experimental data closer than does the predicted response of the 1 mm sheet in Figure 5.38. AA5182 shows a similar trend, however it is not as pronounced as seen with AA5754. For AA6111, there was little difference between the Johnson-Cook and Zerilli-Armstrong model predictions. As seen in Figure 5.41, both models follow the experimental data closely and the difference between them is indiscernible.

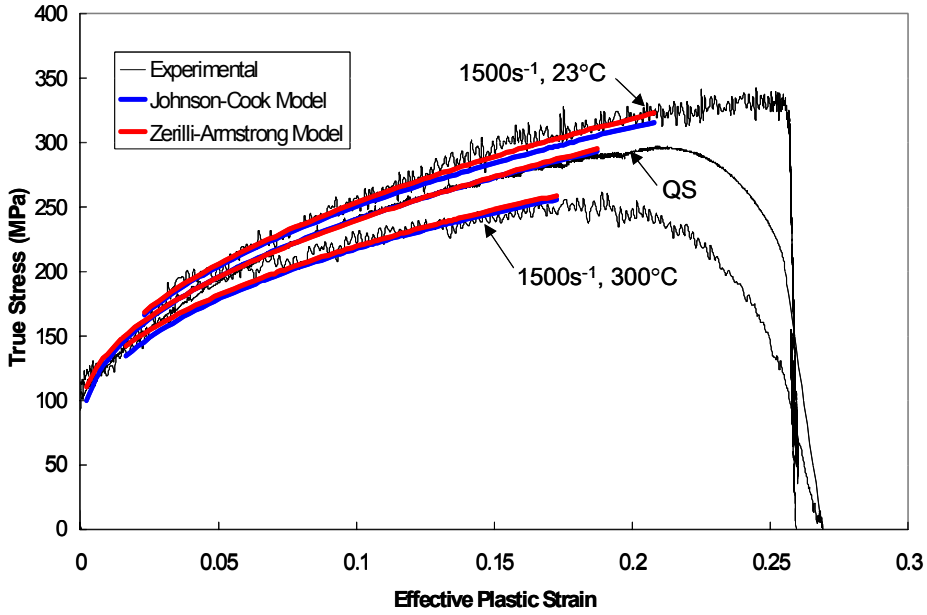

Figure 5.37 – Comparison of Johnson-Cook and Zerilli-Armstrong Model Predictions With Experimental Results for AA5754, 1.6 mm

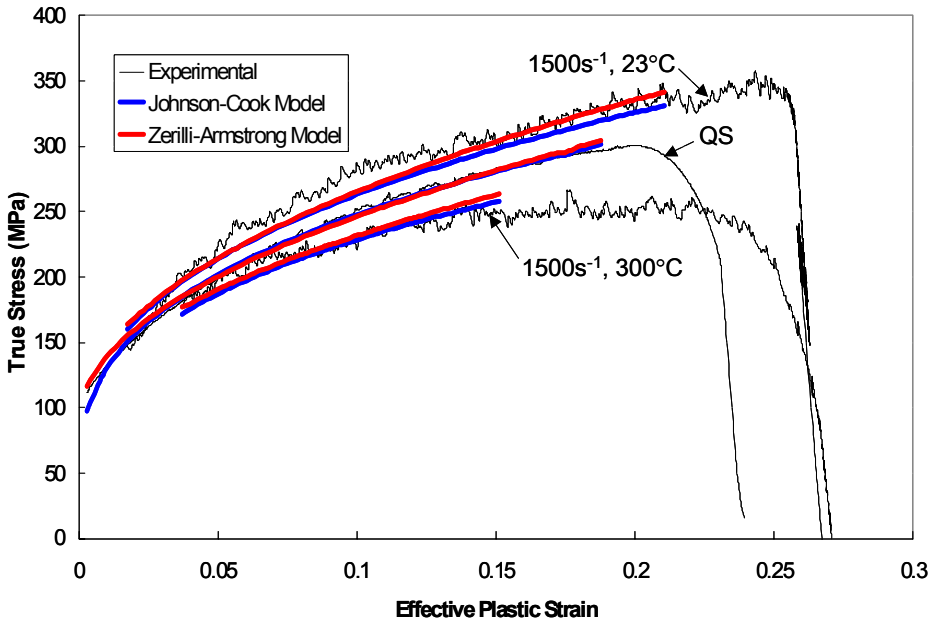

Figure 5.38 – Comparison of Johnson-Cook and Zerilli-Armstrong Model Predictions With Experimental Results for AA5754, 1 mm

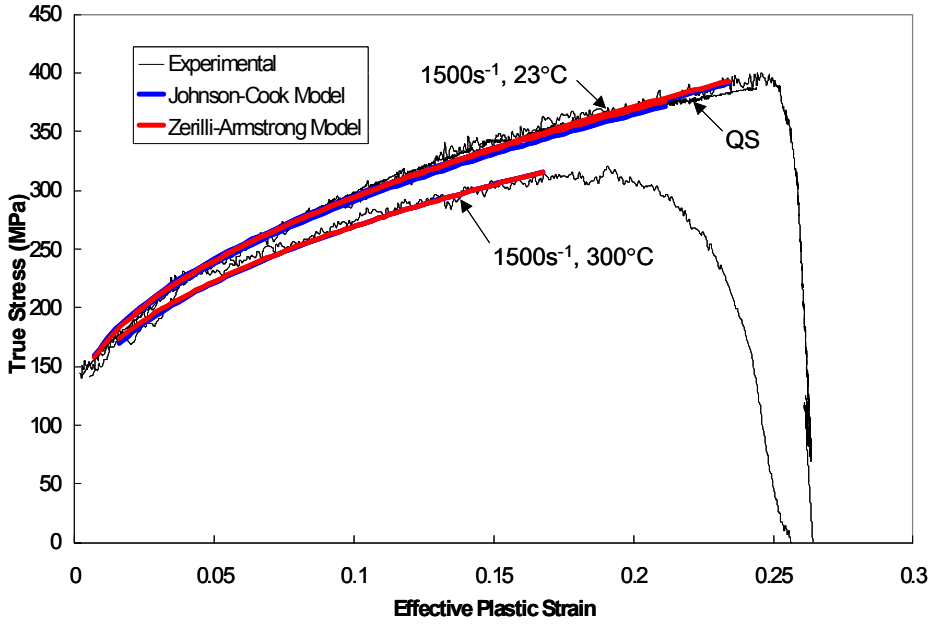

Figure 5.39 – Comparison of Johnson-Cook and Zerilli-Armstrong Model Predictions With Experimental Results for AA5182, 1.6 mm

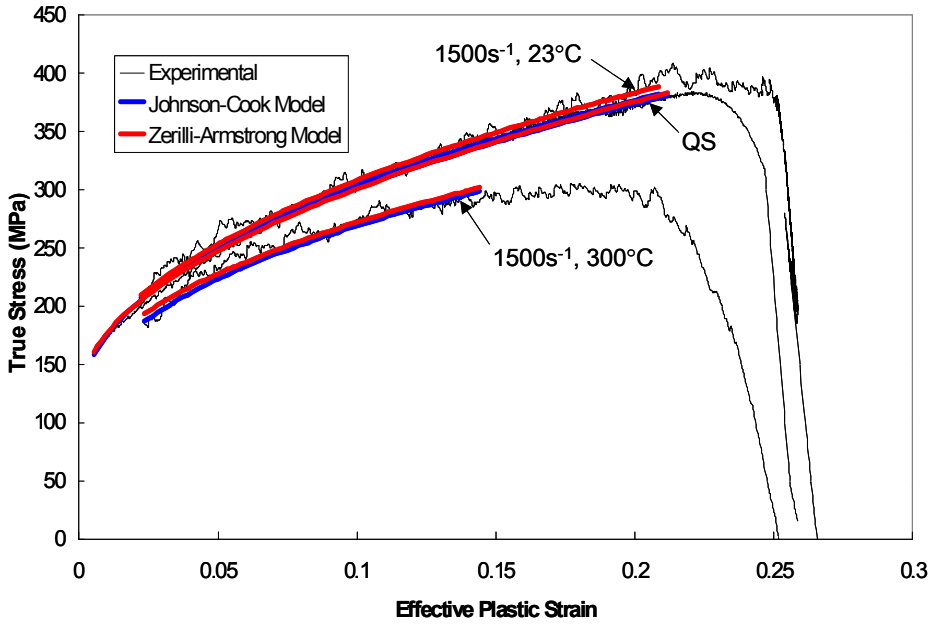

Figure 5.40 – Comparison of Johnson-Cook and Zerilli-Armstrong Model Predictions With Experimental Results for AA5182, 1 mm

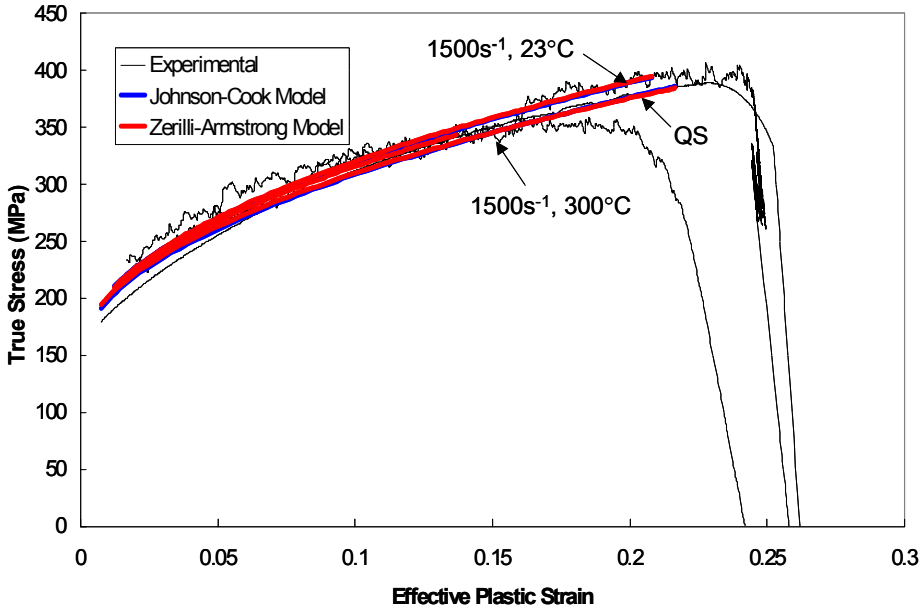

Figure 5.41 – Comparison of Johnson-Cook and Zerilli-Armstrong Model Predictions With Experimental Results for AA6111

6 NUMERICAL RESULTS

The purpose of the simulations was to evaluate the performance of the Johnson-Cook and Zerilli-Armstrong material models in simulating the experiments conducted in this work, and to investigate the source of the increases in elongation witnessed at high strain rates that was presented in Chapter 5. The model mesh, boundary conditions and loading adopted in the models follow that outlined in Chapter 3.

6.1 MATERIAL MODEL EVALUATION

In order to evaluate the parameters listed in Section 5.5 for the Johnson-Cook and Zerilli-Armstrong material models, numerical simulations of the quasi-static and dynamic tensile tests were performed. Strain rates of quasi-static, 600 s^{-1}, 1100 s^{-1} and 1500 s^{-1} were all used in the simulations to evaluate each material model's ability to capture the strain rate response witnessed in the experiments. In order to save computation time, the numerical simulation for the quasi-static strain rate was accelerated to 10 s^{-1}; from the as-tested condition of $3.3x10^{-3}$ s^{-1}. For this model, the reference strain rate used in the material model was scaled accordingly to represent quasi-static conditions. Simulations of the elevated temperature experiments were conducted at 150°C and 300°C, at a strain rate of 1500 s^{-1}, in order to verify the thermal softening treatment. The elevated temperature experiments conducted at 600 s^{-1} were not considered since the temperature effect was very small at this strain rate for the initial temperatures investigated. The velocity profiles applied in the numerical models were taken directly from the experiments for each strain rate. In order to calculate the nominal strain, the change in length of the gauge section was extracted from the simulations, while the stress was calculated using the net axial force measured at the restrained nodes in the stationary clamped region. The numerical predictions of the engineering stress-strain response are compared with experimental results in Figure 6.1 through Figure 6.10.

6.1.1 NUMERICAL PREDICTIONS OF CONSTITUTIVE RESPONSE

The constitutive response predicted by the numerical simulations for AA5754, are compared in Figure 6.1 through Figure 6.4. As seen in Figure 6.1, the Johnson-Cook model under predicts the flow stress at strain rates of 1100 s^{-1} and 1500 s^{-1} for the 1.6 mm thick AA5754. For the 1 mm thick AA5754 (Figure 6.3), the response at 1500 s^{-1} is predicted well by the Johnson-Cook model, however the flow stress at 1100 s^{-1} and the quasi-static response are under predicted. The numerical predictions using the Zerilli-Armstrong model captured the strain rate sensitivity of AA5754 more closely, as can be seen in Figure 6.2 and Figure 6.4.

The numerical predictions of the flow stress of AA5754 at a strain rate of 1500 s^{-1} and 300°C are found to be acceptable using the Johnson-Cook model, however, at 150°C, the flow stress is over predicted. The Zerilli-Armstrong model is found to be more accurate in capturing the thermal softening across the range of temperatures used in the experiments. The hardening rate predicted at 300°C and 15% strain using the Zerilli-Armstrong model is still greater than the experiments yielded, causing the flow stress to be over predicted at strains above 15%. This is particularly noticeable for 1 mm AA5754 shown in Figure 6.4, where the model prediction begins to diverge greatly from the experimental results due to the onset of necking in the experiments. The Johnson-Cook model does capture the hardening rate at strains above 15% at 300°C more closely, however the flow stress is under predicted at strains between 5% and 10%.

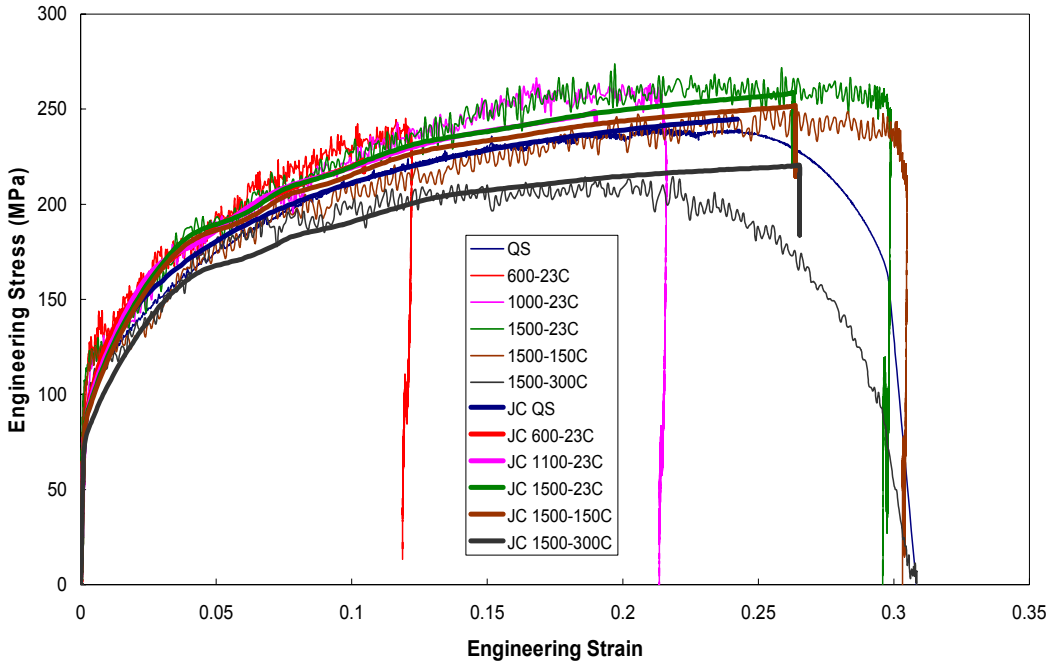

Figure 6.1 – Comparison of Numerical Results Using Johnson-Cook with Experimental Results for 1.6 mm AA5754

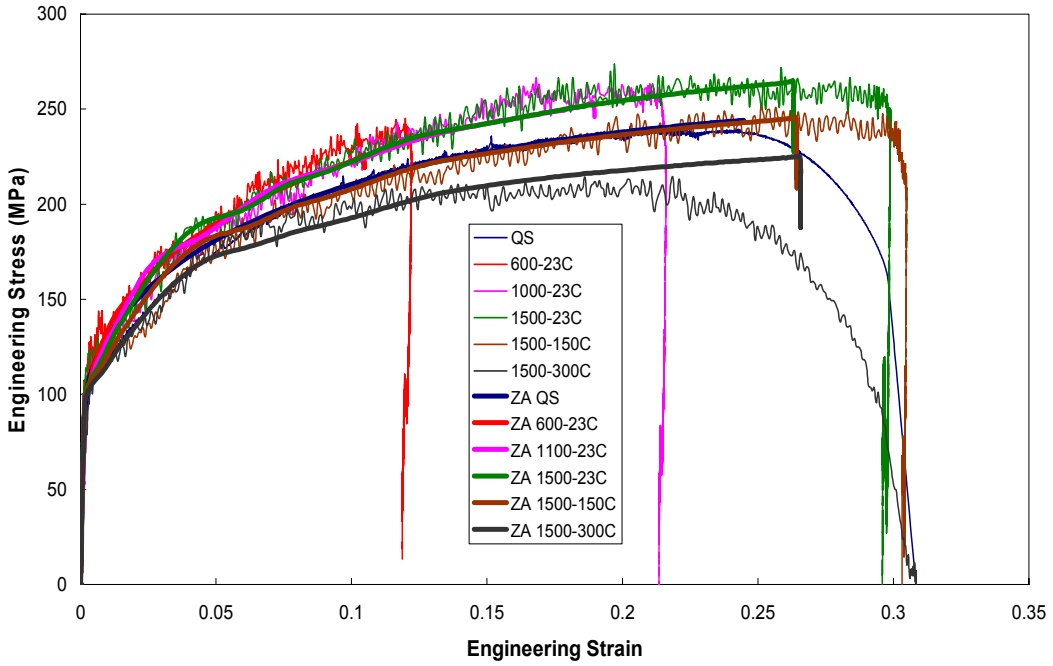

Figure 6.2 – Comparison of Numerical Results Using Zerilli-Armstrong with Experimental Results for 1.6 mm AA5754

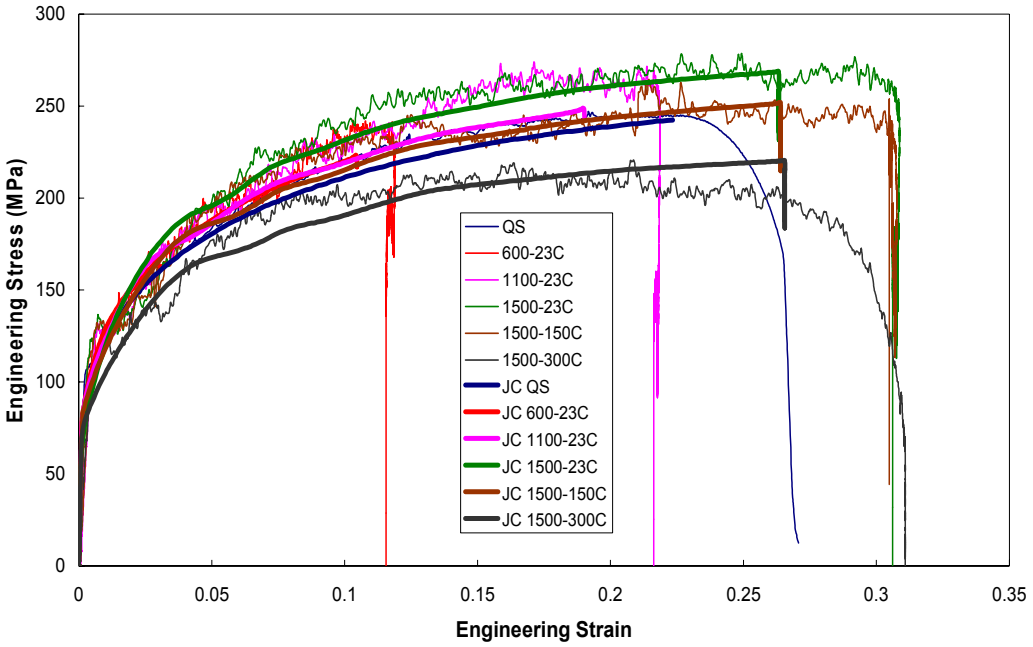

Figure 6.3 – Comparison of Numerical Results Using Johnson-Cook with Experimental Results for 1 mm AA5754

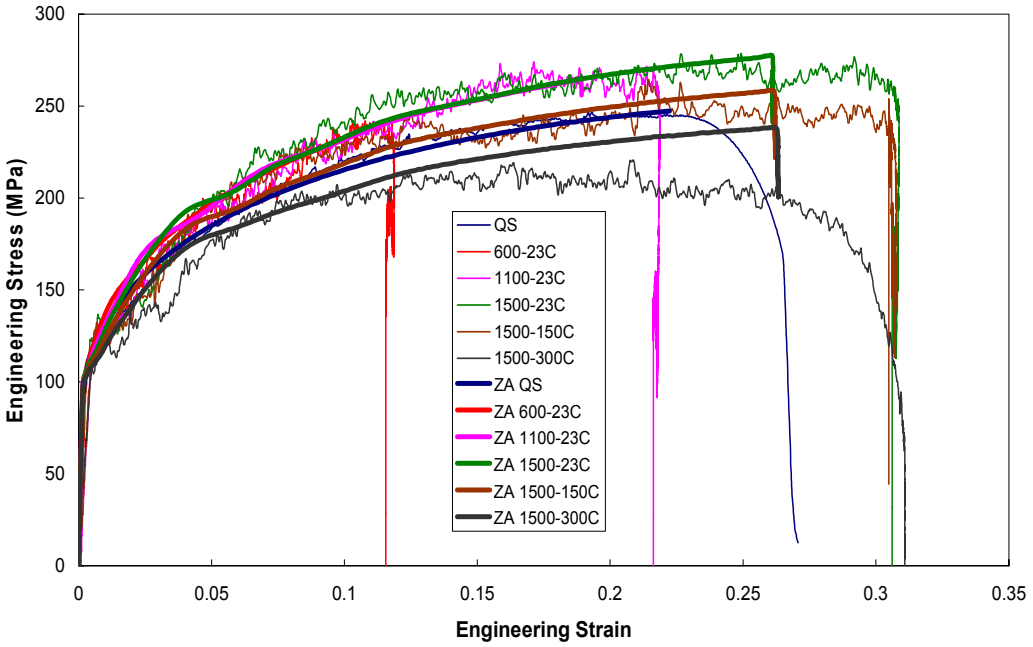

Figure 6.4 – Comparison of Numerical Results Using Zerilli-Armstrong With Experiment Results for 1 mm AA5754

Since the strain rate sensitivity of AA5182 was found to be very low, both the Johnson-Cook and Zerilli-Armstrong constitutive models closely predict the flow stress within the range of strain rates investigated. Also, as seen for AA5754, the Johnson-Cook model over predicts the flow stress at 150°C at a strain rate of 1500 s^{-1}. This is most apparent in the numerical predictions for 1 mm AA5182, where it is seen in Figure 6.7 and Figure 6.8, that the Zerilli-Armstrong model follows the experimental results at 150°C more closely than does the prediction using the Johnson-Cook model. However, the Johnson-Cook model is the slightly more accurate of the two in capturing the strain hardening response at 300°C at a strain rate of 1500 s^{-1}.

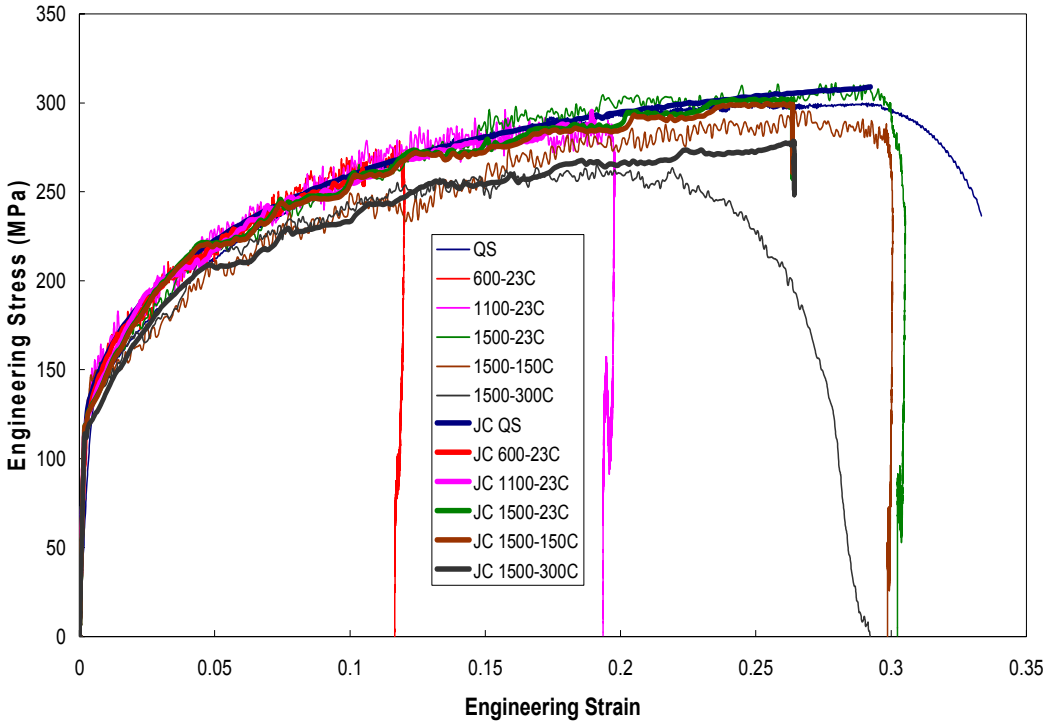

Figure 6.5 – Comparison of Numerical Results Using Johnson-Cook with Experimental Results for 1.6 mm AA5182

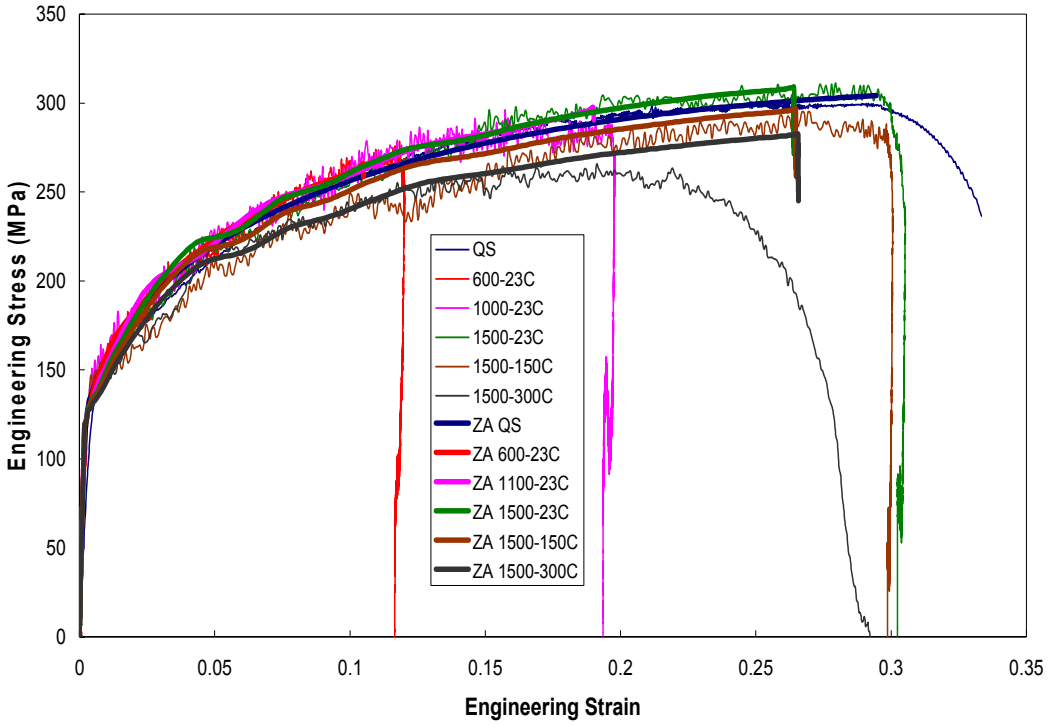

Figure 6.6 – Comparison of Numerical Results Using Zerilli-Armstrong With Experimental Results for 1.6 mm AA5182

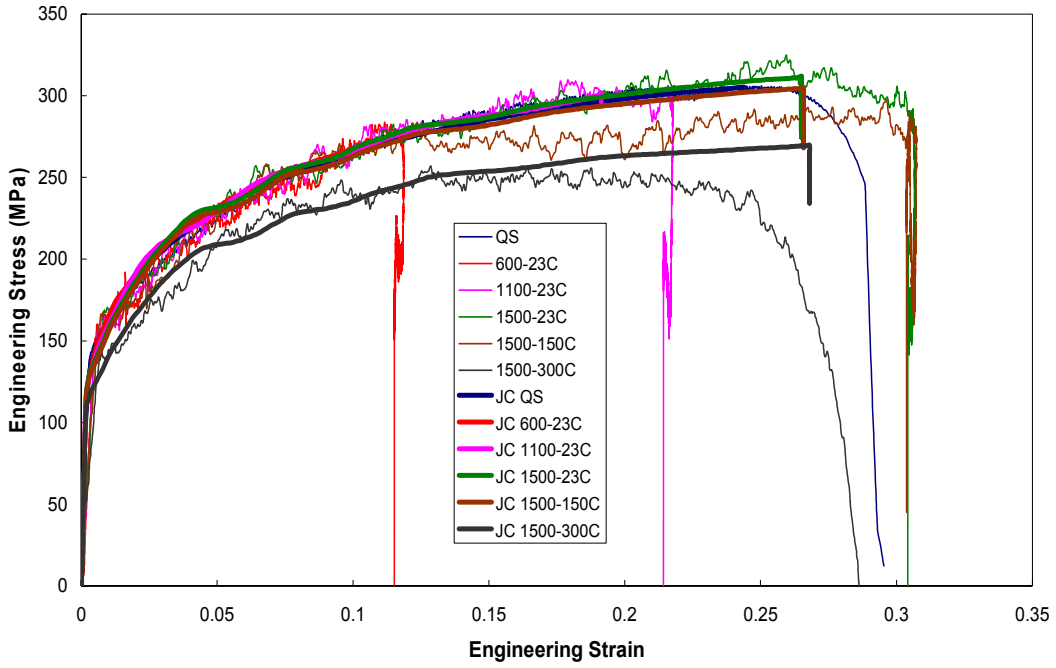

Figure 6.7 – Comparison of Numerical Results Using Johnson-Cook With Experimental Results for 1 mm AA5182

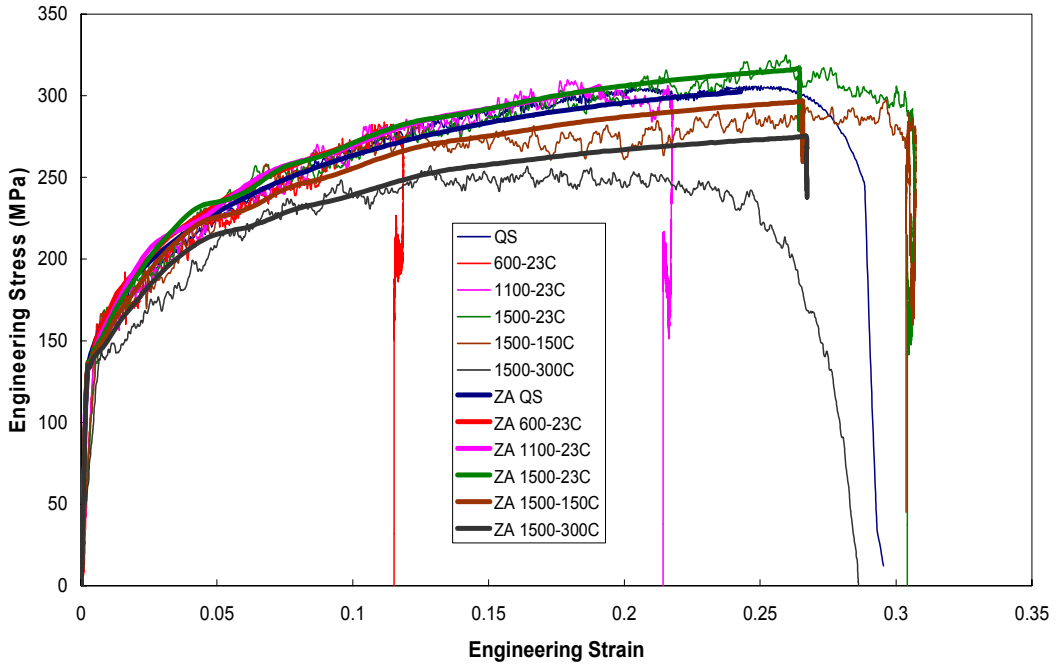

Figure 6.8 – Comparison of Numerical Results Using Zerilli-Armstrong With Experimental Results for 1 mm AA5182

In the numerical simulations performed for AA6111, similar differences between the predictions using both constitutive models are seen as those discussed for the other two alloys. Furthermore, the Johnson-Cook model is unable to capture the thermal softening at 300°C at 1500 s^{-1}. In fact, no thermal softening effects are captured, as seen in Figure 6.9, due to the high thermal softening parameter *m* that was determined from the non-linear regression.

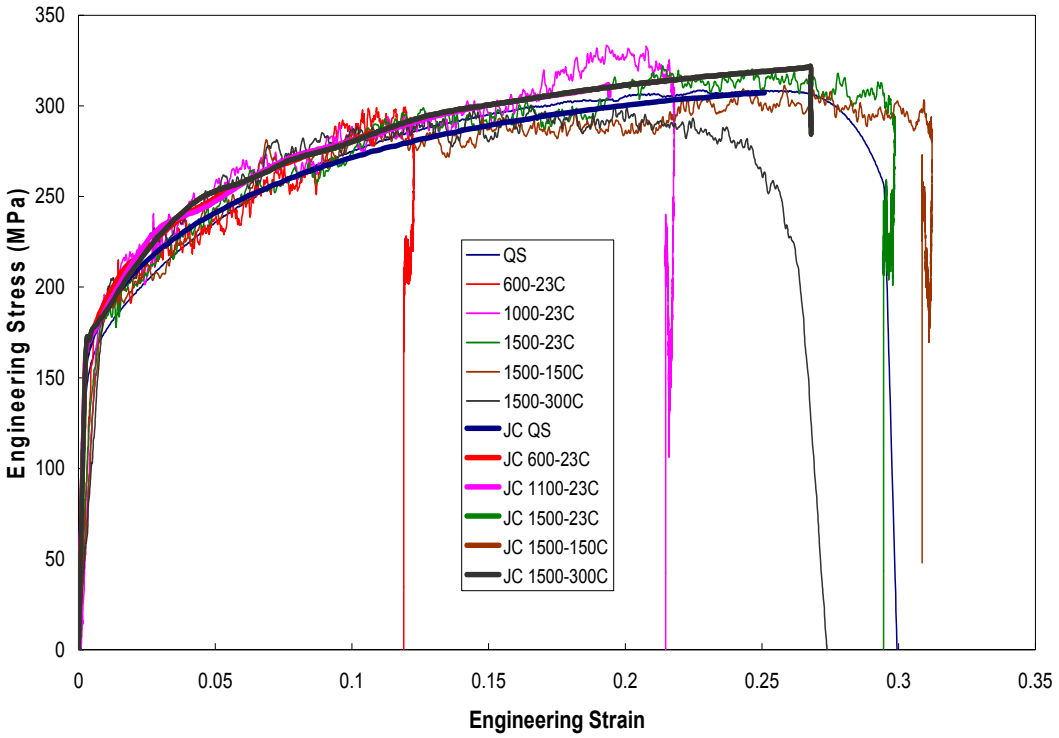

Figure 6.9 – Comparison of Numerical Results Using Johnson-Cook With Experimental Results for AA6111

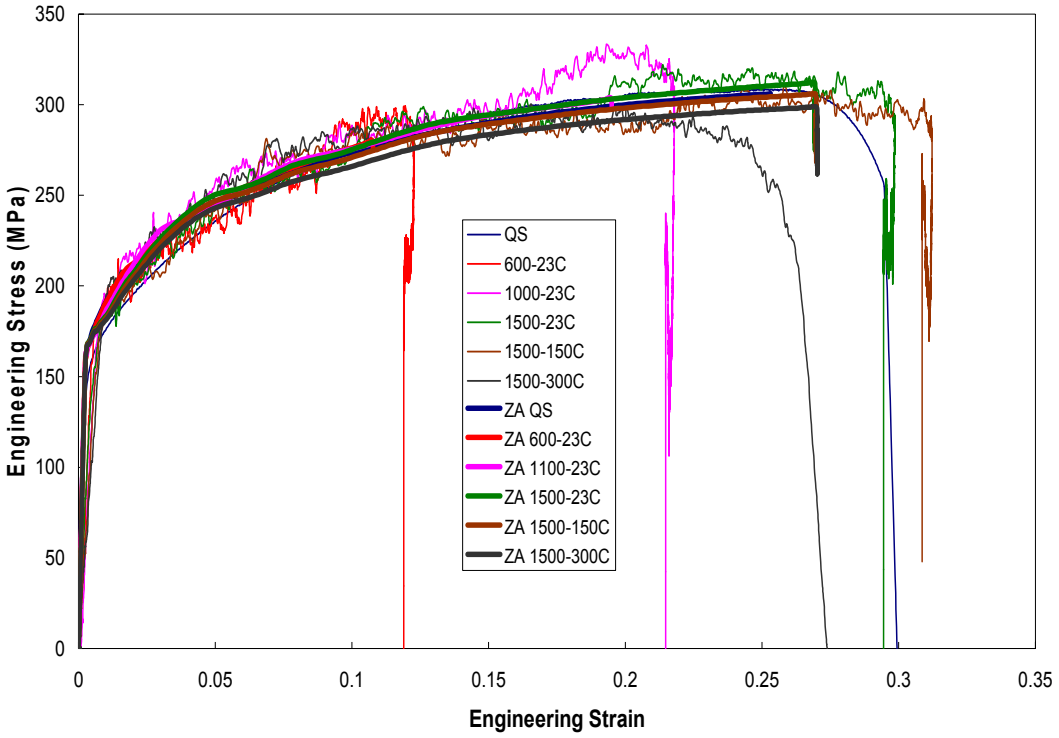

Figure 6.10 – Comparison of Numerical Results Using Zerilli-Armstrong With Experimental Results for AA6111

Overall, the Zerilli-Armstrong constitutive model provides a closer prediction of the experimental results than does the Johnson-Cook model. This can be expected based upon the better fit to the experimental results presented in Chapter 5. The data collected from the dynamic and elevated temperature experiments showed that the hardening response of these particular materials changed with strain rate and temperature, while the yield stress remained near constant. Hence, it can be expected that the Zerilli-Armstrong model for FCC materials would predict the constitutive response of these materials more accurately than the Johnson-Cook model.

6.1.2 Numerical Predictions of Necking

One important result from the experiments conducted on these sheet alloys, was that their elongation to failure increased with increasing strain rate. This trend was found to be true for

all of the alloys tested. Several numerical models were created with extended loading durations in order to assess the ability of the simulations to accurately predict necking at various strain rates. These simulations were conducted under quasi-static conditions and at a strain rate of 1500 s^{-1}, at ambient temperature. The materials used were 1 mm AA5754, since it showed the highest degree of strain rate sensitivity in the range considered, and 1.6 mm AA5182, because it showed the lowest. Choosing these two materials gave insight into the effects of strain rate sensitivity on changes in elongation. The constitutive fits for both the Zerilli-Armstrong and Johnson-Cook models were considered for each material.

Figure 6.11 shows the predicted engineering stress-strain response using the constitutive fits and model for 1 mm AA5754. The models greatly over-predict the total elongation, compared to the values presented in Section 5.2.1. This over-prediction could be due to insufficient mesh refinement or the need to introduce a material damage model, for example the Gurson-Tvergaard-Needleman model. Nonetheless, the numerical simulations did predict an increase in the strain at which necking occurred, as the strain rate increased from quasi-static conditions to 1500 s^{-1}. Using the Zerilli-Armstrong model, the strain at which localization occurred increased by approximately 16.7% strain when the strain rate increased from quasi-static to 1500 s^{-1}, compared to an increase of approximately 18.2% strain witnessed in the experiments. The numerical simulation conducted using the Johnson-Cook model only showed an increase of approximately 5.7% strain until necking for the same increase in strain rate.

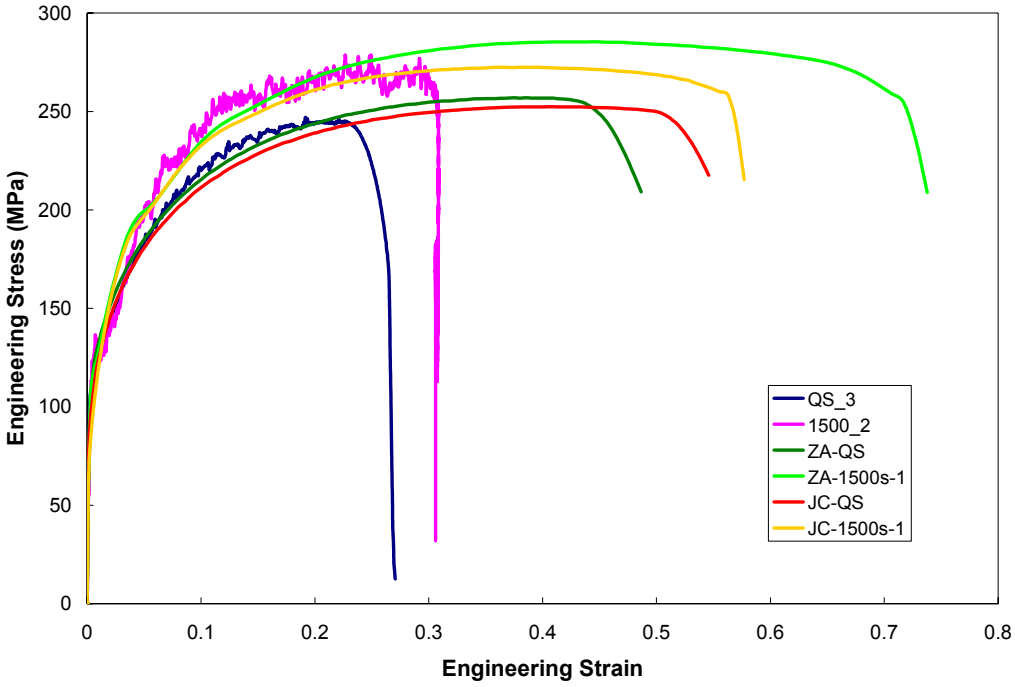

Figure 6.11 – Engineering Stress-Strain Response of 1 mm AA5757 Comparing the Numerical Predictions of Elongation With Experimental Data Under Quasi-Static Conditions and at 1500 s^{-1}

An interesting feature captured by the numerical simulation for 1 mm AA5754, is the formation of a double neck at a strain rate of 1500 s^{-1}. The contour plots in Figure 6.12 show the formation of an initial neck near the moving end of the specimen, followed by a second neck near the fixed end of the specimen. Both necks grow, however the initial neck formed near the moving end dominates and continues to localize while the second neck stabilizes. A similar feature was found in several 1 mm AA5754 specimens tested at this strain rate.

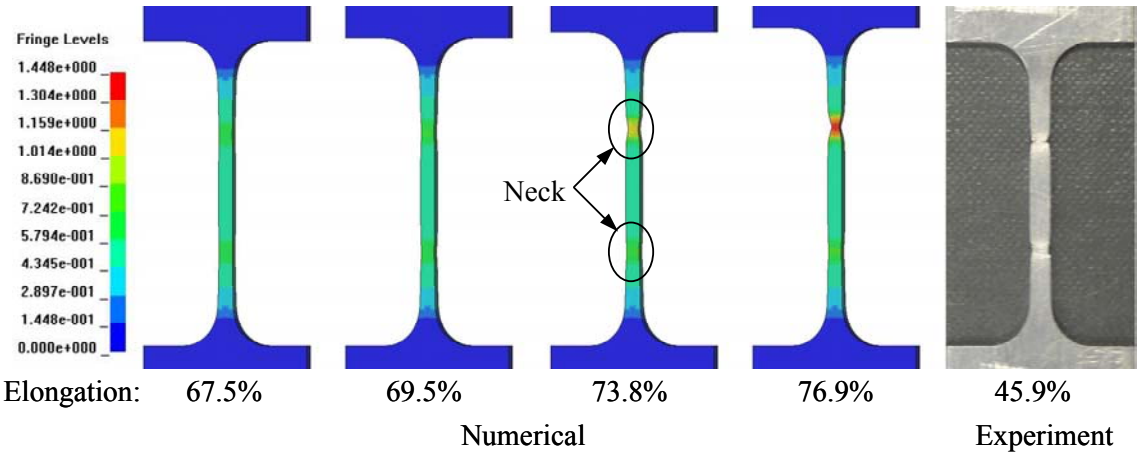

Figure 6.12 – Contour Plots of Effective Plastic Strain at Various Elongations Showing the Development of a Double Neck in 1 mm AA5754

For the numerical simulations of 1.6 mm AA5182 the total elongation greatly exceeded that seen in the experiments, as seen in Figure 6.13. An increase in elongation with strain rate was only predicted using the Zerilli-Armstrong constitutive fit and as for AA5754, the magnitude of the increase showed a good agreement with the increase in the experiments. The increase in elongation to the onset of necking was predicted to be 8.6% strain in comparison to 7.9% strain seen in the experiments. Increases in elongation were not predicted by the Johnson-Cook fits due to the negative strain rate sensitivity parameter. A subsequent simulation was run using the Johnson-Cook model, where the strain rate hardening term was suppressed. The increase in elongation was only predicted to be 1.5% strain. Furthermore, the Johnson-Cook model (equation (1.21)) does not incorporate an increase in strain hardening rate, as is the case for the FCC version of the Zerilli-Armstrong model (equation (5.2)).

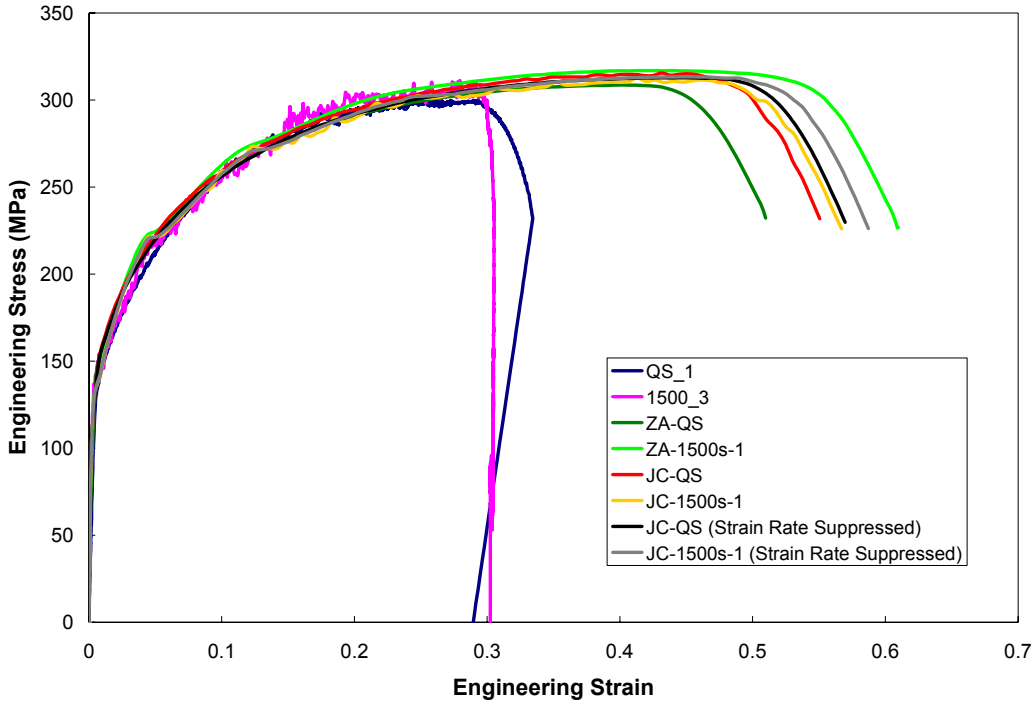

Figure 6.13 – Engineering Stress-Strain Response of 1.6 mm AA5182 Comparing the Numerical Predictions of Elongation With Experimental Data Under Quasi-Static Conditions and at 1500 s^{-1}

From these simulations, it is seen that increases in elongation were only captured for constitutive fits whose strain rate sensitivity was positive, hence implying that the increases in elongation are due to the constitutive response of the material. However, since AA5182 showed no visible strain rate sensitivity, other mechanisms such as inertia may be acting to increase the elongation at high strain rate.

6.2 CONSTITUTIVE AND INERTIAL EFFECTS ON ELONGATION

The dynamic tensile experiments conducted as part of this work, showed that the elongation to failure of AA5754, AA5182 and AA6111 increased with increasing strain rate. The exact mechanisms responsible for this behavior are still unknown at the present time, but several possibilities include inertial effects as well as constitutive response.

El-Magd *et al.* [53,54,55] postulated that the increase in elongation witnessed at high strain rates is due to strain rate hardening occurring within the neck region, which would stabilize the necked region, diffusing deformation to other regions of the specimen. Using the numerical simulations, the strain rate predicted in the neck region, once localization occurred, was compared to the nominal strain rate experienced by the entire gauge length. Necking occurred within a region that was approximately 0.89 mm in length initially and can be seen in Figure 6.14 at various stages of deformation.

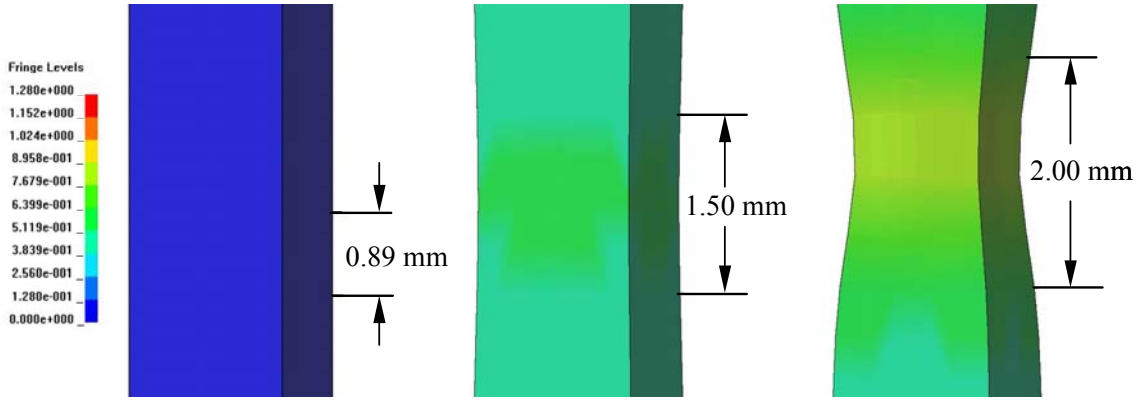

Figure 6.14 – Contour Plots of Effective Plastic Strain Showing Neck Region Predicted in Numerical Simulations

When necking began, this region was approximately 1.38 mm (1.5 mm shown) in length. The velocity at one end of this region reduces to zero, while the other end is accelerated to the velocity of the moving end of the specimen. The strain rate in this region was calculated by taking the relative velocity of the nodes defining this region, and dividing it by the current distance between them. Comparing the strain rate of the necked region with the nominal strain rate of the simulation, as given in Figure 6.15, it can be seen that the strain rate of the neck region is approximately 66 s^{-1} for a nominal simulation strain rate of 10 s^{-1} (near quasi-static conditions), while at a nominal simulation rate of 1500 s^{-1}, the neck region experiences a strain rate of approximately 9970 s^{-1}. This is a dramatic increase in strain rate and is beyond the range of strain rates which constitutive data was collected for in the Hopkinson bar experiments. Many aluminum alloys, along with other materials, have shown a logarithmic dependence of flow stress on strain rate. It is possible that AA5754, AA5182 and AA6111

may exhibit stronger strain rate sensitivity at strain rates in the range of 10000 s^{-1}, thus giving rise to the need for constitutive data at these rates.

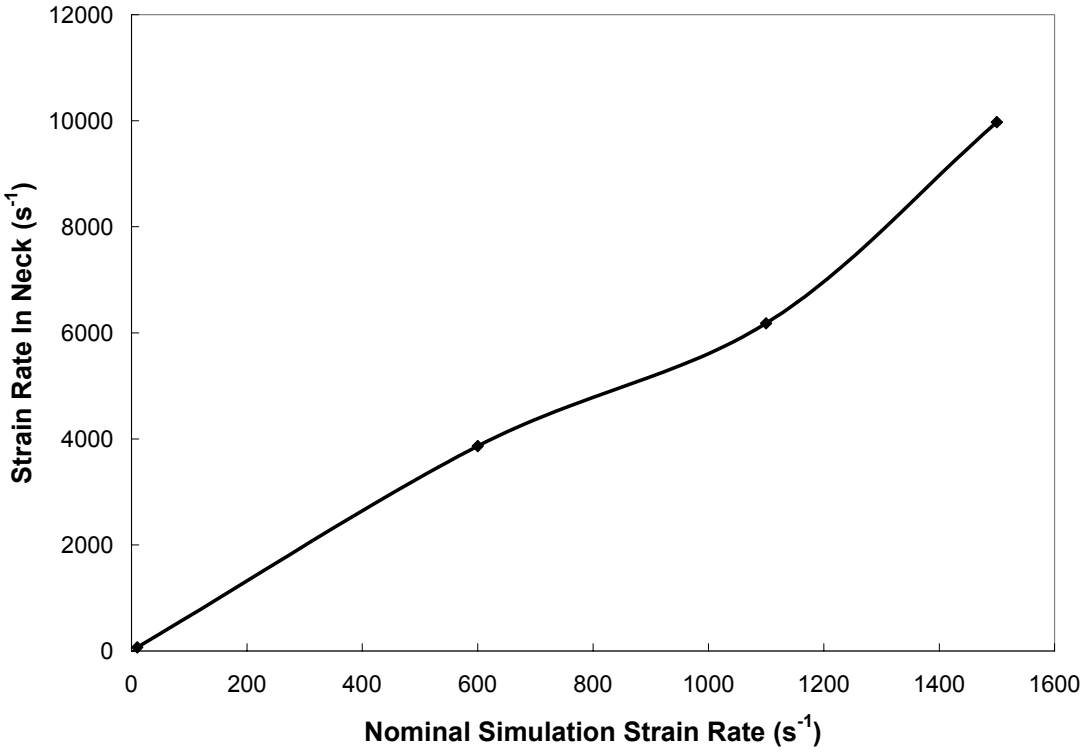

Figure 6.15 – Peak Nominal Strain Rate within Neck Region as Function of the Nominal Strain Rate of the Numerical Simulation

After the onset of necking, the velocity profile along the gauge length is changed from linear, to one that may resemble a step function [41,43,46,47]. This change occurs over a short period of time. High, non-uniform material accelerations rates are generated during this change, resulting in inertial forces that unload the region where localization is occurring. Using the numerical simulations, the acceleration of the region where necking occurs was compared at rates of 10 s^{-1} (near quasi-static conditions) and 1500 s^{-1}. The acceleration was taken as the time derivative of the relative velocity between the nodes defining the neck region in Figure 6.14. Figure 6.16 shows that this region accelerates at 22.17 m/s^2 during localization at 10 s^{-1} (near quasi-static), compared to 776,760 m/s^2 at 1500 s^{-1}. Using equation (3.18) along with values for $\dot{\varepsilon}$, $\ddot{\varepsilon}$, and neck dimensions extracted from the simulation, the inertial stress measured by the output bar is only 1.6 MPa for a simulation conducted at a nominal strain rate

of 1500 s^{-1}. This value is low in comparison to the flow stress of the material. Nonetheless, the increase in acceleration experienced by the material undergoing necking is four orders of magnitude when the strain rate increases from 10 s^{-1} to 1500 s^{-1}, and inertial forces can become significant.

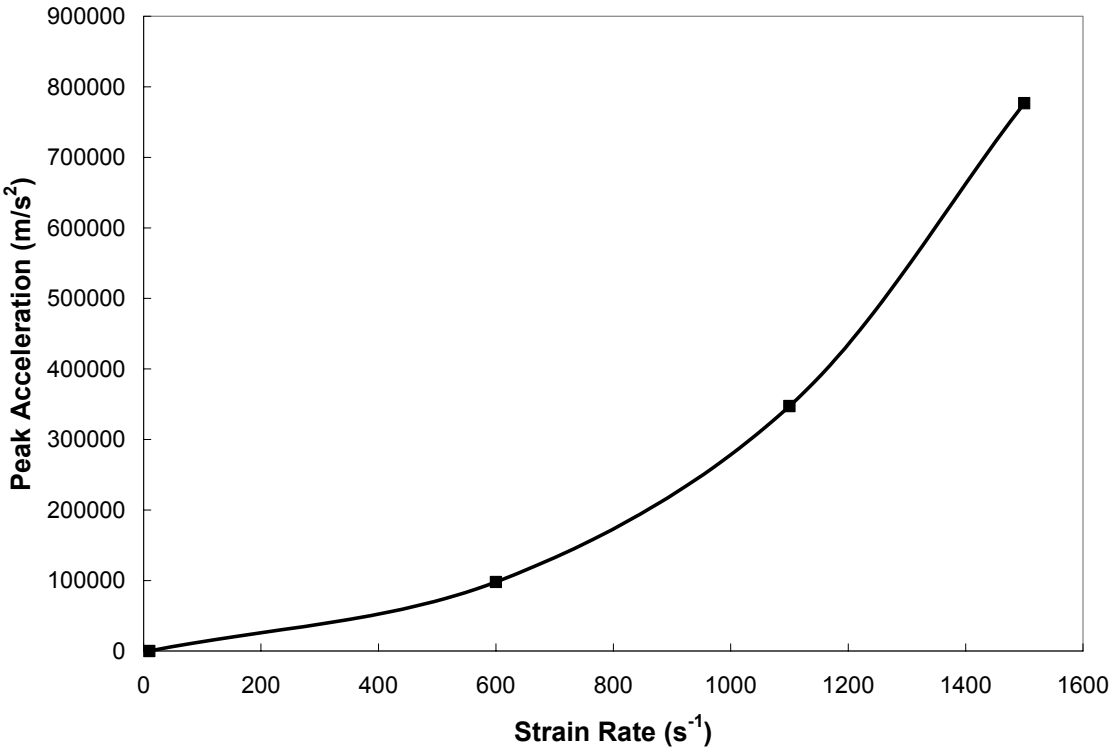

Figure 6.16 - Axial Acceleration Rate of Neck Region as Function of the Nominal Strain Rate of the Numerical Simulation

7 DISCUSSION

The investigation carried out on the TSHB apparatus showed that threads in the input and output bars distort the incident wave as it reaches the specimen. A novel method of gripping a tensile specimen in a TSHB apparatus utilizing a wire-EDM cut slot for a single specimen was developed. The low mechanical impedance introduced by this grip minimized wave distortion, and provided enough clamping force to prevent the specimen from slipping during the experiment.

The nature of high rate testing using a TSHB apparatus imposes limits on the size of the specimen. A short gauge length is desired in order to reduce the specimen ring-up time. However, the wavelength of the neck seen in a short specimen has been found to be similar to that in a much longer ASTM specimen. Although through numerical simulations it has been shown that a uni-axial stress state is present in the short specimen until localization occurs, the post-uniform deformation scales the apparent strain to failure.

The dynamic experiments performed on AA5754, AA5182, and AA6111, showed that the flow stress of these alloys has a very low sensitivity to strain rate in the range of rates considered. This is similar to the results shown by Mukai *et al.* [57] for Al-3%Mg. Of the three alloys, AA5754 showed the highest sensitivity. The results showed that the yield stress did not increase noticeably with strain rate, but the strain hardening rate did, which is consistent with the FCC Zerilli-Armstrong constitutive model [35,64,65,66].

The thermal softening of these alloys at a strain rate of 1500 s^{-1} was found to be very low at initial temperatures ranging from ambient to 150°C. At 300°C, a significant decrease in the flow stress was witnessed in AA5754 and AA5182. The hardening rate of these two alloys decreased, resulting in a lower maximum flow stress. AA6111 on the other hand, showed little change in flow stress at 300°C.

Although the strength of these alloys was not very rate sensitive in the range of strain rates considered, the elongation to failure showed significant sensitivity to strain rate as well as temperature. The elongation of AA5754, AA5182 and AA6111 increased dramatically with strain rate. This is similar to results found by Higashi *et al.* [58,59], who showed that the elongation of AA5182 increases from approximately 30% at a strain rate of $1x10^{-3}$ s^{-1}, to over 40% at strain rates above $2x10^{3}$ s^{-1}. In the current work, the elongation of AA5182 at a rate of 1500 s^{-1} was measured to be approximately 37.5% and 42.5% for 1.6 mm and 1 mm AA5182, respectively. This increase can have an impact on the crash performance of these alloys, since it would imply that the energy absorption of these materials prior to failure will increase at high strain rates.

Analysis of the stress-strain data, using Considere's criterion, showed that the strain at which necking is predicted to occur increases with strain rate. This prediction implies that the increased hardening rate under high rate conditions may be increasing the ductility of the material by delaying the onset of necking. Thickness strain measurements taken from optical micrographs appear to confirm that the onset of necking is delayed. Thickness strains measured for 1.6 mm AA5754 and AA5182 were shown to increase over the entire length of the gauge section at high rates of strain, thus implying that more deformation is occurring under high rate conditions prior to localization.

Damage measurements conducted on 1.6 mm AA5754 and AA5182 showed a dramatic increase in porosity with increasing strain rate due to the higher strains, as well as more severe necking and associated elevated hydrostatic stress. In general, the damage in AA5182 was found to be higher than in AA5754 at all rates due to the higher particle fraction and initial porosity. The second phase particles in AA5182 are also larger in size which leads to higher damage nucleation rates. Although deformation under high rates appears to increase ductility overall, the higher damage accumulation rate of AA5182, compared to AA5754, may be instrumental in limiting the elongation that can be achieved at high rates. This behavior suggests that damage may be important in limiting total elongation at high rates of strain. Under quasi-static conditions, the elongation of AA5182 was greater than AA5754. Under high rate conditions (1500 s^{-1}), this ranking reverses, and AA5754 was found to be the most

ductile alloy of those investigated. This reversal is consistent with the experiments done by Mukai *et al.* [57], who found that the effect of strain rate on elongation decreased with increasing magnesium content.

Numerical modeling was used to gain some further insight into the mechanisms behind the increase in elongation with strain rate that were witnessed. Increases in elongation were predicted for AA5754 and AA5182 using the Zerilli-Armstong fits, whereas an increase in elongation using the Johnson-Cook fits was only predicted for the more rate sensitive AA5754. The modeling provided support for some possible reasons for these changes in elongation. At a nominal strain rate of 1500 s^{-1}, the simulations showed that once the deformation localized, the strain rate in the neck region increased by almost an order of magnitude. The ability of the simulations to capture the increase in elongation using the Zerilli-Armstrong fits, implies that rate sensitivity aids ductility, since the strain rate sensitivity parameter in these fits was positive for both alloys. These alloys may show a further increase in rate sensitivity at approximately 10,000 s^{-1}, which could stabilize deformation as seen in the simulations for AA5754. The numerical simulations also showed that high material acceleration rates occur during localization, and the accompanying inertial forces may also increase ductility.

The constitutive fits for both the Johnson-Cook and the Zerilli-Armstrong constitutive models provide good predictions of the flow stress at strain rates between quasi-static and 1500 s^{-1} for all of the alloys. However, the flow stress within this range of strain rates was captured more accurately using the Zerilli-Armstrong model for FCC materials. This was expected, since the experimental results showed that the strain hardening rate of these materials increased with strain rate, while the yield stress remained near constant. The Zerilli-Armstrong model was also more accurate in capturing the thermal softening at 50°C and 150°C for all materials tested.

Numerical simulations using both models did fail to accurately predict the failure strain, and it was shown that the material models do not soften at a fast enough rate to capture necking at the correct strain. By fitting the model parameters to data captured up to failure, this may be improved. The inclusion of a damage model to soften the material as porosity increases, would

also provide a means of predicting the failure of these alloys more accurately. Mesh refinement could also aid in improving these predictions.

The experimental and numerical investigations carried out in this work provided useful insight into the performance of these alloys at loading rates similar to those witnessed in automotive crash scenarios. The experimental results follow similar trends to those shown by several authors. Mukai *et al.* [57] showed that the rate sensitivity of the flow stress is low for Al-Mg alloys, which is similar to the results found for AA5754 and AA5182 in this project. Shi and Meuleman [60] found that the flow stress of AA6111-T4 was strain rate insensitive between $1x10^{-7}$ and $1x10^{2}$ s^{-1}. This alloy was shown to continue to be insensitive to strain rate at rates up to 1500 s^{-1} in the current work.

In order to build upon the results presented here, stress-strain data up to failure at high strain rates is required for these alloys. The striker length limits the maximum loading duration obtained in the current apparatus. In order to fail the specimens on the first pulse, the loading duration would need to be significantly increased. A preliminary study has shown that the loading duration can be increased by more than two times by using an acrylic striker. This may provide an adequate loading duration to promote failure of these materials in a single pulse at these strain rates.

8 CONCLUSIONS AND FUTURE WORK

8.1 CONCLUSIONS

From this body of work, several conclusions can be drawn:

- The strain hardening rate of AA5754 is mildly sensitive to strain rate in the range of strain rates considered, while AA5182 and AA6111 are relatively insensitive.
- The thermal softening of AA5754, AA5182, and AA6111 was found to be low at initial temperatures between ambient and 150°C at a strain rate of 1500 s^{-1}. At 300°C and a strain rate of 1500 s^{-1}, AA5754 and AA5182 showed a decrease in the strain hardening rate, reducing the maximum flow stress as a result, while the flow stress of AA6111 showed little change.
- The ductility of AA5754, AA5182 and AA6111 was found to increase with strain rate in the range of strain rates considered by the following amounts:

  AA5754, 1.6 mm: 12.9% strain

  AA5754, 1 mm: 18.2% strain

  AA5182, 1.6 mm: 7.9% strain

  AA5182, 1 mm: 12.4% strain

  AA6111, 1 mm: 9.9% strain
- At a strain rate of 1500 s^{-1}, the ductility of AA5754, AA5182 and AA6111 was shown to decrease at a temperature of 300°C to elongations similar to those witnessed under ambient temperature, quasi-static conditions.
- Porosity in AA5754 and AA5182 has been shown to increase at high strain rates to approximately 3.9% and 3.1% void area percent, respectively.
- The Zerilli-Armstrong constitutive model was found to be more accurate in predicting the flow stress of AA5754, AA5182 and AA6111 within the range of strain rates and temperatures considered.
- The numerical simulations over-predicted the strain at which necking occurred.

8.2 FUTURE WORK

The work presented in the thesis has provided some insight into the behavior of AA5754, AA5182 and AA6111 at strain rates similar to those witnessed in automotive crash scenarios. In order to build upon the results presented here and gain a better understanding of the mechanical behavior of these alloys at high strain rates, the following work should be pursued in the future:

- Development of a long duration TSHB apparatus in order to fail the specimen in the first loading pulse
- Re-fit the Johnson-Cook and Zerilli-Armstrong strength models to high strain rate constitutive data obtained up to failure
- Performing dynamic tensile experiments at strain rates intermediate to those in the current study. Strain rates between 30 s^{-1} and 120 s^{-1} can be achieved using a drop tower. Electromagnetic forming experiments can also be conducted at strain rates exceeding those in the current study on the order of 10000 s^{-1} in order to gain an understanding of the behavior of these materials in those regimes
- Performing dynamic tensile experiments using notched samples to gain insight into the behavior of these materials under tri-axial stress states
- Including damage in the constitutive models in order to predict failure strains more accurately

REFERENCES

1 Miller, W.S.; Zhuang, L.; Bottema, J.; Wittebrood, A.J.; De Smet, P.; Haszler, A.; Vieregge A. *Recent Development in Aluminium Alloys for the Automotive Industry.* Journal of Material Science and Engineering A: Structural Materials: Properties, Microstructure and Processing, Vol. 280, No. 1, 2000, pp. 37-49.

2 Wilson, D.V. *Aluminium Versus Steel in the Family Car – The Formability Factor.* Journal of Mechanical Working Technology, Vol. 16, No. 3, 1988, pp. 257-277.

3 Oliveira, D.A. *Electromagnetic Forming of Aluminum Alloy Sheet: Experiment and Model*. Master of Applied Science Thesis, University of Waterloo, 2002.

4 Imbert, J.; Winkler, S.L.; Worswick, M.J.; Golovashchenko, S. *Formability and Damage in Electromagnetically Formed AA5754 and AA6111*. Proceedings of the First International Conference on High Speed Forming Dortmund (Germany) 2004. pp. 202-210.

5 Hopkinson, B. *A Method of Measuring the Pressure Produced in the Detonation of High Explosives or by the Impact of Bullets.* Proceedings of the Royal Society of London Series A, Vol. 213, 1914, pp. 437-456.

6 Kolsky, H. *An Investigation of the Mechanical Properties of Materials at Very High Rates of Loading.* Proceedings of the Physical Society of Great Britain Series B, Vol. 62, 1949, pp. 676-700.

7 Follansbee, P.S. *The Hopkinson Bar.* Metals Handbook, ASM, Vol. 8, 1978, pp.198-203.

8 Gray, G.T. (Rusty) III, *Classic Split-Hopkinson Pressure Bar Testing.* In: Kuhn H., Medlin D., editors. ASM Handbook: Mechanical Testing and Evaluation, Vol. 8. Materials Park, OH: ASM International; 2000. p. 462-476.

9 Lindholm, U.S.; Yeakley, L.M. *High Strain-Rate Testing: Tension and Compression*. Experimental Mechanics, Vol. 8, No. 1, 1968, pp. 1-9.

10 Lindholm, U.S.; Bessey, R.L.; Smith, G.V. *Effect of Strain Rate on Yield Strength, Tensile Strength, and Elongation of Three Aluminum Alloys.* Journal of Materials, Vol. 6, No. 1, 1971, pp. 119-133.

11 Nicholas, T. *Tensile Testing of Materials at High Rates of Strain.* Experimental Mechanics, Vol. 21, 1981, pp. 177-185.

12 Nicholas, T. *Material Behavior at High Strain Rates*, Ch. 8 in: Impact Dynamics, Zukas, J.A. (Ed.), John Wiley & Sons, Inc., New York, 1982.

13 Nguyen, C.H.; Schindler, H.J. *On Spurious Reflection Waves in Hopkinson Bar Tensile Tests Using a Collar.* Journal de Physique IV France, Vol. 7, No. 3, 1997, pp. 85-90.

14 LeBlanc, M.M.; Lassila, D.H. *Dynamic Tensile Testing of Sheet Material Using the Split-Hopkinson Bar Technique*. Experimental Techniques, Vol. 17, No. 1, 1993, pp. 37-42.

15 Quik, M.; Labibes, K.; Albertini, C.; Valentin, T.; Magain, P. *Dynamic Mechanical Properties of Automotive Thin Sheet Steel in Tension, Compression and Shear.* Journal de Physique IV France, Vol. 7, No. 3, 1997, pp. 379-384.

16 Kang, W.J.; Cho, S.S.; Huh, H.; Chung, D.T. *Modified Johnson-Cook Model for Vehicle Body Crashworthiness Simulation.* International Journal of Vehicle Design, Vol. 21, Nos. 4/5, 1999, pp. 424-435.

17 Kang, W.J.; Cho, S.S.; Huh, H.; Chung, D.T. *Identification of Dynamic Behavior of Sheet Metals for an Auto-Body With Tension Split Hopkinson Bar.* SAE Transactions: Journal of Materials and Manufacturing, Vol. 107, 1998, pp. 908-913.

18 Huh, H.; Kang, W.J.; Han, S.S. *A Tension Split Hopkinson Bar for Investigating the Dynamic Behavior of Sheet Metals.* Experimental Mechanics, Vol. 42, No. 1, 2002, pp. 8-17.

19 Pelletier, P. *Mechanical Behaviour of Armco Iron at High Strain Rates and Elevated Temperatures.* Master of Applied Science Thesis, Carleton University, 1995.

20 Meyers, M.A. *Dynamic Behavior of Materials.* John Wiley & Sons, Inc., New York, 1994.

21 Lindholm, U.S. *Dynamic Deformation of Metals*, in: Behavior of Materials Under Dynamic Loading, Huffington, N.J. (Ed.), ASME, 1965, pp. 42-61.

22 Follansbee, P.S.; Frantz, C. *Wave Propagation in the Split Hopkinson Pressure Bar*. Journal of Engineering Materials and Technology, Vol. 105, No. 1, 1983, pp. 61-66.

23 Pochhammer, L. *On the Propagation Velocities of Small Oscillations in an Unlimited Isotropic Circular Cylinder*. Reine Angewandte Mathematic, Vol. 81, 1876, pp. 324-336.

24 Chree, C. *The Equations of an Isotropic Elastic Solid in Polar and Cylindrical Coordinates, Their Solutions and Applications*. Cambridge Philosophical Society Transactions, Vol. 14, 1889, pp. 250-369.

25 Davies, R.M. *Stress Waves in Solids.* British Journal of Applied Physics, Vol. 7, No. 6, 1956, pp. 203-209.

26 Clarke, J.A.M. *High Strain Rate Tensile Testing.* Master of Applied Science Thesis, Carleton University, 1993.

27 Salisbury, C.P. *Spectral Analysis of Wave Propagation Through a Polymeric Hopkinson Bar.* Master of Applied Science Thesis, University of Waterloo, 2001.

28 Davies, R.M. *Critical Study of Hopkinson Pressure Bar*. Royal Society of London – Philosophical Transactions Series A, Vol. 240, No. 821, 1948, pp. 375-457.

29 Davies, E.D.H; Hunter S.C. *Dynamic Compression Testing of Solids by Method of Split Hopkinson Pressure Bar*. Journal of the Mechanics and Physics of Solids, Vol. 11, No. 3, 1963, pp. 155-179.

30 Campbell, J.D.; Ferguson, W.G. *Temperature and Strain-Rate Dependence of the Shear Strength of Mild Steel*. Philosophical Magazine, Vol. 21, No. 169, 1970, pp. 63-82.

31 Weertman, J. *Dislocation Mechanics at High Strain Rates*. In: Metallurgical Effects at High Strain Rates, Rohde R.W.; Butcher B.M.; Holland J.R.; Karnes C.H. (Ed.), Plenum Press, New York, 1973.

32 Follansbee, P.S. *High-Strain-Rate Deformation of FCC Metals and Alloys*. Metallurgical Applications of Shock-Wave and High-Strain-Rate Phenomena, 1986, pp. 451-479.

33 Regazzoni, G.; Kocks, U.F.; Follansbee, P.S. *Dislocation Kinetics at High Strain Rates*. Acta Metallurgical, Vol. 35, No. 12, 1987, pp. 2865-2875.

34 Follansbee, P.S. *The Transition to Drag-Controlled Deformation in Copper at High Strain Rates*. Institute of Physics Conference Series, Vol. 70. Proceedings of the 3rd Conference on Mechanical Properties at High Rates of Strain, Oxford, 1984, pp. 71-80.

35 Zerilli, F.J.; Armstrong, R.W. *The Effect of Dislocation Drag on the Stress-Strain Behavior of F.C.C. Metals.* Acta Metallurgia et Materialia, Vol. 40, No. 8, 1992, pp. 1803-1808.

36 Samanta, S.K. *Dynamic Deformation of Aluminium and Copper at Elevated Temperatures*. Journal of the Mechanics and Physics of Solids, Vol. 19, No. 3, 1971, pp. 117-135.

37 Gorham, D.A. *Specimen Inertia in High Strain-Rate Compression*. Journal of Physics D: Applied Physics, Vol. 22, No. 12, 1989, pp. 1888-1893.

38 Gorham, D.A. *Effect of Specimen Dimensions on High Strain Rate Compression Measurement of Copper*. Journal of Physics D: Applied Physics, Vol. 24, No. 8, 1991, pp. 1489-1492.

39 Gorham, D.A.; Pope, P.H.; Field, J.E. *An Improved Method for Compression Stress-Strain Measurements at Very High Strain Rates*. Proceedings of the Royal Society of London: A, Vol. 438, 1992, pp. 143-170.

40 Field, J.E.; Walley, S.M.; Proud, W.G.; Goldrein, H.T.; Siviour, C.R. *Review of Experimental Techniques for High Rate Deformation and Shock Studies*. International Journal of Impact Engineering, Vol. 30, No. 7, 2004, pp. 725-775.

41 Regazzoni, G.; Johnson, J.N.; Follansbee, P.S. *Theoretical Study of the Dynamic Tensile Test*. Transactions of the ASME: Journal of Applied Mechanics, Vol. 53, 1986, pp. 519-528.

42 Balanethiram, V.S. *Hyperplasticity: Enhanced Formability of Sheet Metals at High Workpiece Velocities*. Doctor of Philosophy Thesis, Ohio State University, 1996.

43 Hu, X.; Daehn, G.S. *Effect of Velocity on Flow Localization in Tension*. Acta Materialia, Vol. 44, No. 3, 1996, pp. 1021-1033.

44 Hu, X.; Wagoner, R.H.; Daehn, G.S.; Ghosh, S. *The Effect of Inertia on Tensile Ductility*. Metallurgical and Materials Transactions A, Vol. 25A, December 1994, pp. 2723-2735.

45 Fressengeas, C.; Molinari, A. *Inertia and Thermal Effects on the Localization of Plastic Flow*. Acta Metallurgica, Vol. 33, No. 3, 1985, pp. 387-396.

46 Balanethiram, V.S.; Daehn, G.S. *Hyperplasticity: Increased Forming Limits at High Workpiece Velocity*. Scripta Metallurgica et Materialia. Vol. 30, No. 4, 1994, pp. 515-520.

47 Altynova, M.; Hu, X.; Daehn, G.S. *Increased Ductility in High Velocity Electromagnetic Ring Expansion*. Metallurgical and Materials Transactions A, Vol. 27A, July 1996, pp. 1837-1844.

48 Banerjee, J.K. *Effects of Inertia Forces on the Plastic Instability of Thin Cylinders During Electromagnetic Bulge Forming*. High Energy Rate Fabrication, 1984: Presented at the 8th International Conference on High Energy Rate Fabrication, pp. 19-23.

49 Holt, D.L.; Babcock, S.G.; Green, S.J.; Maiden, C.J. *The Strain-Rate Dependence of the Flow Stress in Some Aluminum Alloys.* Transactions of the ASM: Transactions Quarterly, Vol. 60, No. 2, 1967, pp. 152-159.

50 Tanaka, K.; Nojima, T. *Strain Rate Change Tests of Aluminum Alloys Under High Strain Rate.* Proceedings of The 19th Japan Congress on Materials Research, 1975, pp. 48-51.

51 Oosterkamp, L. Djapic; Ivankovic, A.; Venizelos G. *High Strain Rate Properties of Selected Aluminium Alloys.* Journal of Materials Science & Engineering A: Structural Materials: Properties, Microstructure and Processing, Vol. 278, Nos. 1/2, 2000, pp. 225-235.

52 Rodriquez, J.; Navarro, C.; Sanchez-Galvez, V. *Some Corrections to the Data Analysis of the Dynamic Tensile Tests in the Hopkinson Bar.* Journal de Physique IV France, Vol. 4, No. 8, 1994, pp. 83-88.

53 El-Magd, E.; Abouridouane, M. *Influence of Strain Rate and Temperature on the Compressive Ductility of Al, Mg and Ti Alloys.* Journal de Physique IV France, Vol. 110, 2003, pp. 15-20.

54 El-Magd, E.; Brodmann, M. *Influence of Precipitates on Ductile Fracture of Aluminium Alloy AA7075 at High Strain Rates.* Materials Science and Engineering A, Vol. 307, Nos. 1/2, 2001, pp. 143-150.

55 El-Magd, E.; Scholles, H.; Weisshaupt, H. *Dynamic Ductility of Metals.* Journal de Physique IV France, Vol. 7, No. 3, 1997, pp. 349-354.

56 Masuda, T.; Kobayashi, T.; Wang, L.; Toda, H. *Effects of Strain Rate on Deformation Behavior of A6061-T6.* Materials Science Forum, Vol. 426-432, No. 1, 2003, pp. 285-290.

57 Mukai, T.; Higashi, K.; Tanimura, S. *Influence of the Magnesium Concentration on the Relationship Between Fracture Mechanism and Strain Rate in High Purity Al-Mg Alloys.* Materials Science and Engineering A: Structural Properties: Properties, Microstructure and Processing, Vol. 176, Nos. 1/2, 1994, pp. 181-189.

58 Higashi, K.; Mukai, T.; Kaizu, K.; Tsuchida, S.; Tanimura, S. *Strain Rate Dependence on Mechanical Properties in Some Commercial Aluminium Alloys.* Journal de Physique IV France, Vol. 1, No. 8, 1991, pp. 341-346.

59 Higashi, K.; Mukai, T.; Kaizu, K.; Tanimura, S.; Tsuchida, S. *The Microstructural Evolution During Deformation Under Several Strain Rates in a Commercial 5182 Aluminium Alloy.* Journal de Physique IV France, Vol. 1, No. 8, 1991, pp. 347-352.

60 Shi, M.F.; Meuleman, D.J. *On Certain Aspects of Strain Rate Sensitivity of Sheet Metals*. Journal of Materials Engineering and Performance, Vol. 4, No. 3, 1995, pp. 321-333.

61 Johnson, G.R.; Cook, W.H. *A Constitutive Model and Data for Metals Subjected to Large Strains, High Strain Rates, and High Temperatures*. Proceedings – 7th International Symposium on Ballistics, Hague, Netherlands, April 1983, pp. 541-547.

62 Johnson, G.R.; Cook, W.H. *Fracture Characteristics of Three Metals Subjected to Various Strains, Strain Rates, Temperatures and Pressures.* Engineering Fracture Mechanics, Vol. 21, No. 1, 1985, pp. 31-48.

63 Rule, W.K.; Jones, S.E. *A Revised Form for the Johnson-Cook Strength Model*. International Journal of Impact Engineering, Vol. 21, No. 8, 1998, pp. 609-624.

64 Zerilli, F.J.; Armstrong, R.W. *Dislocation-Mechanics-Based Constitutive Relations For Material Dynamics Calculations.* Journal of Applied Physics, Vol. 61, No. 5, 1987, pp. 1816-1825.

65 Zerilli, F.J.; Armstrong, R.W. *Dislocation Mechanics Based Constitutive Relations for Dynamic Straining to Tensile Instability.* Shock Compression of Condensed Matter, 1989, pp. 357-360.

66 Zerilli, F.J.; Armstrong, R.W. *Dislocation Mechanics Based analysis of Material Dynamics Behavior: Enhanced Ductility, Deformation Twinning, Shock Deformation, Shear Instability, Dynamic Recovery.* Journal de Physique IV France, Vol. 7, No. 3, 1997, pp. 637-642.

67 Wagenhofer, M.; Erickson-Natishan, M.A,; Armstrong, R.W.; Zerilli, F.J. *Influences of Strain Rate and Grain Size on Yield and Serrated Flow in Commercial Al-Mg Alloy 5086.* Scripta Materialia, vol. 41, no. 11, 1999, pp. 1177-1184.

68 Follansbee, P.S. *Analysis of the Strain-Rate Sensitivity at High Strain Rates in FCC and BCC Metals.* Presented at the Fourth International Conference on the Mechanical Properties of Materials at High Rates of Strain, Oxford, March, 19-21, 1989, pp. 213-220.

69 Follansbee, P.S.; Kocks, U.F. *A Constitutive Description of the Deformation of Copper Based on the Use of Mechanical Threshold Stress as an Internal State Variable.* Presented at the Fourth International Conference on the Mechanical Properties of Materials at High Rates of Strain, Oxford, March, 19-21, 1989, pp. 81-93.

70 Hallquist, J. *LS-DYNA Theoretical Manual*, Livermore software technology corporation, 1998

71 Gupta, A.K.; Marios, P.H.; Lloyd, D.J. *Study of the Precipitation Kinetics in a 6000 Series Automotive Sheet Material.* Material Science Forum: Aluminum Alloys - Their Physical and Mechanical Properties, Vol. 217-222, No. pt 2, 1996, pp. 801-808.

72 Smerd, R.; Winkler, S.L.; Salisbury C.P.; Worswick, M.J.; Lloyd, D.J.; Finn, M. *High Strain Rate Tensile Testing of Automotive Aluminum Alloy Sheet*. International Journal of Impact Engineering, Submitted for Publication, 2005.

73 Matweb http://www.matweb.com

74 Doyle, J.F. *Wave Propagation in Structures – An FFT Based Spectral Analysis Methodology*. New York: Springer-Verlag, 1989.

75 MacDougall, D. *Determination of the Plastic Work Converted to Heat Using Radiometry*. Experimental Mechanics, Vol. 40, No. 3, 2000, pp. 298-306.

76 Hayashi T.; Yamaura H.; Shigeru O. *Temperature Measurement of Metals Under High Velocity Deformation*. Proceedings of the Twentieth Japan Congress on Materials Research. Kyoto (Japan) 1977, pp. 94-98.

77 Radford, D.D. *Mechanical and Constitutve Behaviour of Zr-2.5Nb Pressure Tube Material at High Rates of Tensile Strain*. Doctor of Philosophy Thesis, Carleton University 2000.

78 Bailey S.J.; Baldini N.C.; Barkley E.I.; Peters K.A.; Rosiak J.L.; Simms S.T.; Whealen E.A.; Wilhelm R.F. (Ed.). Annual Book of ASTM Standards: Metals – Mechanical Testing; Elevated and Low Temperature Tests; Metallography. West Conshohocken, PA: ASTM International; 2003, pp. 61-82.

79 Weber, L.; Kouzeli, M.; San Marchi, C.; Mortensen A. *On the Use of Considere's Criterion in Tensile Testing of Materials Which Accumulate Internal Damage*. Scripta Materialia, Vol. 41, No. 5, 1999, pp. 549-551.

80 Wilkinson, Leland. *SYSTAT: The System for Statistics*. Evanston, IL: SYSTAT, Inc., 1990.

Appendix A

Engineering Stress-Strain Data for 1.6 mm AA5754

Note: The reader should be made aware that the specimens were loaded multiple times to failure, as described in Chapter 2. Hence, stress-strain responses are shown only for the first loading pulse. The elongation was determined by directly measuring the failed specimens.

Specimen	G. Length (mm)	Width (mm)	Thickness (mm)	Strain Rate (s^{-1})	Temperature (ºC)	Elongation (%)
QS_1	12.5	1.76	1.57	0.00188	RT	29.8
QS_2	12.5	1.79	1.58	0.0019	RT	28.3
QS_3	12.5	1.79	1.58	0.00187	RT	28.7
600_1	12.5	1.75	1.54	619	RT	36.6
600_2	12.5	1.75	1.53	596	RT	38.4
600_3	12.5	1.73	1.53	594	RT	39.3
1100_1	12.5	1.73	1.52	1060	RT	39.5
1100_2	12.5	1.71	1.52	1072	RT	41.1
1100_3	12.5	1.76	1.52	1090	RT	43.7
1500_1	12.5	1.77	1.53	1531	RT	42.6
1500_2	12.5	1.75	1.55	1525	RT	46.2
1500_3	12.5	1.76	1.54	1532	RT	43.5
600_50C_1	12.5	1.76	1.52	590	50	38.1
600_50C_2	12.5	1.75	1.55	602	50	37.8
600_50C_3	12.5	1.75	1.53	589	50	39.3
1500_50C_1	12.5	1.75	1.54	1574	50	42.9
1500_50C_2	12.5	1.75	1.55	1547	50	45.6
1500_50C_3	12.5	1.73	1.55	1543	50	43.5
600_150C_1	12.5	1.74	1.53	586	150	36.7
600_150C_2	12.5	1.74	1.55	590	150	39
600_150C_3	12.5	1.75	1.53	591	150	37.4
1500_150C_1	12.5	1.72	1.56	1533	150	41.3
1500_150C_2	12.5	1.72	1.54	1548	150	40.2
1500_150C_3	12.5	1.7	1.54	1547	150	41
1500_300C_1	12.5	1.74	1.53	1546	300	29.1
1500_300C_2	12.5	1.82	1.54	1566	300	30
1500_300C_3	12.5	1.69	1.57	1582	300	29.3

Appendix A1:

(Quasi-static Data)

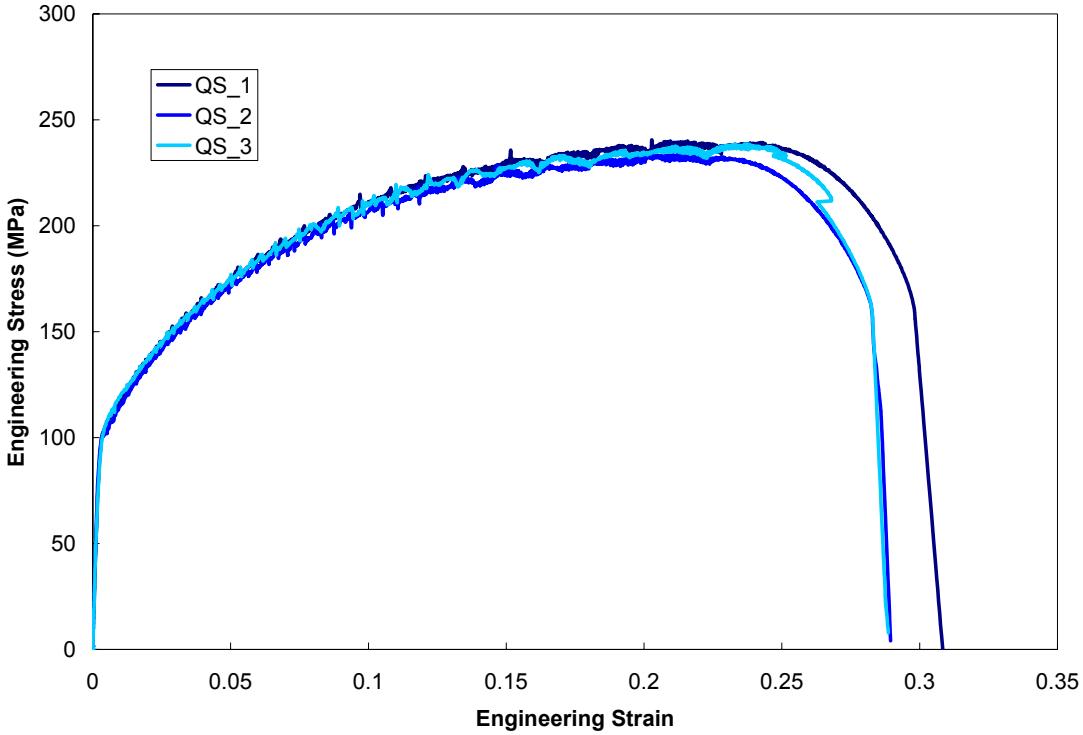

Appendix A2:

(High Strain Rate Data at Room Temperature)

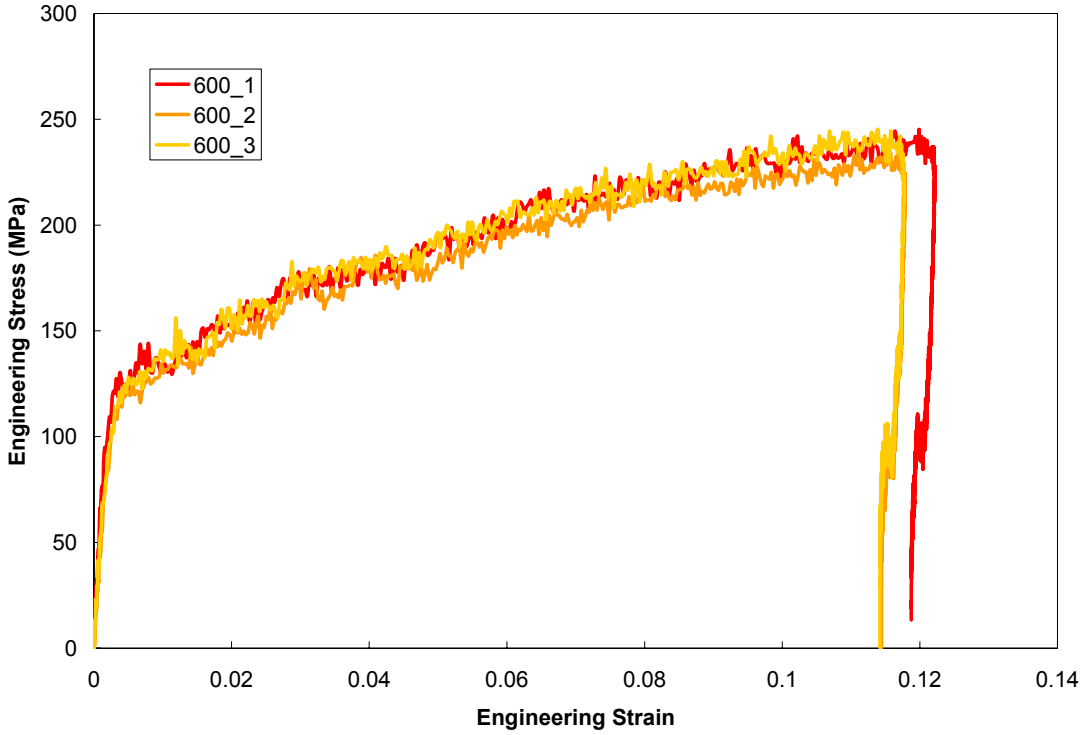

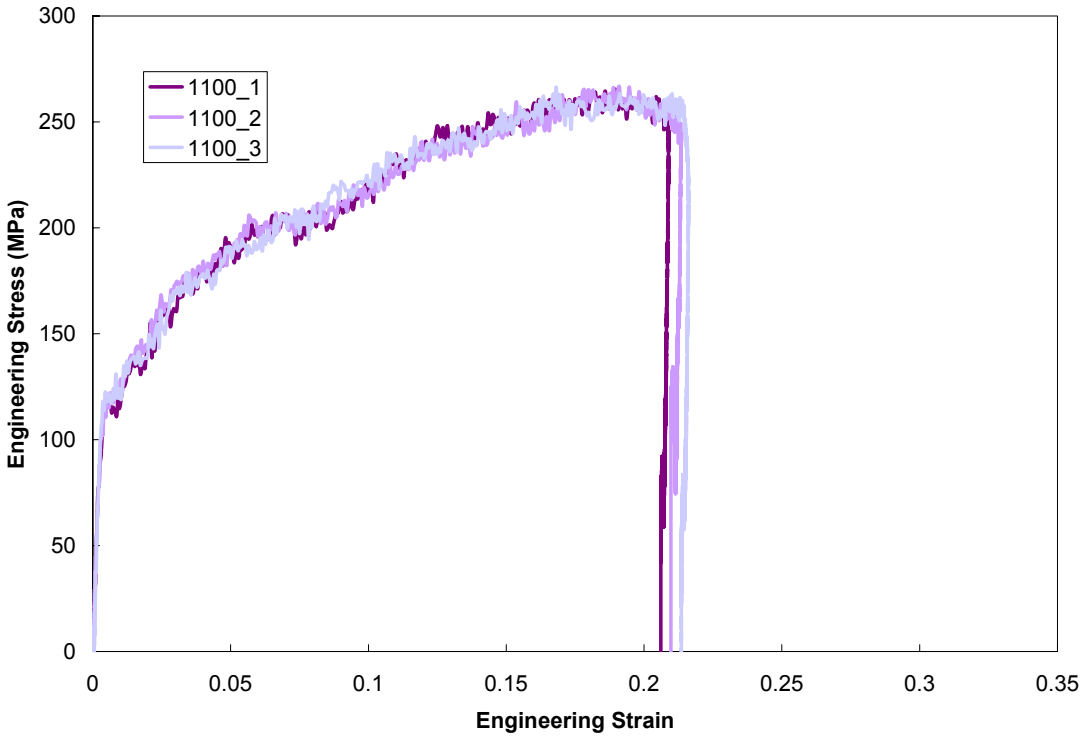

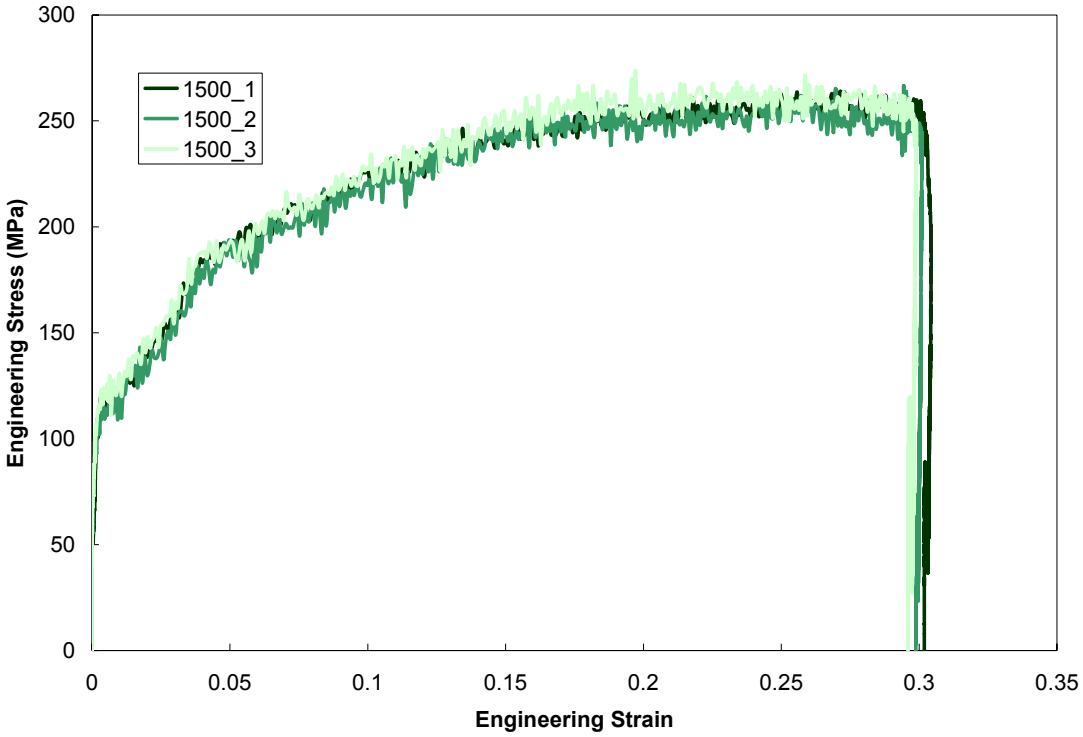
300
250
200
150
100
50
0
Engineering Stress (MPa)
1500_1
1500_2
1500_3
0
0.05
0.1
0.15
0.2
0.25
0.3
0.35
Engineering Strain

Appendix A3:

(Elevated Temperature Data at 600 s^{-1})

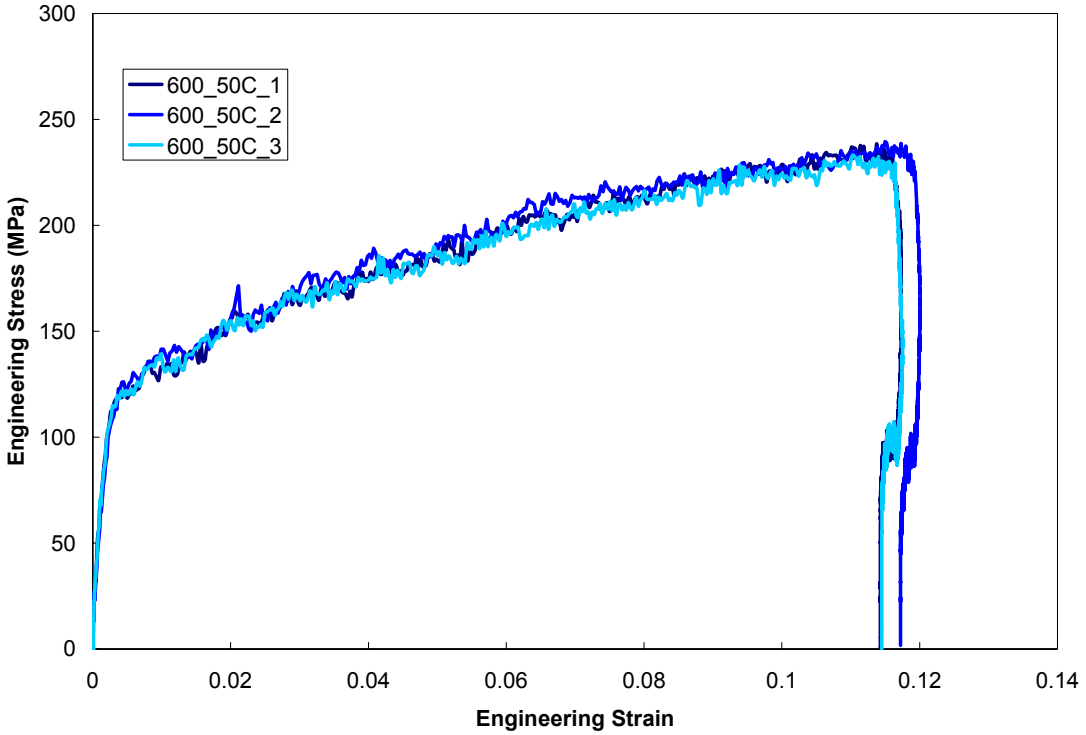

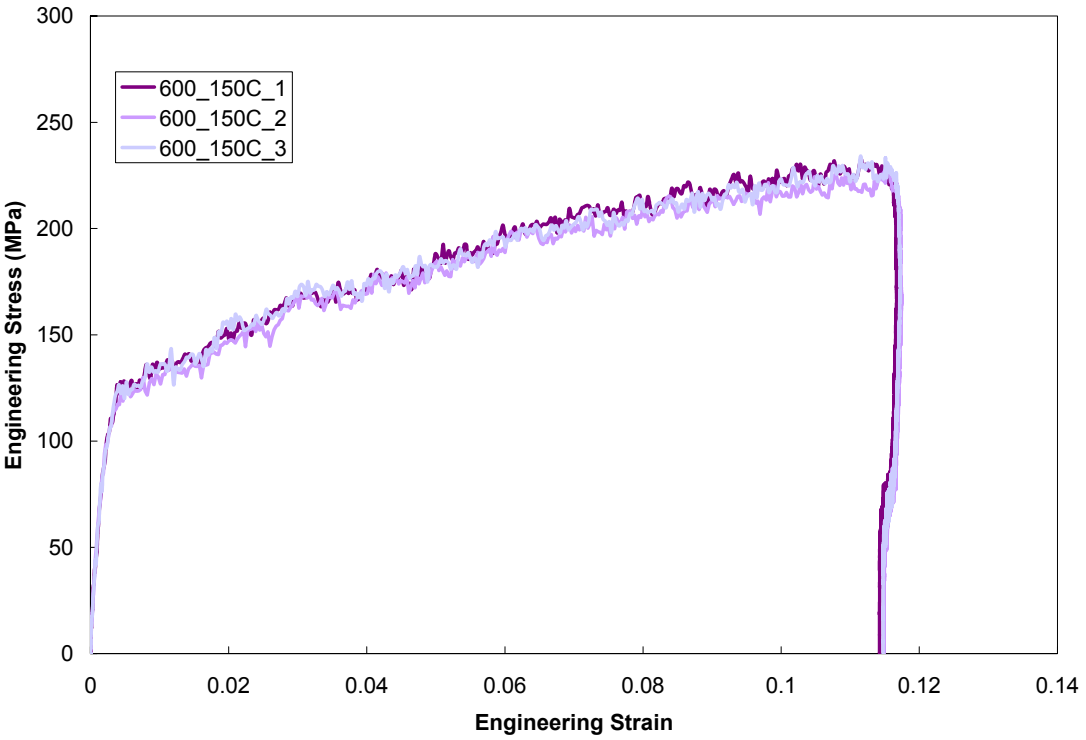

Appendix A4:

(Elevated Temperature Data at 1500 s^{-1})

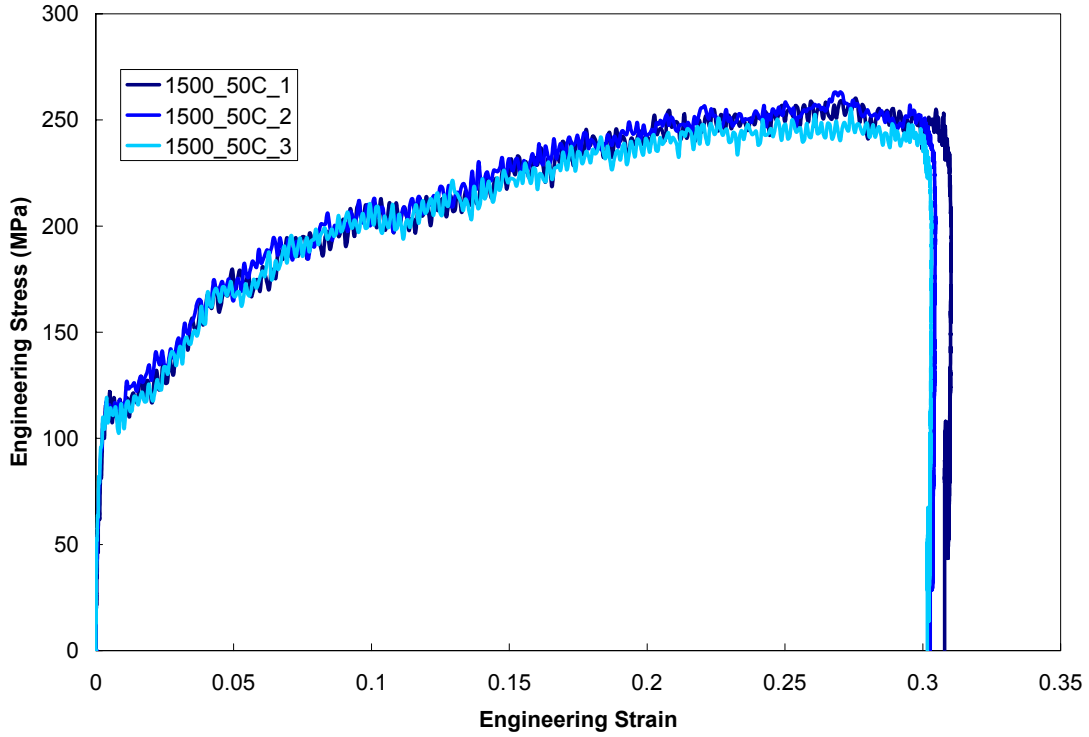

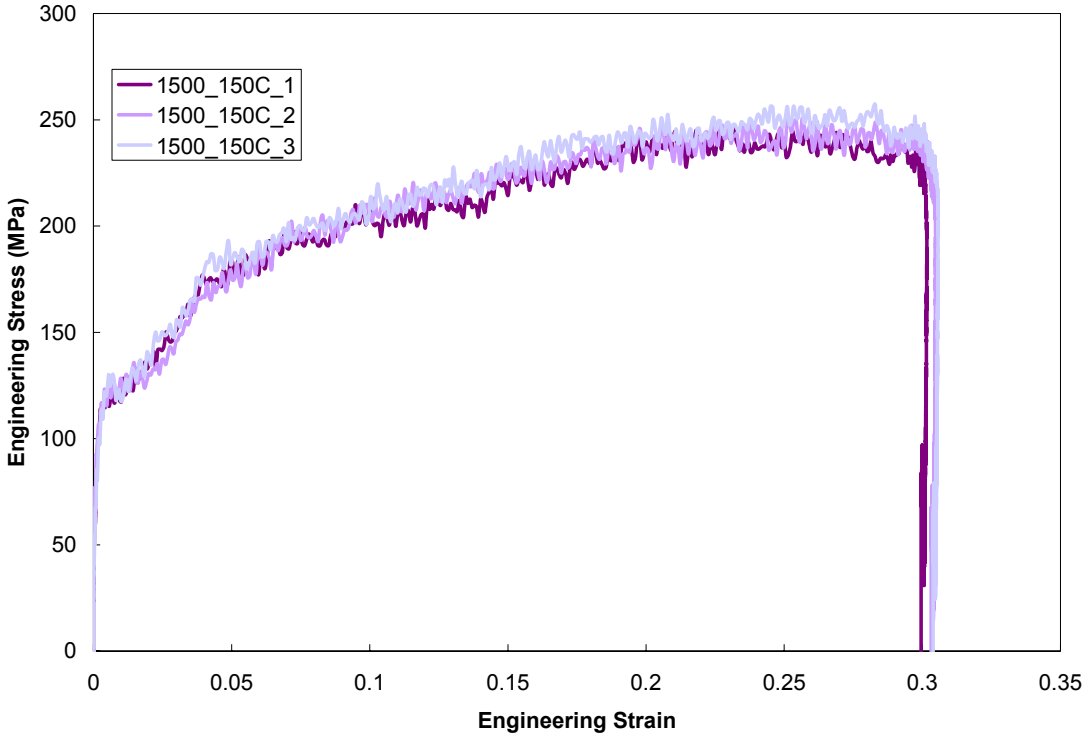

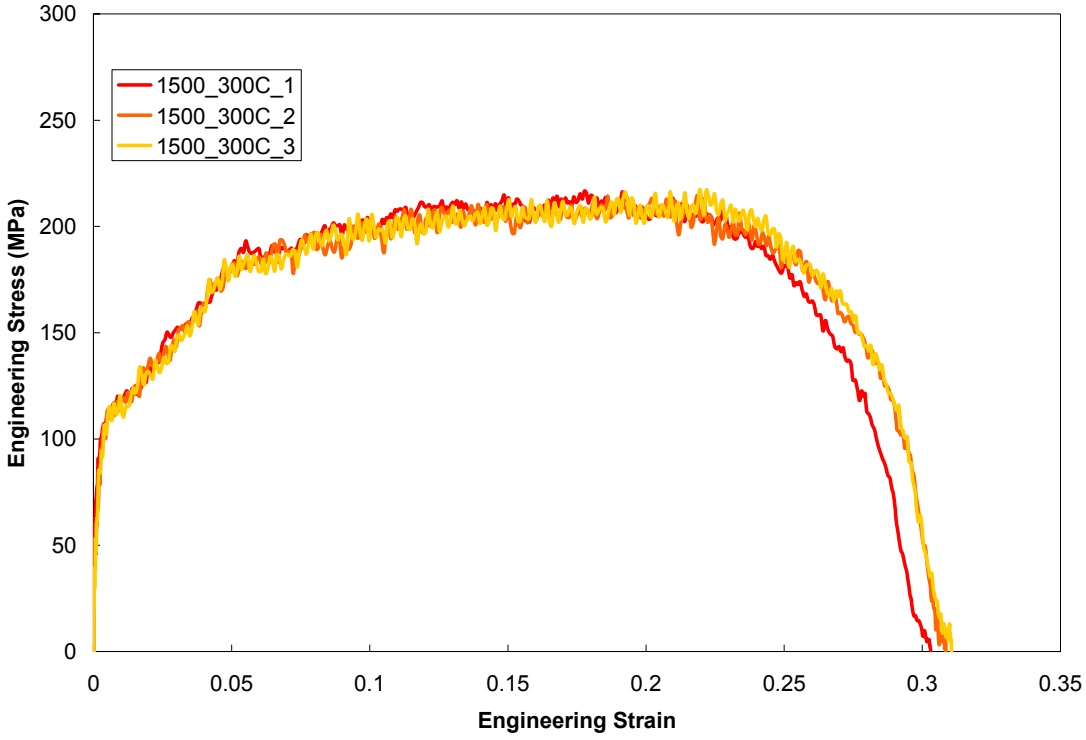
1500_300C_1
1500_300C_2
1500_300C_3
Engineering Stress (MPa)
Engineering Strain
300
250
200
150
100
50
0
0
0.05
0.1
0.15
0.2
0.25
0.3
0.35

Appendix B

Engineering Stress-Strain Data for 1 mm AA5754

Note: The reader should be made aware that the specimens were loaded multiple times to failure, as described in Chapter 2. Hence, stress-strain responses are shown only for the first loading pulse. The elongation was determined by directly measuring the failed specimens.

Specimen	G.Length (mm)	Width (mm)	Thickness (mm)	Strain Rate (s^{-1})	Temperature (ºC)	Elongation (%)
QS_1	12.5	1.72	0.98	0.003058	RT	27.3
QS_2	12.5	1.71	0.97	0.003277	RT	27.8
QS_3	12.5	1.74	1.01	0.003222	RT	27.7
600_1	12.5	1.76	0.99	619	RT	41
600_2	12.5	1.76	1.01	602	RT	42.1
600_3	12.5	1.72	1.00	617	RT	42.6
1100_1	12.5	1.75	0.99	1133	RT	42.7
1100_2	12.5	1.71	0.97	1101	RT	42.1
1100_3	12.5	1.70	0.99	1106	RT	42.6
1500_1	12.5	1.74	0.99	1554	RT	46.7
1500_2	12.5	1.71	0.97	1563	RT	43.8
1500_3	12.5	1.70	0.99	1552	RT	45.9
600_50C_1	12.5	1.76	1.00	615	50	42.8
600_50C_2	12.5	1.76	1.00	600	50	41.4
600_50C_3	12.5	1.72	1.00	592	50	42.6
1500_50C_1	12.5	1.80	1.00	1578	50	45.7
1500_50C_2	12.5	1.78	1.00	1576	50	50.6
1500_50C_3	12.5	1.77	1.00	1571	50	43.4
600_150C_1	12.5	1.75	1.00	612	150	38.2
600_150C_2	12.5	1.76	1.00	596	150	35
600_150C_3	12.5	1.73	1.01	606	150	37.8
1500_150C_1	12.5	1.78	1.01	1558	150	36.9
1500_150C_2	12.5	1.76	0.99	1622	150	35.3
1500_150C_3	12.5	1.76	1.01	1615	150	41.8
1500_300C_1	12.5	1.78	1.02	1579	300	31.4
1500_300C_2	12.5	1.78	0.99	1581	300	32
1500_300C_3	12.5	1.76	0.98	1566	300	30.6

Appendix B1:

(Quasi-static Data)

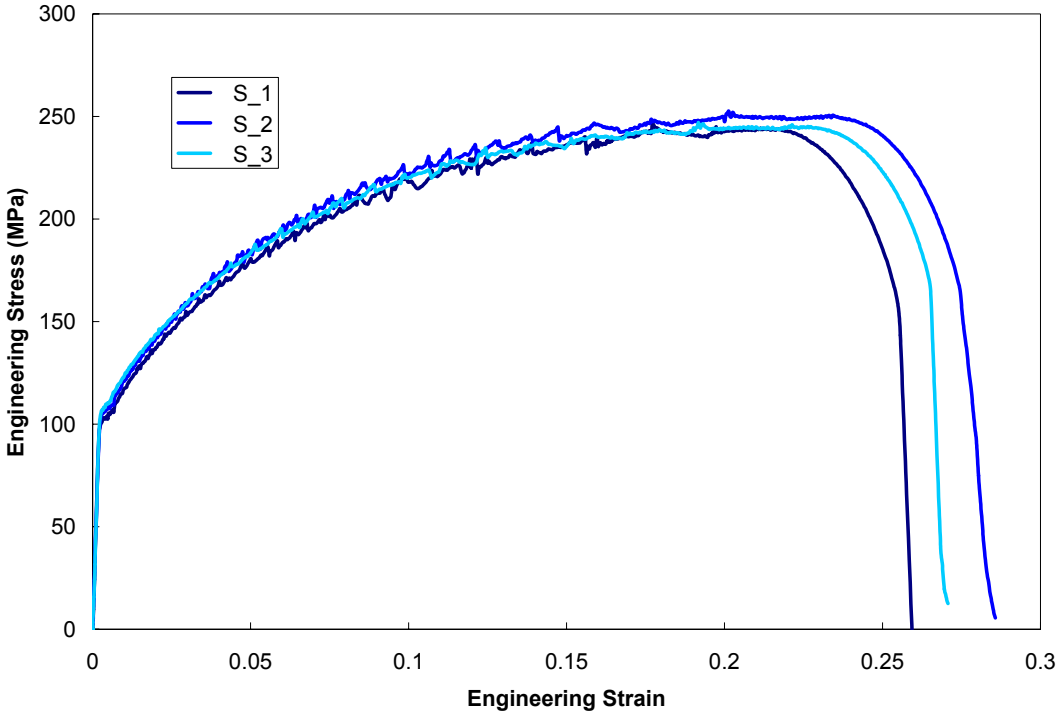

Appendix B2:

(High Strain Rate Data at Room Temperature)

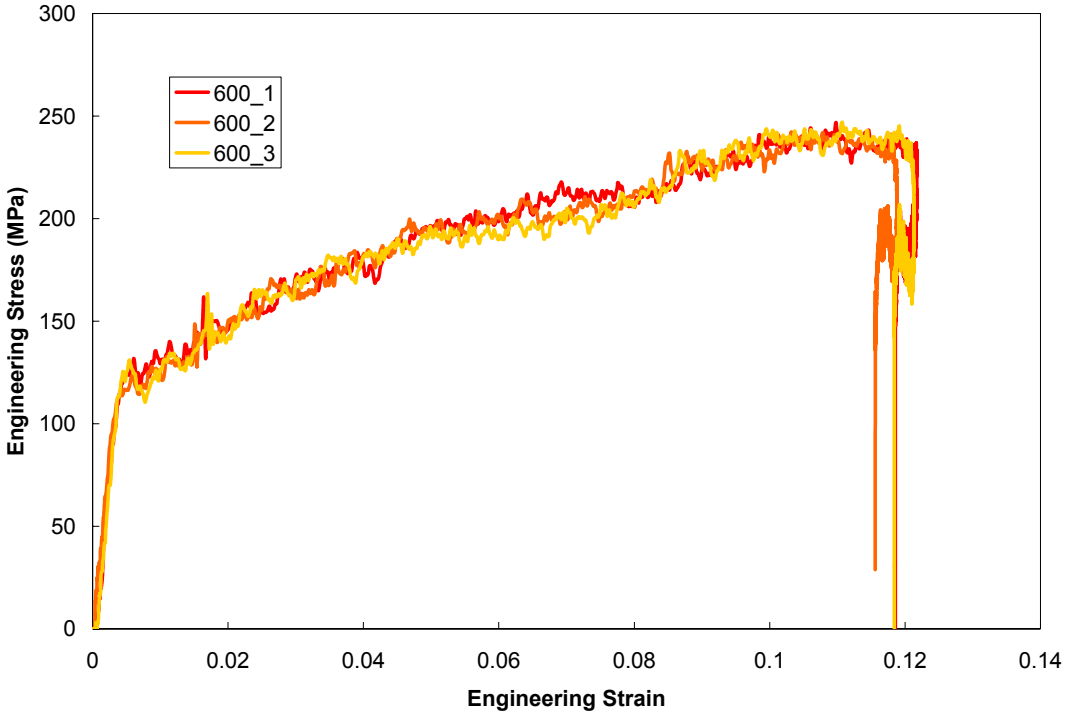

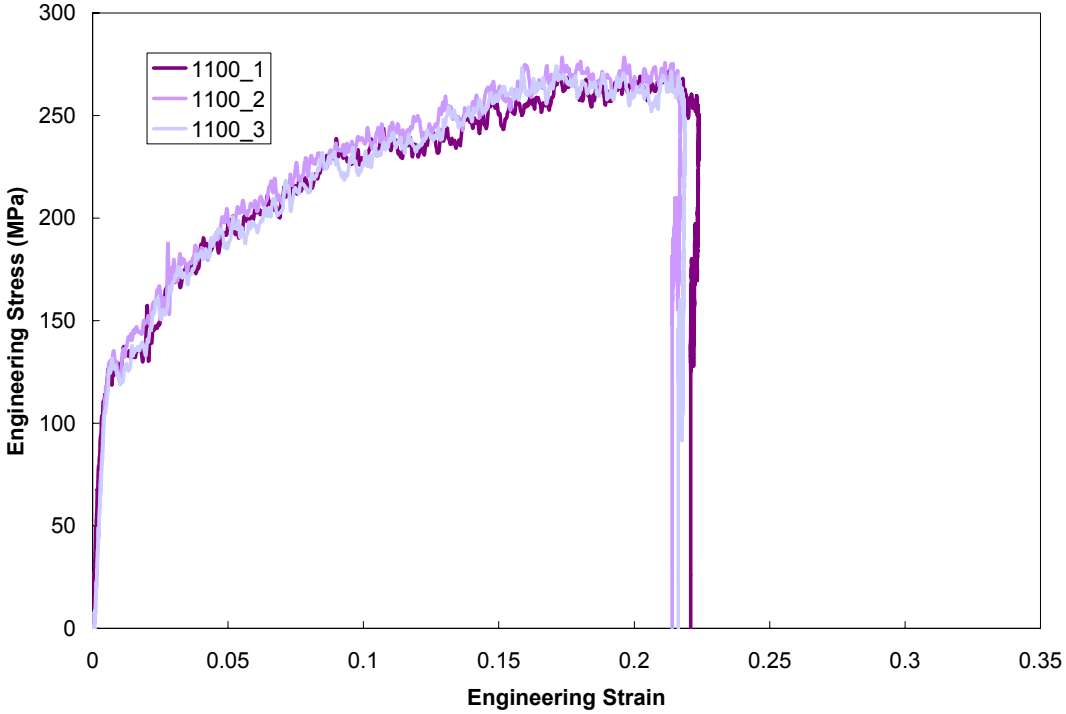

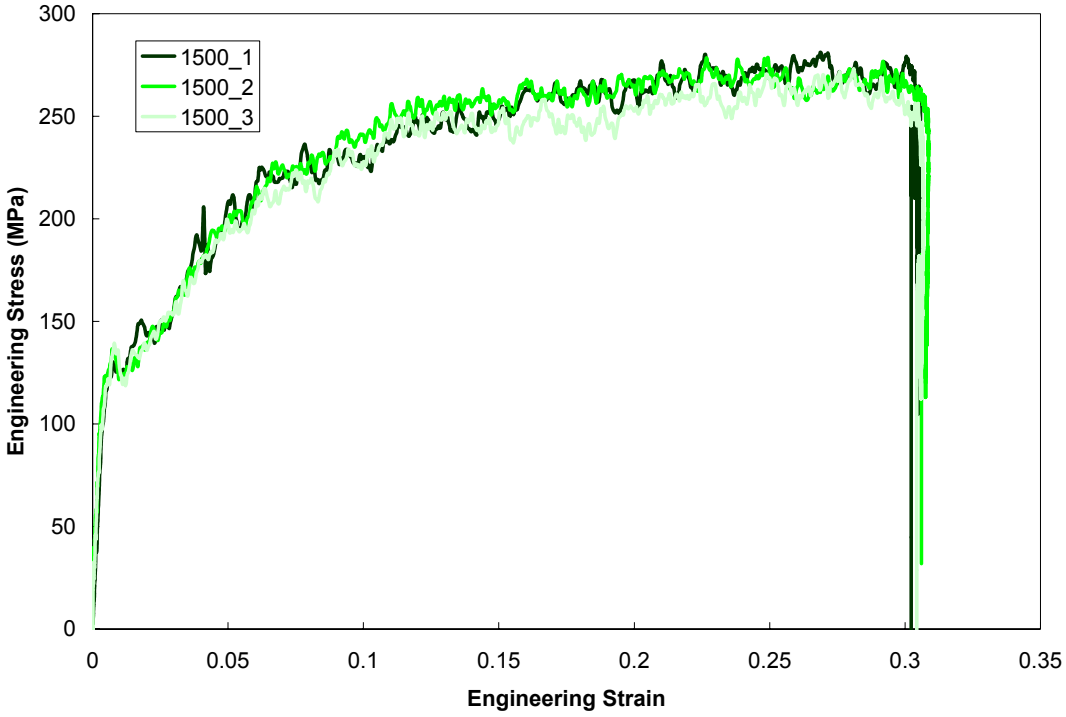
1500_1
1500_2
1500_3
Engineering Stress (MPa)
Engineering Strain
300
250
200
150
100
50
0
0
0.05
0.1
0.15
0.2
0.25
0.3
0.35

Appendix B3:

(Elevated Temperature Data at 600 s^{-1})

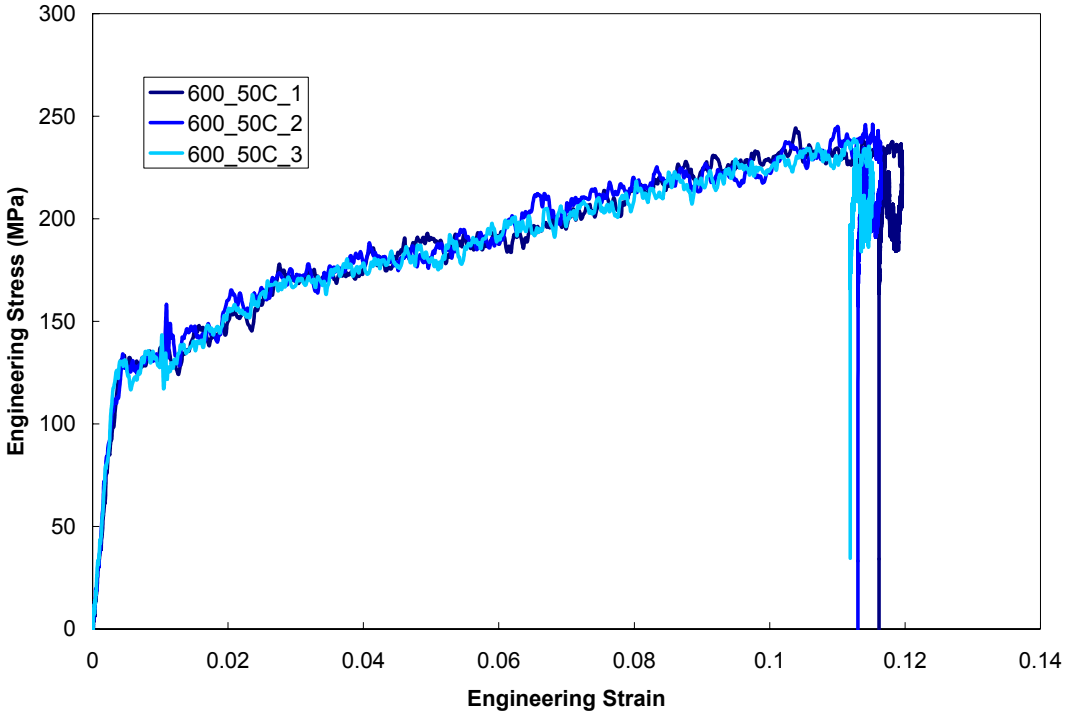

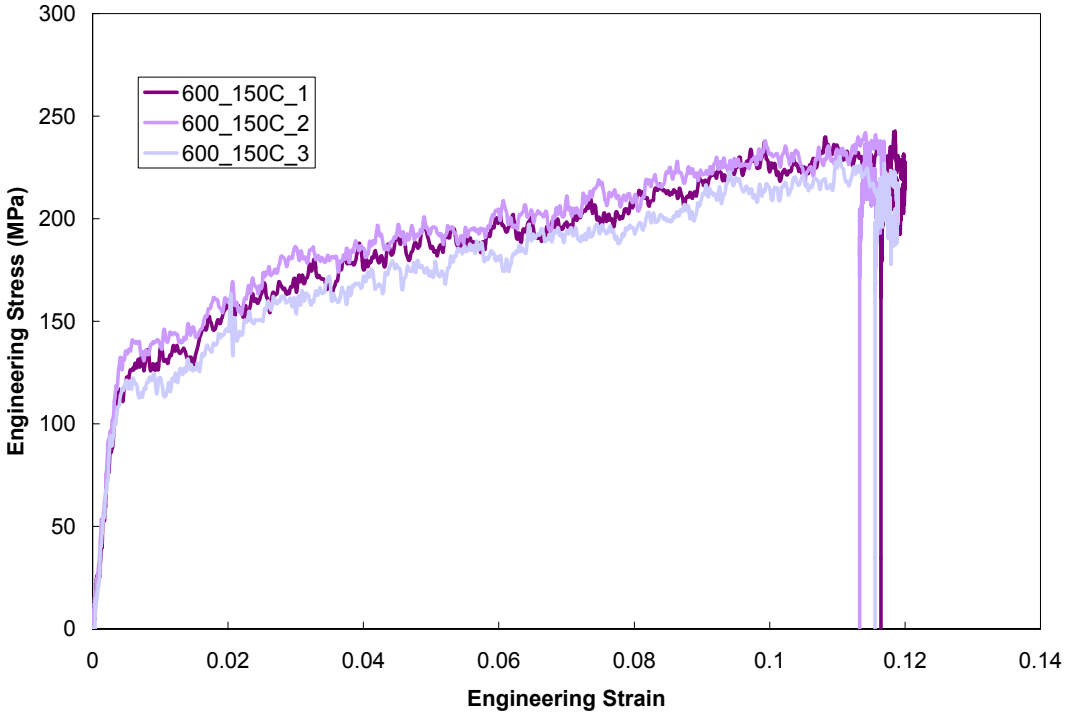

Appendix B4:

(Elevated Temperature Data at 1500 s^{-1})

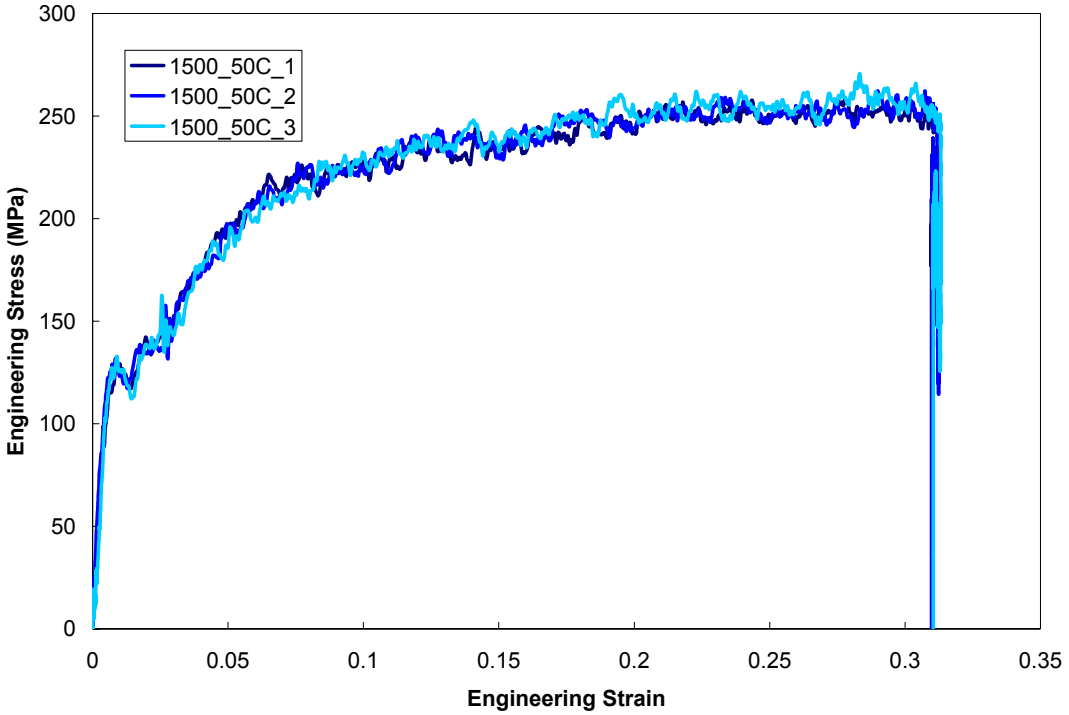

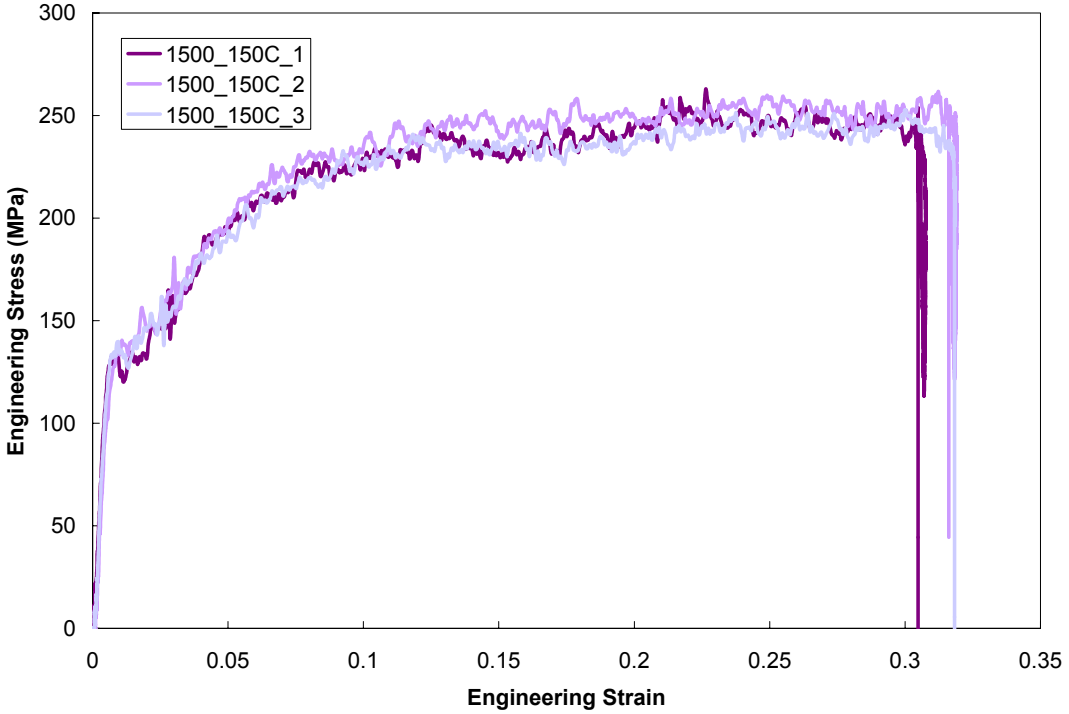

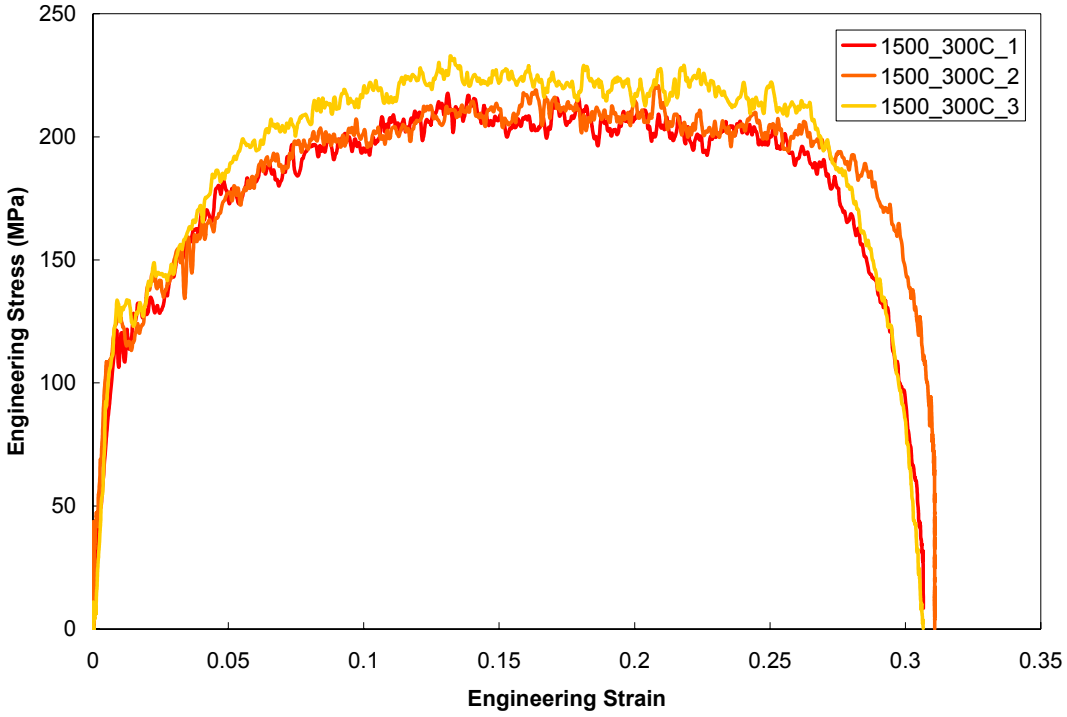
1500_300C_1
1500_300C_2
1500_300C_3
Engineering Stress (MPa)
Engineering Strain
250
200
150
100
50
0
0
0.05
0.1
0.15
0.2
0.25
0.3
0.35

Appendix C

Engineering Stress-Strain Data for 1.6 mm AA5182

Note: The reader should be made aware that the specimens were loaded multiple times to failure, as described in Chapter 2. Hence, stress-strain responses are shown only for the first loading pulse. The elongation was determined by directly measuring the failed specimens.

Specimen	G. Length (mm)	Width (mm)	Thickness (mm)	Strain Rate (s^{-1})	Temperature (ºC)	Elongation (%)
QS_1	12.5	1.75	1.52	0.00301	RT	30.6
QS_2	12.5	1.76	1.51	0.0032	RT	29.6
QS_3	12.5	1.76	1.52	0.00316	RT	29
600_1	12.5	1.78	1.55	608	RT	35.7
600_2	12.5	1.76	1.54	616	RT	33.5
600_3	12.5	1.75	1.49	615	RT	33.1
1100_1	12.5	1.74	1.50	1035	RT	33.2
1100_2	12.5	1.73	1.50	1012	RT	36.7
1100_3	12.5	1.78	1.50	1089	RT	35.4
1500_1	12.5	1.79	1.49	1517	RT	38.8
1500_2	12.5	1.77	1.49	1525	RT	37.5
1500_3	12.5	1.77	1.50	1527	RT	36.1
600_50C_1	12.5	1.77	1.48	597	50	no fail
600_50C_2	12.5	1.75	1.48	606	50	no fail
600_50C_3	12.5	1.77	1.50	585	50	no fail
1500_50C_1	12.5	1.79	1.52	1487	50	38.7
1500_50C_2	12.5	1.76	1.52	1497	50	37.7
1500_50C_3	12.5	1.77	1.48	1613	50	37.2
600_150C_1	12.5	1.78	1.50	593	150	32.8
600_150C_2	12.5	1.74	1.49	587	150	35.9
600_150C_3	12.5	1.79	1.50	579	150	33.6
1500_150C_1	12.5	1.78	1.49	1533	150	35.9
1500_150C_2	12.5	1.79	1.51	1541	150	37.2
1500_150C_3	12.5	1.76	1.50	1514	150	38.4
1500_300C_1	12.5	1.79	1.49	1490	300	28.2
1500_300C_2	12.5	1.76	1.50	1480	300	27.9
1500_300C_3	12.5	1.74	1.49	1512	300	26.5

Appendix C1:
(Quasi-static Data)

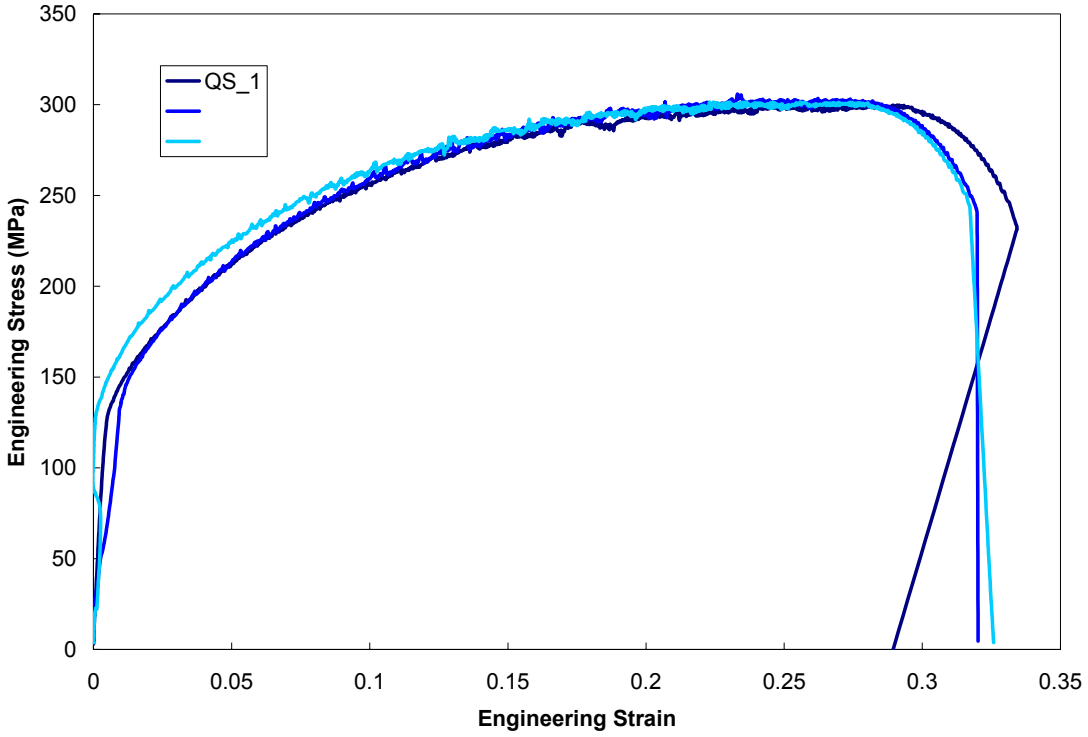

Appendix C2:

(High Strain Rate Data at Room Temperature)

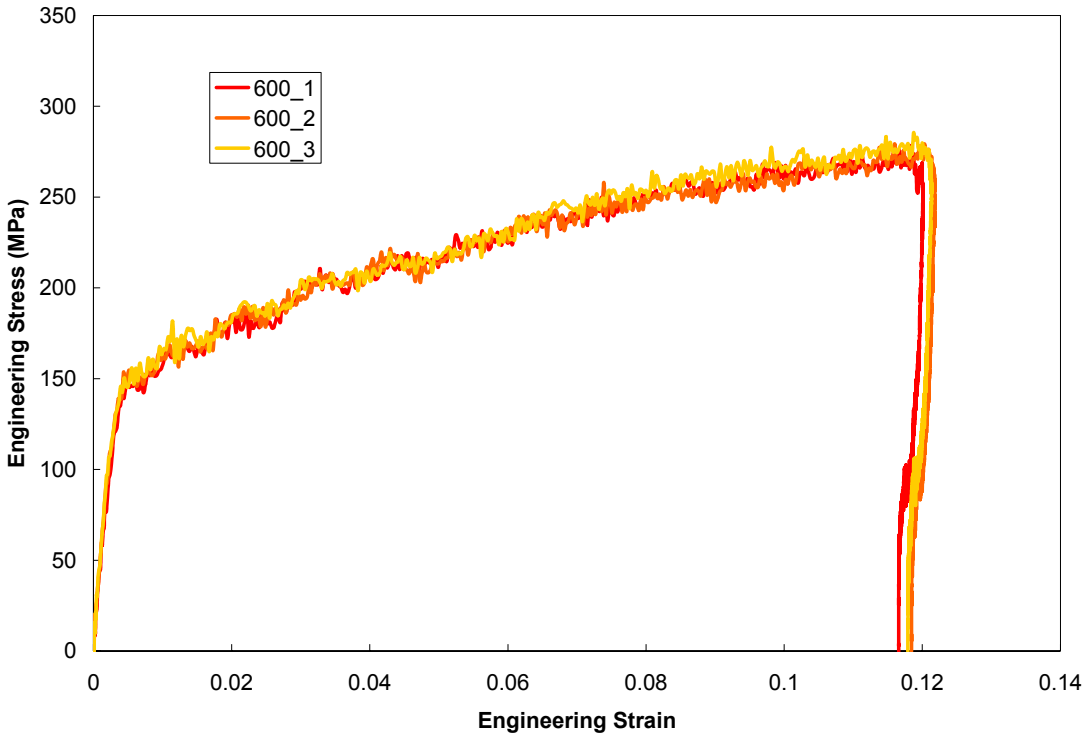

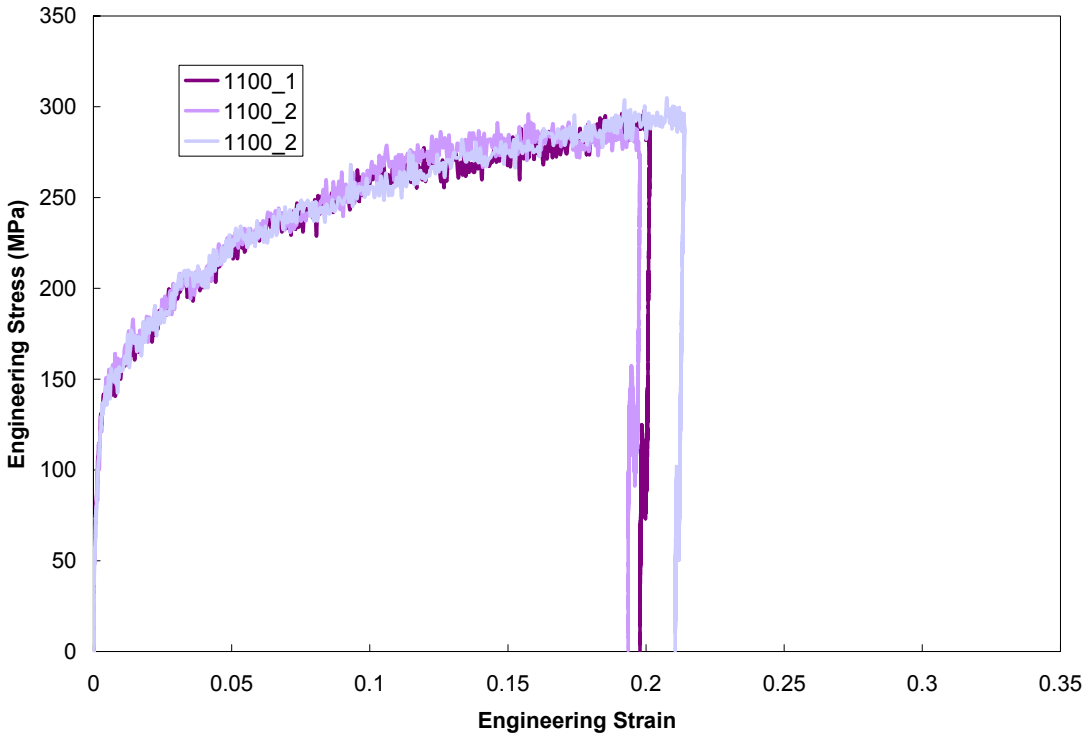

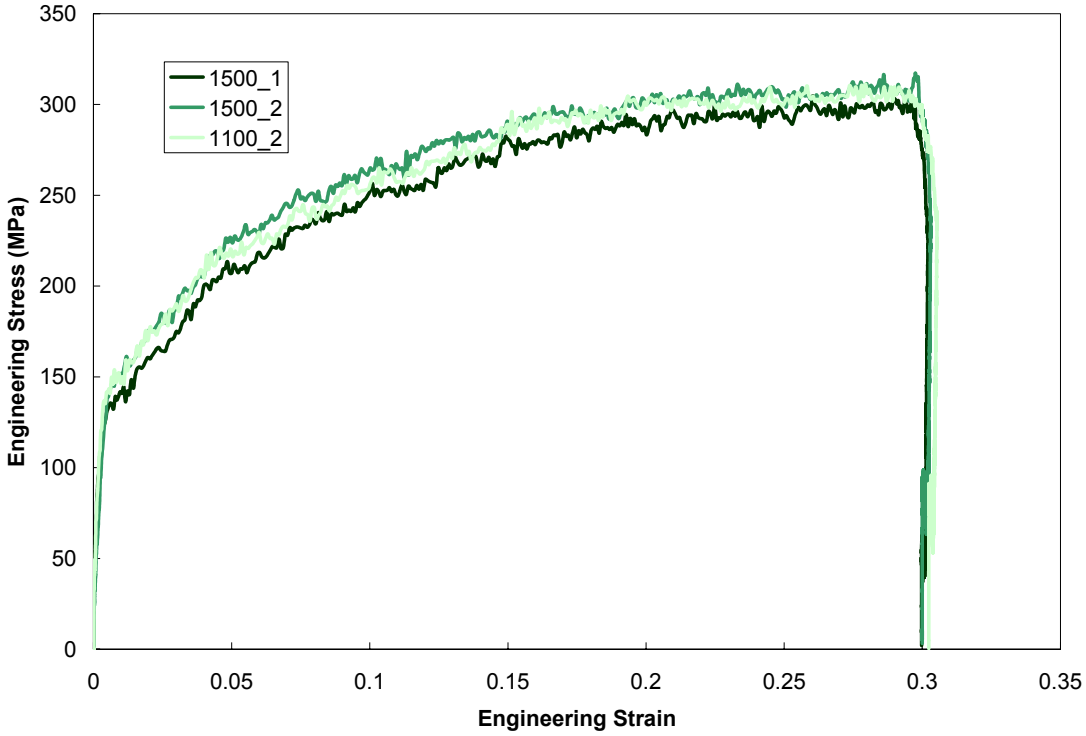
1500_1
1500_2
1100_2
Engineering Stress (MPa)
Engineering Strain
350
300
250
200
150
100
50
0
0
0.05
0.1
0.15
0.2
0.25
0.3
0.35

Appendix C3:

(Elevated Temperature Data at 600 s^{-1})

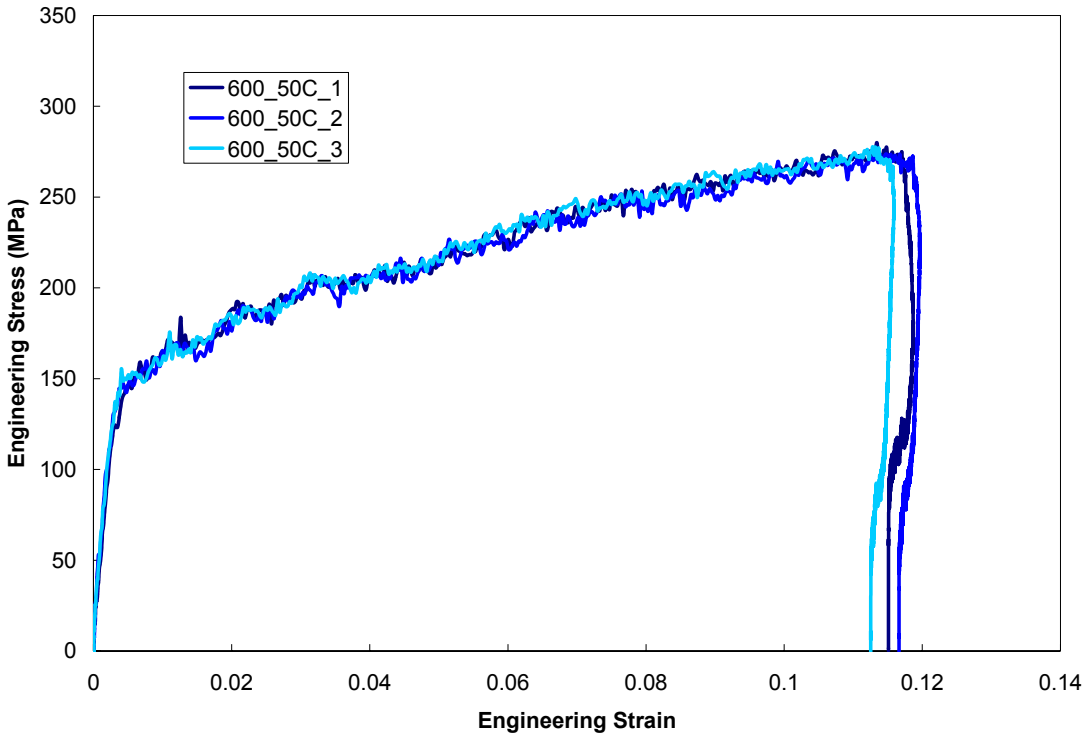

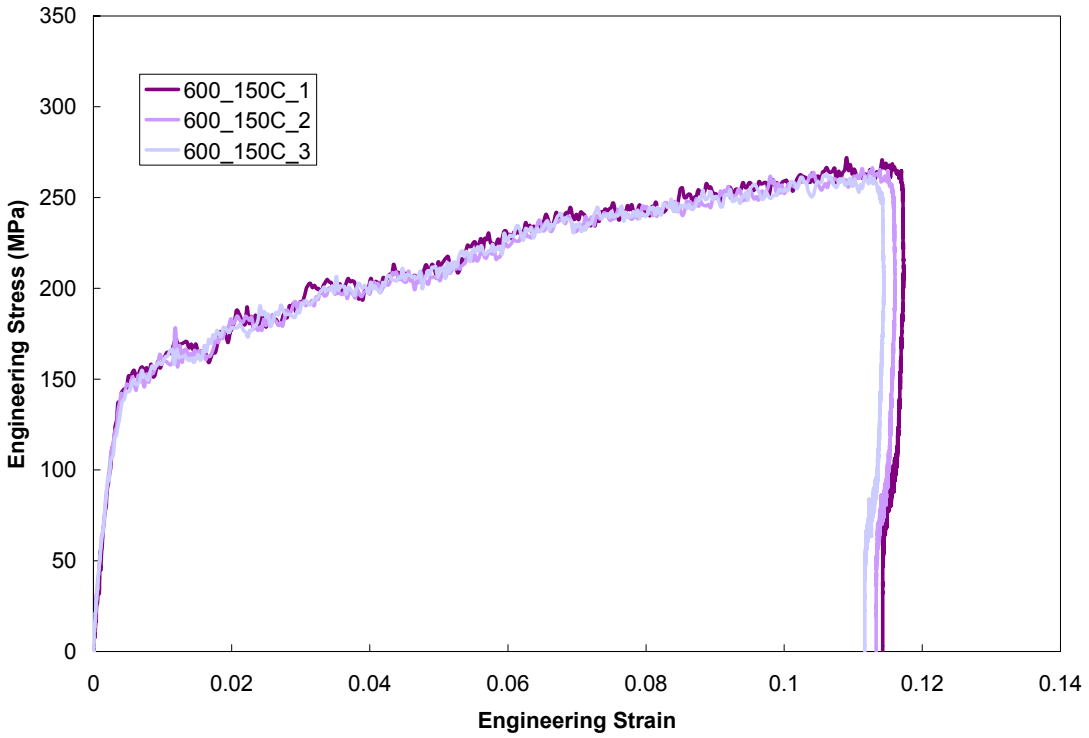

Appendix C4:

(Elevated Temperature Data at 1500 s^{-1})

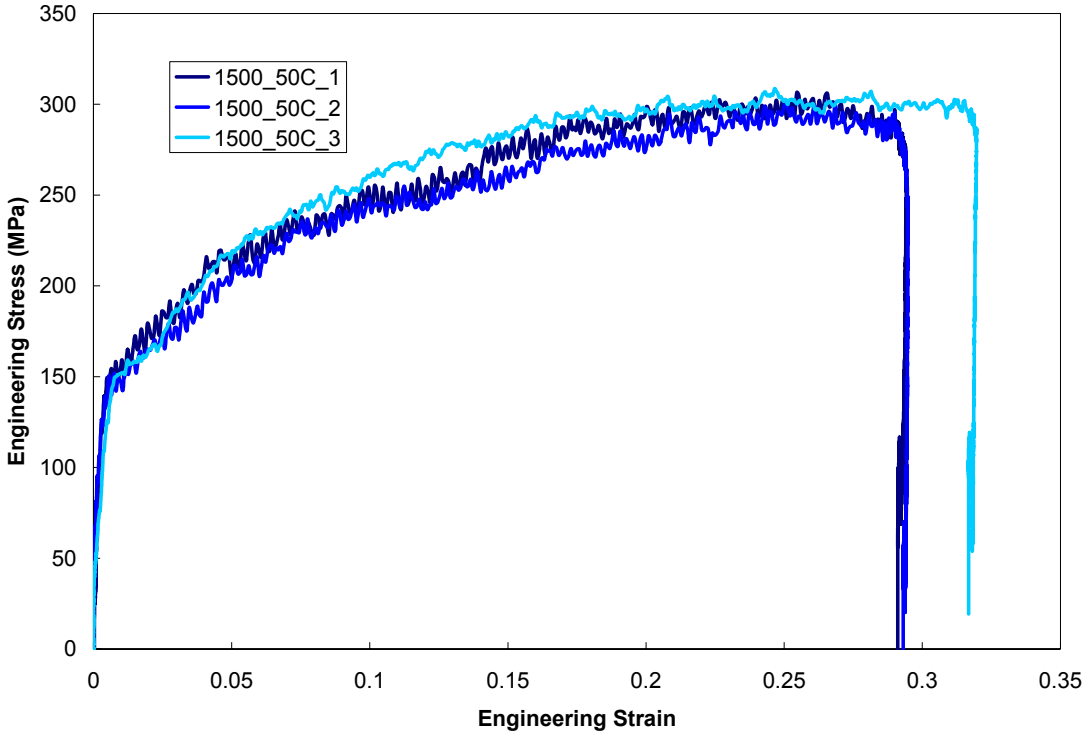

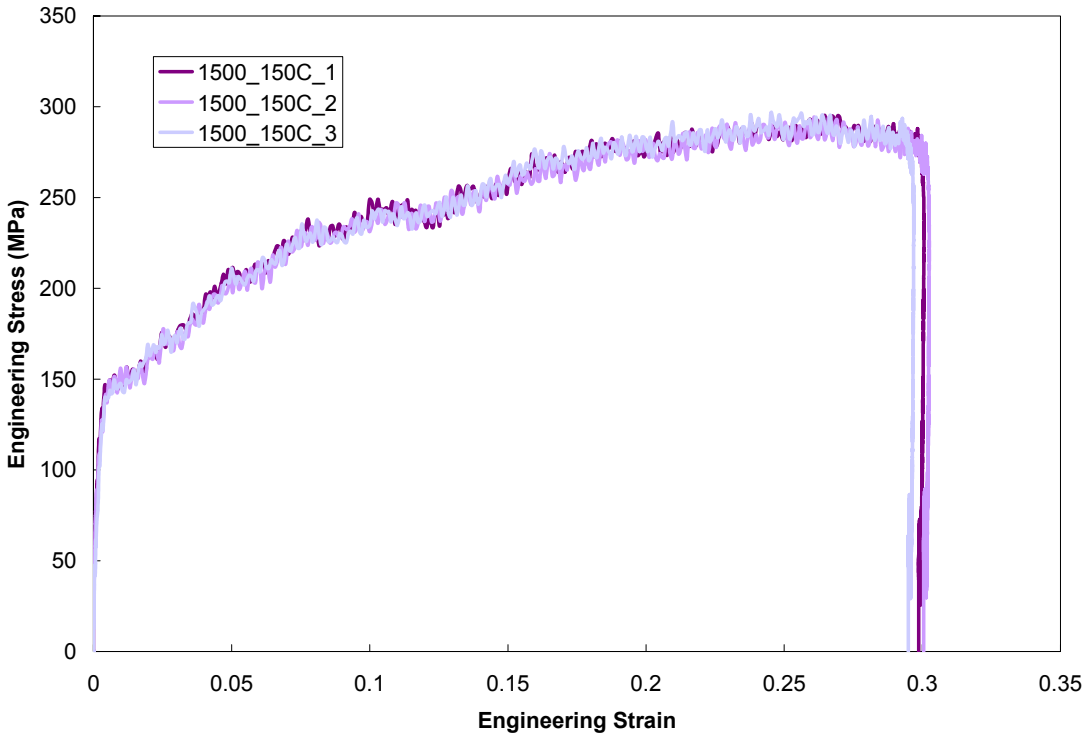

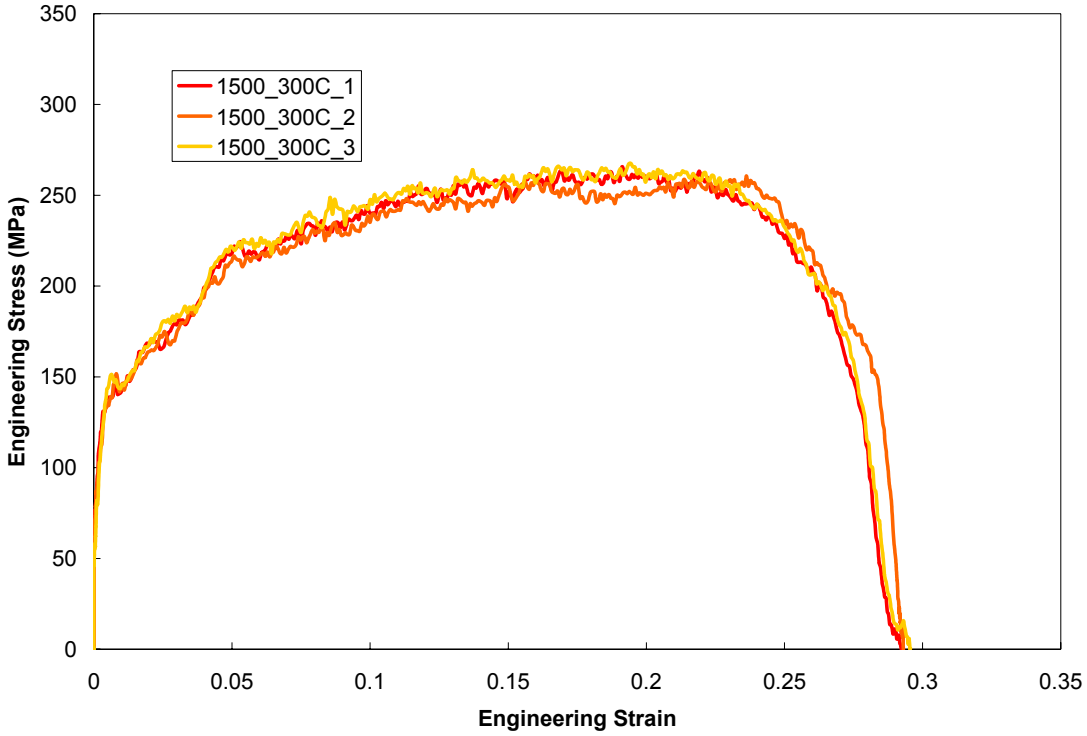
1500_300C_1
1500_300C_2
1500_300C_3
Engineering Stress (MPa)
Engineering Strain
350
300
250
200
150
100
50
0
0
0.05
0.1
0.15
0.2
0.25
0.3
0.35

Appendix D

Engineering Stress-Strain Data for 1 mm AA5182

Note: The reader should be made aware that the specimens were loaded multiple times to failure, as described in Chapter 2. Hence, stress-strain responses are shown only for the first loading pulse. The elongation was determined by directly measuring the failed specimens.

Specimen	G. Length (mm)	Width (mm)	Thickness (mm)	Strain Rate (s^{-1})	Temperature (ºC)	Elongation (%)
QS_1	12.5	1.74	1.00	0.003304	RT	31.4
QS_2	12.5	1.75	1.00	0.003306	RT	28.4
QS_3	12.5	1.70	0.99	0.003296	RT	30.1
600_1	12.5	1.76	0.99	603	RT	40
600_2	12.5	1.76	0.96	616	RT	36.9
600_3	12.5	1.73	1.02	608	RT	39.8
1100_1	12.5	1.79	1.00	1098	RT	37.9
1100_2	12.5	1.80	1.00	1116	RT	44.9
1100_3	12.5	1.71	0.99	1123	RT	44.2
1500_1	12.5	1.77	1.01	1529	RT	39.4
1500_2	12.5	1.77	0.98	1539	RT	43.3
1500_3	12.5	1.77	1.01	1525	RT	42.5
600_50C_1	12.5	1.77	0.97	610	50	39.2
600_50C_2	12.5	1.79	0.99	611	50	39
600_50C_3	12.5	1.77	0.98	613	50	38.6
1500_50C_1	12.5	1.76	0.99	1563	50	44.6
1500_50C_2	12.5	1.76	1.01	1518	50	43.1
1500_50C_3	12.5	1.76	0.98	1564	50	41
600_150C_1	12.5	1.76	1.00	610	150	36.1
600_150C_2	12.5	1.76	1.02	613	150	36.6
600_150C_3	12.5	1.77	1.00	614	150	38.2
1500_150C_1	12.5	1.81	1.00	1552	150	37.6
1500_150C_2	12.5	1.74	1.00	1547	150	37.5
1500_150C_3	12.5	1.80	0.99	1567	150	37.4
1500_300C_1	12.5	1.78	1.01	1564	300	27.9
1500_300C_2	12.5	1.75	0.99	1581	300	27.7
1500_300C_3	12.5	1.80	1.03	1586	300	29.4

Appendix D1:
(Quasi-static Data)

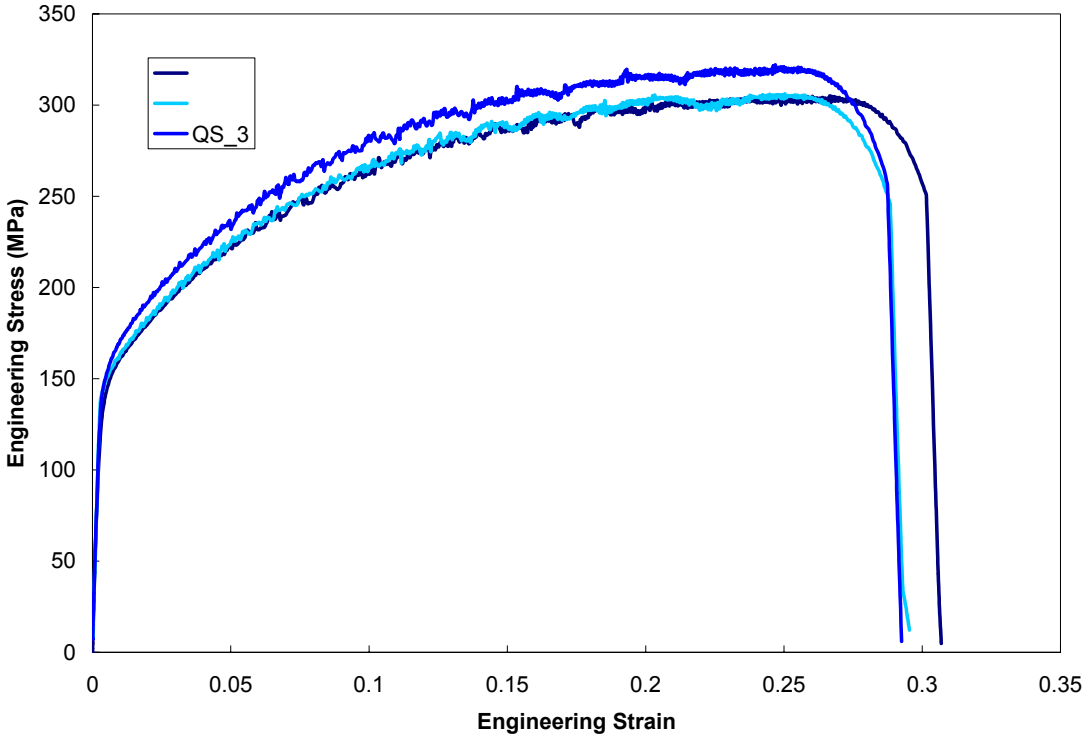

Appendix D2:

(High Strain Rate Data at Room Temperature)

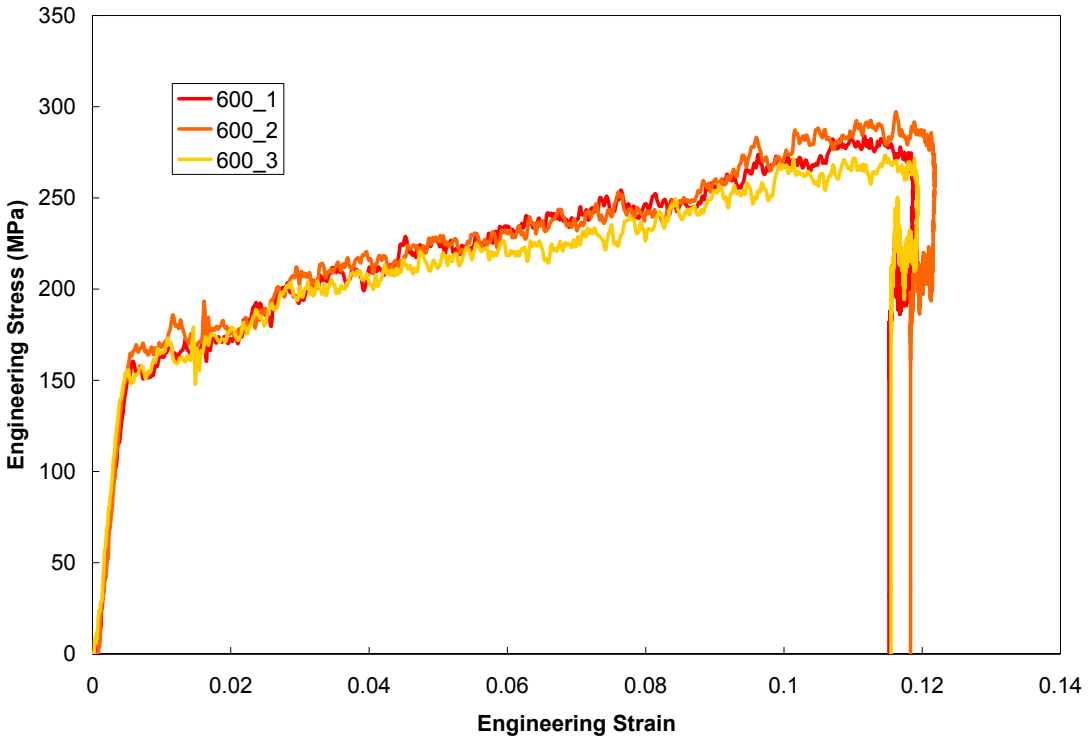

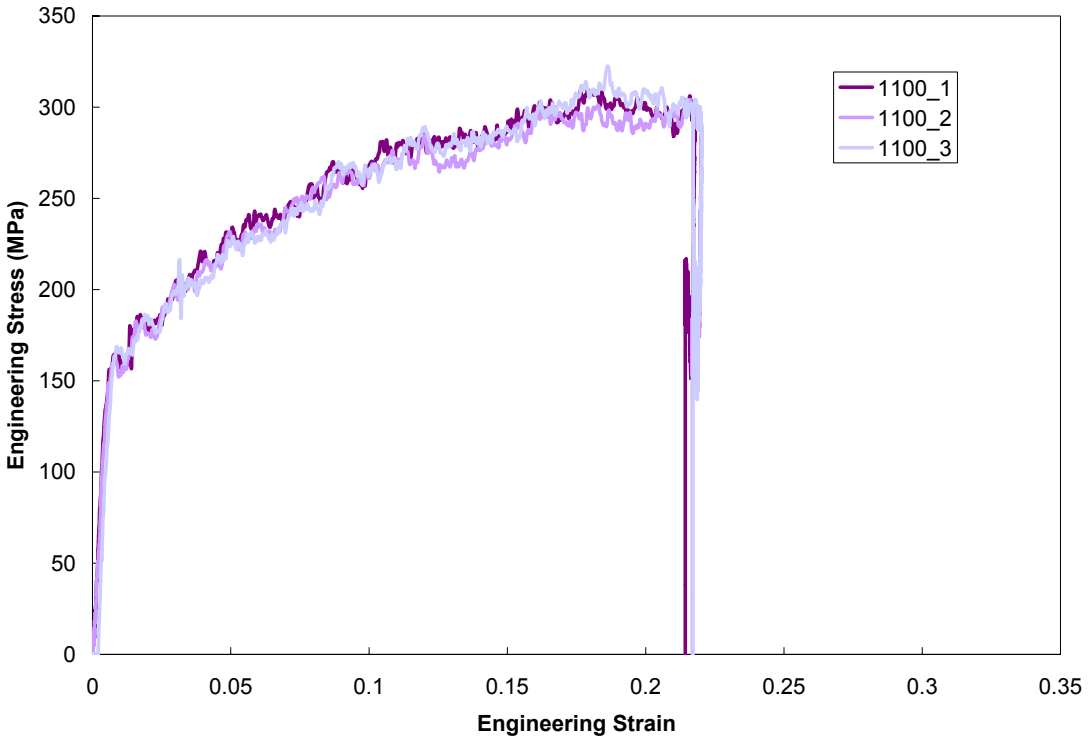

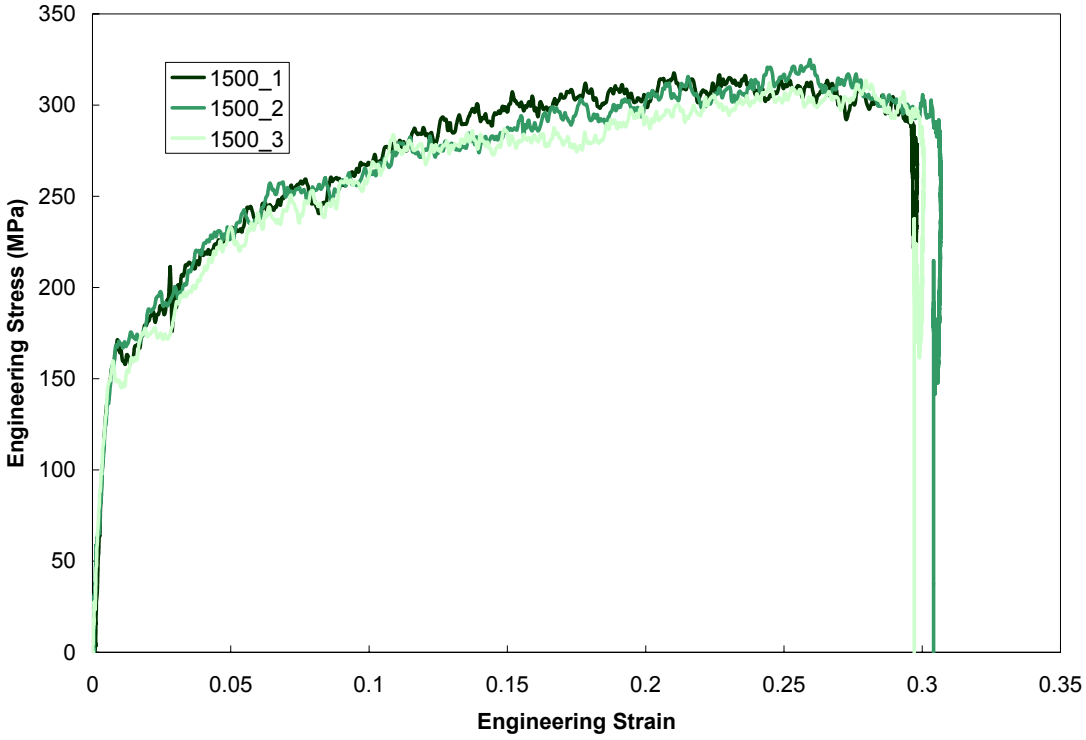
1500_1
1500_2
1500_3
Engineering Stress (MPa)
Engineering Strain
350
300
250
200
150
100
50
0
0
0.05
0.1
0.15
0.2
0.25
0.3
0.35

Appendix D3:

(Elevated Temperature Data at 600 s^{-1})

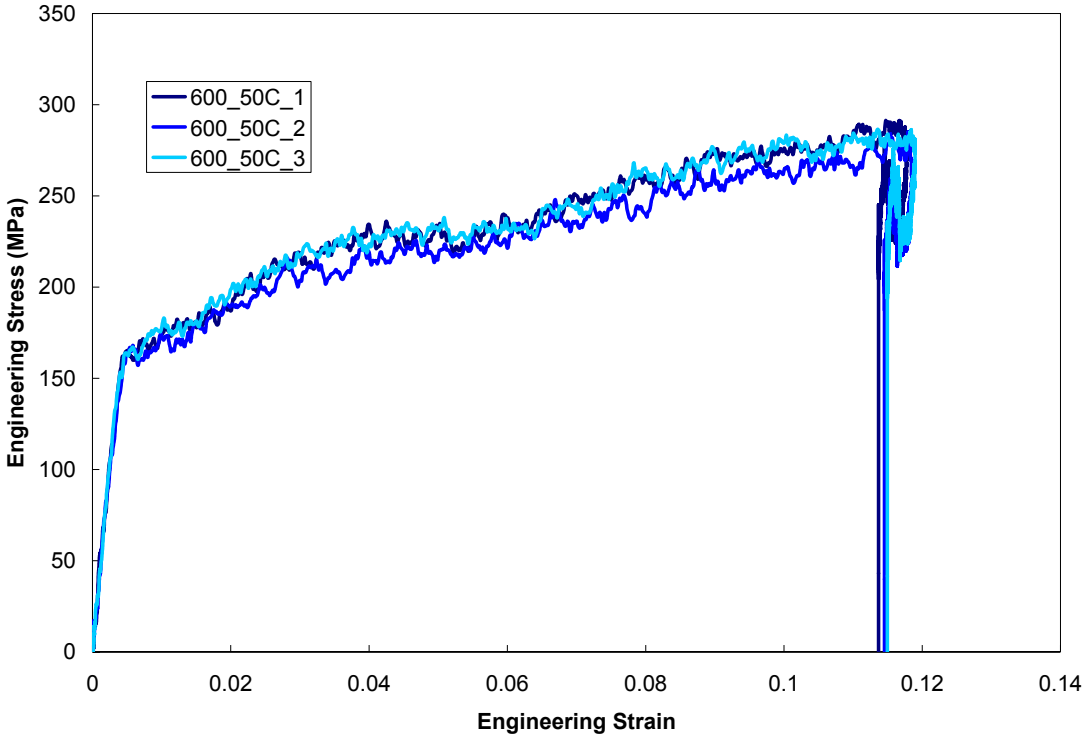

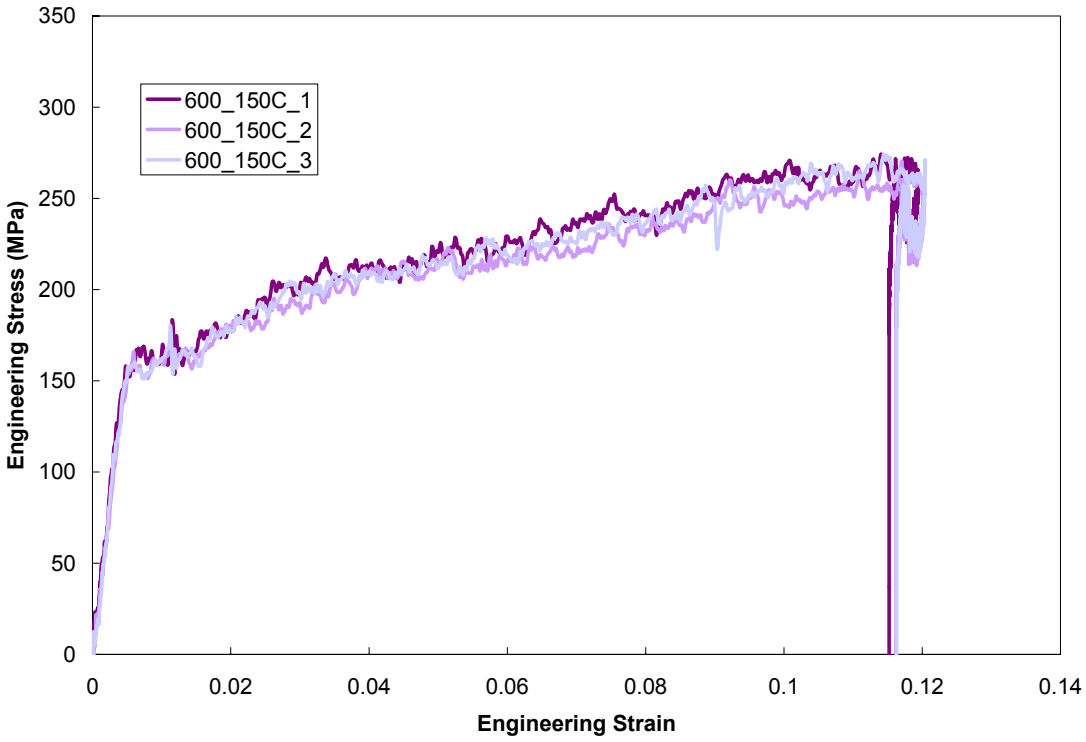

Appendix D4:

(Elevated Temperature Data at 1500 s^{-1})

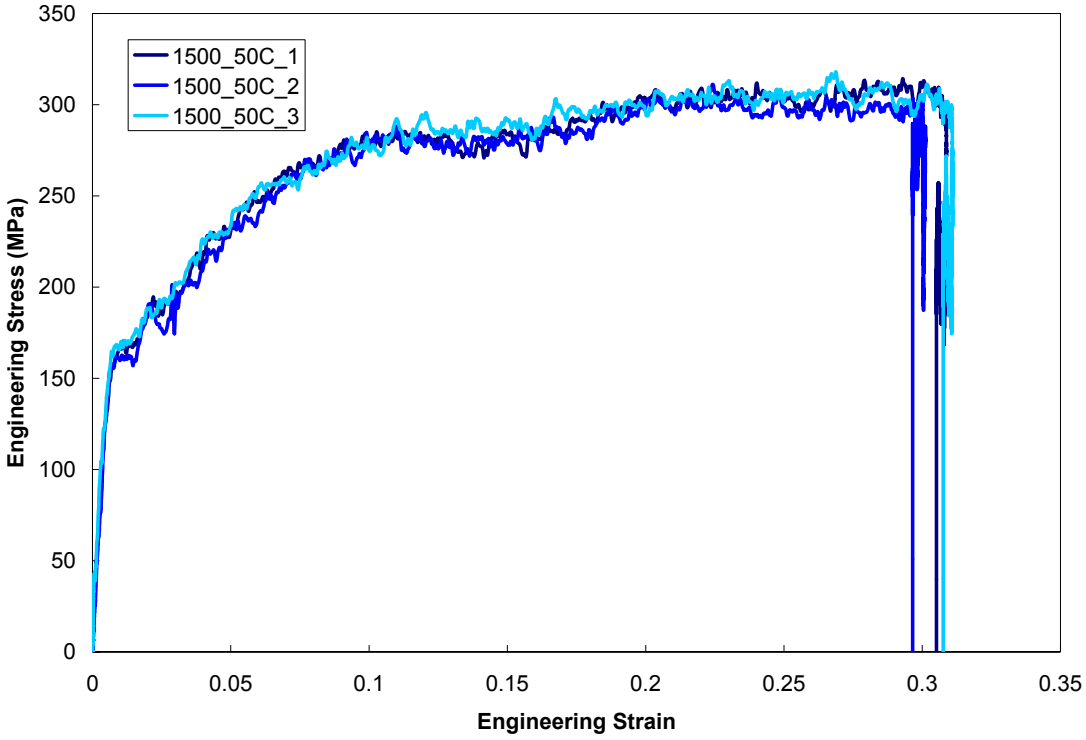

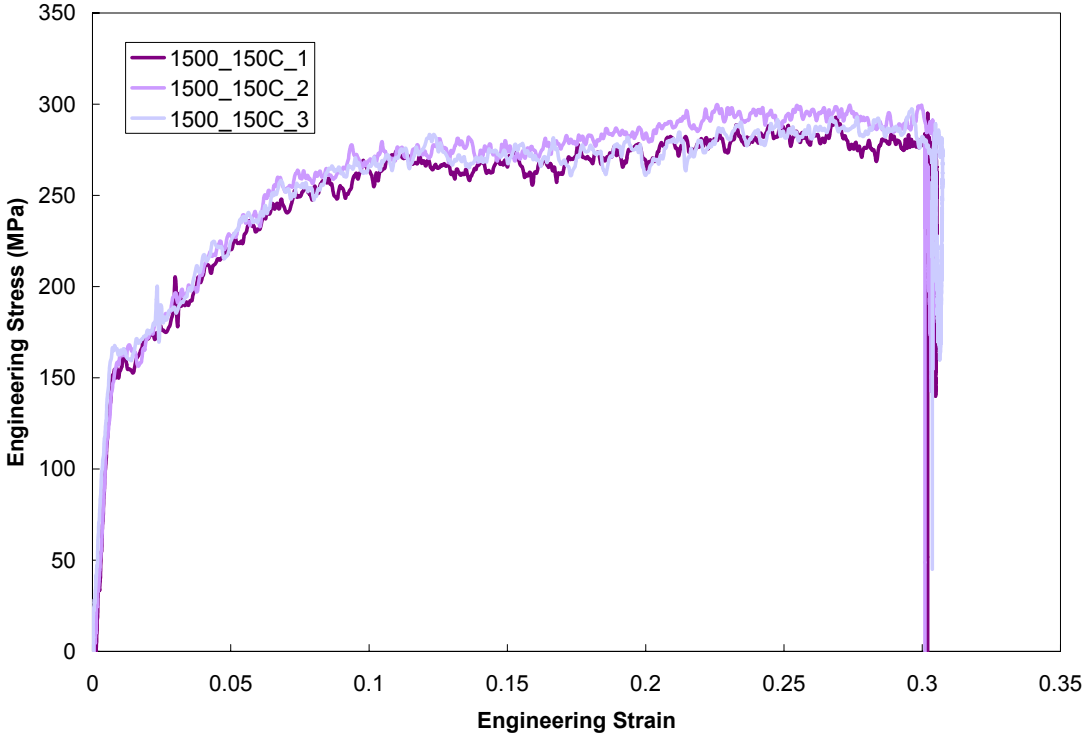

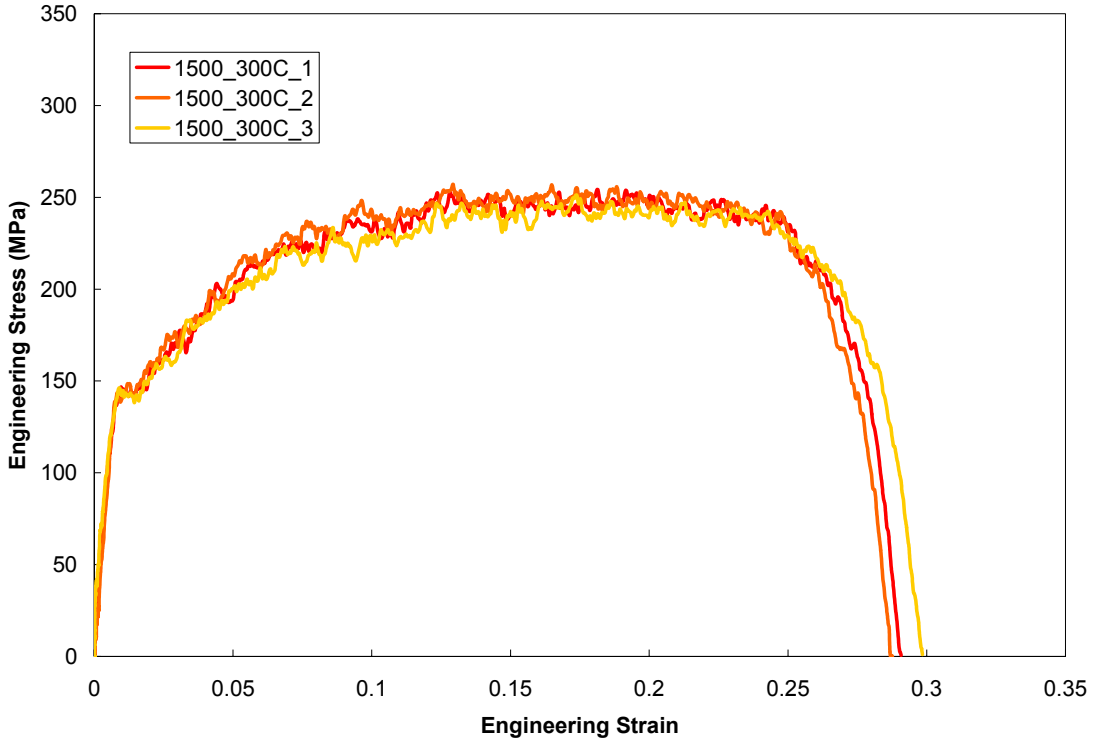
1500_300C_1
1500_300C_2
1500_300C_3
Engineering Stress (MPa)
Engineering Strain
350
300
250
200
150
100
50
0
0
0.05
0.1
0.15
0.2
0.25
0.3
0.35

Appendix E

Engineering Stress-Strain Data for 1 mm AA6111

Note: The reader should be made aware that the specimens were loaded multiple times to failure, as described in Chapter 2. Hence, stress-strain responses are shown only for the first loading pulse. The elongation was determined by directly measuring the failed specimens.

Specimen	G. Length (mm)	Width (mm)	Thickness (mm)	Strain Rate (s^{-1})	Temperature (ºC)	Elongation (%)
QS_1	12.5	1.72	0.97	0.003285	RT	28.1
QS_2	12.5	1.70	0.96	0.003309	RT	28.1
QS_3	12.5	1.70	0.96	0.003292	RT	27.3
600_1	12.5	1.76	0.96	618	RT	32.8
600_2	12.5	1.75	1.00	622	RT	32.2
600_3	12.5	1.75	0.99	623	RT	36.2
1100_1	12.5	1.80	0.99	1089	RT	36.7
1100_2	12.5	1.78	0.99	1115	RT	36.3
1100_3	12.5	1.75	0.95	1126	RT	37.2
1500_1	12.5	1.80	1.00	1519	RT	38
1500_2	12.5	1.79	0.99	1527	RT	38.4
1500_3	12.5	1.81	0.99	1519	RT	35.8
600_50C_1	12.5	1.77	0.97	588	50	33.6
600_50C_2	12.5	1.78	0.96	593	50	34
600_50C_3	12.5	1.77	0.97	594	50	33.6
1500_50C_1	12.5	1.79	1.00	1568	50	31.7
1500_50C_2	12.5	1.78	0.98	1574	50	33.8
1500_50C_3	12.5	1.75	0.98	1568	50	32.1
600_150C_1	12.5	1.79	1.00	596	150	38.5
600_150C_2	12.5	1.78	0.99	596	150	35
600_150C_3	12.5	1.79	1.00	596	150	36.2
1500_150C_1	12.5	1.81	1.00	1576	150	34.6
1500_150C_2	12.5	1.74	1.00	1598	150	32.8
1500_150C_3	12.5	1.80	0.99	1570	150	34.4
1500_300C_1	12.5	1.77	0.99	1558	300	26.2
1500_300C_2	12.5	1.80	0.99	1563	300	28.1
1500_300C_3	12.5	1.80	1.00	1411	300	26.9

Appendix E1:
(Quasi-static Data)

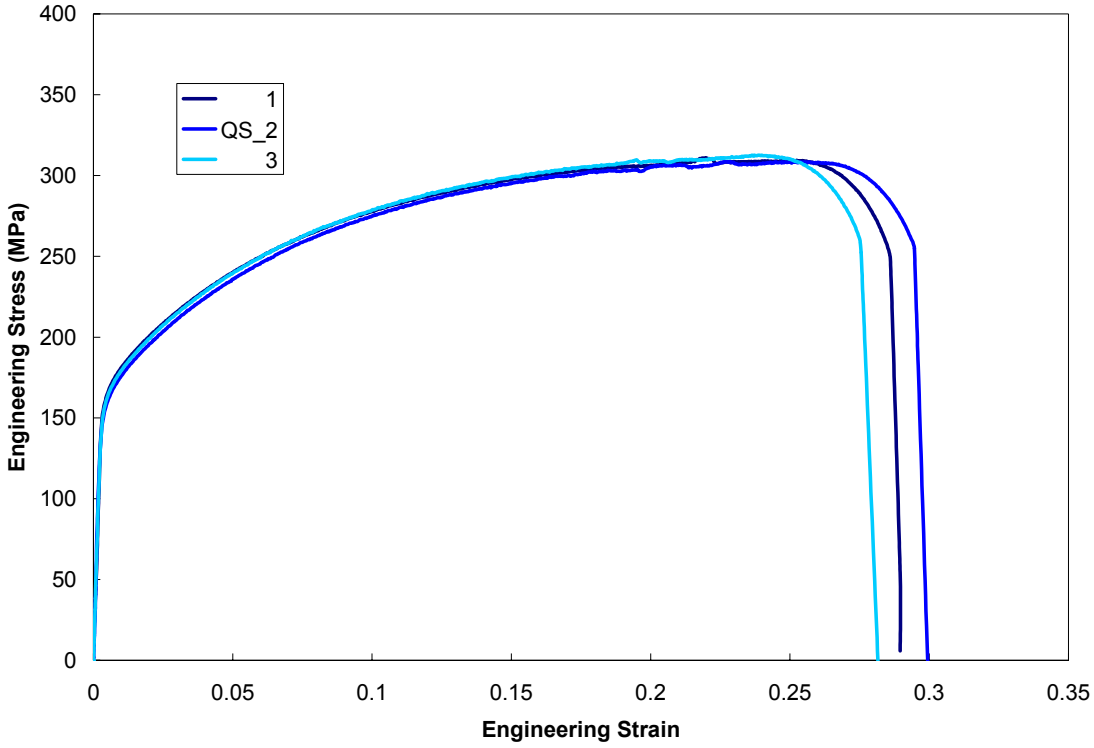

Appendix E2:

(High Strain Rate Data at Room Temperature)

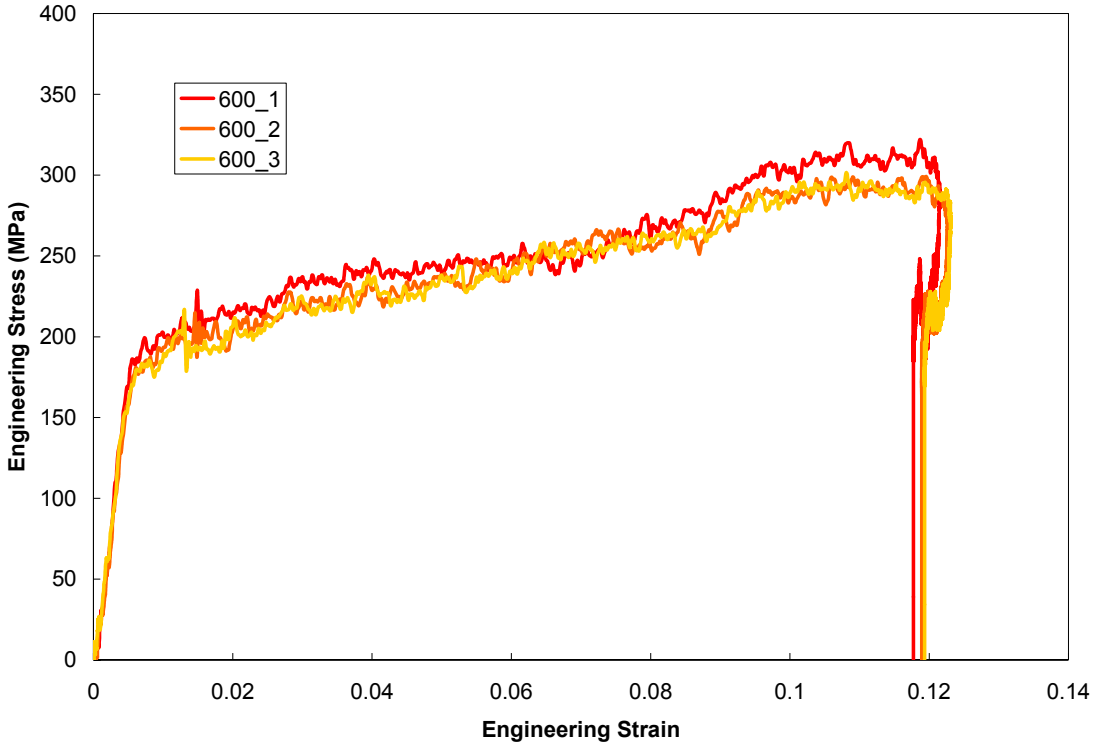

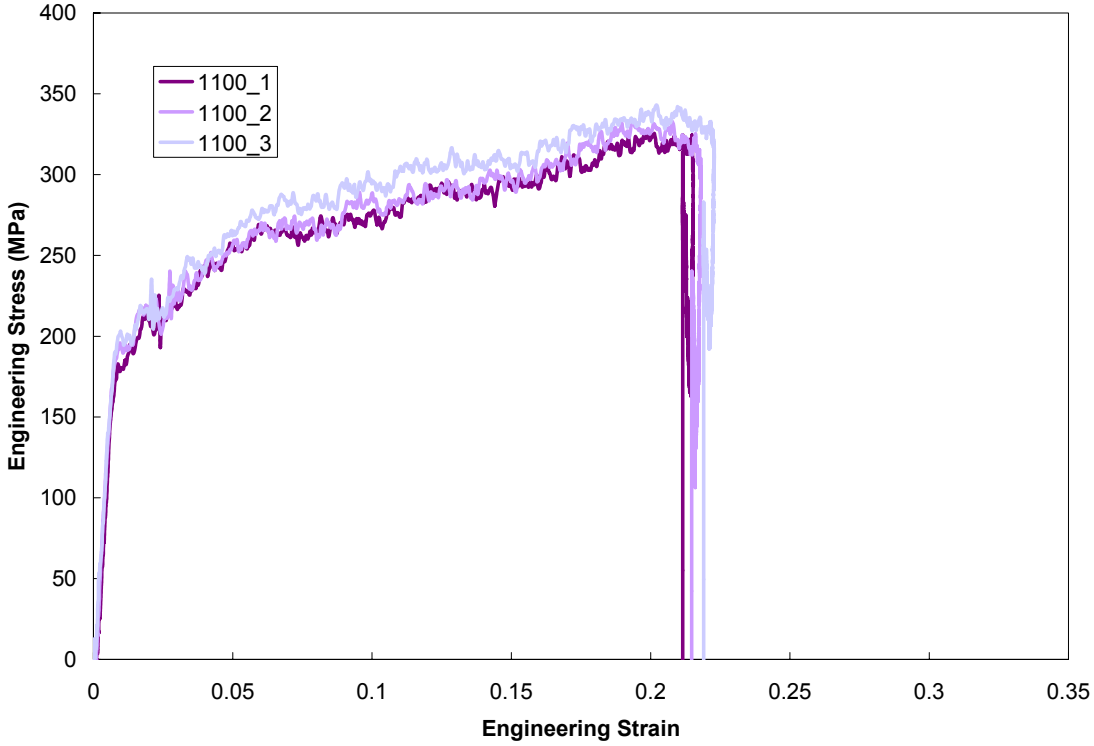

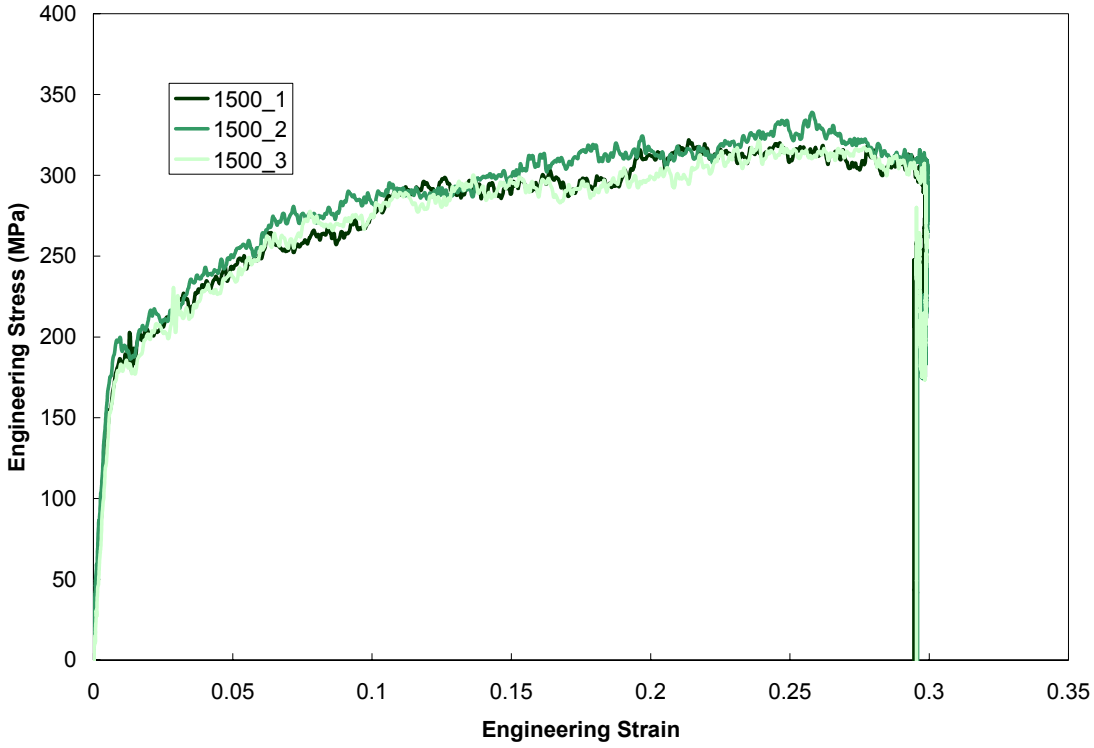
400
350
300
250
200
150
100
50
0
Engineering Stress (MPa)
1500_1
1500_2
1500_3
0
0.05
0.1
0.15
0.2
0.25
0.3
0.35
Engineering Strain

Appendix E3:

(Elevated Temperature Data at 600 s^{-1})

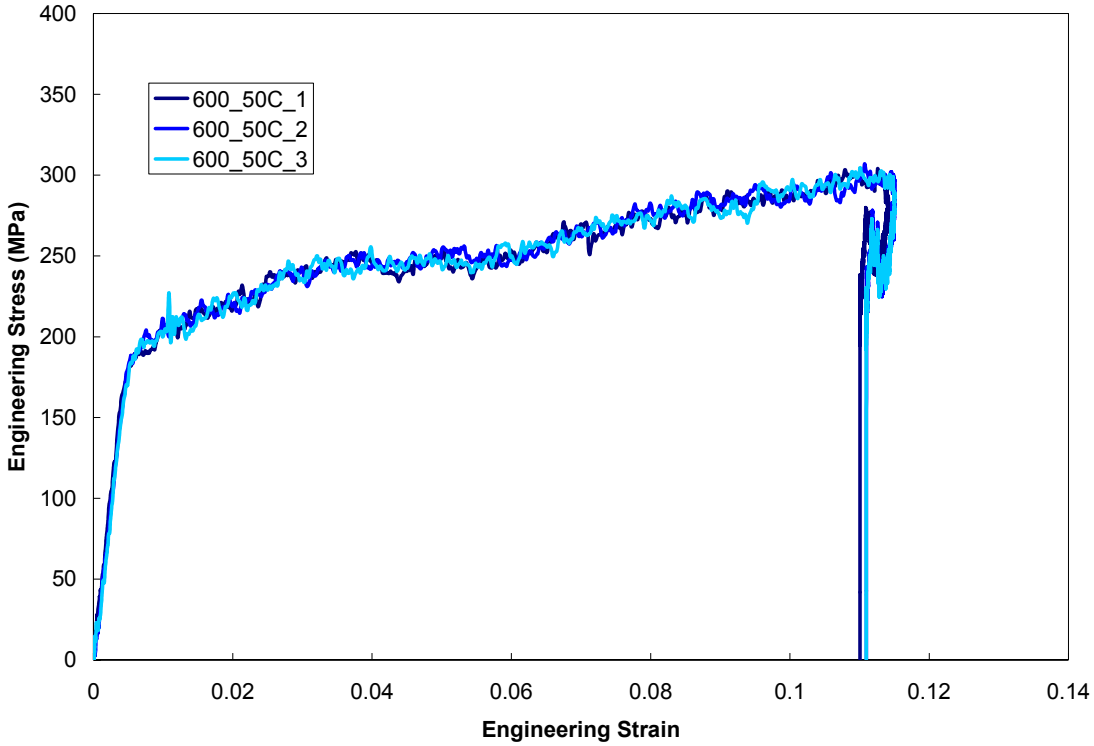

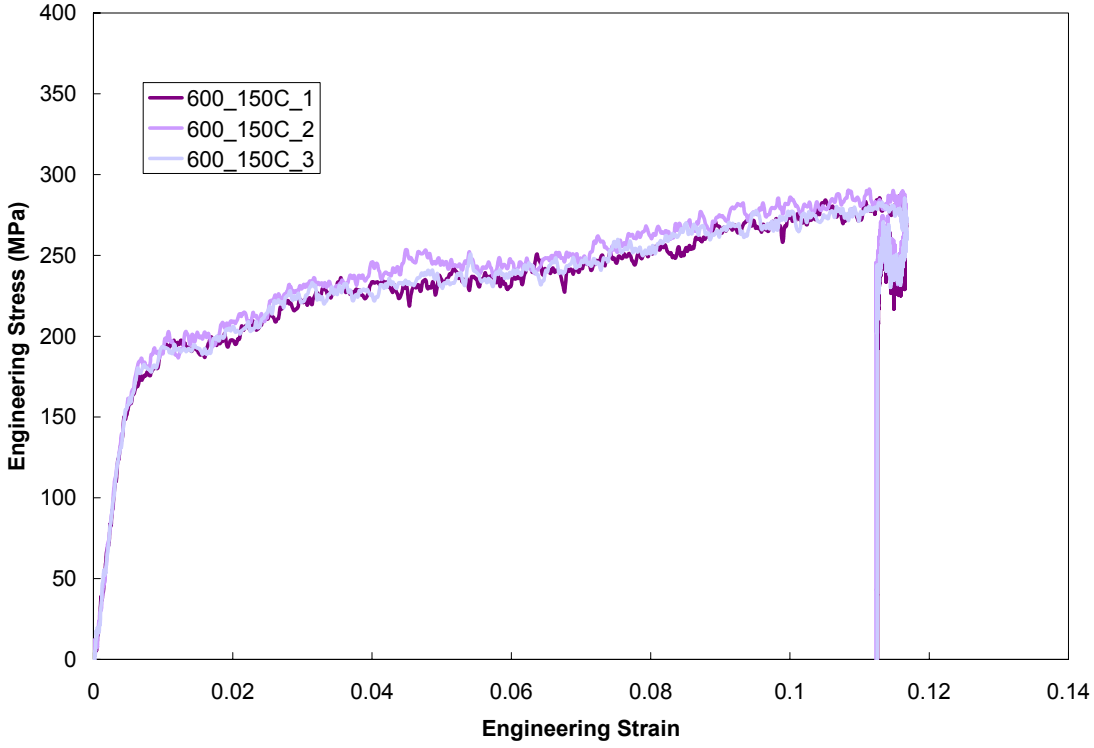

Appendix E4:

(Elevated Temperature Data at 1500 s^{-1})

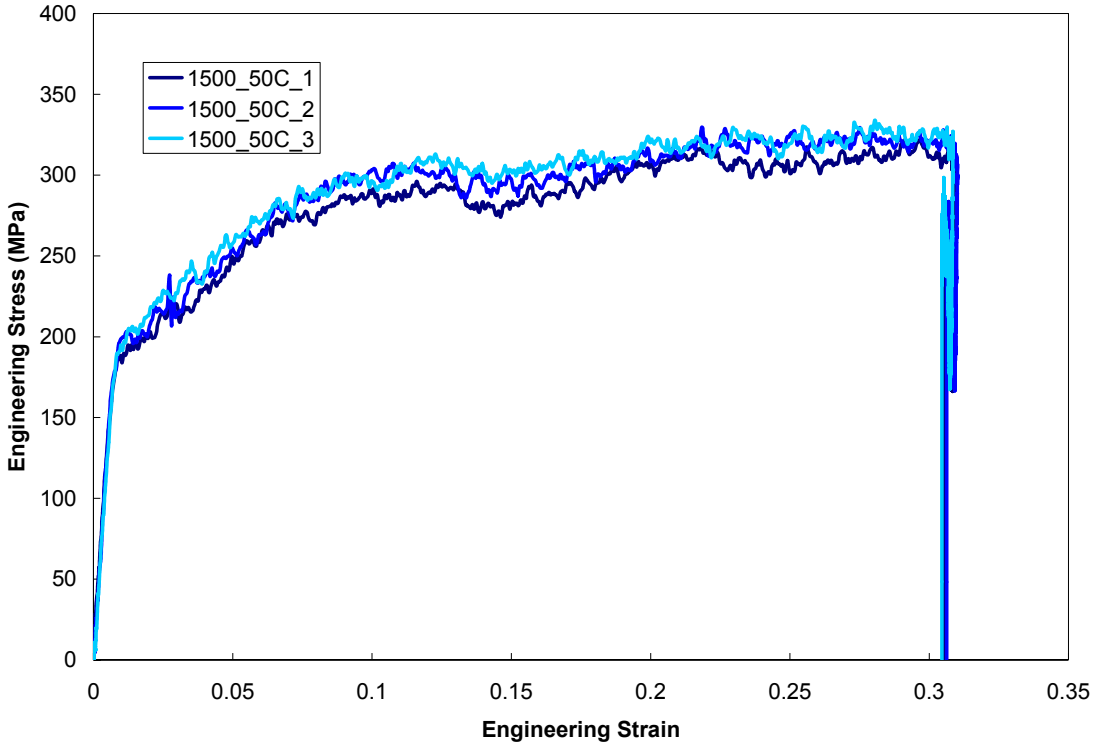

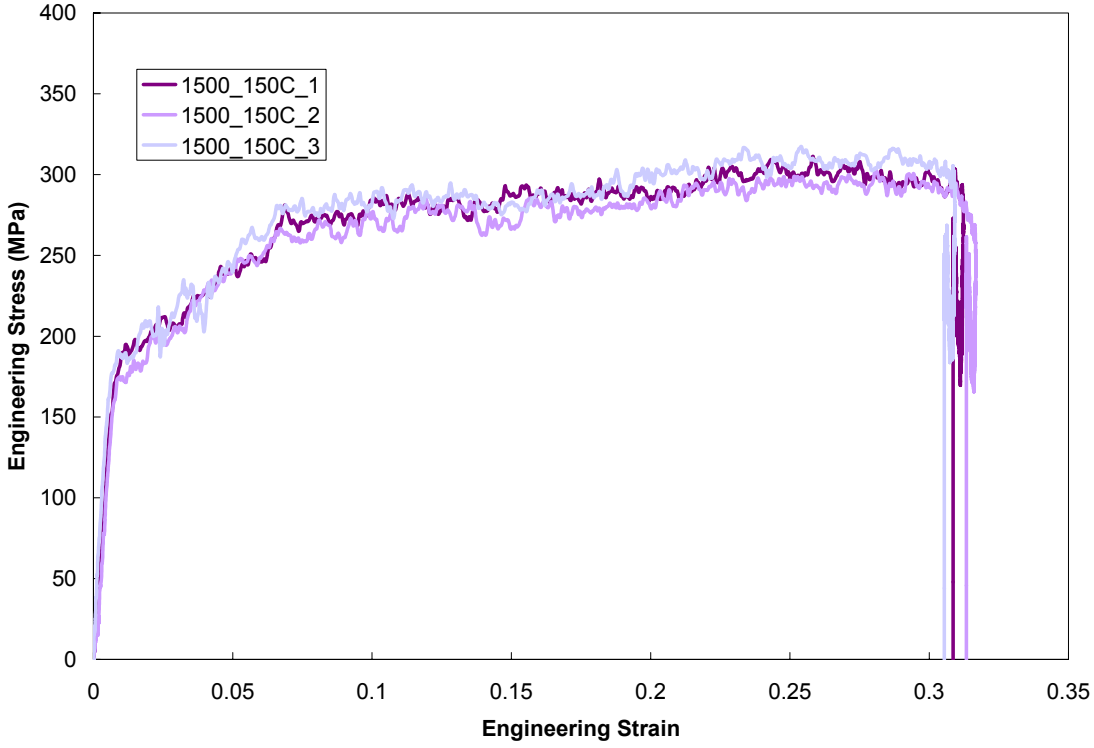

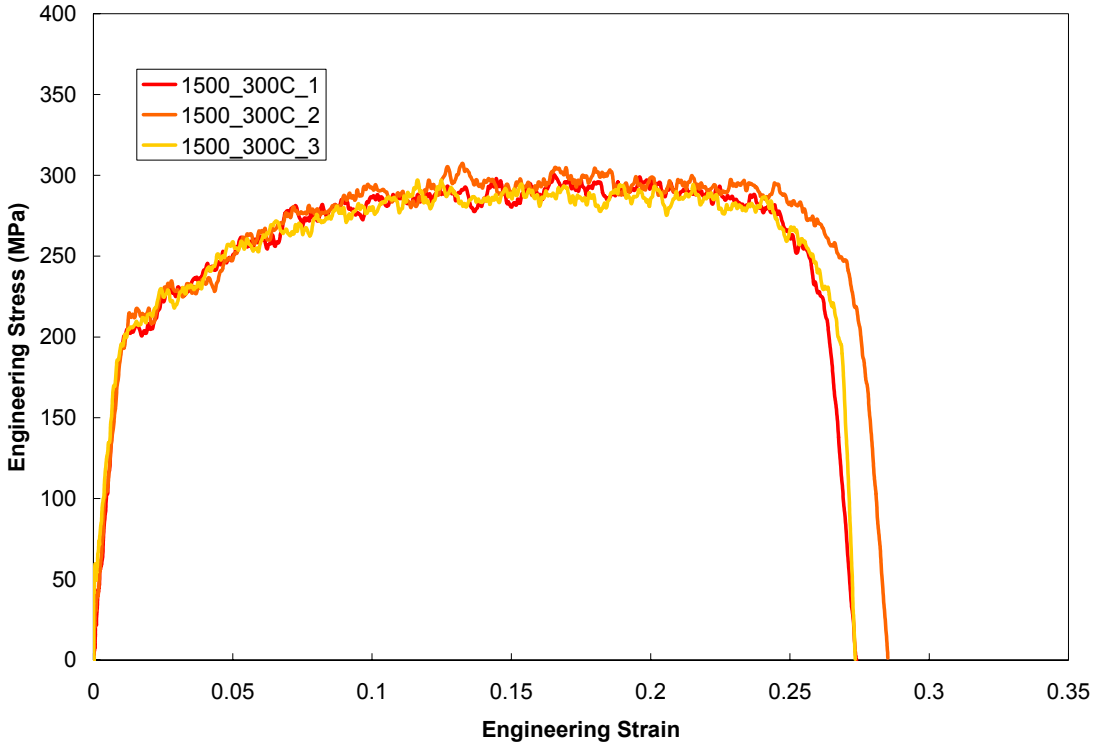
1500_300C_1
1500_300C_2
1500_300C_3
Engineering Stress (MPa)
Engineering Strain
400
350
300
250
200
150
100
50
0
0
0.05
0.1
0.15
0.2
0.25
0.3
0.35